Metallurgical Risk Factors in Grade 91 Steel

by

Sharhid Jabar

A thesis submitted in partial fulfilment of the requirements for the degree of Doctor of

Philosophy in Engineering at the University of Warwick

The department of Warwick Manufacturing Group, Advanced Steel Research Centre

May 2022

Table of Contents

Acknowledgements

I would like to thank God and my religion of Islam for instilling a disciplined and moral way of life in which I dealt with many ups and downs during my 4+ year PhD journey. I would like to thank my parents, family and partner for their everlasting support and an upbringing which always pointed me in the direction of education and knowledge.

I would like to acknowledge my colleagues whom I've befriended along my PhD journey; Dr Arunava Sengupta, Bruno Rodriguez, Martin Olowe, Dr Bharath Bandi, Theint Theint Htet, Dr Ishwar Kapoor, Anand Mohan, Yu Xiong, Dr Jiaqi Duan, Dr Carl Slater, Cameron Bee, Dr Darbaz Khasraw, Josephine White, Simon Pitt, Keith Andrews, Dr Fanfu Wu, Dr Hiren Kotadia, Numan Islam, Raheil Khan, Kashmir Bassi, (and those who I have missed) and my everlasting friendship with Dr Mir-Hamza Khan.

Thanks to the staff at WMG I have been able to complete all my work, this includes Professor Claire Davis, Professor Barbara Shollock, Dr Sam Marks, Dr Sabrina Yan, Dr Fengzai Tang, Tom Moore, Dr Evans Mogire, Mick Green, Dr Prakash Srirangam and the entire advanced steel research team. Furthermore, I would like to thank the Loughborough Surface Analysis (LSA) team for the SIMS work presented in this thesis.

I am grateful to the Electric Power Research Institute (EPRI), due to their funding and support of this project I was able to take up such an opportunity. This includes my industrial supervisor Dr John A Siefert and Dr Tapsavi Lolla, Dr Jon D Parker and the rest of the EPRI team.

Last but not least, I would like to express sincere gratitude to my academic supervisors Dr Geoffrey D West and Dr Martin Strangwood for his knowledge and discussions with publishing work and thesis writing.

Declaration

I, Sharhid Jabar can confirm that the work presented in this thesis is my own. It has been written and compiled by myself and has not been submitted anywhere else. The work in this thesis has been undertaken by me except where stated otherwise.

SHARHID JABAR
May 2022

Publications

S. Jabar, J. A. Siefert, M. Strangwood, and G. D. West. A Standardised Procedure for the Quantification of Inclusions in Grade 91 Steels. In Progress.

S. Jabar, J. A. Siefert, M. Strangwood, and G. D. West. The Effect of Micro-Segregation on the Quantification of Microstructural Parameters in Grade 91 Steel. Metallurgical and Materials Transactions A 52, 426–437 (2021). https://doi.org/10.1007/s11661-020-06062-y

S. Jabar, J.A. Siefert, B. Shollock and G.D. West. Metallurgical risk factors in Grade 91 steel. Joint EPRI-123HiMAT International Conference on Advances in High-Temperature Materials, 235–245 (2019).

G. D. West, J.A. Siefert, B. Shollock, T. Lolla and **S. Jabar**. A standardised approach for the quantification of microstructure in 9Cr steels. Joint EPRI-123HiMAT International Conference on Advances in High-Temperature Materials, 294–303 (2019).

Abstract

The quantification of key microstructural parameters as a function of creep conditions is commonplace in the assessment of Grade 91 and other creep strength enhanced ferritic (CSEF) power-plant steels. This thesis analyses a broad range of Grade 91 steels which include, ex-service, developmental and more recently produced steels; each distinct in terms of creep performance and composition. Characterisation was performed using a combined series of techniques that provided through-length scale chemical analysis and site-specific quantification.

Initial steps involved quantitatively assessing the chemical homogeneity of the steels using micro-X-ray fluorescence (μ-XRF) and scanning electron microscope (SEM) based chemical mapping. All steels displayed micro-segregation although it was greatest in the ex-service steels. In these steels the micro-hardness was found to vary from 190 to 225 HV primarily due to compositional heterogeneity caused by micro-segregation. Focussed ion beam (FIB-SEM) imaging and thin foil lift-outs analysed using scanning transmission electron microscopy (STEM) chemical mapping showed area coverages of $M_{23}C_6$ carbides and V-rich carbo-nitrides were greater in positively segregated regions. Site-specific quantification using SEM-back scattered electron (BSE) imaging of the Laves phase showed a difference of up to a factor of two in the number density of particles and area coverage due to micro-segregation. For ex-service steels this was consistent with thermo-dynamic predictions. A procedure for quantification of inclusions was developed which considered optimal voltage parameters investigated through studies and simulations, micro-segregation effects and fine (down to 0.25 μm) inclusions. These are all important deviations from conventional automated SEM procedures.

This work shows that micro-segregation can have significant effects on micro-hardness and characteristics of various second phase particles. Since the performance of a material is likely to be controlled by local microstructural extremes rather than average properties, these findings have important implications for the characterisation and failure assessment of Grade 91 and other CSEF steels.

List of Abbreviations

μ-XRF – Micro X-ray fluorescence

ASTM – American society for testing and materials

BCC – Body centred cubic

BF – Bright field

BSE – Back-scattered electron

CER – Carbon extraction replica

CSEF – Creep strength enhanced ferritic

DF – Dark field

DOE – Department of energy

DTSA-II – Desk-top spectrum analyser 2

ECD – Equivalent circle diameter

EDS – Energy dispersive X-ray spectroscopy

EMS – Electromagnetic stirring

EPRI – Electric Power Research Institute

ESR – Electro-slag remelting

FCC – Face centred cubic

FEG-SEM – Field emission gun scanning electron microscope

FIB-SEM – Focussed ion beam scanning electron microscope

Gr. 91 – Grade 91

Gr. 92 – Grade 92

HFW – Horizontal field width

ICP-OES/MS – Inductively coupled plasma-optical emission spectrometry / mass spectrometry

IGF – Inert gas fusion

JFE – Japan Fe engineering (steel corporation)

kgf – Kilogram force

LCAK – Low carbon aluminium killed

LSA – Loughborough Surface Analysis

MJF – Modified J-factor

NMI – Non-metallic inclusion(s)

ORNL – Oak Ridge National Laboratory

ROA – Reduction of area

SCRA – Systematically collected random areas

SDAS – Secondary dendrite arm spacing

SDD – Silicon drift detector

SE – Secondary electron(s)

SEM – Scanning electron microscope

SIMS – Secondary ion mass spectroscopy

STEM – Scanning transmission electron microscope

TEM – Transmission electron microscope

TRC – Twin-roll strip continuous casting

List of Tables

List of Figures

Chapter 1 : Introduction

1.1 Background

Since the global energy crisis in the 1970s, increasing efforts have been made to improve the efficiency of power generation plant [1][2]. An outcome of the drive for increased fossil fuelled power plant efficiency was the elevation of steam conditions, with the construction of the first super-critical (SC) plant in 1989 (31 MPa at 566 °C), this was the first increase in steam conditions in over 20 years. Subsequently, newly erected power plant continued to raise steam conditions (up to 24 MPa at 600 °C) reaching efficiencies of up to 42% [3][4]; elevated steam pressures and temperatures reduce the turbine cycle heat consumption, therefore, increasing turbine efficiency. Joint international efforts between Japan, Europe and the USA were launched in the early 1980s to achieve ultra super-critical (USC) conditions (exceeding conventional super-critical conditions) using ferritic 9-12 wt % Cr steels. Previous generation plants were designed to function on a single load with no adjustment function. These requirements were well met by austenitic stainless steels, however for the modern start-stop on demand cycles, ferritic steels provide a much smaller thermal expansion coefficient for thick-walled components (~50% [4]), which in turn reduce thermal stresses from heating and cooling, alleviating any fatigue failures [2][4] and since have been the material of choice. Now regarded as creep strength enhanced ferritic (CSEF) steels, as of 2013 the range consists of 9 wt % Cr steels (Gr. 91, Gr. 92, Gr. 911), 12 wt % Cr steel (Gr. 122) and 2.25 wt % Cr steels (Gr. 23, Gr. 24). Grade 91 (Gr. 91) was developed in the USA, Gr. 911 and Gr. 24 in Europe and the other 4 steels in Japan [5]. *Figure 1.1* shows the evolution in development of these steels as well as some of the latest projects currently under development. It can be seen that most of the improvements in creep performance were related to the substitution (partly or fully) of Mo by W, and the controlled additions or refinement of V, Nb, Co and B [6]. Today fossil fuelled power plant are still the major contributors to electricity generation in the world [7]. This is because, although renewable energy sources are increasing, so is the world population and demand due to for example the electrification of the automotive industry. Furthermore, renewable infrastructure can be rather intermittent (e.g. wind energy), therefore, fossil fuelled power plant are

required to provide the shortfall from renewable sources when required to do so [8] (also tying in with the need for stop-start functions mentioned earlier). In some densely populated parts of the world, such as China, fossil fuelled power plant are still being built in large numbers to support the immense electricity demand [9].

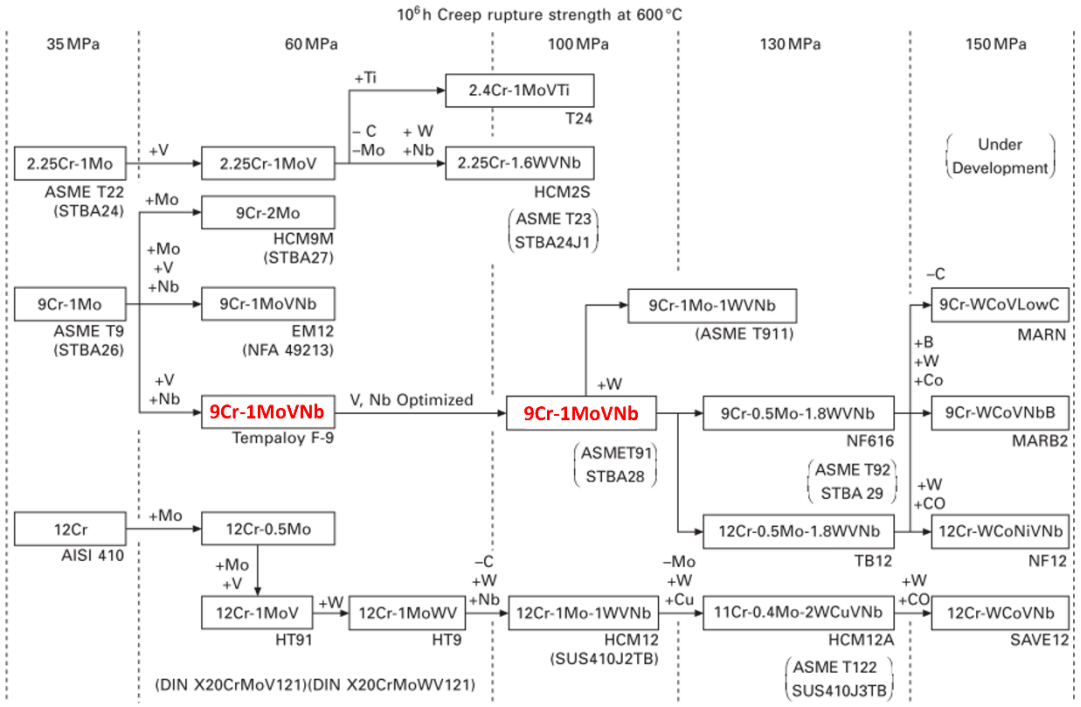

Figure 1.1: The development of CSEF steels for power generation application [6] (Gr. 91 variants highlighted in red).

1.2 The Development of Grade 91 Steel

The fundamental properties of 9-12 wt % Cr CSEF steels are a good resistance to corrosion and oxidation, weldability, toughness, ease of fabrication and availability in multiple product forms, cost and, of course, enhanced creep rupture strength for large diameter thick-walled pipes. High strength CSEF steels are used as low-cost alternatives for expensive nickel-based alloys. 12 wt % Cr steels are primarily used in limited applications when temperatures can reach up to 650 °C, thanks to a greater oxidation resistance than 9 wt % Cr [2]. In comparison to conventional 2.25Cr-1Mo steels (Gr. 22, Gr. 23), Gr. 91 can be used with thinner pipe walls, improving thermal conductivity and reducing costs as well as improved oxidation and corrosion resistance due to the higher Cr content [2].

In the fabrication of a typical superheat outlet header there are many components required for the finished product as shown in *Figure 1.2* [10]. As well as the piping and tubing, other product forms include safety valves, attachments, forgings and castings; all of these in a combined welded form will produce a complete header. Gr. 91 steel is unique in comparison to other CSEF steels due to the ease of availability of all the various product forms, meaning substitutional materials with varying or over-performing properties as well as dissimilar metal welds, which can compromise the performance of the final product, are not necessary. This is a major reason why Gr. 91 is the most common CSEF steel used today and is likely to remain so for many years to come [10]. After shaping, individual Gr. 91 components are subjected to a series of normalising and tempering heat treatments carried out in the temperature ranges of 1040 - 1080 °C and 730 - 800 °C respectively [11]. The purpose of these heat treatments is to form a uniform tempered martensitic microstructure strengthened by four primary mechanisms; 1) solid solution strengthening via Mo alloying, 2) dislocation strengthening via the tempered martensite matrix 3) precipitation strengthening via $M_{23}C_6$ (M=Fe,Cr) type carbides and MX type carbo-nitrides (M=V,Nb)(X=N,C) [12] and 4) boundary/ sub-boundary hardening [6]. It is often difficult to isolate the effect of each strengthening mechanism individually as they work in combination to provide the required properties for their application.

Gr. 91 CSEF steel was developed by the Oak Ridge National Laboratory (ORNL) and Combustion Engineering [13] over a 10 year period beginning in the mid-1970s, using 9Cr-1Mo (ASME T9) as a base material to modify for the purpose of improved creep strength. The composition of the modified 9Cr-1Mo steel was achieved by careful additions of V and Nb for (nano-) precipitation strengthening, and the optimisation of the C, Ni and Al content [14]. By the 1980s a modified 9Cr-1Mo steel was developed to produce creep properties equal to that of the 304 austenitic stainless steels up to 590 °C. In the early 1990s ASME approved Gr. 91, designated as SA-335 for seamless pipes (P91) [11] specifications (and SA-387 for plate specifications).

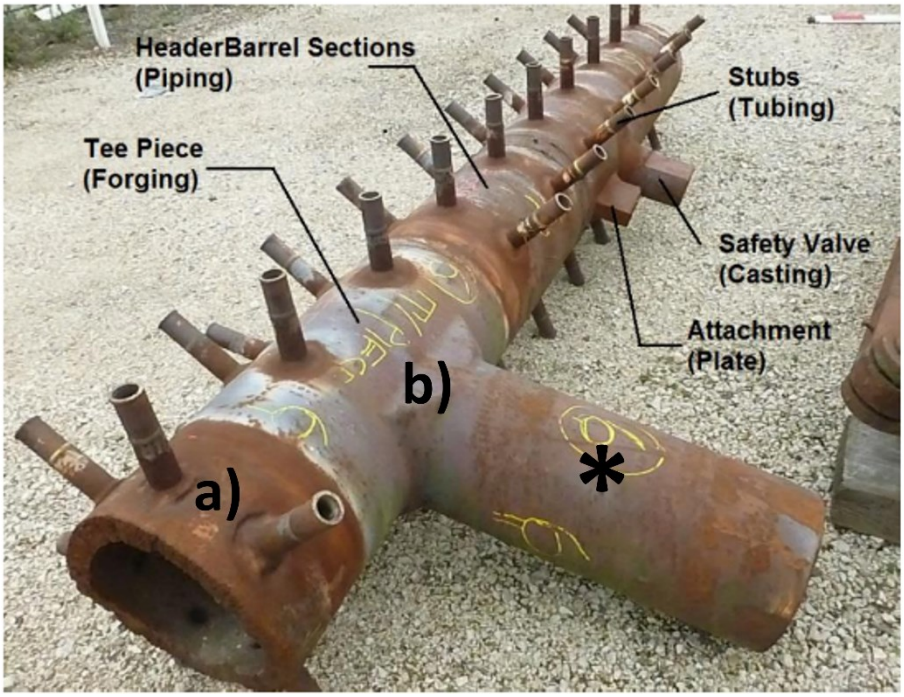

Figure 1.2: Photograph of the ex-service superheat outlet header showing (a) a typical barrel section (B2/Es-P) and (b) a typical tee-piece section (TP1/Es-F) [10] (asterisk marks where TP1/Es-F was taken from).

Since initial designations, further recommendations and revisions have been made to the specifications of Gr. 91 steels during the 21st century, due to many creep tested Gr. 91 steels showing reduction of areas (ROA) well below the guideline of at least 70% set by the development program of modified 9Cr-1Mo (ORNL 6303 [13]) as well as premature times to failure for creep lives of up to 100,000 hours [15], which can be seen in *Figure 1.3*. It should be noted *Figure 1.3* shows the variability of Gr. 91 steels from a single supplier at a fixed temperature, and all steels were within the composition specification, therefore, the extent of variability is very severe. Previous work has also suggested a low N:Al ratio for being the reason of creep failure [16], due to the strong affinity of Al with N during tempering of the steel [17] and formation of coarse aluminium nitride (AlN) precipitates, therefore, depleting the steel of VN-type MX precipitates [16][18]. Furthermore the formation and presence of AlN precipitates in Gr. 91 has been linked to a reduction in creep rupture ductility and subsequent creep rupture strength [19]–[23]. In light of this, EPRI recommended a more controlled composition that imposed limits for Al, Ni and a range of tramp and inclusion-forming elements (Cu, Sn, Sb, Pb, As, S) [19]. Furthermore, the American

Society of Mechanical Engineers of Boiler and Pressure Vessels (ASME-BPV) released the Code Case 2864, which limited similar elements as well as the reduction of allowable stresses [24], these compositions can be found in *Table 1.1*. Following these recommendations, Gr. 91 steels were manufactured to more tightly controlled compositions / specifications which showed a reduction in creep ductility during long-term (> 10,000 hours) testing [25][26]. Some attributed this to the theory that Ni accelerated the nucleation and growth of the Z-phase as well as $M_{23}C_6$ precipitate coarsening [26].

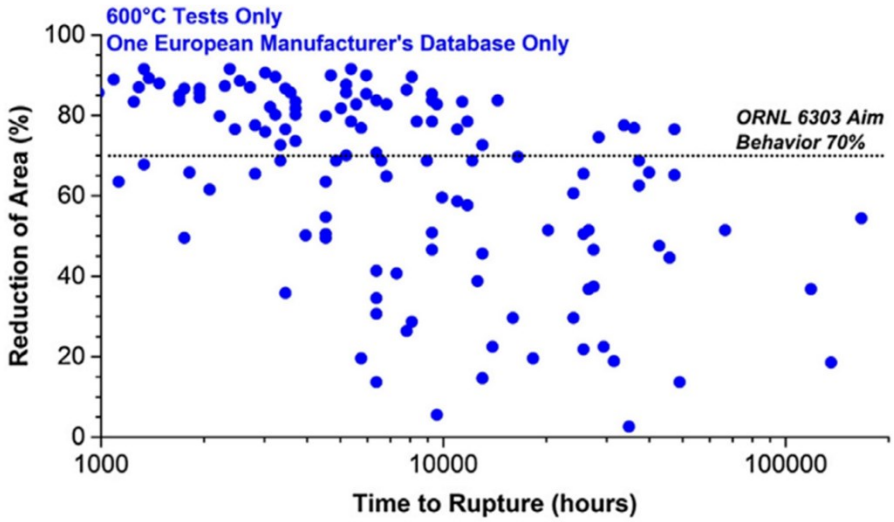

Figure 1.3: Graph of the variations in reduction of area of various Gr. 91 steels using plain creep bars with uniaxial tension, all at 600 °C [13][15].

Table 1.1: Chemical compositions for Gr. 91 steels, including ASTM/ASME, ORNL and EPRI chemical composition limits for tramp elements (in wt %).

Element	ORNL Spec[13]	ORNL Target[13]	ASTM SA-335[11]	EPRI, 2015[19]	Code Case 2864[24]
C	0.08-0.12	0.1	0.08-0.12	0.08-0.12	0.08-0.12
Mn	0.30-0.50	0.4	0.30-0.50	0.30-0.50	0.30-0.50
P	0.020 Max	<0.010	0.020 Max	0.020 Max	0.020 Max
S	0.10 Max	<0.010	0.010 Max	0.005 Max	0.005 Max
Si	0.20-0.50	0.2	0.20-0.50	0.20-0.40	0.20-0.40
Cr	8.0-9.0	8.5	8.00-9.50	8.00-9.50	8.0-9.5
Mo	0.85-1.05	0.95	0.85-1.05	0.85-1.05	0.85-1.05
V	0.18-0.25	0.21	0.18-0.25	0.18-0.25	0.18-0.25
Nb	0.06-0.10	0.08	0.06-0.10	0.06-0.10	--
N	0.030-0.070	0.05	0.030-0.070	0.035-0.070	0.035-0.070
Ni	0.20 Max	<0.10	0.40 Max	0.20 Max	0.20 Max
Al	0.04 Max	<0.02	0.02 Max	0.15 Max	0.020 Max
Ti	0.01 Max	<0.01	0.01 Max	0.01 Max	0.01 Max
Zr	<0.01	<0.01	0.01 Max	0.01 Max	0.01 Max
Cu	0.20 Max	<0.10	--	0.10 Max	0.10 Max
As	--	--	--	0.10 Max[1]	0.010 Max
Sn	--	--	--	0.10 Max[1]	0.010 Max
Sb	<0.001	<0.001	--	0.003 Max[1]	0.010 Max
B	<0.001	<0.001	--	<0.001	0.001 Max
W	<0.010	<0.010	--	<0.010	0.05 Max
Pb	--	--	--	<0.001 Max[1]	--
N:Al[19]	--	--	--	4.0 Min	4.0 Min

1.3 Microstructural Evolution during Creep

More recently further emphasis has been put on investigating the effects of tramp elements and non-metallic inclusions (hereafter referred to as inclusions) in the reduction of creep ductility by researchers from EPRI, whom suggested that 'hard particles' from the steel making process are nucleation sites for creep void formation [21][27][28]. This has been highlighted as a factor in some other studies (e.g. [29]), although, as EPRI point out, the cavitation mechanisms in CSEF steels are often overlooked [30]. Low ductility failures (at 600 °C) are often linked to the nucleation and growth of creep cavities, which are thought to start to nucleate early in the creep life of the materials [27][29]. The extrapolation of long-term creep performance from short-term data is known to over-estimate performance compared with service experience or long-term testing. In the literature this overestimation has largely been explained by microstructural degradation effects which occur whilst the material is under creep conditions [31]. Examples of this are the coarsening of $M_{23}C_6$ carbides [32], formation of the intermetallic Laves phase Fe_2X (X=Mo) at the expense of Mo (solid solution strengthening) [33][34] and Z-phase (Cr,(V,Nb)N) formation at the expense of MX and $M_{23}C_6$ [35][26]. In addition, the dislocation density decreases through recovery of the matrix with lath coarsening, formation and growth of sub-grains and, eventually, recrystallisation [36]. The combination of these factors contributes to the continual decrease in creep rupture strength during service, but it is often difficult to isolate the effect of each factor with regards to the nucleation of creep cavities.

1.4 Micro-segregation in Grade 91 Steel

Most of the heat treatments for Gr. 91 are based on the bulk composition, but solidification of the alloy into shaped, e.g., turbine casings, or semi-finished, e.g., ingots, products introduce potential chemical segregation (both micro and macro). Gr. 91 contains many elements which, during solidification, partition preferentially into the liquid. The level of segregation depends on composition, e.g., strong carbide formers such as Cr and Mo show greater segregation when C is also present and partitioning, and processing history, e.g., solidification rates and post-casting thermo-mechanical heat treatments. The scale of segregation, both the difference between

maximum and minimum concentrations and the spatial separation between positively and negatively segregated regions decreases with increasing thermal exposure and mechanical deformation at temperatures where solid-state diffusion (reducing composition amplitude) can occur along with section size reduction (reducing separation).

The theory of the cause and effect of macro- and micro-segregation has been studied in depth [37][38][39] but the implications have yet to be systematically researched in 9 - 12 wt % Cr martensitic boiler steels; only recently a few in-depth studies have been published by Japanese institutes [40][41]. It is particularly important to link the potential segregation to large area, relevant microstructural quantification since many studies continue to rely on 'basic' quantification methods for investigating complex martensitic microstructures, where steels are traditionally considered chemically homogenous.

1.5 Organisation of the Thesis

This thesis consists of 8 individual chapters. The current chapter details the background and scope of the project. *Chapter 2* contains a comprehensive literature review on the main themes of this research project which include chemical segregation in steel, inclusions in steel and cavitation in CSEF steels. *Chapter 3* covers the background and details of the 6 Gr. 91 steels in this project, the sample preparation procedures and the various techniques used for the characterisation of the steels. *Chapters 4, 5 and 6* present results from this project. Chapter 4 covers the chemical micro-segregation in each of the steels, using μ-XRF and SEM-EDS, as well as SIMS on a few select samples. *Chapter 5* covers the quantification and analysis of the Vickers micro-hardness, Laves phase and other nano-precipitates in the steel in relation to the micro-segregation analysed in *Chapter 4. Chapter 6* provides a comprehensive study of the inclusions in the steels, also considering the effects of micro-segregation as well as optimal accelerating voltages for automated SEM-EDS inclusions analysis, this chapter also includes the work done on creep damage association and cavity quantification in the steels. The final *Chapter, 8,* concludes the work done in this project with key findings and their impact for future research, as well as providing suggestions for future work on Gr. 91 steels.

Chapter 2 : Literature Review

This literature review will cover a comprehensive evaluation of chemical segregation in steel on the macro and micro level, inclusions in steel and cavitation behaviour in Gr. 91 and other CSEF steels. As well as this, a brief review of the metallurgy of 9 - 12 wt % Cr CSEF steels will be provided together with an overview of the roles that major alloying elements play within these materials. This review will also cover commonly reviewed aspects of Gr. 91 and other CSEF steels, which include microstructural degradation, e.g., the formation of the Laves phase, modified Z-phase, coarsening of the $M_{23}C_6$ carbides and MX carbo-nitrides and recovery of the matrix and growth of sub-grains. For these aforementioned topics, a number of existing theses [10][42]–[45] also contain thorough reviews.

2.1 Metallurgy of 9 - 12 wt % Cr Creep Strength Enhanced Ferritic (CSEF) Steels

2.1.1 Fe-C System

The Fe-C system shows the basic form of steel without any other alloying additions; various crystal structures can exist based on the temperature and carbon concentration as shown in the binary phase diagram [46] (*Figure 2.1a*). Above 2.1 wt % C, the Fe-C system is no longer regarded as steel, this is because 100% austenite (γ) cannot be formed, and it is referred to as cast-iron. For hypo-eutectoid C compositions (< 0.8 wt %) heating to from a purely face-centred cubic crystal (FCC) austenitic structure, and cooling, results in an equilibrium mixture of body-centred cubic crystal (BCC) α-ferrite structure and cementite. Furthermore, cooling rate also has an effect on the formation of phases, which are not stable at equilibrium conditions (not shown in the Fe-C binary phase diagram); for example, the body-centred tetragonal crystal (BCT) martensitic structure. This can be represented using a continuous cooling transformation (CCT) diagram [47], as in *Figure 2.1b*, showing a CCT diagram of a Gr. 91 steel with a defined composition. The roughly parallel downward sloping lines represent the cooling rate, with the lines to the left being faster cooled than the lines to the right.

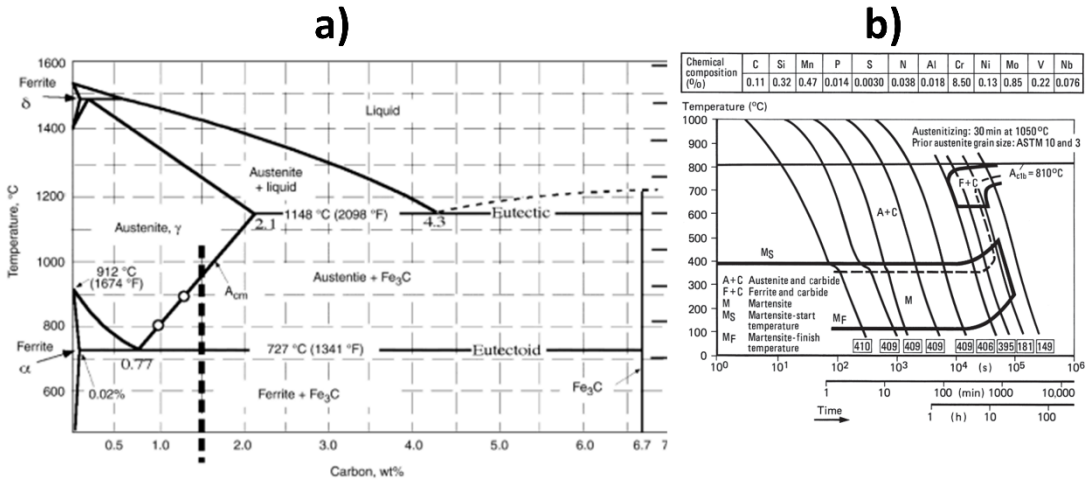

Figure 2.1: (a) Fe-C binary phase diagram [46] (b) continuous cooling diagram of a Gr. 91 steel [47].

2.1.2 Fe-C-Cr System

Chromium is added to increase the hardenability and corrosion resistance of steels. The hardenability of a steel is defined as the ability for a ferrous alloy to form a fully martensitic structure when quenched from a temperature which is above the Ac_3 temperature (austenitising temperature) [48]. From *Figure 2.1(b)*, the ferrite and carbide phases are supressed, meaning a high martensite volume form during sufficiently fast cooling. Its addition significantly modifies the Fe-C system; due to Cr being a strong ferrite stabiliser, there is a change in the temperatures at which equilibrium phases form based on Cr concentration. *Figure 2.2* shows a section from a Fe-C-Cr phase diagram at which the C concentration was fixed at 0.1 wt % [49]. From the diagram, below 14 wt % Cr there is a ferrite and austenite region (~11 - ~14 wt %) and a completely austenite region. Above 14 wt % Cr austenite formation is not possible under equilibrium conditions as seen from the α and γ phase boundaries. Regarding 9 - 12 wt % Cr steels, it can be seen in *Figure 2.2* at typical normalising temperatures (~1100 °C) the equilibrium phase exists as austenite (the addition of austenite stabilisers increases the austenite range for steels with the larger amount of Cr); at tempering temperatures (~750 °C) there may be a significant formation of carbides, and at power plant operating temperatures (~600 °C) there remains the existence of ferrite and carbides at equilibrium. Various alloying elements are added

as well as Cr, some austenite stabilising and others ferrite stabilisers, furthermore some elements are added that suppress the formation of δ-ferrite, which may form at near liquid temperatures (> 1400 °C) as seen in *Figure 2.2*.

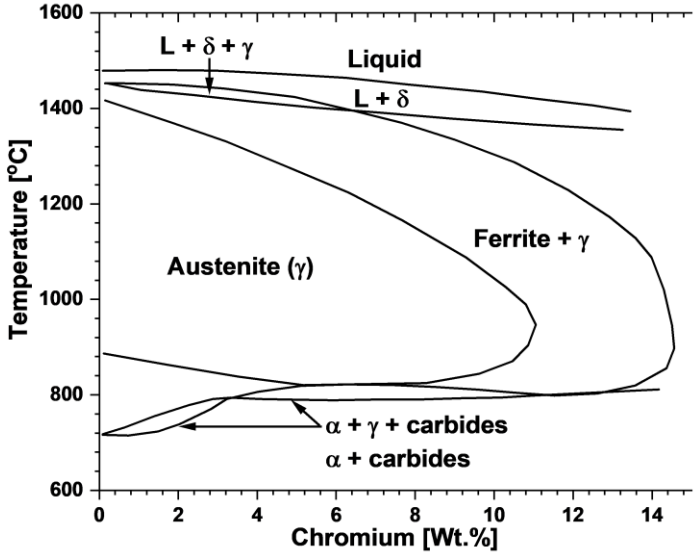

Figure 2.2: Vertical section through a ternary phase diagram for a Fe-Cr-0.1C system [49].

2.1.3 Martensite Matrix

After 9 - 12 wt % Cr steel products are made, they are then subjected to normalising and tempering heat treatments, upon normalising and cooling the microstructure consists of martensite, after tempering the microstructure is then considered to be tempered martensite. Tempering forms 2nd phase nano-precipitates (i.e., $M_{23}C_6$ carbides and V-rich MX carbo-nitrides). Precipitates in CSEF steels are found as fine non-metallic phases, which form during the heat treatments, with the purpose of strengthening the microstructure. Martensite formation from austenite is diffusion-less and quenching has to be fast enough to prevent the diffusion of C. This transformation is such where each atom only has a slight displacement from the FCC structure, an example of a BCT unit cell is given in *Figure 2.3a*. The BCT unit cell is very similar to that of ferrite (BCC), however the difference is the dimensions of the c-axis which has been elongated.

The low-carbon martensitic BCT crystal structure has few easy slip planes, which in turn increases hardness, strength and creep resistance in CSEF steels. The

complexities of this martensite microstructure can result in several strengthening mechanisms that include; substitutional and interstitial solid solution strengthening, dislocation strengthening, grain / lath boundary/size and precipitation of nano-precipitates [50] as demonstrated in *Figure 2.3b*. Due to the metastable nature of martensite, upon reheating (tempering), carbon atoms can diffuse out of the crystal lattice and can bind with elements to form carbides and other precipitates, namely Fe, Cr, V and Nb; this is one of the main strengthening mechanism in 9 - 12 wt % Cr CSEF steels for influencing creep rupture strength. The tempering heat treatment also reduces some of the residual stresses (by rearrangement / annihilation of excess dislocations), which are a result of the rapid cooling from the normalising heat treatment, which restores some of the ductility and improves toughness.

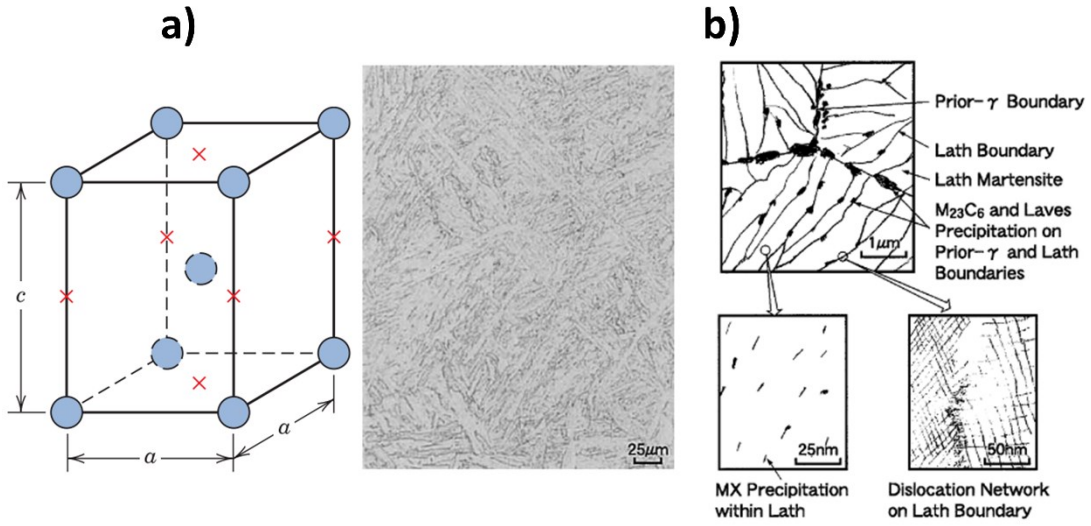

Figure 2.3: (a) Diagram of the BCT martensite unit cell, iron atoms are represented as circles, and sites which may be occupied by carbon are represented as '×'s (c > a) [51] (b) Image of a typical tempered martensite microstructure, as well as diagrams of the lath structure, precipitates and dislocations [2].

The amount of carbon in a martensitic alloy influences the amount of distortion in the BCT crystal structure, *Figure 2.4* shows how the c-axis lattice parameter in the BCT unit cell increases significantly as the amount of carbon in the alloy increases [51]. In low carbon steels, such as 9 - 12 wt % Cr steels (where the carbon content is typically less than 0.2 wt %) a fine needle-like martensitic lath microstructure forms with high dislocation density, multiple laths make up a block, multiple parallel blocks make up

a packet, and multiple packets are encased within a prior austenite grain (PAG). Although beneficial to dislocation strengthening, the high dislocation density (high amount of stored energy) of martensite makes it susceptible to the metallurgical process of recovery during operating temperatures in service (~600 °C); this is shown through the formation and growth of the sub-grain structure and lath width coarsening.

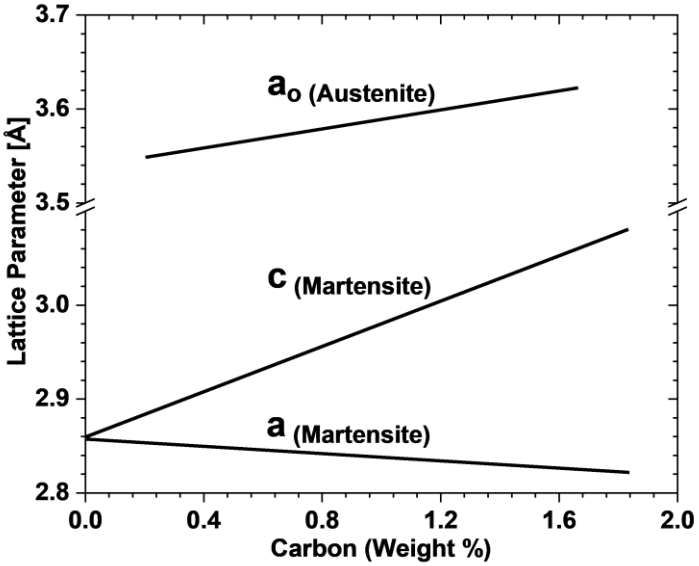

Figure 2.4: Graph showing the difference in lattice parameters for varying carbon concentrations in martensite [51].

2.2 Major Alloying Additions in Grade 91 Steel.

The simplest way of understanding the alloying elements in Gr. 91 is by grouping them according to properties and effects as follows.

2.2.1 Carbon and Nitrogen

C and N are austenite stabilisers and occupy interstitial sites in the lattice, therefore, they inhibit the formation of δ-ferrite. The content of these elements relates to the formation of carbides and carbo-nitrides. Lower C content improves weldability [6]; it was also found in a Gr. 91 steel that a lower C content (< 0.05 wt %) precipitated fewer $M_{23}C_6$ carbides, however a larger amount of VN-type MX carbo-nitrides, which were finer in size (2 - 20 nm). VN-type MX carbo-nitrides have a greater resistance to coarsening compared to the $M_{23}C_6$ carbides [52]. The purpose of N is to combine with V and Nb to form MX-type carbo-nitrides, which provide precipitation strengthening.

2.2.2 Chromium

Cr is the major alloying element in CSEF steels, it is a ferrite stabiliser and readily forms $M_{23}C_6$ carbide phases. Increased amounts of Cr improve oxidation and corrosion resistance. High strength is associated with Cr concentration of 2 wt % and 9 - 12 wt %, the strength declines between 2 and 9 wt %, the reason for which is unknown [2]. It is also the main component in the deleterious Z-phase with chemical formula Cr(V,Nb)N. Although, the Z-phase is not often reported in Gr. 91 steels, this is because it is only observed after prolonged aging times such as > 30,000 hours, even at relatively high temperatures such as 650 °C [36][53][54].

2.2.3 Molybdenum

Mo is a solid solution strengthener through substitution for Fe atoms, is widely used in CSEF steels for this purpose and is a ferrite stabilising element. If added in excess, δ-ferrite will form, which is detrimental to strength [2]. If exposed to elevated temperatures, Mo can form the intermetallic Laves phase in Gr. 91 steels with the formula Fe_2X, where X signifies Mo (or W for W-containing CSEF steels such as Gr. 92).

2.2.4 Vanadium, Niobium, Titanium

These 3 elements are ferrite stabilisers and can combine with C or N to form carbides, nitrides or carbo-nitrides. V and Nb are known to show optimal performance when their content is around 0.2 wt % and 0.05 wt %, respectively [2].

2.2.5 Silicon and Manganese

Si is a ferrite stabiliser, whereas Mn is an austenite stabiliser. Mn helps to prevent the formation of δ-ferrite during austenitisation and also forms manganese sulphide (MnS) inclusions with S. Mn also contributes to solid solution strengthening in CSEF steels. Si is added for de-oxidation so may form oxide inclusions, it may positively affect the oxide layer, hence increase oxidation resistance [10]. Si may also promote the formation of the intermetallic Laves phase [2].

2.2.6 Nickel and Aluminium

Similar to Mn, Ni is an austenite stabiliser and helps to prevent the formation of δ-ferrite during austenitisation. Ni contents above 0.40 wt % in CSEF steels can cause

the acceleration of coarsening of the $M_{23}C_6$ carbides, as well as the formation of the Z-phase. Al is a ferrite stabiliser and is added for the purpose of de-oxidation, although when in the presence of excess Al, N can preferentially form needle-like lenticular AlN precipitates during tempering, reducing the potential for the formation of MX-type nitrides by the depletion of N.

2.3 Typical Heat Treatments

2.3.1 Normalising

Normalising heat treatments in Gr. 91 steels are typically carried out in the temperature ranges of 1040 - 1080 °C [11]. The normalising heat treatment is carried out at the austenitisation temperature and then air cooled, typically any precipitates formed during the steelmaking process are dissolved. After normalising (and the rapid cooling process) the primary microstructure is martensite; there may also be some undissolved carbides, delta ferrite and retained austenite [44]. Normalising at a temperature either above or below the desired normalisation temperature can have a drastic effect on the creep properties of the steel. When the normalising temperature was increased from 1050 to 1100 °C, there was a 10 - 15 % increase in the room temperature strength in Gr. 91 steel. This was because the lower normalising temperature dissolved fewer of the carbide and nitride precipitates [55]. Conversely, the over-normalising of CSEF steels can also be detrimental to the mechanical properties, this is due to grain growth and heterogenous grain size distributions as well as the formation of delta ferrite, these factors are all considered intolerable for pressurised components (CSEF steels) [56]. The effects of under-normalising are difficult to detect due to the indistinguishable hardness values, as well as the microstructural features, as compared to the microstructures of adequately normalised CSEF steels.

2.3.2 Tempering

The normalised steel is then tempered, typically in the 730 - 800 ºC temperature (below austenitisation) range and then air cooled [11]. As a result, the martensitic microstructure is strengthened by $M_{23}C_6$ carbides which precipitate on the lath and grain boundaries which provides resistance to lath width coarsening. Also, V and Nb rich carbo-nitrides which precipitate within the laths and sub-grains which strengthen

the lath interiors. Carbo-nitrides are not effective at this size at pinning lath boundaries [45]. A typical normalised and tempered 9 - 12 wt % Cr steel is shown in *Figure 2.5*. Tempering temperatures that are at the low end of the temperature range are typical for steel components where a high tensile strength is required (e.g., turbine rotors). Whereas at the high end temperature range the typical steel components are pressurised (e.g., steam pipes) and toughness is a greater requirement [53]. A reversion in the hardness has been reported when the tempering temperatures were in excess of 800 ºC, this was due to the relatively low A_{C1} temperature of the Gr. 91 steel, which allowed the re-transformation of the martensitic microstructure. Ennis et al. [57] found in a Gr. 92 steel, that increasing the tempering temperature within the range of 750 - 800 ºC, led to an enhanced rate of martensite recovery, which led to a decrease in the dislocation density and reductions in the creep strength. In a more recent study by Shrestha et al. [58] who investigated the effects of normalising and tempering temperatures and times, a decrease in hardness was found, when higher temperatures and longer times were used for both heat treatments. This was attributed to the increase in martensite lath/grain size, decreases in the dislocation density, and coarsening of the precipitates.

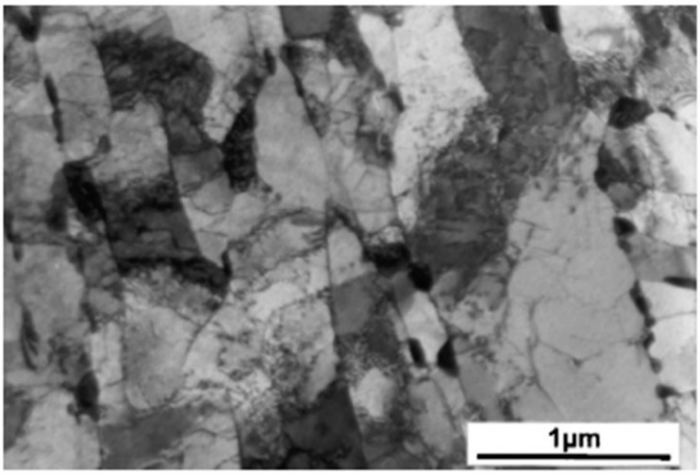

Figure 2.5: A typical tempered martensitic microstructure of a 9-12 wt % Cr steel [53].

2.3.3 Strengthening Mechanisms in CSEF steels

A properly processed and heat treated martensitic CSEF steel will possess a range of strengthening mechanisms as listed below.

1. Solid solution strengthening via Mo or W (dependent on CSEF steel) alloying. These elements have a larger atomic size than solvent iron and are commonly deployed as solid solution hardeners for CSEF and austenitic stainless steels. Solid solution strengthening is essentially superimposed on other forms of strengthening [59].
2. Dislocation strengthening via the tempered martensite matrix, which is given by the *Equation (2.1)* [60].

$$\sigma_p = 0.5MGb(\rho_f)^{1/2} \qquad \textit{Equation (2.1)}$$

Where, M (= 3) is defined as the Taylor factor, G is defined as the shear modulus, b is defined as the magnitude of the Burgers vector and ρ_f is defined as the free dislocation density in the matrix. At ambient temperatures, dislocation strengthening is an important mechanism, with tempered martensitic CSEF steels reported to contain dislocation densities of 1 - 10 × 10^{14} m^{-2} in the matrix [60].

3. Strengthening precipitates such as $M_{23}C_6$ carbides and MX type carbo-nitrides are non-metallic particles which are formed intentionally during heat treatments with the purpose of strengthening the steel. Precipitation strengthening, the presence and dispersion of these nano-sized precipitates helps with stabilising (or pinning) the lath / sub-grain structure and any free dislocations against recovery during creep [12]. This effect further enhances the dislocation and sub-boundary strengthening mechanisms. Several mechanisms have been proposed for the threshold, or stress required for a dislocation to pass through a precipitate particle, of which there is the Orowan mechanism, general climb mechanism, local climb mechanism and the Srolovitz mechanism [59]. The Orowan mechanism is defined by *Equation (2.2)* [60].

$$\sigma_{or} = 0.8MGb/\lambda \qquad \textit{Equation (2.2)}$$

Where, λ is the mean interparticle spacing.

4. The final basic method for strengthening is by boundary and sub-boundary hardening [6]. After normalising and tempering heat treatments, the martensitic microstructure consists of finely structured packets, blocks and laths as shown in *Figure 2.3b* with a high dislocation density. Fine carbo-nitrides decorate the lath and block boundaries and interior of the laths. These boundaries can produce a sub-boundary strengthening mechanism which is defined by the *Equation (2.3)* [60].

$$\sigma_{sg} = 10Gb/\lambda_{sg} \qquad \textit{Equation (2.3)}$$

Where, λ_{sg} is the shortest width of the elongated lath and block boundaries. Boundaries with a misorientation of 2 to 15 degrees (and > 50) are classified as low angle boundaries, which are the sub-grain, lath and block boundaries. The high angle boundaries are classified through their 15 to 50 misorientation angle, which can be identified as prior austenite grain boundaries (PAGB) or packet boundaries [61].

2.4 Microstructural Evolution during Creep or Thermal Aging of CSEF steels

When CSEF steels are exposed to service-like conditions, evolution of the microstructure occurs, which can reduce the resistance of the steel to creep deformation. There are three main degradation mechanisms which directly reduce the effectiveness of the strengthening mechanisms discussed in *Section 2.3.3*, recovery of the martensite matrix, coarsening of the strengthening precipitates and depletion of the solid solution strengthening elements, the latter two will be categorised into the secondary phase evolution section. These mechanisms as well as creep cavitation *Section 2.7* can also lead to softening of the material.

2.4.1 Recovery of the Martensite Matrix

Orlova et al. [62] found that the sub-grains in a Gr. 91 steel became more equiaxed in crept specimens during isothermal aging (head section) and creep (gauge section). Fundamentally, when considering *Equation 2.3* the value of λ_{sg} increases during this

process which reduces the boundary and sub-boundary strengthening effects. The authors also found that the sub-grain size growth was accelerated under creep conditions, compared to stress-free aging, due to degradation in grain boundary pinning from precipitation strengthening. This is caused by the coarsening of grain boundary precipitates, which is discussed in detail in Section 2.4.2.3. The movement of the sub-grain boundaries can absorb the excess dislocations from inside the martensite matrix (laths and blocks), which reduces the dislocation density and results in softening of the steel [59].

Similarly Qin et al. [63] investigated the difference of thermal aging and creep on the sub-grain structure in a 12 wt % Cr CSEF steel. It was found that there was no significant sub-grain coarsening during the aging, whereas the crept specimens showed a clear increase in the size. *Figure 2.6* shows these effects in terms of the size of the sub-grains for the 'annealed' and crept specimens, it should be noted the term 'annealed' refers to the head section of the creep specimen in that study, which is known to experience significantly less stress. The aged specimen retained a consistent size of sub-grains, whereas the crept specimen showed a significant increase at a high Z/h (where Z stands for temperature compensated creep time), which in that study meant a high temperature (650 °C) and low stress (76 MPa). It was also shown that the sub-grains that had disappeared during recovery had left their boundary-pinning precipitates behind, and that the sub-grains with a lower density of boundary precipitates disappeared more quickly by migrating and recombining with the other boundaries. In another study on Gr. 92 and 12 wt % Cr steels the effects of thermal aging were investigated through a 1000 h holding at 700 °C, no significant change in the sub-grain sizes were observed, although the morphology of the sub-grains did change from elongated to equiaxed [64].

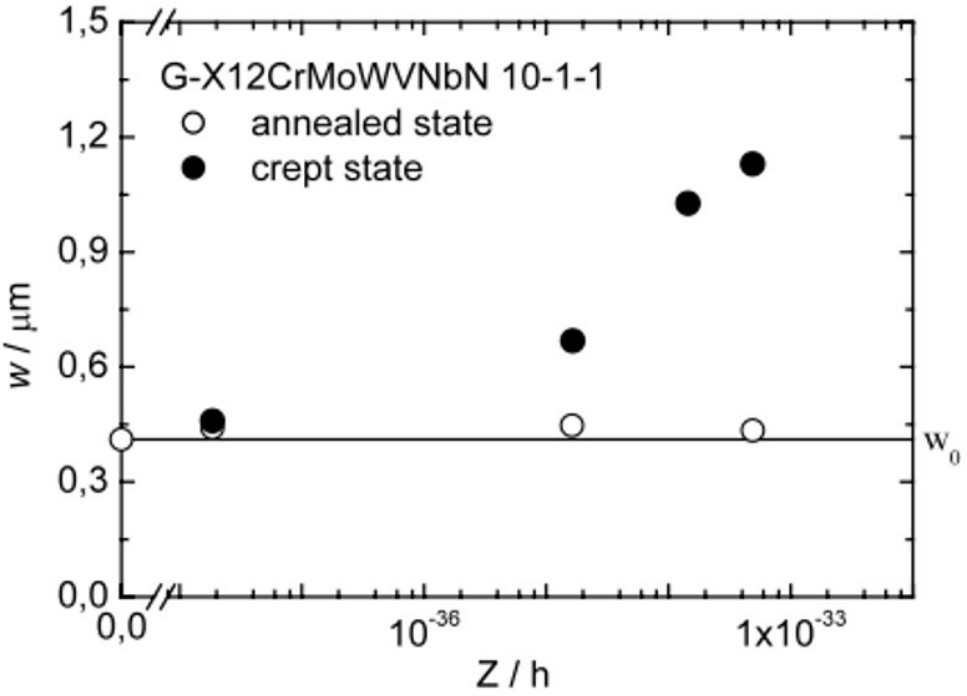

Figure 2.6: The size of the sub-grains as a function of time for the aged and crept states of a 12 wt % Cr CSEF steel [63].

Panait et al. [36] performed a comprehensive microstructural study on a Gr. 91 steel after 113,431 h creep exposure time at 600 °C and 80 MPa. Electron back-scatter diffraction mapping (EBSD) was used to compare the virgin material (no creep exposure) to the crept specimens; this can be seen in *Figure 2.7*. The EBSD maps showed the formation of equiaxed sub-grains, as compared to the virgin elongated sub-grain structure. The formation of equiaxed sub-grains was also found closer to the fracture point than further (25 mm) away from it, meaning there was more sub-grain evolution in the highly strained region close to fracture. It was also concluded that since creep cavities were evenly distributed throughout the gauge region, recovery of the martensite matrix was not necessarily enough to induce creep failure. Furthermore, the authors identified the formation of finely sized grains with high angle boundaries (15 to 50 degrees) which signified the recovery or recrystallisation of the matrix. In comparison to the aforementioned studies on the recovery of the matrix [63][64], Panait et al. [36] found recovery also in the head sections of the creep specimens, of

which the other studies [63][64] found little to none, this may have been due to the particularly long creep exposure time in Panait et al.'s study (113, 431 hours).

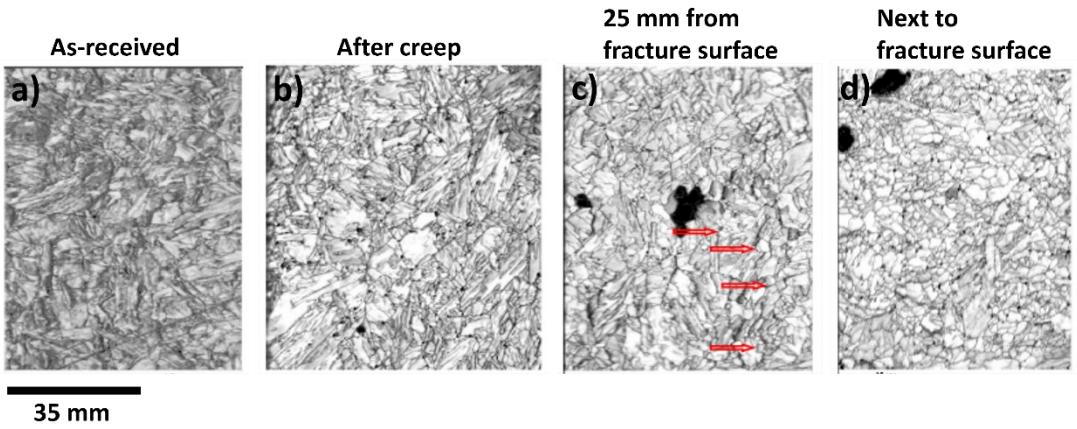

Figure 2.7: Electron back-scatter diffraction image quality maps showing the effect of creep on a Gr. 91 steel at 600 °C and 80 MPa for 113, 431 hours for the (a) virgin material (without any creep), (b) after creep, (c) after creep 25 mm from the fracture and (d) after creep next to the site of fracture [36]. (Red arrows signify the formation of equiaxed sub-grains in Figure 2.7c).

2.4.2 Secondary Phase Evolution

When Gr. 91 and other CSEF steels are subjected to creep conditions or thermal aging (~ 550 °C), the precipitation of other phases may occur, which do not form during the tempering or normalising heat treatments. These include the intermetallic Laves phase (Fe_2Mo) and modified Z-phase (Cr(V,Nb)N), which are detailed in *Section 2.2*. Further to this the coarsening of these two types of precipitates as well as the coarsening of the $M_{23}C_6$ carbides and MX type carbo-nitrides can drastically reduce the precipitation strengthening effects. More specifically, the coarsening of the $M_{23}C_6$ carbides will decrease the sub-grain boundary pinning effect which will cause the martensite laths and blocks to lose their effectiveness quicker [59].

2.4.2.1 Laves Phase

The intermetallic Laves phase is known to precipitate and grow early during high-temperature exposure through the segregation of Mo and Si to martensite lath boundaries located next to $M_{23}C_6$ carbides [65]. Sawada et al. [66] found that in an 11 wt % Cr martensitic steel (TAF650) that the Fe_2(W,Mo) Laves phase particles were not found in creep tested Gr. 91 (mod. 9Cr-1Mo) steel, this was because at the

temperature of 650 °C the Laves phase was expected to be dissolved in Gr. 91. The formation of Laves phase will result in a loss of solid solution strengthening from W/ Mo. The precipitation strengthening from Laves phase in these steels is likely to be limited because it coarsens rapidly at normal service temperatures (i.e., ~ 600 °C) for these materials [36]. Due to the rapid coarsening nature of the Laves phase, it can reach near micron sizes and can act as sites for cavity nucleation due to its reported misfit with the iron-based steel matrix [33]. However, if coarsening can be restricted some benefits to creep strength have been reported [67].

Energy filtered transmission electron microscopy (EF-TEM) based quantification of the Laves phase in a 12 wt % Cr CSEF steel creep tested at 600 and 650 °C by Hofer et al. [68] showed no significant influence of stress on the average size of Laves particles (~ 5 % increase, which may have been due to scatter of measurements). In the same study, only the $M_{23}C_6$ carbides were reported to show a pronounced increase in the average size. Using the same steel with scanning electron microscope (SEM) back-scattered electron (SEM-BSE) imaging techniques, Dimmler et al. [69] found a significantly lower median value of particle size for the Laves phase. This discrepancy was attributed to the much larger area that was analysed with the SEM-BSE imaging, providing better statistical quantification of the full-size range of Laves particles. Panait et al. [36] also found no significant difference in the Laves phase populations between the head and gauge sections of a creep specimen, in an extended creep exposure Gr. 91 steel specimen. The size distributions of the Laves phase are shown in *Figure 2.8,* which shows similar curves in both the head and gauge, the small differences were attributed to general data scatter in the measurements as no consideration for the effects of micro-segregation was made.

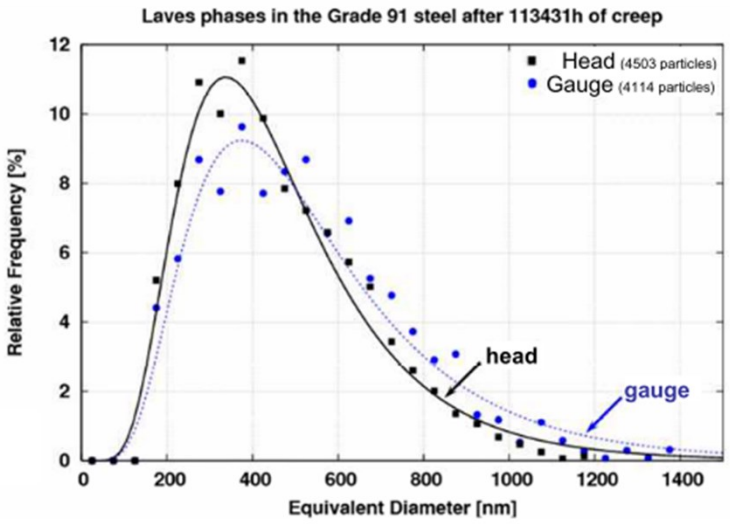

Figure 2.8: Size distribution comparison of the Laves phase in a Gr. 91 steel creep tested at 600 °C and 80 MPa for 113, 431 hours, comparing the head and gauge sections.

2.4.2.2 Z-Phase

Z-phase in these steels is well known for its detrimental effect on creep performance as it forms at the expense of smaller MX precipitates, which results in net lower precipitation strengthening. Z-phase is not often reported in 9 wt % Cr steels, this is likely because it is only observed after extended creep or thermal aging times even at relatively high temperatures (i.e., 600 °C) [36][53][54].

Long-term creep tests by Panait et al. [36] and Cipolla et al. [70] were performed on Gr. 91 steels for over 100,000 hours. For the former study using randomly selected precipitates from STEM mapping only 41 out of 640 identified precipitates were the Z-phase, which is roughly 6.4 %; for the latter study less than 1 % of the precipitates identified were the Z-phase. *Figure 2.9* shows the changes in the number of particles per unit area of the MX and Z-phase from a study by Sawada et al. using STEM mapping [71] performed on a Gr. 91 steel under creep conditions of 600 °C and 70 MPa. A considerable reduction in the MX phase was not found up until 70,000 hours in the gauge sections, furthermore the grip (or head) section of the creep specimen did not show as significant a change in the MX phase. This suggested that stress in the gauge section was important in accelerating the formation of the Z-phase during creep. One of the main components of the Z-phase is Cr (46.5 at %) [36], therefore, CSEF

steels with greater amounts of Cr may be more susceptible to the formation and coarsening of the Z-phase. This was studied by Sawada et al. [72] by comparing Z-phase formation in Gr. 91 and T122 steels (9 vs 12 wt % Cr, respectively), *Figure 2.10*, which shows that Z-phase formation in the T122 steel was considerably faster at the same temperatures than in Gr. 91 steel.

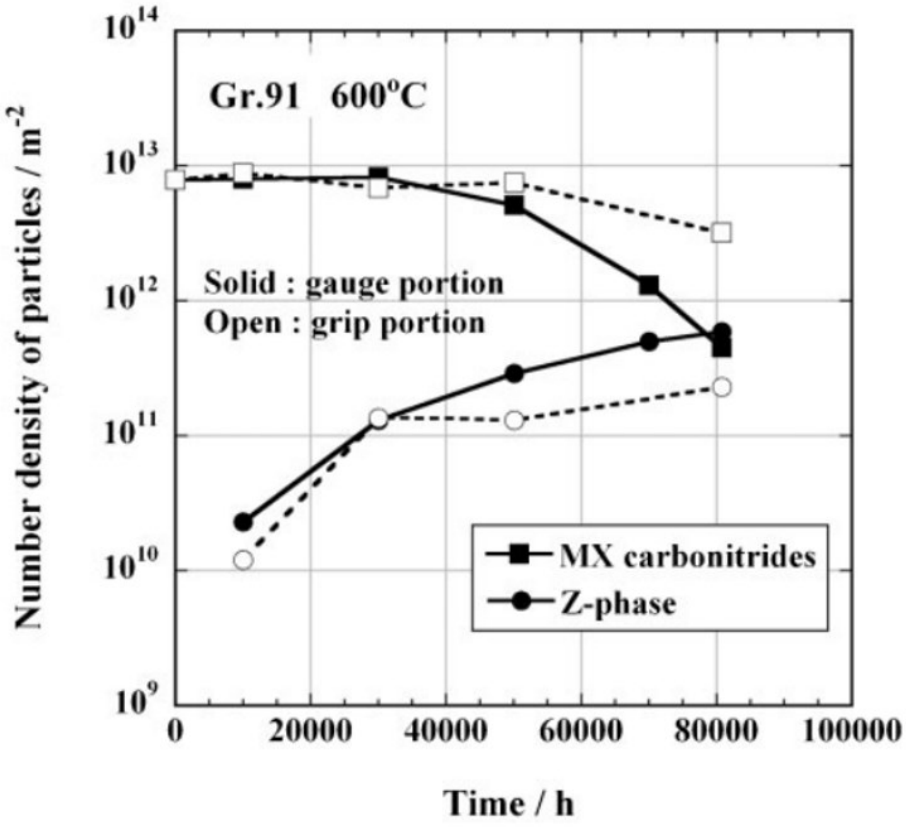

Figure 2.9: Graph showing the change in the number density of MX and Z-phase precipitates in the grip (head) and gauge sections of a Gr. 91 steel creep tested at 600 ℃ and 70 MPa [71].

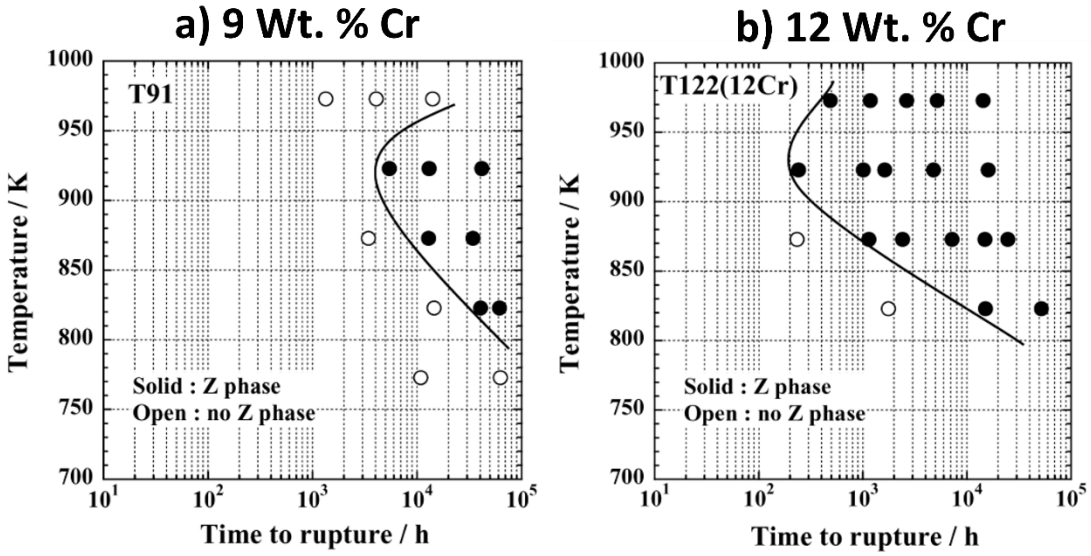

Figure 2.10: Graphs showing the time to rupture of (a) Gr. 91 steel and (b) T122 steel for various temperatures with regards to which creep test contained Z-phase and which did not [72].

2.4.2.3 Coarsening of the $M_{23}C_6$ carbides and MX type carbo-nitrides.

The MX carbo-nitride strengthening precipitates mainly form within the lath interiors and the sub-grain and the $M_{23}C_6$ carbides (and Laves phase) tend to precipitate on the lath boundaries and PAGBs [73]. All three of these precipitates are subjected to coarsening during exposure to creep conditions. Therefore, the precipitation strengthening effects of these (in the few cases Laves phase is considered precipitation strengthening) can be reduced. Orlova et al. [62] found that creep stress accelerated the coarsening of precipitates, which reduced their pinning effect of the martensite laths. The coarsening behaviour has been described by the Ostwald ripening *Equation (2.4)* by Wagner [74] and Lifshitz and Slyozov [75].

$$r^3 - r_0^3 = Kt \qquad \textit{Equation (2.4)}$$

Where r and r_0 are defined as the average precipitate radius before and after creep testing for the time period, t. The K value is defined as a coarsening constant and was originally developed for binary alloy systems and can be defined by the *Equation (2.5)*.

$$K = \frac{8DC_e\gamma V_m^2}{9RT} \qquad \textit{Equation (2.5)}$$

Where D is defined as the diffusion coefficient, C_e is defined as the equilibrium solute concentration, γ is the interfacial energy and the molar volume of the precipitate is defined by V_m. Since then, the K coarsening constant has been modified many times to account for multi-component systems such as CSEF steels. The version proposed by Umantsev and Olson [76] and Agren et al. [77] was used by Hald and Korcakova [32], in order to predict the coarsening behaviours of the $M_{23}C_6$ carbides, MX carbo-nitrides and Laves phase in Gr. 91 and 92 steels which had undergone thermal aging, for which the *K* value proved to be an acceptable fit.

The rate at which the $M_{23}C_6$ carbides and MX carbo-nitrides coarsen can also be influenced by their location (at particular grain boundaries). In a study by Kaneko et al. [73] the coarsening rates were investigated for these precipitates based on their grain boundary location. It was found the $M_{23}C_6$ carbides that tended to form on the PAGBs (high angle boundaries) were subjected to faster coarsening compared to the MX carbo-nitrides which mainly precipitated on the low angle boundaries (lath and block sub-grain). This phenomenon was due to the faster diffusion paths at the high angle boundaries. The agglomeration and/or coarsening of precipitates at grain boundaries during creep can promote the climbing and redistribution of dislocations (at the grain boundaries), which can start a chain reaction of the same event [59]. Although, the authors did not consider the same precipitate type, the faster coarsening of the $M_{23}C_6$ carbides as compared to the MX carbo-nitrides may have been due to the precipitate type rather than the boundary type.

TEM and EFTEM investigations on a 12 wt % Cr steel by Hofer et al. [68] for 33,000 hours under creep conditions of 600 °C and 110 MPa showed that only the $M_{23}C_6$ carbides were influenced in the stressed gauge region of the creep specimen, whereas the Laves phase and MX carbo-nitrides were unaffected by the stress. Other authors have found the coarsening of the MX carbo-nitrides to be accelerated due to stressed conditions in the gauge sections of creep specimens in Gr. 91 and 92 steels, respectively [78][79], but at a slower rate than of the $M_{23}C_6$ carbides. Another reason suggested for the difference in coarsening rates between the $M_{23}C_6$ carbides and MX carbo-nitrides is the high solubility of Cr in the steel matrix [80]. *Figure 2.11* shows the size distribution curves of the MX carbo-nitrides in a Gr. 92 steel, it can be seen

that a large size distribution curve is present in the gauge sections as compared to the head sections, which experienced significantly less stress [79]. It can also be seen that the size of the MX carbonitrides in the virgin tempered steel is roughly 30 nm, which is the approximate size of the MX carbo-nitrides in all virgin state CSEF steels. Panait et al. [36] reported the average size of the $M_{23}C_6$ carbides at approximately 100 nm in the virgin state and approximately 300 nm after 113, 431 hours of creep at 600 °C; Cipolla et al. [70] reported a size of approximately 250 nm for the $M_{23}C_6$ carbides after 50,000 hours at 600 °C. Abe et al. [31] suggested that improvement in the stabilisation of the sub-grain structure was achieved by the controlled addition of boron in a 9 wt % Cr CSEF steel which was claimed to have slowed down the coarsening of the $M_{23}C_6$ carbides .

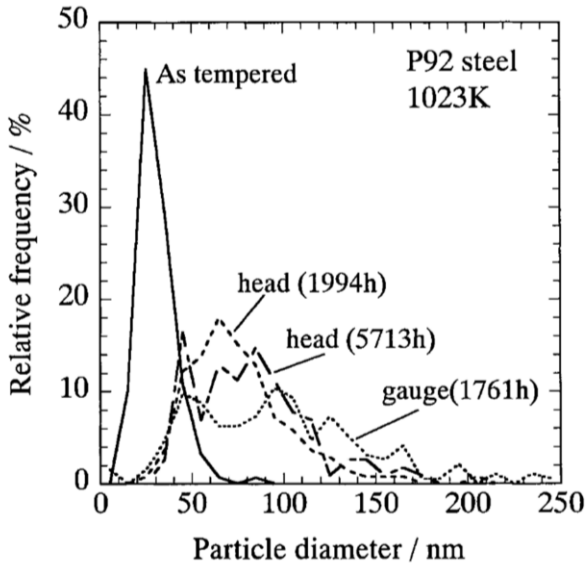

Figure 2.11: Size distribution curves of the MX carbo-nitrides from a Gr. 92 steel at 750 ℃ and a constant load [79].

2.4.4 Effects on the Micro-hardness

In the virgin state CSEF steels possess a hardness of approximately 220 HV (or 230 HV in Gr. 91 [36]). A 5 % decline is expected from thermal aging for approximately 30,000 hours at 650 °C, or a 20-30 % decline due to creep conditions after around 10,000 – 30,000 hours, which is associated with the microstructural evolution discussed in this section as well as creep cavitation (in the gauge of crept specimens) [81]. The differences in hardness can be related to three material conditions.

1. The virgin state, where the steel possessed the normalised and tempered martensitic microstructure.
2. In the head section of the creep specimen, where the material has only experienced the thermal aging with significantly less stress.
3. The gauge section of the creep specimen, where other (or more aggressive) microstructural evolution processes have taken place due to the stress from the creep test. This can include coarsening of the precipitates, recovery of the martensite matrix and nucleation (and growth) of creep cavities.

Panait et al. [36] provided a clear view on the effects of aging and creep on micro-hardness via microstructural evolution of Gr. 91 steel. *Figure 2.12* shows the micro-hardness spread from the study; the base virgin material can be seen with an average micro-hardness of approximately 230 HV. The head section of the creep specimen possesses a micro-hardness roughly 4-5 % lower at approximately 220 HV. A steep drop into the gauge section can be seen to approximately 195 HV, with a steady decrease to 170-180 HV at the failure region due to the excessive deformation there. Many factors can influence the micro-hardness, such as the presence of creep cavities, populations of precipitates and inclusions, and changes in the sub-grain and dislocation densities. Although some authors [81][82], believe the increase of lath width and decrease in dislocation density during microstructural evolution are solely responsible for the decline in hardness and can enable estimation of creep resistance.

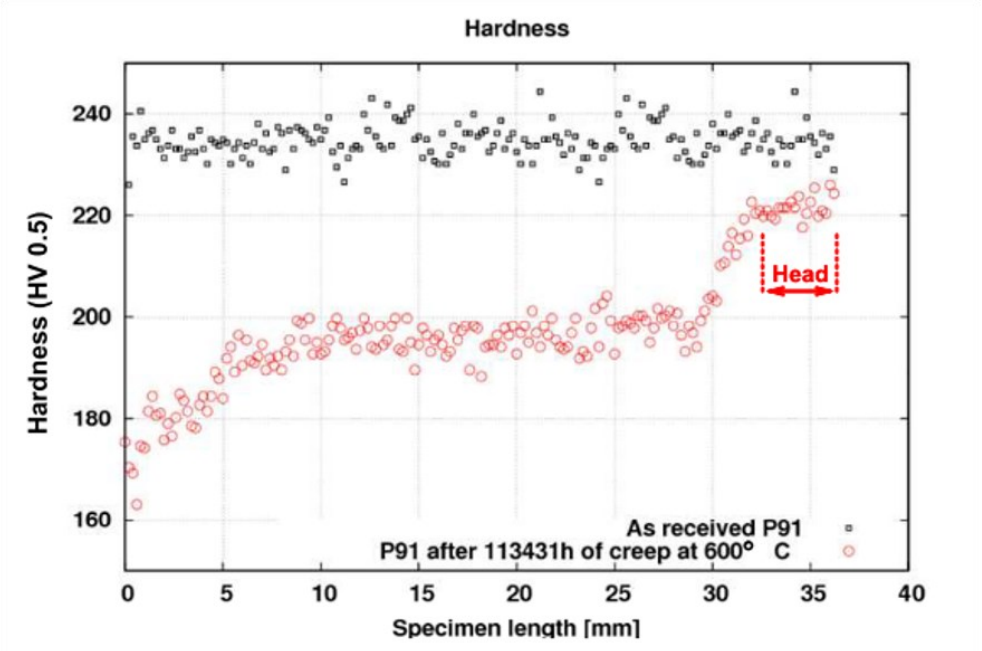

Figure 2.12: Changes in micro-hardness along the gauge length of a Gr. 91 creep specimen tested at 600 °C and 80 MPa for 113, 431 hours, highlighting the micro-hardness in the virgin, aged and crept states [36].

2.5 Chemical Inhomogeneity in Steel

2.5.1 Steelmaking process

Gr. 91 and other CSEF steels are produced through conventional steelmaking processes, which can be split into three categories: primary, secondary and tertiary. Primary steelmaking involves the smelting of iron ore into 'pig' iron using a blast furnace, which is referred to as basic oxygen steelmaking (BOS). Although the recycling of steel scrap using an electric arc has become more popular for the melting process, as a more environmentally friendly and economically effective process. It is now the common method used in steelmaking for Gr. 91 steels, this second method is referred to as the electric arc furnace (EAF).

The EAF process is accompanied by the argon oxygen decarburisation (AOD) process which can be regarded as secondary steelmaking (refining of the liquid steel). The purpose of this is to refine the liquid steel (reducing the C and impurity contents) whilst minimising unwanted oxidation of valuable elements such as Cr, which is the major alloying element in Gr. 91 steel [83]. During this process samples are taken from the

liquid steel, and if any deliberate alloying elements are not in sufficient amounts, then they are added into the liquid. Another common refining process is vacuum oxygen decarburisation (VOD), the main difference between AOD and VOD being that the liquid steel needs to be transferred to a ladle and then into a vacuum environment for VOD, whereas AOD makes use of argon, as well as oxygen decarburisation. EAF and AOD can be referred to as a duplex process, although triplex processes exist and can be implemented if the liquid steel needs further refinement, this will depend on customer specifications / requirements, raw material availability, cost and other factors [84].

2.5.2 Ingot and Continuous Casting

After the liquid steel has been refined to the desired chemical composition, the tertiary stage in the steelmaking process takes place, involving the casting, shaping and heat treatment of the product. Ingot and continuous casting are two possible methods for producing Gr. 91 steels. The desired method is dependent on the size of the pipe/tube required and will be discussed in subsequent sections.

Continuous casting has been widely adopted across the world, today it accounts for 95% of steelmaking [85]. Initial continuous casters were vertical, although curved continuous casters are much more common now due to the vertical casters occupying more space and forming bulges, chemical segregation and cracking due to the ferro-static pressure of the liquid steel within the solidifying section [85]. A schematic diagram of a typical curved continuous casting setup is shown in *Figure 2.5c*. The general process consists of liquid steel passing from the ladle into a tundish before passing through the water-cooled mould, where solidification starts. The partially solidified strand exits the mould and is cooled by water sprays with and electromagnetic stirrers (EMS) being applied to induce mixing in the liquid using magnetic fields from induction coils [86]. The diagram shows the outer sides solidifying first due to the initial contact/cooling points for the liquid metal. Completely solidified sections are then cut to size, these are known as semi-finished products, and depending on size, can be classed as blooms, slabs or billets [85]. Depending on requirements, further processing can take place, which can create steel products such as sheets, bars and seamless pipes. This method has many advantages

compared to previous steelmaking processes such as ingot casting, which include improved yields, productivity and efficiency, standardisation of the processes and better control through automation. Furthermore, there is more control of the quality of the cast, such as uniformity of grain size and reductions in chemical segregation [86]. The large size of this type of continuous caster means that it is only viable for production of 100s of tonnes and so is not suitable for the smaller tonnages of CSEF steels. The 'continuous' process applied to CSEFs is that of electro-slag remelting (ESR), *Section 2.4.3* in which a continuous variation of ESR process is used for producing CSEF steels similar to that shown by Shi et al. [87].

Another major limitation for continuous casting is the maximum size which can be produced, and so larger sections produced by ingot casting may be required. Some of the typical applications where ingot casting would be required include turbine blades for power engineering, large sections for the oil and gas industry, ship building and other heavy forgings. *Figures 2.13a* and *b* show top and bottom poured ingot variations, bottom poured ingots are more commonly used for ingot casting due to less turbulence during the filling of liquid steel, which improves surface finish and overall quality [88]. The solidification process in ingot casting is similar to that described for continuous casting. The solidification starts from the mould walls due to the initial contact; further cooling can be encouraged by water spray on the outside of the mould walls.

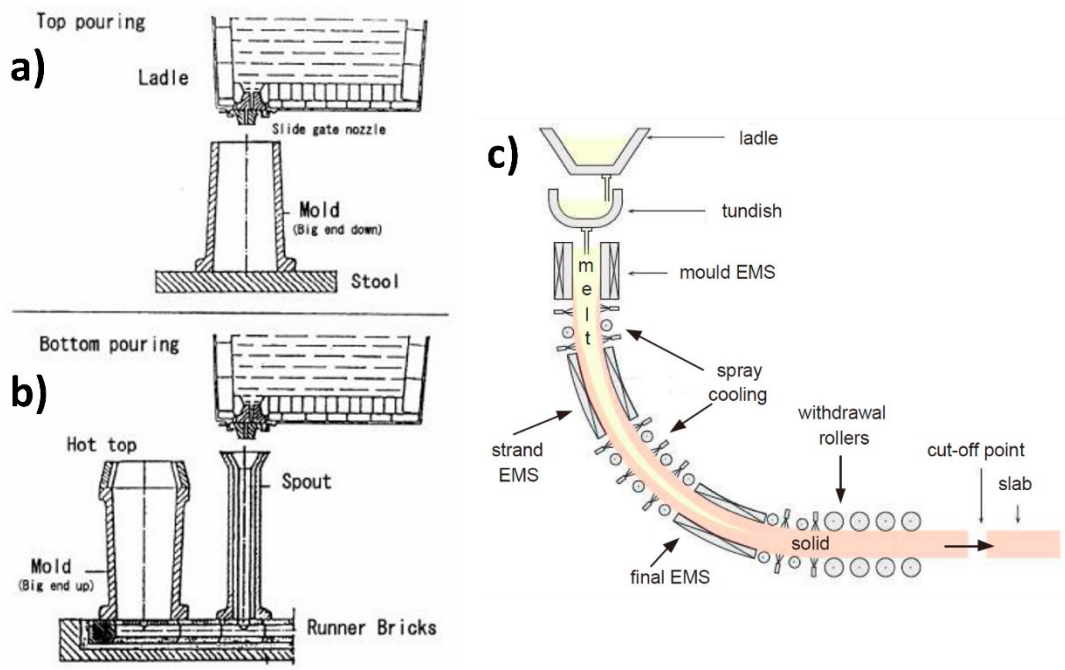

Figure 2.13: A schematic diagram of a (a) typical top poured ingot (b) bottom poured ingot [210] *and (c) a curved continuous casting process, showing various features of the system* [86].

2.5.3 Electroslag Remelting (ESR)

The electroslag remelting (ESR) process is commonly employed, mainly for the further refinement of large steel ingots, for critical applications where compositions need to be carefully controlled. The fundamental processes include the removal of segregation, porosity, control of non-metallic inclusions, reducing secondary dendrite arm spacing and desulphurisation. These aforementioned features are commonly found in large steel ingots and can often cause issues in terms of mechanical properties and quality. An example of two identical ingots processed with and without ESR are shown in *Figure 2.14*. A more homogenous macro-structure can be seen in the ESR-processed ingot (*Figure 2.14b*). The refinement is achieved through the slow melting and transfer of the steel ingot (consumable electrode) through a compositionally controlled slag layer, which is melted by resistance heating, within a water-cooled mould, a diagram of an ESR process is shown in *Figure 2.15*. The overall product is much better in quality than the original continuously cast billet or large ingot. ESR is often employed for segregation sensitive steels as macro- and micro-scale segregation is reduced in extent. (Homogenising heat treatments can also be given in the furnaces

prior to any piercing or shaping, more information on homogenisation is given in *Section 2.4.8*). Since ESR processing is not performed under vacuum (reduced pressures or inert gas atmospheres are sometimes used), ingots of up to 100s of tonnes in weight can be processed. For smaller ingots of less than approximately 50 tonnes in weight the ESR process may come after vacuum induction melting. This can provide improved refinement through an extra step or homogenisation and refinement [89][90]. The ESR process should be able to deliver solidification, which is steady state and radial for the hemispherical cap melt pool, Figure 2.15; this directional solidification can be important in applications where a controlled microstructure and properties are desired. ESR should theoretically eliminate central porosity and segregation as well as negative base and V-type segregation in ingots (as in conventional continuous casting). However, some segregation types such as channel-type and centreline (radial) have been found in ingots processed by ESR [90][91].

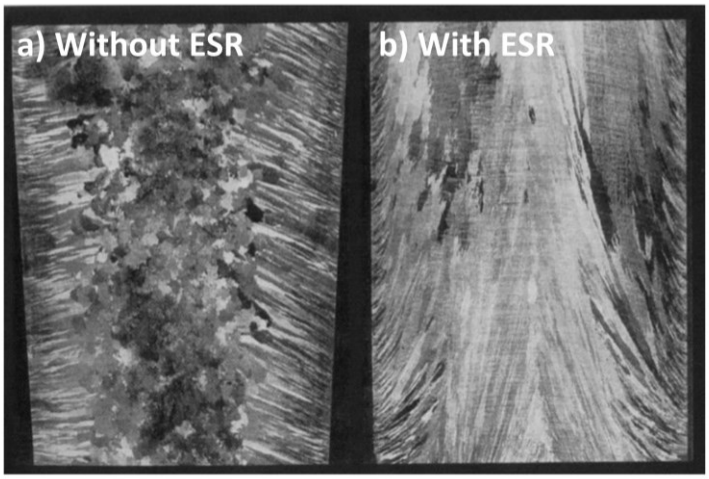

Figure 2.14: Cross-section of two steel ingots cast under the same conditions, but without ESR processing (a) and with ESR processing (b), scale bar is not provided [92].

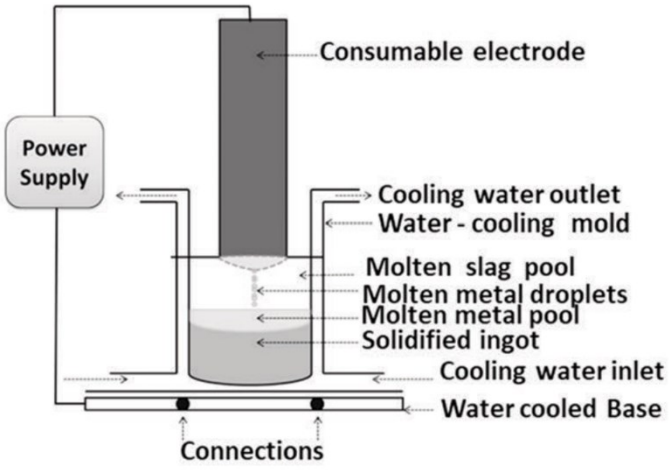

Figure 2.15: A schematic diagram of ESR processing [93].

2.5.4 Seamless Pipe/Tube-making and Forgings

During the development of modified 9Cr-1Mo steel (ORNL 6303), the main processes used for producing pipes or tubes were the mandrel mill process (hot rotary pierced) and the plug mill process (hot extruded) [13]. Relatively speaking, these are used for smaller and larger tube/pipe diameters for the mandrel and plug mill processes, respectively. *Table 2.1*, summarises typical size ranges for mandrel mill and plug mill pipe/tube making from JFE steel corporation, Japan [94] and Vallourec, France [95].

Table 2.1: Typical size ranges for finished products from the common tube/pipe making processes from JFE [94] *and Vallourec* [95].

Processing Route	Size Ranges		
	Outer Diameter (mm)	Wall Thickness (mm)	Length (m)
Mandrel mill, JFE	25.4 - 177.8	2.3 - 35	4 - 15.3
Mandrel mill, Vallourec	26.9 - 180	--	--
Plug mill, JFE	177.8 - 426	4.8 - 55	5.5 - 13.6
Plug mill, Vallourec	300 - 1,500	20 - 50	--

The first step in the mandrel mill process is to evenly reheat the cylindrical billet in a rotary hearth heating furnace so it can be physically deformed in subsequent steps, this can be seen in *Figure 2.16a*. It is then gripped by rollers which rotate and push it into

a piercer, this creates a hole through the length of the billet *(Figure 2.16b)*, the pierced billet is then passed over a mandrel via several rollers until the outside diameter and wall thickness are sufficiently modified *(Figure 2.16c)*. This shell is then reheated and further passed through a stretch reducing mill where it is reduced further to the required dimensions. The product is then heat treated, straightened, end finished, tested and inspected before shipping [94][96]. The plug mill process is similar to that of the mandrel mill, the difference being that, after the billet is pierced, a plug is inserted into it, the billet is then pushed through a die in an extrusion process [97]. For these processes, rolling elongation can range in between 4 to 7 times the original length, and the diameter reduction of the billet can reduce up to 85 % [98]. For pipes up to 1,500 mm in outer diameter and 150 mm in wall thickness, Vallourec process a cast ingot through the steps of vertical piercing, drawing, heat treating, straightening, and then internally and externally boring and grinding [95].

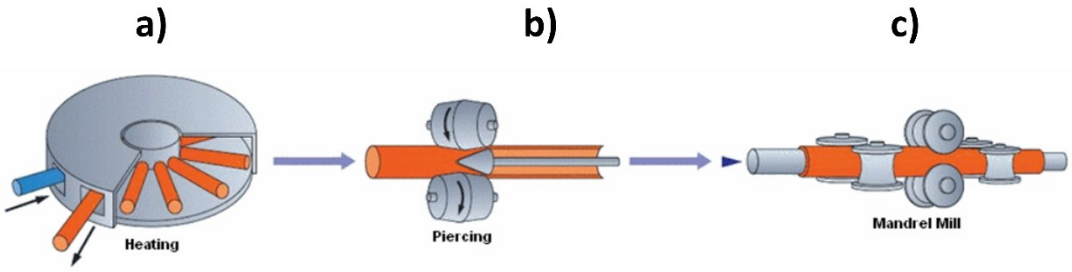

Figure 2.16: Diagrams of the first 3 steps in the rotary pierced pipe-making process (a) the rotary hearth heating furnace (b) the piercing process and (c) the mandrel milling process [97].

Forging processes are also used but for more geometrically complex or large components such as tee-pieces and elbow sections [13][94]. Forging can be performed hot, cold or warm and is classed into three main categories:

i. Drawing increases the length of the component whilst the cross-section decreases.
ii. Upsetting decreases the length of the component whilst the cross section increases.

iii. Compressing (in closed dies) into a distinct shape which creates a multi-directional flow.

The closed-die forging process without flash is commonly used for the aforementioned components, flash during forging refers to the excess materials which is squeezed out between the dies when they are closed together. During closed-die forging without flash a billet or ingot, with a carefully controlled volume is deformed by the punch in order to fill a cavity within the die. Several individual pieces will make up the punch and die [99]. For tee-pieces or pipe/tubes multiple presses with different directions may be used for the various hollow structures.

2.5.5 Solidification Structures

During the continuous casting process many solidification structures can form. Assuming a binary alloy system and a flat mould wall, the 3 most common microstructures formed are equiaxed dendritic, columnar dendritic and equiaxed non-dendritic [100] as shown in *Figure 2.17*. Equiaxed dendritic structures are most frequently found in most steels, due to heterogeneous nucleation or a dendrite multiplication process. If these 2 processes are not sufficient then a columnar dendritic structure forms, which apart from dendrite arrangement is very similar to the equiaxed structures. The third common type (equiaxed non-dendritic) forms when a dynamic force is applied to the system during the early stages of solidification, this is regarded as dendritic multiplication. Typical dendritic structures can no longer form, instead there are spheroidal structures that nucleate from growth centres [100].

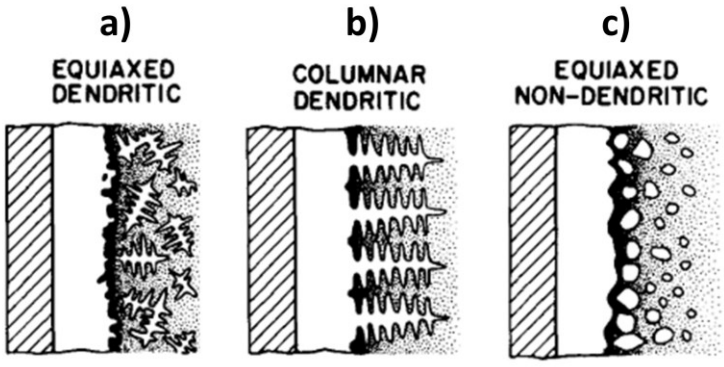

Figure 2.17: Diagrams of typical (a) equiaxed dendritic (b) columnar dendritic and (c) equiaxed non-dendritic structures which can form during solidification [100].

These 3 typical structures from castings/ingots are defined by a relatively low G/R (thermal gradient/ growth rate) ratio value. If the G/R ratio is increased (by adding and taking away heat from different ends of a solidifying alloy) then other solidification structures will form such as cellular and plane front single/dual phase. Each grain in a solidified system contains thousands of dendrite arms, which all originally nucleate from the same growth point, and the crystallographic orientation of the grain will be uniform [100].

2.5.6 Micro-segregation

Depending on its scale, segregation can be divided into micro- or macro-. Micro-segregation occurs in between the dendritic and interdendritic regions of solidifying dendrites and is usually on a micron scale (1/2 the distance of the secondary dendrite arms), whereas macro-segregation is on the scale of the cast itself. The fundamentals of segregation in steel have been detailed by Flemings [100] and more recently other researchers [38][39]. In micro-segregation there are 3 zones during solidification; solid, mushy and liquid [100]. The mushy zone consists of dendrites surrounded by interdendritic liquid, where positive segregation (enrichment) occurs due to the rejection of solutes from the dendrite core (which is the purest) to the interdendritic liquid. Negative segregation (depletion) occurs when dendrite tips detach and concentrate creating purer regions in addition to dendrite coring. Further to this, at the solid fraction of (approximately) 90% the secondary dendrite arms impinge each other, which traps enriched interdendritic liquid from surrounding regions [101]. *Figure 2.18* displays a diagram showing an ideal columnar dendrite with various dendrite arms labelled [85]. From a binary phase diagram, the lever rule can be used to define the equilibrium partitioning coefficient (K_e) which defines the solute redistribution in a system and is defined by *Equation 2.6* [39].

$$k_e = \frac{c_S}{c_L} \qquad \textit{(Equation. 2.6)}$$

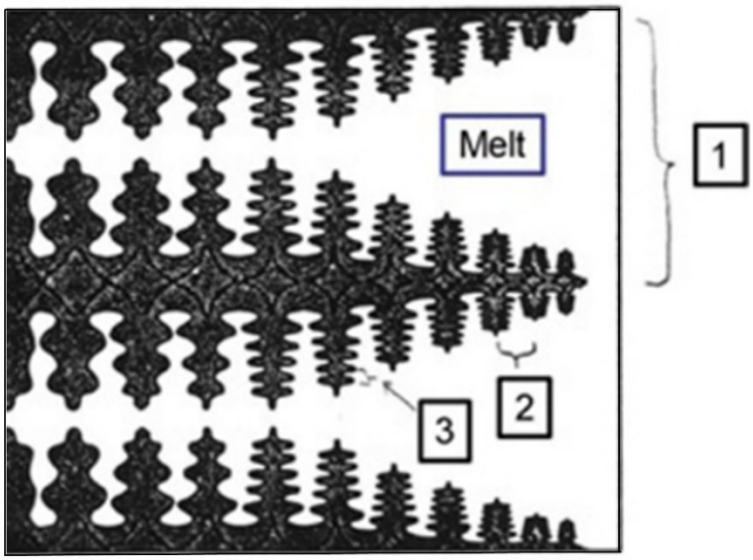

Figure 2.18: A schematic diagram of an ideal columnar dendrite, with primary dendrites (arm spacing), secondary dendrites (arm spacing) and tertiary dendrites (arm spacing) labelled, 1, 2 and 3 respectively [85].

Where c_S and c_L are the respective concentrations of an element in the solid and liquid phase. The assumption is often made that the liquidus and solidus lines are straight so that ke is constant, but in reality, the solidus and liquidus lines are not straight, therefore the value of k_e changes during solidification. For values of k_e is under the value of 1 then micro-segregation is positive (the lower the k_e the greater the degree of segregation), the value of k_e is dependent on the solubility of the individual element in δ-iron and γ-iron, with δ-iron stabilisers having a lower k_e in γ-iron due to lower solubility which means they will segregate more (e.g., Cr, Mo, Si, V). The γ-iron stabilisers will work in the opposite manner (e.g. Mn, Cu, Ni, C, N) [85]. This is because of the similarities in crystal lattice structures, for example γ-iron stabilisers tend to have the same FCC crystal structure and δ-iron stabilisers tend to have the BCC crystal structure [102]. Depending on the post-casting shaping of the steel the micro-segregation may take different forms, which is known as its chemical structure [39] (e.g. a banded chemical microstructure due to rolling [103]). A list of theoretical k_e values for elements in δ-ferrite and austenite are given in *Table 2.2*, these values are assumed to be independent of temperature and were defined from binary phase diagrams [101].

Table 2.2: Equilibrium partitioning coefficients and diffusion coefficients for elements in δ-ferrite and austenite found in literature [101] *(and* [39][104] *where stated).*

Element	k_e δ-ferrite	k_e Austenite (γ)	D^{δ} (m^2/s)	D^{γ} (m^2/s)
C	0.19	0.34	0.0127E-4*Exp(-81379/RT)	0.0761E-4*Exp(-134429/RT)
Si	0.77	0.52	8.0E-4*Exp(-248948/RT)	0.3E-4*Exp(-251458/RT)
Mn	0.76	0.78	0.76E-4*Exp(-224430/RT)	0.055E-4*Exp(-249366/RT)
P	0.23	0.13	2.9E-4*Exp(-230120/RT)	0.01E-4*Exp(-182841/RT)
S	0.05	0.035	4.56E-4*Exp(-214639/RT)	2.4E-4*Exp(-223426/RT)
V	0.93	0.63	4.8E-4*Exp(-239994/RT)	0.284E-4*Exp(-258990/RT)
Nb	0.4	0.22	50E-4*Exp(-251960/RT)	0.83E-4*Exp(-266479/RT)
Cr	0.95	0.86	2.4E-4*Exp(-239785/RT)	0.0012E-4*Exp(-218991/RT)
Ti	0.38	0.33	3.16E-4*Exp(-247693/RT)	0.15E-4*Exp(-250956/RT)
Ni	0.83	0.95	1.6E-4*Exp(-239994/RT)	0.34E-4*Exp(-282378/RT)
Mo [39]	0.80	0.60	0.83E-4*Exp(-225500/RT) [105]	0.11E-4*Exp(-255200/RT) [105]
N [39]	0.28	0.54	0.5E-4*Exp(-77000/RT) [104]	0.91E-4*Exp(-168600/RT) [104]
Al [39]	0.92	--	30E-4*Exp(-234500/RT) [104]	--

A range of micro-segregation models has been developed over the years to help study and understand solute re-distribution during dendritic solidification. In a study by Gui et al. [106] previous fundamental equations for various models were reviewed, on the basis of creating a model which considered the effect of a variable partitioning coefficient during solidification of a high S steel. It was noted that many models used a fixed partitioning coefficient; that the Scheil model is considered appropriate for rapid solidification modelling (such as in 9 - 12% wt Cr martensitic steels); and that the Brody-Flemings model suitable for solidification of columnar dendrites [106].

In continuous and ingot casting

Daamen et al. [107] studied the micro-segregation levels and spacing (SDAS) in a steel ingot and a twin-roll strip casting. The ingot cast was carried out in a pure Ar

atmosphere at 600 mbar, a top pouring process was used with an ingot size of 140 mm (x), 140 mm (y) and 650 mm in height, which weighed approximately 100 kg. The ingot showed a SDAS of approximately 50 μm, in comparison the strip casting showed SDASs of 4 μm close to the strip surface and 7.5 μm close to the strip centre. The deviation of the Mn content was measured across the SDAS for both casting processes and, a similar deviation of up to 4.7 wt % was found for each. In a study on ingot casts by Zhang et al. [108] the SDAS was measured in 40 tonne ingots which were 250 cm in height and 150 cm in their mean diameter. The SDAS was found in the range of 470 - 536 μm for the ingots in the study. However, a cooling rate was not provided for the experiments, furthermore, all the measurements were taken from the centre of the ingot rather than throughout its thickness or height. However, this does signify the scale of the SDAS and therefore the spatial scale of any micro-segregation.

Choudhary at el. [109] found a SDAS of 125 μm in a continuously cast high carbon steel billet; the estimated cooling rate was around 0.24 K/s. Alizadeh [110], created a model for investigating the effects of various continuous casting process parameters on the cooling rate and SDAS in a bloom steel. The parameters which were investigated included the mould level, mould oscillation frequency, thickness, flow rate of cooling water, casting velocity and the viscosity of the mould powder. It was found that increasing the casting speed, flow rate of the cooling water, mould frequency and viscosity of the mould powder led to a smaller SDAS. Increasing the mould thickness from 15 cm to 23 cm meanwhile, led to coarser a SDAS (from 42.4 to 44.6 μm). In this work a good fit was found between the model and experimental data.

The scale of the micro-segregation is dependent on the secondary dendrite arm spacing (SDAS), which is influenced by a number of solidification parameters. Zhang et al. [111] found that reducing the SDAS increased the magnitude of Mn segregation in high-strength low alloy steel. The SDAS increases with a slower cooling rate, increased distance from a chill surface and increased distance from a (mould) interface [38][85][100]. The variation of SDAS can be seen in *Figure 2.19a* as a function of distance from the surface of a steel billet. The changes in the SDAS are as a result of the different zones, for example in the initial chill zone the SDAS is approximately 10

μm, it then increases to around 200 μm due to the reduced cooling in the secondary zone, finally the SDAS decreases to roughly 115 μm in the central equiaxed zone (final zone not shown in the graph) [109]. The experimental variation in SDAS as a function of cooling rate can be seen in *Figure 2.19b,* these data are for a set of steels containing 0.14 - 0.88 wt % C from Suzuki et al. [112]. Since the cooling rate during steel solidification is directly related to the SDAS, *Equation 2.7* can be used to relate one to the other [113].

$$\lambda = a\dot{T}^{-b} \qquad \textit{(Equation 2.7)}$$

Where λ is the dendrite arm spacing in μm (either primary or secondary), a and b are constants and $\dot{T}$ is the localised cooling rate in K/s. Depending on the steel composition, different values have been proposed by researchers. For example, Suzuki et al. [112] found values of 146 and -0.386 (for a and b, respectively) to best fit their experimental findings shown in *Figure 2.19b*.

Sufficient high temperature heat treatments must be undertaken to eliminate the effects of micro-segregation through homogenising of the composition profile. This is not ideal because the steel plant productivity would be negatively affected due to the amount of time that would be required for such homogenising treatments [38]. Casting smaller sections would be a solution to reducing the SDAS. However, as discussed earlier, the requirement of large ingots is sometimes necessary for larger Gr. 91 products. When comparing micro-segregation between large ingot casts and continuously cast steels, the solidification or cooling rate would typically be slower in the larger ingot as shown in some of the previous studies [107]-[110] which covered large ingots as well as smaller continuously cast sections. This would lead to a lower level of micro-segregation (composition amplitude) due to a longer time for diffusion during post-solidification cooling but a coarser SDAS. Whereas continuous casting would generally have a faster cooling rate due to inherently smaller sections, this would mean greater micro-segregation in terms of composition amplitude but a finer SDAS. The finer SDAS can also be effective in negating the effects of the micro-segregation through faster and easier homogenisation heat treatments [85][107].

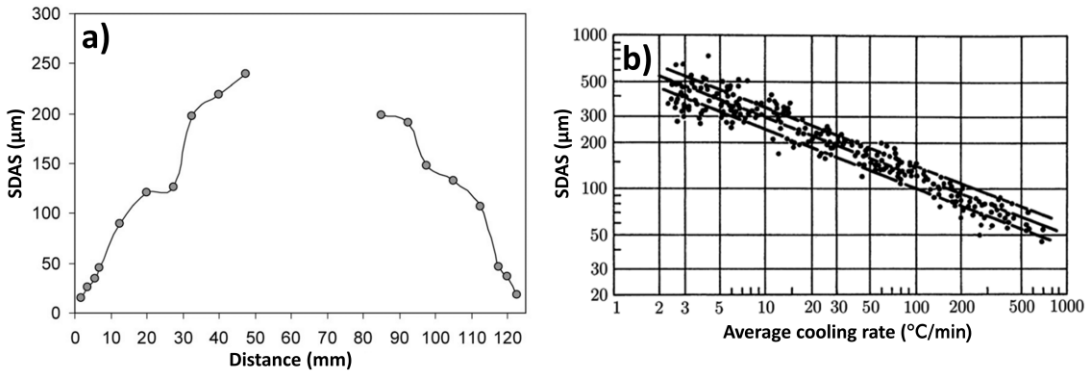

Figure 2.19: The variation of the SDAS from the surface to the centre of a 125 mm² high carbon steel billet (a) [109]*, and the experimental variation of the SDAS in 0.14-0.88 wt % carbon steels with regards to the cooling rate (b)*[112].

2.5.7 Macro-segregation

Macro-segregation in steels is usually on a much larger (1 cm - 1 m) scale and occurs during the casting of an ingot or continuous casting [85][100]. It is often accompanied by other defects such as cracking and porosity, which have adverse effects on the casting's quality [100][106]. Furthermore, the presence of macro-segregation can severely affect the hardenability and subsequent mechanical properties of the final product. The degree of macro-segregation is dependent on numerous factors, which include the equilibrium partitioning coefficients of the solute elements (K_e) and the R/K_m (where R is equal the growth rate and K_m is equal to the mass transfer coefficient); the movement of the solid and liquid phases during the solidification process; the extent of chemical reactions (i.e., inclusion formation), size and morphology of the casting; and mode of heat extraction [39][109]. In general, the overall level of macro-segregation is lower in continuously cast products, when compared to conventional ingot casting, this is both in the longitudinal and transverse directions. Only rarely, with poor control, can the level of centreline segregation be much greater in continuous casting than the segregation found in ingots [109].

In Ingot Casting

Fluid flow on a macro scale during solidification can be defined by the term thermo-solutal convection, which is a combination of thermal and solutal convection. The thermal convection arises due to the temperature gradient in the liquid steel phase and the solutal convection is due to the density gradients due to partition (rejection of

solutes into the interdendritic regions). In addition there can be forced convection from solidification shrinkage [39]. *Figure 2.20a* shows the different types of macro-segregation formed in a steel ingot, which include concentrated positive and negative regions as well as other distinctive formations such as A- and V-type segregation [114][113]. The 4 types are summarised in the following points:

- Bottom negative or 'gravity' segregation forms due to the settling of negatively segregated equiaxed grains at the bottom of the ingot, due to gravitational forces.
- Positive or 'hot-top' segregation forms in the late stages of solidification due to the flow of positively segregated liquid from the head of the ingot. If the temperature gradient from the top of the ingot is sufficient for inducing solidification, then a dendritic formation will expand from the top of the ingot downwards. Enriched liquid will then form the basis of the positive segregation, just below the top of the ingot, as seen in *Figure 2.20a*.
- A-type segregation is classified as channels of positively segregated regions within the final solidified ingot, at the transition from columnar to equiaxed grains. The enriched interdendritic liquid rises via thermo-solutal convection. As the liquid rises it gets hotter, which delays solidification of the solid around it. This creates positively segregated channels which are also referred to as 'freckles'.
- V-type segregation occurs in the central zone of the ingot between the loosely connected equiaxed grains. V-type segregation arises due to solute-liquid filling the open channels down the central region of the casting as the final solidification stage. The open channels associated with V-type segregation are the return (downward) flow paths for the solute-enriched liquid that rose in the A-type segregation channels further out from the centre of the casting. Such open networks arise due to metallostatic pressure from the weight of the material above, as well as solidification shrinkage.

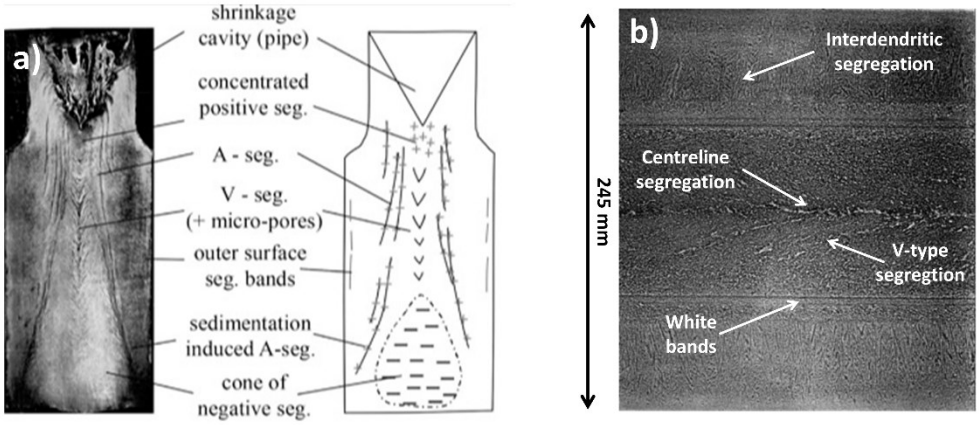

Figure 2.20: Diagrams of typical macro-segregation manifestations in a steel ingot (a) [114] *and in a cross-section of a continuously cast carbon steel slab (b)* [115].

The extent of macro-segregation in ingot casting has been reported by many researchers. *Figure 2.21* shows two examples of the spatial distribution and magnitude of macro-segregation in large steel ingots. The first example (*Figure 2.21a*) from Lesoult [115], shows the macro-segregation of C in a 65 tonne steel ingot. The nominal composition of the steel is 0.22 wt %, the columnar zone can be seen as homogenous with regards to the nominal C content. The bottom of the ingot, which contains gravity segregated material, can be seen to have below the nominal composition, in two regions with 0.16 and 0.18 wt %. This bottom negative segregation region can also be seen to extend to almost 50 % of the height of the ingot. The top of the ingot shows intensive positive segregation with over 3 times the nominal C composition of the ingot. The second example in *Figure 2.21b* shows the Cr content variation, the nominal composition of Cr in this ingot was 4.88 wt %. The presence of the bottom negative and also the positive segregation at the top of the ingot can be seen quite clearly, although to a lower compositional extreme and scale when compared to the example in *Figure 2.21a.* This may be due to a number of factors including the size of the casting (it should be noted that the two studies presented are from different sources and are of different sizes) and partitioning coefficients of Cr and C, for which C has a much higher tendency to segregate. Nevertheless, the Cr composition can be seen to reach as high as 6.36 wt % and as low as 4.43 wt %, the positive segregation being the more pronounced different of the two extremes with regards to the nominal

composition. A-type segregation can also be seen too, as bright strings, after the columnar zone on the sides, up to 0.5 metres in length.

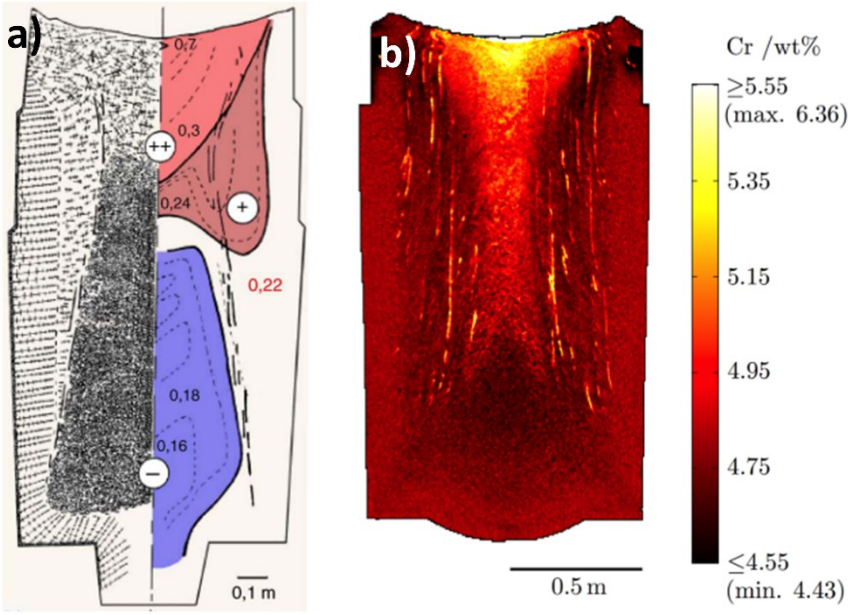

Figure 2.21: Longitudinal centre of ingot cross sections of (a) a 65 tonne steel ingot showing the spatial distribution and magnitude of macro-segregation of C [115] *and (b) a smaller ingot showing the spatial distribution and magnitude of Cr* [90].

In Continuous Casting

In continuous casting, the effects of macro-segregation are also observed but in different forms compared to ingot casting. During solidification from the mould walls towards the centre of the continuous cast product if the columnar grain growth does not change to equiaxed then a large degree of macro-segregation can be present, which is similar to the 'zone refining' process. Interdendritic liquid can also add to the centreline segregation, in extreme cases a mini-ingot like structure can form during continuous casting [39], however this is unlikely in a well-controlled continuous casting process. *Figure 2.20b* shows the various types of macro-segregation structures which can be observed in a continuously cast steel. These include, interdendritic segregation, centreline segregation, V segregation and white bands [115]. The 4 types are detailed in the following points:

- The interdendritic segregation is micro-segregation and can be seen in the columnar grain regions in both the upper and lower parts of the slab.

- Centreline segregation is positive segregation along the centre of cast and is considered the most harmful in continuous casting. Due to unsteady heat transfer and liquid flow, some columnar grains can grow rapidly and form bridges across the centre of the section. This can prevent fresh liquid from feeding into the shrinkage cavities and instead lead to enriched liquid to be fed into the central region, this can also lead to centreline porosity [39].
- V segregation in continuous casting consists of several interconnected macro-segregation spots. In cast sections with mostly an equiaxed structure and no centreline segregation, off centred V segregation is present. Due to the small spatial size of V segregation, it is not considered detrimental for less critical steel grades [109]. The direction of V segregation would indicate that this was cast at an extreme speed, either very fast to get a change in the solidification direction or very slow to allow re-circulation during solidification. In ESR produced Gr. 91 ingots, the presence of V segregation is highly unlikely.
- The white bands are regions of negative segregation, where the solute elements are below the metals nominal average. These white bands form due to liquid flow parallel to the solidification front, i.e., during electromagnetic stirring (EMS). Although undesirable, these white bands are not as harmful as positive macro-segregation [115].

In order to reduce centreline segregation during continuous casting, countermeasures have been introduced since the 1980s which include mechanical and thermal soft reduction. Mechanical soft reduction is used to decrease the overall thickness of the section during its solidification process with the purpose of tapering the semi-solidified section in order to compensate for solidification shrinkage [115]. Thermal soft reduction is the application of a faster cooling rate towards the end of the solidification process [101]. An example of the magnitude and spatial distribution of centreline segregation in a continuously cast billet can be seen in *Figure 2.22*. The nominal composition of the elements of interest for this steel were 0.80 C, 0.74 Mn, 0.02 P and 0.03 S (all wt %). The width of the centreline segregation was approximately 34 mm and also shows considerable porosity which presents a problem in quality control [109]. The degree of segregation can be seen to be the greatest for

S, which is 2.6 times the nominal amount. C and P levels at approximately 2 times their nominal amount was reported.

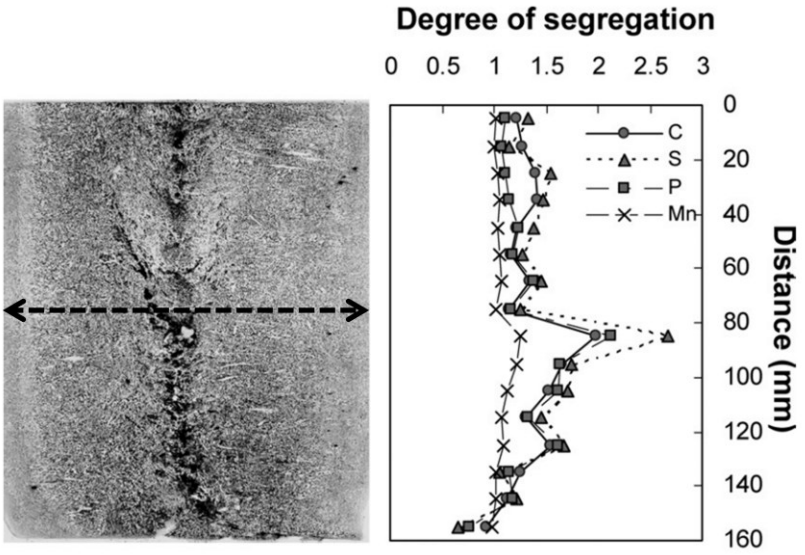

Figure 2.22: Micrograph showing a sulphur print of centreline macro-segregation in a continuously cast billet as well as the degree of the segregation of C, S, P and Mn as a function of distance [109].

2.5.8 The effects of ESR on steel microstructure

The final product after ESR processing is dependent on many initial conditions and process parameters. Some of these include the inclusion content in the electrode, furnace atmosphere, type of slag system as well as the amount, the melting rate, power input, and the scale of the ESR process [93].

One of the main purposes of ESR is to reduce the S content in steels, through a process called desulphurisation. Ali et al. [93] investigated the effects of ESR on removing inclusion-forming elements in three heats of ultra-high strength steel (UHSS). The authors used a 70 % CaF_2, 15 % CaO and 15 % Al_2O_3 slag system which is known for its high desulphurising ability as well a high removal of inclusions. The impurity element level can be calculated from the compositions acquired in the study and expressed as a Modified J-Factor (MJF), which is an impurity index [116]; more information on the MJF is provided in *Section 2.5.3*. The authors also provided an impurity measure in the form of Total Impurity Level (TIL) which was measured as the total of O, N and S in wt %. *Table 2.3* shows the MJF and TIL of the three heats

of steel, each of them with and without ESR processing. The S levels in each of the steels was almost halved, along with the TIL content. The MJF did not show a significant decrease, however the MJF also includes the As, Sn and Pb levels, which were not accounted for in the referenced study. Entezari et al. [117] also compared the compositions of a 10 kg ingot (low carbon bainitic steel). Half of the ingot was processed via ESR using a 30 % CaF_2 and 70 % Al_2O_3 slag system to give a comparison of compositions. The S content was reduced from 0.030 to 0.012 wt % after ESR processing, the MJF was also reduced from 593 to 392. Shi et al. [118] showed that the S content was reduced from 0.018 wt % in the electrode to 0.002-0.0047 wt % in ingots produced from argon atmosphere ESR, and 0.002-0.0052 wt % in open air ESR. Wang et al. [119] also found that the S content decreased from an average of 0.0097 wt % in the electrode to 0.0044 wt % in the ESR processed ingot in open air environment. Furthermore, the effects of macro-segregation were eliminated in the ESR processed ingot, this was considered to result from a homogenous distribution of S throughout the ESR ingot (from surface to centre), whereas in the electrode a larger magnitude of S was found in the core than at the surface.

Table 2.3: Data on the chemical compositions for ultra-high strength steel (UHSS) which were processed with and without electro-slag remelting (ESR) [93].

Heat	ESR	MJF	TIL	S (wt %)
UHSS – 1	No	431	0.051	0.024
	Yes	311	0.028	0.013
UHSS – 2	No	441	0.056	0.025
	Yes	331	0.039	0.014
UHSS – 3	No	401	0.056	0.022
	Yes	350	0.038	0.015

ESR processing is also effective in reducing the SDAS in steels. Liu et al. [120] measured the SDAS in a 35.5 kg ESR ingot of a two-piece ingot, which was connected via welding, the dual composition were CrMoV and NiCrMoV, the average SDAS was in the range of 35.3 to 61.5 μm, the variation was found from the bottom to the top of the ingot, respectively. The difference was due to the different cooling

conditions during ESR, which were calculated to be cooling rates of 11.1, 4.5 and 2.3 °C/s in the bottom, middle and top of the ingots, respectively. Yan et al. [121] studied the SDAS and cooling rates in a large (5 tonne) GCr15SiMn ESR processed steel, the cooling rates and SDAS can be seen in *Figure 2.23*. From the edge of the ingot to the centre, the SDAS first increased and then decreased, and from the bottom of the ingot to the top of the ingot the SDAS increased. The variation from the bottom to the top was due to the greater cooling at the bottom of the ingot from a water tank. Whereas the middle and top of the ingot only had water cooling applied to the mould wall. For the variation from the edge to the centre, the differences were due to the formation of a columnar dendritic structure which increases the SDAS and then an equiaxed zone in the centre which then decreased the SDAS.

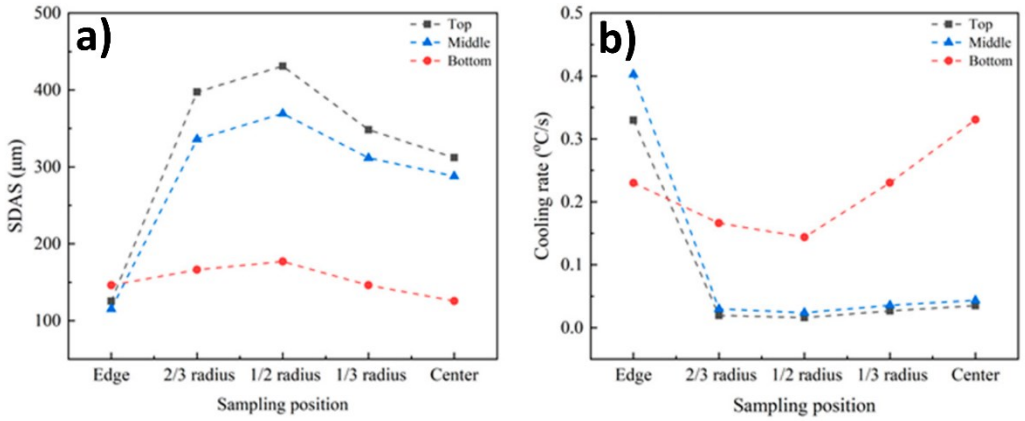

Figure 2.23: Graphs showing the (a) SDAS and (b) cooling rates of a GCr15SiMn ESR processed steel ingot [121].

The melting rate of the consumable electrode (also referred to as the melting rate during ESR) is one of the most important parameters which influences the final solidification structure. This is due to the influence on the solidification time and rate of the liquid steel [87][122]. Shi et al. [87] also measured the SDAS in industrial scale tool steel billets (160 mm^2 in cross-section) which were processed using ESR. SDASs of 110, 118, 128, and 150 μm were measured for 4 different billets. These SDASs corresponded to calculated cooling rates of 4.25, 3.38, 2.63 and 1.64 °C/s, respectively. The coarser SDASs and slower cooling rates corresponded to faster melting rates of the electrode, due to an increase in the local solidification time. The micro-segregation levels increased with the faster melting rates. This was due to

dendrite coarsening which increased the amount of enrichment in a smaller amount of interdendritic liquid and back-diffusion was unable to compensate for the effect. Zhu et al. [122], also investigated the melting rates during ESR. The higher melting rates created a deeper molten metal pool and wider mushy zone so that elemental segregation became more severe with the wider mushy zone. Samples from ESR ingots which were melted at 150 and 133 kg/h were analysed and the schematic diagram in *Figure 2.24* represents the respective microstructures. The authors found micro-segregation was closely related to the dendritic growth. At the higher melting rate, the molten metal pool was deeper, and the dendrite growth was slower. This was due to the increased heat transmission into the molten metal pool. At the lower melting rate, the molten metal pool was shallower, which increases the relative cooling intensity in the mushy zone. As a result, secondary dendrite arms grew more rapidly, which resulted in the more enclosed region seen in *Figure 2.24.* The enrichment of solute was prevented in the closed regions (lower melting rate), and in the higher melting rate the solute atoms aggregated in the central regions between the dendrites.

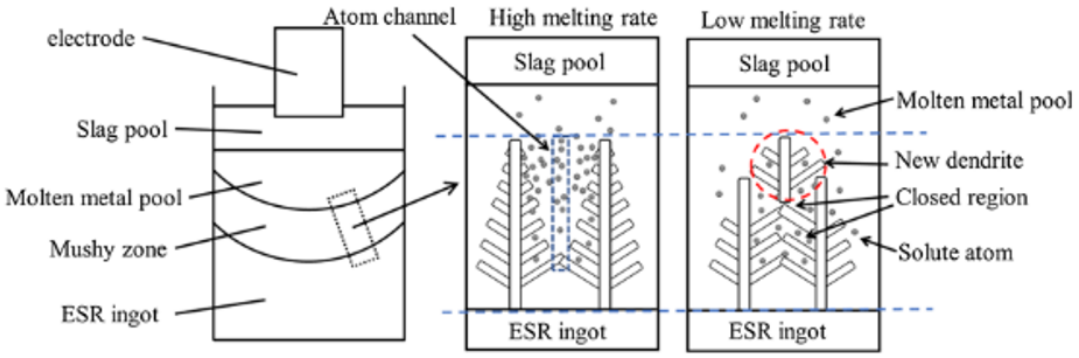

Figure 2.24: A schematic diagram showing the effect of the high (150 kg/h) and low (133 kg/h) melting rates on the interdendritic micro-segregation [122].

ESR processing is also commonly used for the removal or modification of inclusions in steel. In the study by Wang et al. [119], the inclusion content was measured in the electrode and ESR ingot using SEM imaging. The average area coverage of inclusions decreased from 0.313 % to 0.107 %, between the electrode and ESR ingot, respectively. Furthermore, the number per unit area of inclusions decreased by 62.9 %. Before ESR processing, many complex inclusions were present in the steel, which formed in the refining process. However, after ESR, the inclusions were more based

on $CaO\text{-}Al_2O_3$ and Al_2O_3 inclusions. It should be noted, for both desulphurisation and inclusion removal, the levels of inclusions and S in the consumable electrode, the remelting rate and different slag systems have an impact on the cleanliness of the final ESR ingot [123].

2.5.9 Macro- and Micro-segregation in Pipes and Forgings

Macro- and micro-segregation can often manifest itself in CSEF steel pipes and forgings. The problem of macro-segregation is a common quality issue in large ingots and forgings in the power generation industry [124][125][126]. The main concern as highlighted in the previous literature review (*Section 2.4.7*) is the positive, V-type and A-type segregation in ingot casting and the centreline segregation in continuous casting.

When pipes are manufactured as discussed in *Section 2.4.4* the central part of the billet is pierced as shown in *Figure 2.25a,* any residual macro-segregation which may be from continuous casting, or an ingot, may remain in the steel. For continuously cast sections centre-line segregation will remain on the inside surface of a pipe, likewise, positive and gravity segregation from a cast ingot would remain on the inside surface as well. The 'A' and 'V' macro-segregation types would be distributed through the wall thickness of the tube. Typically, for these processes, the rolling elongation can be between 4 to 7 times the original length and the diameter reduction can be up to 85 % [98]. For large diameter pipes approximately 1.5 m in diameter, the inside of it is bored [95], which means central macro-segregation is removed, but not A- or V-type. For large ingots which need to be forged into a component with a hollow centre, the central core is removed through a process called trepanning. This removes most of the V-type and some of the A-type segregation in an ingot, as shown in *Figure 2.25b*. The head, where there is positive segregation, as well as the bottom may be cropped as necessary. However, if a hollow centre is not required, then central and A- and V-type macro-segregation will remain within the finished product [125]. Therefore, addressing and minimising the macro-segregation during the manufacturing process is very critical for the quality of the final product.

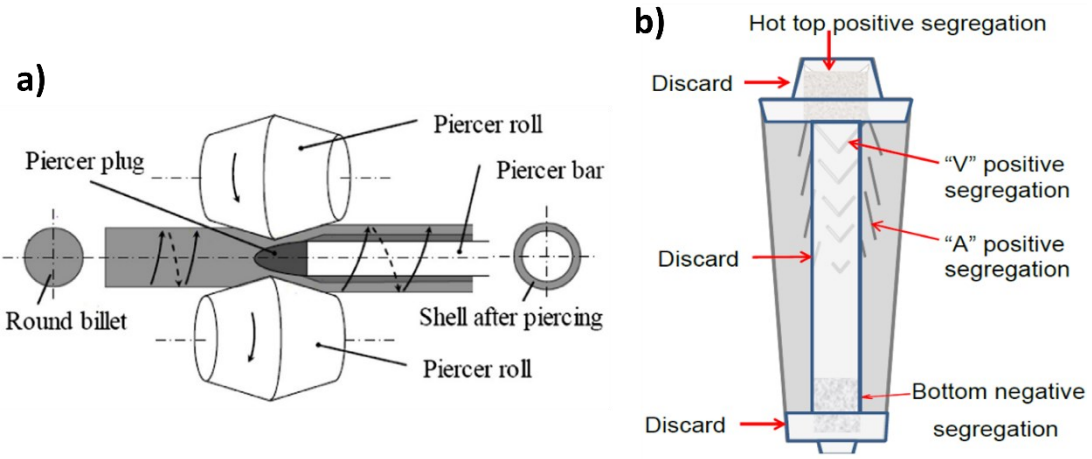

Figure 2.25: Schematic representation of (a) the piercing process for seamless pipe making [127]*, and (b) the possible removal of material from an ingot which will be forged into a hollow component* [125].

The microstructure and therefore micro-segregation morphology is significantly influenced by the method in which CSEF components are manufactured, e.g., pipe or forging. Sawada et al. [40][41] has shown that when Gr. 91 or Gr. 92 pipes are stretched or extruded during the pipe-making process, the micro-segregation takes the form of an elongated band in the longitudinal direction. In forged CSEF products the multi-directional nature in the closed-die forging means no dominant strain direction can be seen, as compared to the pipe or tube products. However, on a macro-scale the structure follows the 'flow' of the forging or die shape. An example of which can be seen in a study by Alves dos Santos et al. [128] on a stainless steel.

2.5.10 Homogenising heat treatments

Gr. 91 and other CSEF steels are typically given homogenising heat treatments post-casting and before any pipe/tube making processes, with a purpose to eliminate any micro-segregation which forms during the solidification process. Such heat treatment consists of holding the metal at a particular temperature for a time period suitable for improving the chemical homogeneity. For a cast ingot with a SDAS of approximately 100 µm, a diffusion distance of approximately half the SDAS is considered appropriate for homogenising [129]. In the same study, a two-stage homogenisation heat treatment cycle was given to CSEF steel, which was 1125 °C for 1 hour followed by 1250 °C for 8 hours. The effectiveness was compared via creep testing of the

homogenised alloys with equivalent commercial products, from which the homogenised alloy performed approximately 3 times longer with regards to time to rupture at 650 °C at 138 and 172 MPa. Directly linking homogenisation to an improved time to rupture can be misleading, due to the many other factors which may have been different between the two sets of steels, such as other heat treatment, ductility and other phase formations. Kun et al. [130] used an homogenising heat treatment of holding 1200 °C for 2 hours, for a wire-arc additively manufactured Gr. 91 steel (20 mm thick) with superior ductility, ultimate tensile strength and yield strength compared to the wrought equivalent Gr. 91 steel. The 2 hours were experimentally validated as being sufficient to dissolve all of the δ-ferrite and MX carbo-nitrides originally present.

The homogenising heat treatments are governed by the diffusion of the constituent atoms in the steel. The general expression for the diffusion coefficient, D, is expressed in *Equation 2.8* [131].

$$D = D_0 \, Exp(-\frac{Q}{RT}) \qquad \textit{Equation 2.8}$$

Where D_0 is defined as the frequency factor, R is defined as the universal gas constant, T is defined as the temperature in K and Q is the activation energy. *Table 2.2* gives the equations for most of the major alloying elements in Gr. 91 steel, with the D_0 and Q values substituted into the equations. The diffusion distance (l) in metres is given by the *equation 2.9.*

$$l = \sqrt{Dt} \qquad \textit{Equation 2.9}$$

Where t is defined as the time in seconds. *Table 2.4* shows the typical diffusion distances for some of the major alloying elements in Gr. 91 steel using a homogenising heat treatment of holding 1200 °C for 2 hours as an example by Kun et al. [130].

Table 2.4: Typical diffusion distances of elements in a Gr .91 steel when homogenised for 2 hours at 1200 °C.

Element	Diffusion distance, l, (mm)	Element	Diffusion distance, l, (mm)
C	3.45	Cr	0.07
Si	0.09	Ti	0.06
Mn	0.08	Ni	0.06
P	0.12	Mo	0.08
S	0.28	N	2.58
V	0.10	Al	0.32
Nb	0.05	--	

2.5.11 The Effects of Segregation on Steel Microstructure

The effects of segregation are often not acknowledged when quantifying microstructural features, with regards to metallurgically complex CSEF steels. In other steels analysis of segregation effects have been acknowledged, although detailed microstructural quantification has not been performed, possibly due to limited resources at the times of those studies.

In Gr. 91 and Other CSEF Steels

Recently Sawada et al. [40][41] have investigated the effects of Cr micro-segregation on creep rupture life of Gr. 91 (T91) and Gr. 92 (T92) steel microstructures, both studies contained a similar structure, experimental procedures and key findings.

It was concluded that Gr. 91 and 92 steels with a greater degree of Cr micro-segregation had a shorter creep rupture life under all creep conditions studied. It was assumed a greater super-saturation of Cr was responsible for the premature creep failure of specimens with severe Cr banding. Other major alloying elements like V and Nb were also found to be banded but were not the focus of the study. The abnormally high concentration of Cr was responsible for a greater driving force in the nucleation and growth rate of Z-phase. Z-phase in CSEF steels is known for its detrimental effect on creep performance as it forms at the expense of smaller MX

particles, which results in net lower precipitation strengthening. Furthermore, the decrease in number density of $M_{23}C_6$ carbides, MX carbo-nitrides and high angle boundaries in the strongly segregated steels led to a faster rate of creep deformation [40][41]. It was, however, suggested that a homogenising heat treatment at 1200 °C significantly improved the creep rupture life by reducing the large Cr concentration gradient [40].

It was shown that the locations of Cr micro-segregation banding were also locations for the enrichment of other precipitates, namely Nb/V-rich type MX and Al_2O_3 inclusions, as well as Cr-rich $M_{23}C_6$ carbides [40]. The chemical banding was seen along the longitudinal axis for various elements (V, Nb, Cr and C) through electron probe micro-analyser (EPMA) maps although the scale is difficult to determine. In a macro-segregation study by Wang et al. [132] in a large cast of CB2 ferritic heat resistant steel, MnS inclusions and coarse NbC MX were found in the positively segregated regions of steel, although in this study a qualitative rather than systematic quantitative analysis of inclusions was performed. Sawada et al. [41] concluded that the positive areas of Cr micro-segregation were greater in Vickers micro-hardness due to the extra $M_{23}C_6$ precipitated. The Vickers micro-hardness in Gr. 91 steel is an important assessment tool for the power generation industry in order to determine microstructural degradation at creep conditions and remaining life assessment in boiler steel components. The monitoring of microstructural degradation is critical for determining the strategies for repairing or replacing components, which has significant financial implications in addition to the need to prevent catastrophic in-service failures [133]. Wang et al. found similar results but on a macro-scale, the hardness gradually increased from the edges to the centre of the cast structure due to macro-segregation, which was attributed to an increased amount of solute and strengthening precipitates [132].

Figure 2.26 shows the differences in $M_{23}C_6$ carbides and MX carbo-nitrides from the two Sawada et al. studies, respectively [40][41]. In both graphs the number densities of precipitates were greater in the inside of the micro-segregation bands than outside of them. It was also noted by the authors that the heats in which the greater difference in precipitate populations were found, showed a greater degree of micro-segregation

from the previous steps of chemical maps, using SEM-EDS and electron micro-probe analysis (EPMA). Overall, this difference in strengthening precipitate populations would lead to a net decrease or increase in strengthening, depending on the region. However, a clear systematic approach was not used on the quantification of the precipitates. It is assumed carbon extraction replicas were used for the quantification of $M_{23}C_6$ carbides, which when used are extremely difficult to locate specific regions of a steel sample, especially concerning 10 - 20 µm wide segregation zones [40]. This raises questions on how these positively and negatively site-specific segregated areas were located and provides an opportunity to perform an improved method of analysis.

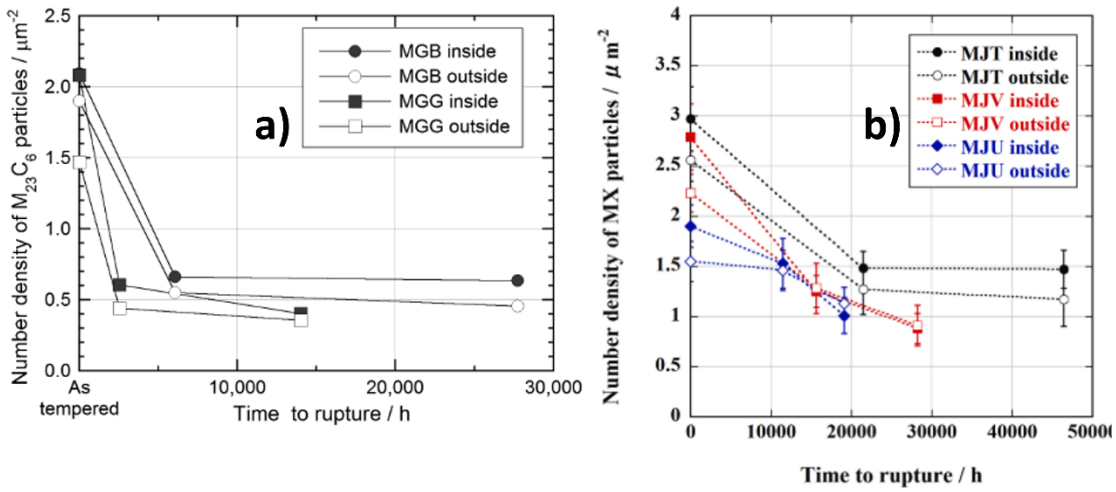

Figure 2.26: Graphs showing the relationship between the time to rupture and number density of (a) $M_{23}C_6$ carbides [40] *and (b) MX carbo-nitrides* [41] *(with respect to micro-segregation) in Gr. 91 and Gr. 92 steels at 650 ℃, respectively.*

Thermodynamic simulations by Santella et al. used the theory of micro-segregation of C, Cr, Mn and Ni to explain how retained austenite was found in weld deposits of a Gr. 91 weld, leading to a weaker performing weld [134]. Examples of the Thermo-Calc Scheil solidification simulations performed are provided in *Figure 2.27*, showing the enrichment of some of the major alloying elements (Cr, Mn) due to interdendritic segregation during the solidification process.

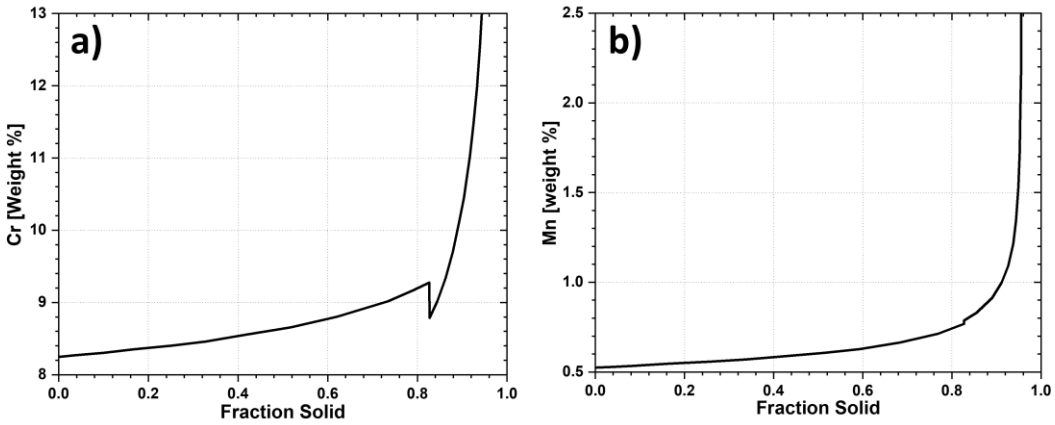

Figure 2.27: Thermo-Calc simulated micro-segregation curves using the Scheil-Gulliver model of (a) Cr and (b) Mn using a P91 weld composition (Fe-0.099C-0.61Mn-0.17Si-9.33Cr-0.97Mo-0.80Ni) [134].

In Low Alloy Steels

In non-CSEF steels, studies for HSLA steels [111], [135], [136] and in C-Mn automotive steels [103], have shown that considering micro-segregation is important. In the case of HSLA steels, a study by Wang et al. into the segregation of Nb and subsequent formation of an increased amount of Nb-rich precipitates in the interdendritic regions led to a banded microstructure with a bimodal/abnormal grain size distribution due to the extra grain boundary pinning effects [135]. Bimodal grain size distributions do not affect mechanical properties such as hardness very significantly, however, they do affect crack resistance properties [137]. In C-Mn automotive steels, Slater et al. found a Mn segregated steel sample only showed a partly recrystallised microstructure for the same holding times as an unsegregated (homogenised) sample due to the variations of Mn in providing solute drag that altered the rate of nucleation and growth of recrystallised grains during thermo-mechanical deformation [103]. Examples of segregated and homogenised Mn elemental maps derived from μ-XRF EDS maps are shown in *Figure 2.28*, displaying clear banding and micro-segregation of Mn. In both examples the motivation for the research was to investigate the variations in mechanical properties of the final product due to micro-segregation.

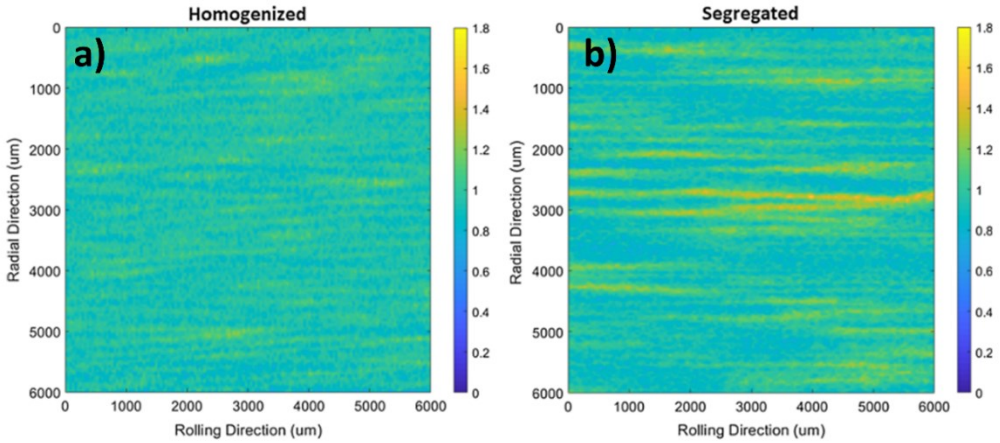

Figure 2.28: µ-XRF chemical maps of Mn showing (a) homogenous distribution and a (b) segregated distribution showing micro-segregation banding [103].

2.6 Inclusions in Steel

Inclusions can form in steel during its production and/or processing steps and can be considered by-products of steelmaking [138]. During the steelmaking process inclusions can be introduced at various points, which include during refining, transfer between vessels, and during the original steel solidification in the solid and liquid state. Exogenous inclusions can be trapped from external sources, such as refractories or slag layers. Indigenous inclusions would form in the liquid or during solidification and would include oxides, silicates, sulphides, nitrides and phosphides. This does not include the fine carbides, nitrides and carbo-nitrides which form during heat treatments, but would include coarse nitrides, such as TiN, that formed in the liquid or during cooling in the high temperature austenite phase field.

The critical size for inclusions in fatigue-limited applications has been widely studied. For example, Chen et al. [139] studied brittle inclusions in a bearing steel and categorised the effect of inclusions based on size ranges. For inclusions smaller than 3 µm it was found that variation in the 0 – 3 µm size range would have a big influence on the lifetime, in terms of fatigue. For inclusions 3 – 15 µm in size, the stress proportionally increased with size. For inclusions larger than 15 µm, the size had little effect on the lifetime. Yang et al. [140] developed a relationship between the critical inclusion diameter for the initiation of fatigue cracks and the hardness of the steel

matrix, also depending on the inclusion position in the steel, these relationships can be seen in *Figure 2.29.*

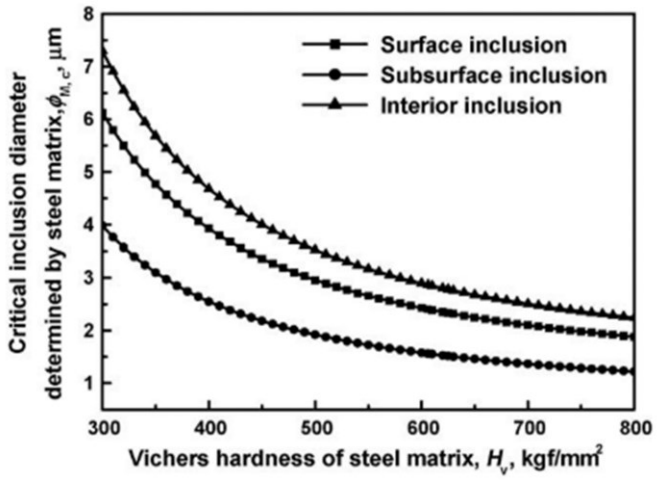

Figure 2.29: The relationship between the inclusion diameter and Vickers micro-hardness of steel matrix for the initiation of fatigue cracks [140].

Inclusions can be split into two classes, indigenous and exogenous and via the types, aluminates, oxides, silicates, sulphides, nitrides, and combinations. Indigenous inclusions precipitate during the solidification of the liquid steel due to the decrease in solubility of the elements in the steel. Some examples are alumina (Al_2O_3) inclusions from low carbon aluminium killed (LCAK) steels, or silica (SiO_2) inclusions from silicon killed steels; and nitrides and sulphides due to N and S in steels [141]. Indigenous inclusions are more uniformly distributed and finer in size than exogenous inclusions, furthermore, since they are naturally occurring, they cannot be completely eliminated but only reduced. Exogenous inclusions form due to the mechanical and chemical interactions of liquid steel with its surroundings, such as slag entrapment and erosion of the refractory lining. They are usually irregular shaped, multi-phase, and large in size, usually above 50 μm [138].

Refinement of liquid steel takes place in ladles, before casting into ingots or being transferred into a tundish, from which it is then poured into the continuous casting mould, a diagram of this setup can be seen in *Section 2.3.1, Figure 2.13c*. Modern continuous casting steelmaking provides opportunities for inclusion removal from ladles, tundish and moulds. During the production of a bottom poured ingot casting

there are also many processes which allow the control of inclusions, as the liquid steel is poured through a runner system and then into the moulds. The system is quite often flooded with Ar inert gas to lessen any oxidation. Within the mould are suspended mould powders (in bags) which are released by the steel burning through them. These mould powders then form a slag layer which protects the liquid steel from atmospheric oxidation and contaminants and also removes inclusions [142].

2.6.1 Types of Inclusions (and Precipitates)

Spinels, Oxides and Aluminates

The liquid steel transfer during casting is a complicated system involving flow and turbulence of the liquid steel, and slag and mould powders (which are used to protect the liquid steel from the vessel it is in). This complex system can create sources for the formation of inclusions in continuously and ingot cast steels [141][143]. During liquid steel transfer in continuous casting there may be a build-up around the tundish nozzle and submerged entry nozzle. These build ups, as well as impeding flow, may contain Al- or Ca-rich inclusions / particles that can break apart and form exogenous inclusions in the final steel structure [141]. These inclusions are usually identified as 'spinels' as $MgO\text{-}Al_2O_3$ (-CaO) crystals, which contain differently charged ions distributed between layers of O that balance the charge [141]. An example of a spinel inclusion is shown in *Figure 2.30* from a recent study by Persson et al. [144]. Although this inclusion is fine in size, spinels can be found upwards of 50 μm in size. In that study, ingots produced from ESR and P-ESR (protected atmosphere) were compared to determine the effect of the controlled atmosphere on the formation of spinel-type inclusions, it was found that almost double the amount of oxide inclusion formed in the ESR method than in the P-ESR method.

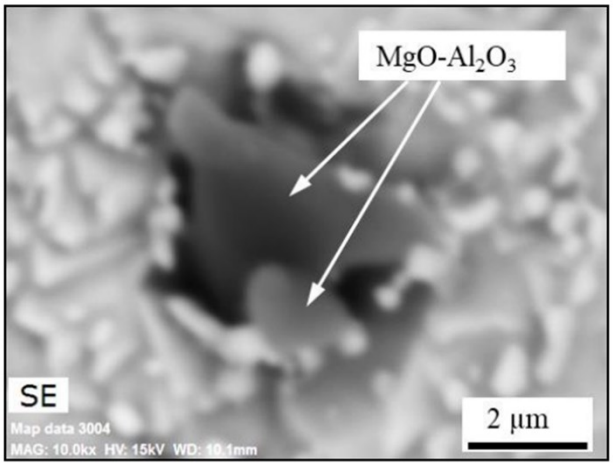

Figure 2.30: SEM-SE image of a spinel inclusion ($MgO\text{-}Al_2O_3$) in a martensitic stainless steel produced from an ESR ingot [144].

Many elements which are acceptable within a steel composition can act as deoxidisers, due to their high affinity with O and so can form oxide inclusions [145]; some examples of deoxidisers are Mn, Al, and Si [146][147]. Examples of common Al_2O_3 cluster morphologies can be seen in *Figure 2.31*, showing dendritic, typical (with no specific morphology) and coral-like formations [148]. At liquid steel temperatures oxide inclusions may be present as a liquid phase as spherical droplets. Oxide inclusions tend to be very hard relative to the steel matrix [146][141]. During hot work the deformation of the matrix may lead to decohesion and separation of oxides with the matrix, forming voids. Furthermore, alumina inclusions are known to cluster during steelmaking, which can mean they start from 1 - 5 µm individual inclusions but cluster to sizes of up to several hundreds of microns [146].

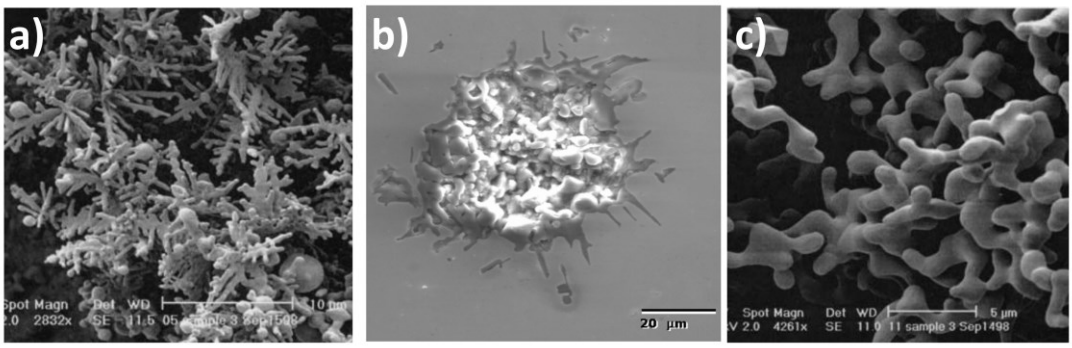

Figure 2.31: SEM-SE images showing the morphology of alumina inclusions produced during the deoxidation process of LCAK steels for (a) dendritic alumina

cluster (b) a typical alumina cluster with no specific morphology and (c) a coral-like alumina cluster [148].

Sulphides

With regards to S, apart from Fe there are only a few elements that have enough affinity with S to form sulphide inclusions, these are Mn and elements with low solubility in iron, for example Ca and Mg. Therefore, most of the S in steel needs to be removed during the refinement stage in the liquid steel via desulphurisation. The remaining S in the liquid steel precipitates during solidification as inclusions, the most common type is MnS inclusions which are normally found below the size of 10 μm [146]. However, the formation of MnS is one of the reasons Mn is considered beneficial to steels; without Mn, S would form FeS, which would be detrimental to the hot workability of the steel due to its low melting point [141] or would be in solution leading to grain boundary embrittlement. MnS inclusions in steel have been classified into 3 fundamental types by Sims et al. [149] as summarised below:

- Type 1: Usually found in a globular form, randomly distributed in the matrix of a steel, spherical shape is largely attributed to S- and O-rich globules. These form early in the solidification of steel and usually with MnO inclusions. An example of a type 1 MnS inclusion can be seen in *Figure 2.32* [150]**.**
- Type 2: These form clusters of fine rods within interdendritic regions, often found in highly deoxidised Al-killed steels. A faster cooling rate will favour the formation of type 2 MnS inclusions.
- Type 3: Usually form with irregular and angular geometries with a range of size distributions, randomly distributed within the matrix of the steel. Often found in steels killed with large amounts of Al and, which contain high C and P levels.

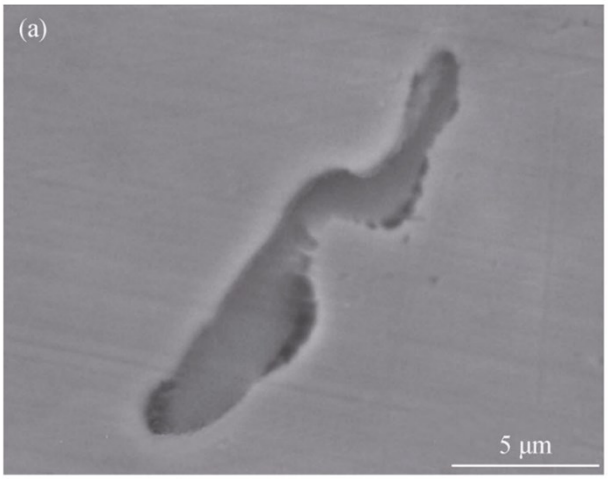

Figure 2.32: SEM-BSE image showing the morphology of a type 1MnS inclusion in a C-Mn steel [150].

MnS inclusions are plastic at hot working temperatures and will deform during hot working operations. This can induce shape anisotropy to the inclusions, which can be reflected in the mechanical properties of the steel [141][146], for example in the role of orientation of elongated MnS inclusions in fatigue applications [151]. In efforts to alleviate this problem of directionality of mechanical properties in steel, sulphide shape control approaches are taken in steel making. These methods include adding Ca to produce harder, more spherical sulphide inclusions, which maintain their shape much better during any hot working [141]. However, the addition of Ca should be carefully controlled as the formation of excess CaS inclusions can lead to nozzle clogging during continuous casting [85].

Two main factors that influence the amount and size distribution of MnS in steels are the content of S and the cooling rate [152]. In a simulation by You et al. [86] a slower cooling rate resulted in the size distribution of the MnS inclusions shifting to larger sizes and having a lower total number per unit area. These changes are related to less enrichment of the Mn and S solute during the solidification process. With regards to the S concentration in the steel, when it is increased, the size of the MnS inclusions increased, however, the total number of the MnS inclusions remained the same, so overall the total MnS inclusion content increased. In summary, finer and fewer MnS

inclusions can be achieved in steel with a rapid (faster) cooling rate and less inherent S concentration in the steel melt.

Another variation of sulphide which is often overlooked is the copper sulphide (CuS). Copper is commonly found in steels as a residual element which is difficult to remove during the steelmaking process. This is an important aspect to consider due to the increase of recycled scrap steel, which can contain increased amounts of Cu. A common problem induced by excessive Cu during steelmaking is hot shortness, which is the grain-boundary cracking phenomenon during solidification due to the presence of Cu. It should be noted that the presence of Cu has also been linked with improved mechanical properties and improved resistance to corrosion in certain applications [153][154]. For example, in a study by Liu et al. [155], comparisons between pure and impure low carbon steels with regards to Cu, P and S showed an improved yield strength in the impure variant. This was due to the formation of copper sulphide precipitates, which were on average 15 nm in size.

It is reported in literature that Cu is often located at inclusion-matrix interfaces [156], more specifically fine copper sulphide (Cu_2S) inclusions have been found between oxide inclusions and the steel matrix [157], which in Gr. 91 steel has been linked with a premature time to failure due to a loss in creep ductility [30]. Three variations and morphologies of copper sulphides have been found and studied in low carbon strip steel, all of which exhibited an FCC structure, the first of which was the plate-like Cu_2S which formed in the austenite phase temperature range and may have been related to the coherency between the sulphide and the γ-iron. The second type was shell-like, which formed at low temperatures. The shell-like morphology was due to the low diffusion coefficient of Cu in the γ-iron phase. The final type was nano-sized which formed at low temperatures in the γ-iron range, but more so in the α-iron temperature range due to a decrease of solubility of the sulphides [153].

Silicates

As mentioned earlier, deoxidisers in the steel bind with O to form oxide inclusions. However, sometimes silicate inclusions also form, usually by the use of silicon-manganese deoxidation products. These inclusions are easily deformable during hot

working and are preferred in thin wire applications, over relatively hard and un-deformable alumina inclusions [85].

Nitride Precipitates

Alloying elements such as B, Ti, V, Nb, Al and Zr commonly form nitrides in steel by binding with N atom. Ti and Nb nitrides can be an effective tool for inhibiting grain growth in thermo-mechanical heat treatment processes such as annealing [158][159]. The addition of titanium is sometimes beneficial in small amounts to tie up excess N in some steels, such as boron-containing steel (MarBN) [141], or in steels to stop austenite grain growth [160][161]. Some examples of typical nitride precipitates are shown in *Figure 2.33*, showing Al, B, Nb and Ti nitrides and their common angular morphologies; nitrides are often fine in size but can be found up to 20 µm in size [158].

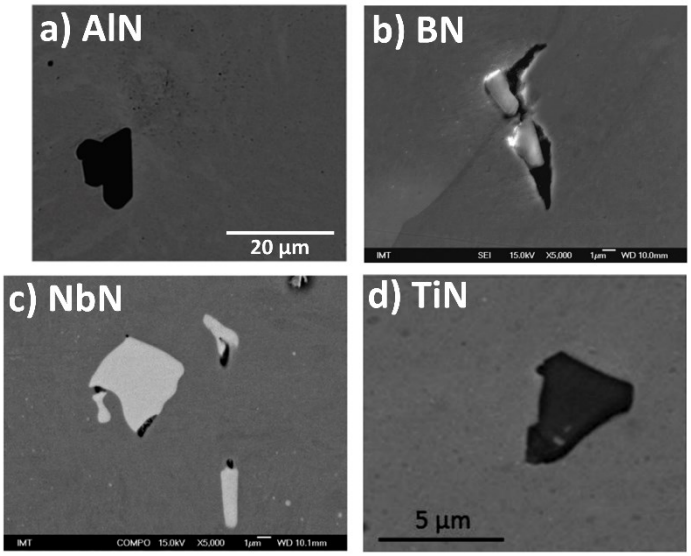

Figure 2.33: SEM images showing 4 variations of nitride inclusions which are commonly found in steels (a) an SEM-BSE image of an AlN (b) an SEM-SE image of a Boron Nitride (BN) which nucleated on an alumina inclusion (c) an SEM-BSE image of a Niobium Nitride (NbN) and (d) an SEM-BSE image of a Titanium Nitride (TiN) [158].

2.6.2 Effects of Casting Routes on Inclusions

In Ingot Casting

The distribution of inclusions in a cast ingot is influenced by a number of factors which include the solidification rate of the steel, fluid flow and heat transfer. These factors determine the likelihood of the centre of the solidifying ingot trapping liquid (which includes inclusions) [148]. A slower solidification rate, less segregation and smaller protrusions on the solidification front can decrease the amount of entrapment by growing dendrites, however, increase the pushing of inclusions by the solidification front into the central region. However, slower solidification allows more time for indigenous inclusions to grow in the liquid making their trapping by the growing solid more likely. The SDAS is a measure of the micro-forces applied on the inclusions by the advancing solidification front; if the SDAS is in the same size range as that of the exogenous inclusions then it can influence the inclusion entrapment. In a study of a top poured ingot, the larger inclusions were found concentrated in distinct portions of the ingot, which included the central bottom portion and outer portions of the top. Whereas, in bottom poured ingots, the large inclusions were distributed much more evenly throughout the ingot. When the temperature of the liquid steel was increased (teeming temperature), the number of large inclusions decreased. This was because the greater temperature helped the floatation and removal of inclusions by natural convection, with the solidifying steel near the mould walls encouraging downwards flow, which creates upward flow in the central region carrying the inclusions with it. The slower solidification gives the larger inclusions time to collide and coagulate, followed by the central upward flow to the slag layer which allows for the separation. After the ingot is completely solidified the top and bottom inclusion-rich parts of the ingot are cut off, although this decreases the yield of the cast, it is necessary for improving the quality of the final product [148].

In Continuous Casting

After the liquid steel is refined in ladles it is then transferred to a tundish. In the tundish a slag layer protects the liquid from external oxygen which otherwise would react with the metal and form oxide inclusions. Curved continuous casters have largely replaced vertical variants due to the space saving offered, however it should be noted curved

continuous casting processes in general leads to uneven distributions of inclusions. This is because inclusions attach to the inner arc of the curved mould variant, which leads to a non-uniform distribution of inclusions through the thickness of the solidifying strand. In vertical continuous casting the inclusions can float up to the meniscus due to their lower density, which means inclusion control is much easier. Submerged entry nozzles (SENs) are used to transfer liquid steel from the tundish to the continuous casting mould. These nozzles can often become blocked with the agglomeration of coarse inclusions; calcium treatment and argon injection are the main two methods of mitigating these problems, with the former modifying inclusions into a calcium-based liquid inclusion at the liquid steel temperatures [85].

Electro-magnetic stirring (EMS), which was introduced to improve steel cleanliness, also affects the distribution of inclusions by reducing the number density and area coverage of the inclusions in a continuously cast section compared with a continuously cast section without EMS [162][163]. Although EMS has been found to be effective in separating smaller inclusions it is not as effective for the larger inclusions (above 100 μm), this is because larger inclusions move to the centre part of the swirl where it is more difficult to float out [85]. EMS is believed to decrease the penetration speed of the liquid steel; without EMS and high penetration speeds all the inclusions follow the liquid flow along the casting direction. With EMS the penetration speed is slowed down which is ideal for separating inclusions. In conjunction with EMS, casting speed is an important parameter to control, for which a slow casting speed is ideal for steel cleanliness.

2.6.3 Quantification Methods for Non-metallic Inclusions

There are 2 common approaches for the quantification of inclusions in steel. These consist of direct and in-direct methods. Direct methods usually involve taking 2-dimensional cross-sections of solidified products and using metallographic procedures to analyse the cross-sections, other direct methods are via 3-dimensional scans through the steel matrix, typically with ultrasound or X-ray waves. In-direct methods are more common in the steel industry due to cost and time saving, and sampling difficulties from metallographic procedures for direct methods. These methods involve analysis

of the metal in the liquid or molten state [148] although these methods do not provide the quantitative results obtained from direct methods.

Some examples of 2-dimensional direct methods are metallographic optical microscopy [164], SEM(-EDS) [165]–[167], laser microprobe mass spectrometry [168], and auger electron spectroscopy [169]. Some of the 3-dimensional direct methods are ultrasound scanning [170], X-ray detection/tomography [165], electron beam melting [171] and magnetic particle inspections [135][172]. Some in-direct methods include nitrogen pick-up [142], total oxygen content [167] slag composition [173] and element concentration measurements [174]; a more in-depth review of the different techniques can be found in work by Zhang and Thomas [148][175]. The following discussion in this section will mainly focus on the 2-dimensional direct method of SEM-EDS, this technique allows many details to be collected in the inclusion analysis, such as size, chemistry and local position of individual inclusions and their types. This is not as accurate with any of the other direct or in-direct technique mentioned above.

A widely used inclusion quantification method is the ASTM-E45 standard for determining inclusion content in steel. This standard utilises optical microscopy that classifies inclusions based on shape and size into 4 categories; sulphides, aluminates, silicates and globular oxides [176]. There are a few drawbacks to this technique, which include the collection of a limited size distribution of inclusions (a focus on large inclusions above 5 μm), in the case of creep-related inclusion analysis finer inclusions are also detrimental in regards to forming creep cavitation, for example AlN precipitates which are fine but considered highly detrimental [18][22]. Furthermore, this technique fails to distinguish inclusion types based on composition because inclusions are purely quantified on shape and greyscale.

The ASTM-E2142 standard utilises SEM-EDS to quantify and classify inclusions in steel [166]. The standard recommends an accelerating voltage of 10 - 15 kV in BSE mode as appropriate to use for the inclusion analysis; this is to avoid any excessive increase in the penetration depth from the use of higher accelerating voltages. The variation in greyscale threshold is used to distinguish inclusions from the matrix. The

chemical composition available from the EDS detector will allow inclusions to be classified based on a customised classification system, and higher magnifications can be used in order to detect fine inclusions which are unable to be detected using the procedure from standard ASTM-E45 [166].

Automated SEM-EDS is a commonly employed direct technique for steel cleanliness or inclusion analysis. Typically, there are 2 main measures for inclusion-related steel cleanliness proposed in literature, for comparison between steels, these 2 measures are the number per unit area of inclusions and the area fraction (coverage) of inclusions [177]. Another steel cleanliness measure which can be linked into this is the Modified J-Factor (MJF), which is defined in *Equation 2.10*; the MJF is a dimensionless measure of steel cleanliness [116]. As an example, a recent study of a 26NiCrMoV14.5 steel, which is used for heavy section forgings, recommended an MJF no greater than 100 [178]. It should, however, be noted the MJF takes into consideration both the inclusion-forming elements and the tramp elements in the steel.

Modified J-Factor: $(Si+Mn) \times (S+P+As+Sn+Sb) \times 10^4$ *(Element concentrations in wt %)* *Equation (2.10)*

With SEM-EDS, not only is the composition provided, but also the position, shape and size of the inclusions. A key benefit being that all the inclusions (of sufficient size based on microscope parameters) are scanned in the sample in an automated manner, manual methods are limited to the operator's judgement which may not be representative of the sample [167]. An early study, by Nuspl et al. [179] highlighted how inclusions can come in sizes from sub-micron up to 100s of microns, the solution for characterising the broad size range was the use of an automated SEM-EDS unit which had the size range ability and detected large numbers of inclusions. Although, it should be noted that the smallest inclusion measured was 1 μm in this study [179]. More recent studies such as [180][181] also made use of the automated SEM-EDS technique for quantifying inclusions, furthermore the benefits of obtaining a chemical composition for the inclusions as well as relative distribution in the steel was discussed [180]; again both of these studies quantified inclusions down to the size of only 1 μm. A summary table *(Table 2.5)* is provided showing the SEM parameters used for some

previous automated SEM-EDS inclusion quantification studies. It should be noted the minimum inclusion size measured from all these inclusion analysis was 1 μm; this is because the larger the inclusion is, the smaller the area of the matrix surrounding the inclusion is [182]. Therefore, for fine inclusions (i.e. below 1 μm in size) the matrix effect is much larger around the inclusion relative to the size of the electron beam, which is known to produce errors due to the interaction volume of the electron beam which can result in often inaccurate chemical or size measurements and so a 1 μm cut-off is often incorporated [167]. Most studies incorporate a 15 or 20 kV accelerating voltage and not 5 or 10 kV, the higher voltages have an inherently larger interaction volume as is also documented in the ASTM-E2142 standard [166].

Many automated SEM-EDS studies and standards for quantifying inclusions are readily available, the main focus of them is on larger inclusions which affect strength in structural or fatigue applications. The critical size for an inclusion is difficult to determine because the interparticle (or inter-inclusion) spacing is also an important factor to consider. In the case of creep-related applications there is no guideline or basis for quantifying inclusions in which even fine inclusions / large precipitates are a cause of concern as possible locations of creep cavity nucleation.

Table 2.5: A summary table of parameters used for inclusion analysis experiments in a range of literature studies.

Study	Material	Total Area Analysed [mm^2]	Energy of Beam [keV]	Smallest Particle Detected [μm]
Nuspl et al. [179]	Low Carbon Steel	--	15	1
Winkler et al. [180]	TRIP/TWIP Steels	100	20	1
Michelic et al. [181]	Stainless Steel	Up to 200	15	4
Kaushik et al. [177]	Range of Steels	180	20	1

2.6.4 The Effects of Inclusions on Steel Microstructure

Some of the properties of inclusions are critical to the behaviour observed in steels. When present in steels, inclusions increase stress concentrations within a localised area, effectively acting as stress-raisers. This is due to the harder nature of many non-metallic inclusions compared with the metallic matrix [183]. As temperature increases, some inclusions become more plastic [146]. *Figure 2.34* shows how thermo-mechanical treatments influence various inclusions depending on the type of inclusion and treatment. It can be seen for 'hard' inclusions which have a low bonding affinity with the matrix of the steel, voids can form quite easily during thermo-mechanical treatments. However, for plastic inclusions, shape anisotropy is introduced when thermo-mechanical treatments are used that induce further anisotropic effects on the mechanical performance of the steel [146].

MnS inclusions have a low bonding strength to the steel matrix, which means that the interface is susceptible to the initiation of cracks [184]. In the case of (type 2) elongated MnS stringers, a decrease in ductility (reduction of area) is often reported due to the anisotropy of the inclusions, although the ductility is not affected in the direction perpendicular to the elongated MnS stringers [184]. TiN inclusions have homogenous structure with a cubic morphology that is tightly bound within steel matrix and show no sign of separation at the interface. However, when TiN inclusions are subjected to high levels of stress, they can crack. These cracks can then propagate into the steel matrix [185]. Coarse TiN inclusions (> 0.5 μm) have been considered as the critical size for cleavage nucleation sites, although finer TiN inclusions are able to pin grain boundaries from excessive growth to help offset the crack-initiating aspect [160][161]. Villavicencio et al. [186] found micro-cracks which were formed around Al_2O_3 inclusions in a low carbon pipeline steel. These cracks were thought to have formed during the heating and cooling processes for the manufacturing of the pipeline steel. The formation of the cracks was due to the significant mechanical and different physical property between the inclusion and the steel matrix, such as thermal expansion. This mismatch generated a stress concentration at the interface between the inclusion and steel matrix that can cause debonding of the interface or excessive work hardening and ductile rupture in the matrix.

Studies on the effect of steel inhomogeneity have found variations in number density (per unit area) of MnS inclusions in large casts, as well as characterising type 1 and type 2 MnS inclusions as dendritic and interdendritic respectively [187]. This is consistent with fundamental principles [100], in which Al_2O_3 inclusions tend to form first during solidification and are pushed into the interdendritic liquid and can act as nucleation sites for type 2 elongated MnS inclusions. Furthermore, the effect of micro-segregation is also highlighted in a study related to fracture toughness, where a large localised number of coarse TiN inclusions were sampled at fatigue pre-cracks [160].

Overall it is concluded that the type, morphology, spatial distribution, and number density of inclusions can play an important role with regards to mechanical properties in steel and should all be considered when evaluating inclusions in a steel [146][183], especially with regards to critical mechanical properties such as creep rupture strength and ductility for high performance speciality steels.

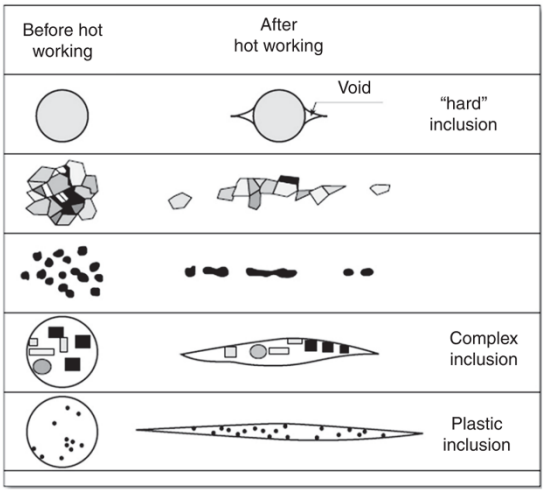

Figure 2.34: Diagram showing the effects of thermo-mechanical treatments on various inclusion types [146].

2.7 Creep Fundamentals and Cavitation

The mechanisms of creep can be divided into two categories, diffusional creep and dislocation creep. For each of these mechanisms, the main three factors which determine the creep behaviour are temperature, stress state and the condition of the material.

In the case of diffusional creep, there are two sub-categories, bulk diffusion (Nabarro-Herring) creep and grain boundary diffusion (Coble) creep. For either of the two diffusional creep mechanisms to be active a temperature of over 50 % of the melting point of the material would be required, which for Gr. 91 would be over the permissible 650 °C [10]. Dislocation creep can be defined by the *Equation (2.11)* [188].

$$\dot{\varepsilon} = A\sigma^{n} \qquad \textit{Equation (2.11)}$$

Where $\dot{\varepsilon}$ is defined as the creep strain rate, σ is defined as the applied stress, A and n are temperature- and stress-dependant constants, respectively. At higher n values, dislocation pipe diffusion dominates, whereas at lower n values, volume diffusion dominates. In a computational study by Liu et al. [189], three mechanisms of dislocation evolution were proposed in a precipitation strengthened BCC material based on the stress levels; i) at high stresses, dislocation multiplication is dominant, which is driven by dislocation glide and cross slip. This creates a dense dislocation network that envelopes particles. ii) At low stresses, dislocations are stopped by particles and dislocation climb is the dominating mechanism causing bypass. Therefore, the climb process controls the strain rate. However, plastic deformation is mainly governed by the dislocation glid and cross slip. iii) At intermediate stresses there is a combination of dislocation climb, cross slip and climb. Examples of the three aforementioned dislocation evolution types are shown in *Figure 2.35* [190].

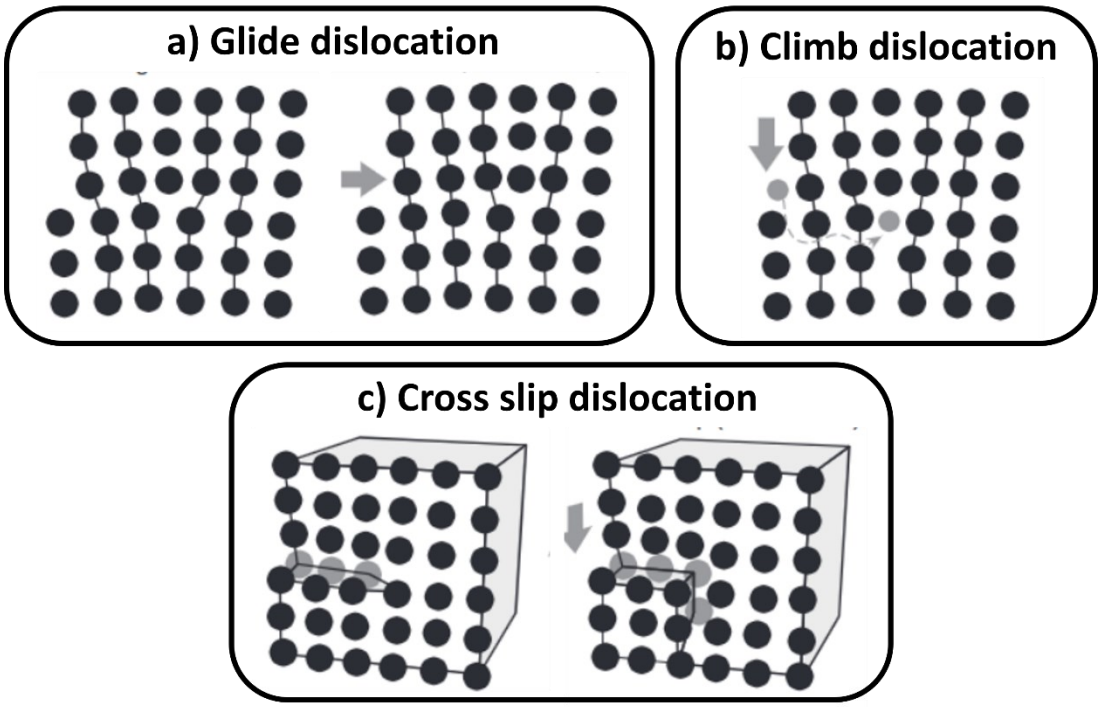

Figure 2.35: Dislocation motion types (a) glide of a dislocation, (b) climb of a dislocation and (c) cross-slip of a dislocation [190].

In a review by Kassner and Hayes [191] a number of creep cavitation nucleation mechanisms have been proposed for polycrystalline metals and alloys, these are presented in *Figure 2.36*. The main types are as follows; a) grain boundary sliding at boundary ledges and triple points, b) vacancy condensation in high stress regions, c) nucleation from Zener-Stroh mechanism which is the pile up of dislocations along a slip plane and d) due to particles (as well as in conjunction with the other mechanisms). The presence of second phase particles or inclusions has been widely considered as providing cavity nucleation sites [191]. The ability of a steel to fail in a ductile manner is very important in mechanical and structural applications. In creep applications, brittle failures (at 600 °C) are often linked to the nucleation and growth of creep cavities, which are considered to nucleate early in and throughout creep life [27][29]. In service, a brittle failure can significantly increase the risk of a burst type of fracture or a premature failure; high amounts of creep cavitation can be correlated with low levels of creep ductility, in relative terms.

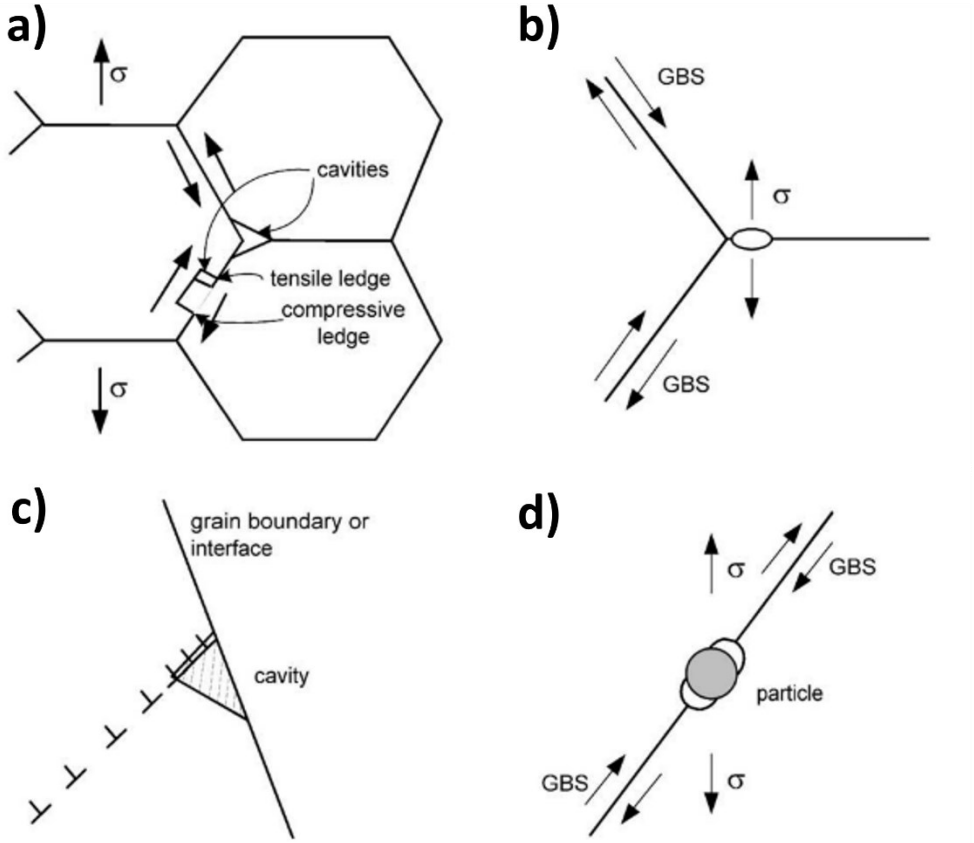

Figure 2.36: Cavity nucleation mechanisms, (a) grain boundary sliding, (b) vacancy condensation, (c) Zener-Stroh mechanism and (d) due to hard particles in a material [191].

In Gr.92 steels creep cavities were associated with ceramic inclusions (BN, MnS, Al_2O_3) which formed during the steel making process (BN during thermo-mechanical heat treatments) [192]–[194]. *Figure 2.37* shows examples from two studies which show the association of the BN inclusions with creep cavitation, Benaarbia et al. [194] found creep cavitation tended to form around inclusions and grew more significantly in size around the necking region *(Figure 2.37a)* of the creep specimen due to the increased plastic strain of the matrix. Gu et al. [192] also found the association of various inclusions types including MnS and Al_2O_3 as well as BN with creep cavitation; 3-dimensional reconstruction studies *(Figure 2.37c* and *ci)* were also used to conclude that the creep cavities had irregular shapes due to the inclusion morphology, around

which the cavity formed. Although Gr. 91 does not contain the BN phase, it can form needle-like AlN precipitates and various other types of inclusions. The presence of MnS and Al_2O_3 inclusions has proven particularly detrimental, due to these inclusion types being ideal cavity initiation sites in a plastically deforming matrix [30][195], as well as their angular or elongated morphologies which can increase localised stress concentrations [15].

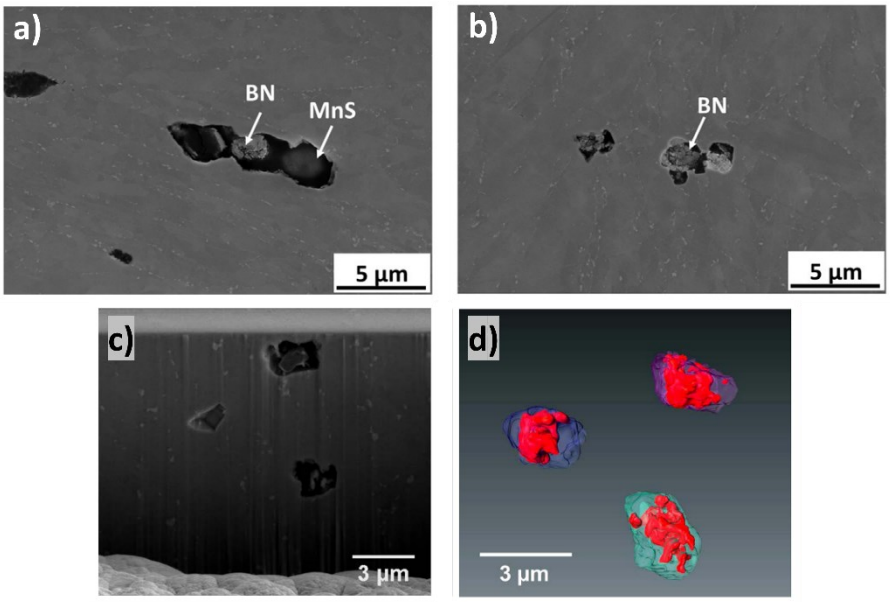

Figure 2.37: SEM-SE images showing the association of BN and MnS inclusions within cavities in a Gr.92 steel near the creep ruptured regions (a) and away from the creep ruptured region (b), at a temperature of 650 °C and stress of 200 MPa [194]. *Also (c) an SEM-SE image of a cross sectional slice taken from a Gr.92 steel 6 mm away from the creep ruptured surface with the corresponding 3-dimensional reconstruction data (d) showing the BN inclusions associated with the cavities* [192].

Various other phases have also been linked with the formation of creep cavities in 9 - 12 wt % Cr CSEF steels. In a study of 12 wt % Cr ferritic steel Eggler et al. [29] believed that segregation of S to grain boundaries, more specifically to the matrix-particle interfaces of $M_{23}C_6$ carbides was the main initiation point for creep cavitation once a critical amount of S was achieved (segregated). Furthermore, some researchers have associated the nucleation of creep cavities with the formation and coarsening of the intermetallic Laves phase. Panait et al. [36][42] found creep cavities were often found around large particles such as Laves phase and associated the overall loss in creep strength to the precipitation and coarsening of the Laves phase, $M_{23}C_6$ carbides

and recovery of the matrix in a Gr. 91 steel after over 100,000 hours at 600 °C and 80 Mpa. However, in this study a systematic method for cavity association to a given microstructural feature was not carried out but rather stated through observation. In a study of a Gr. 92 steel, creep tests were performed at 550, 600 and 650 °C at a fixed load by Lee et al. [34] suggested most creep cavities nucleated around coarse Laves phase particles. The study concluded that the failure mode of the Gr. 92 steel in this specific study was due to the transition of ductile to brittle trans-granular fracture due to precipitation and coarsening of the intermetallic Laves phase. More importantly a critical size of 130 nm was believed to be the threshold. Much like the previous study mentioned, a systematic study was not performed, and due to the nature of the precipitation of the Laves phase which largely decorated the prior austenite grain boundaries an apparent association between the phase and cavity nucleation may be easy to confuse.

2.8 Objectives of the Thesis

This thesis will aim to cover four key aspects, with each having an individual experimental research approach and links to one another.

I. Assess the chemical homogeneity of the studied materials on a macro and micro scale using a range of analytical techniques.
II. Quantification of microstructural features and mechanical properties with regards to area-to-area variations (i.e., chemical homogeneity).
III. Standardised procedures for the quantification of inclusions with sizes that are relevant for creep cavity nucleation.
IV. Linking creep cavitation in the gauge sections to microstructural features.

Chapter 3 : Experimental Procedures

3.1 Material Selection

A mixed range of Gr. 91 steels were analysed in this project, which included, ex-service steels, developmental steels, samples from different processing routes and different compositional ranges.

3.1.1 Ex-service Steels B2 (Es-P) and TP1 (Es-F) From the Aberthaw Header (UK)

These steels were taken from an ex-service final superheat outlet header in a fossil-fuelled power plant. The components operated for 79,000 hours at a bulk steam outlet temperature and pressure of 570 °C and 16.5 MPa, respectively. The subsequent samples analysed in this project were taken from a seamless pipe section manufactured to A335 P91 [11] and designated as B2 and a second sample from a forged tee-piece manufactured to A182 F91 [196] designated as TP1, a photograph of the original header is provided *Figure 1.2*, showing the B2, TP1 and other fitments on the system [10]. B2 had an outer diameter and wall thickness of 450 and 50 mm, respectively, whereas, TP1 had an outer diameter and wall thickness of 210 and 54 mm, respectively [16]. In *Figure 1.2* the section marked with an asterisk signifies where the TP1 sample was taken from. Other information including production details are unavailable. Steels B2 and TP1 will be assigned the names ex-service pipe and forging, with the acronyms Es-P and Es-F, respectively.

3.1.2 Oak Ridge National Laboratory (ORNL) Development Steels 30394b (ORNL-P) and 14361 (ORNL-F)

In the USA, as part of the Department of Energy's (DOE's) development program of modified 9Cr-1Mo steel, ORNL analysed various Gr. 91 heats which had been produced by a range of selected steel manufacturers [13]. Various melting practices, processing methods and final product forms were produced to a specified composition range that can be found in *Table 1.1* denoted as 'ORNL-6303' target composition and an allowable composition range respectively. Production details of the 2 heats of steel investigated in this project, 30394b (pipe – ORNL-P) and 14361 (forging – ORNL-F) are summarised in *Table 3.1*.

Table 3.1: Production details of steels ORNL-P and ORNL-F from the ORNL 6303 report. (AOD = Argon-oxygen decarburisation, ESR = Electroslag remelting) [13]

Heat (Original name)	Melter	Melting Practice	Product	Product Size OD / thickness (mm)	Fabrication method	Fabricator
ORNL-P (30394b)	CarTech	AOD-ESR	Pipe	76 / 13	Hot Rotary Pierced	Timken
ORNL-F (14361)	Electralloy	AOD-ESR	Saddle Forging	781 / 166	Hot Forged	National Forge

Both steels were produced to the normalised and tempered condition, normalising consisted of heating to 1040 °C and holding for 1 hour (for thicknesses up to 25 mm), with subsequent air cooling to room temperature. The normalised steel was then tempered by heating to 760 °C ($A_{C1:}$ 840 °C) and holding for 1 hour (for thicknesses up to 25 mm), with subsequent air cooling to room temperature. The ORNL document does not state the holding times for thicknesses greater than 25 mm, for which ORNL-F was (166 mm), however the document does state a steel of 222 mm in thickness was held for 4.5 hours for the normalising and tempering heat treatments. Therefore, it can be assumed longer holding times were used for steel ORNL-F. ORNL-F is photographed in *Figure 3.1* as well as a typical pipe section (similar to ORNL-P).

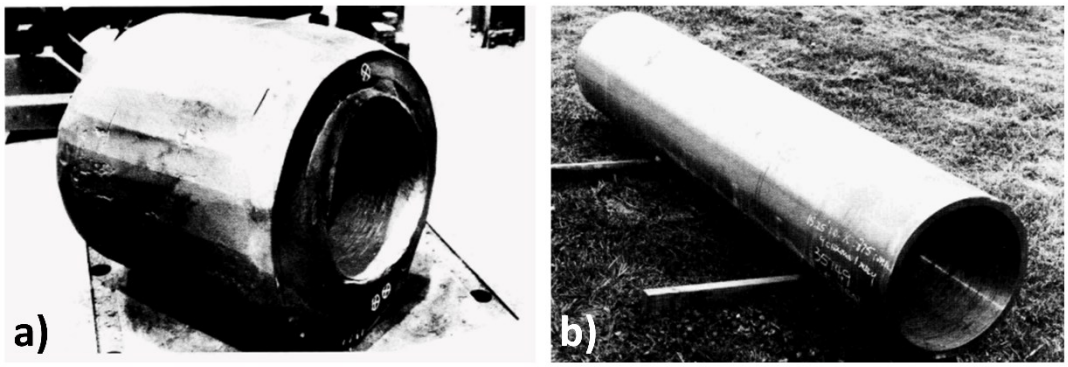

Figure 3.1: Photographs of a) the forged steel ORNL-F from National Forge (USA) b) a typical hot-extruded pipe straight section from Cameron Iron Works (USA) [13].

3.1.3 European Supplier Steels 28145 (Euro-Pi) and 28524 (Euro-P2)

Steels 28145 and 28524 were taken from two P91 products manufactured to the specification of A335 P91. Steel 28145 was taken from a pipe with an outside diameter of 355 mm and wall thickness of 35 mm. Steel 28524 was taken from a pipe with an outside diameter of 219 mm and wall thickness of 26 mm. Normalisation and tempering were carried out at temperatures of 1040 °C and 760 °C (with air cooling), respectively, for both steels. Both steel samples were taken from the axial position at the nominal pipe centreline. All other information on the production details or history are unavailable. Steels 28145 and 28524 will be assigned the names Euro pipe and pipe 2, with the acronyms Euro-Pi and Euro-P2, respectively. *Table 3.2* provides a summary of all the known sample details for the six steels in this project, comprehensive creep test conditions and compositions are discussed in the following sections and tables.

Table 3.2: A summary of all the known sample details for each of the six Gr. 91 steels in this project.

Steel	Ex-service?	Melting Practice	Product	Product Size OD /thickness (mm)	Fabrication Method
Es-P	Yes	No ESR (assumed)	Pipe	450/50	Plug Mill (assumed)
Es-F	Yes	ESR (assumed)	Tee-Piece Forging	210/54	Forged then Bored (assumed)
ORNL-P	No	AOD-ESR	Pipe	76/13	Hot Rotary Pierced
ORNL-F	No	AOD-ESR	Saddle Forging	781/166	Hot Forged
Euro-Pi	No	No ESR (assumed)	Pipe	355/35	Plug Mill (assumed)
Euro-P2	No		Pipe	219/26	

3.1.4 Steel Compositions and Creep Performance

All 6 steels were creep tested and supplied by the Electric Power Research Institute (EPRI) as shown in *Figure 3.2* in their as-received state. Data on the creep performance was also provided by EPRI in *Table 3.3*, optical examination techniques were used to make the ROA assessments similar to the work referenced here [21]. The compositions of all the steels were measured using ICP-OE/MS combustion and Inert Gas Fusion (IGF) by Dirats Laboratories (Westfield, MA, USA) and are documented in full in *Table 3.4*. Steels Es-P, Es-F, ORNL-P and ORNL-F were produced to ASTM/ASME requirements in the early 1990s and late 1970s respectively, which at the time allowed a maximum Al content of 0.04 wt %, this was later reduced to 0.02 wt % after the production of these 4 steels [11].

*Table 3.3: Single creep test conditions and performance of all steels in this project. (*Reduction of area values for steels Es-P and Es-F are were taken from their equivalent smooth bar tests [28])*

Material ID	Type of Test	Test Conditions			Reduction of Area (%)
		Temp. (°C)	Stress (MPa) at Notch*	Time to Failure (hours)	
Es-P	Type 1 Double Notch Bar	625	100	1,408	26.5*
			~50*	~1.5% life fraction	
Es-F			100	6,714	83.0*
			~50*	~1.5% life fraction	
ORNL-P	Smooth Bar	625	100	1,259	47.5
ORNL-F		649	75.8	29,363	13.0
Euro-Pi		600	100	66,431	7.5
Euro-P2		600	110	38,504	30.0

Table 3.4: Compositions for all steels in this project, measured using ICP-OE/MS combustion and Inert Gas Fusion (IGF) in wt %.

Element	Es-P	Es-F	ORNL-P	ORNL-F	Euro-Pi	Euro-P2
C	0.10	0.10	0.091	0.12	0.149	0.092
Mn	0.41	0.40	0.44	0.52	0.53	0.50
P	0.009	0.012	0.006	0.009	0.011	0.015
S	0.010	0.002	0.001	<0.001	0.0025	0.001
Si	0.41	0.33	0.42	0.29	0.248	0.242
Cr	8.77	8.30	8.11	8.75	8.548	8.411
Mo	0.94	0.94	1.02	0.96	1.06	1.02
V	0.224	0.214	0.22	0.23	0.195	0.199
Nb	0.071	0.070	0.077	0.072	0.072	0.071
N	0.0454	0.0424	0.0519	0.0396	0.0568	0.0432
Ni	0.12	0.19	0.09	0.12	0.10	0.11
Al	0.04	0.02	0.031	0.011	0.002	0.003
Ti	0.002	0.002	0.002	0.002	0.002	0.003
O	0.0043	0.0018	-	0.0027	0.0051	0.0044
Cu	0.19	0.05	0.042	0.076	0.110	0.135
As	0.0128	0.0042	0.0036	0.0036	0.005	0.007
Sn	0.0080	0.0030	0.0015	0.0026	0.006	0.007
Sb	0.0023	0.00063	0.00005	0.0004	0.0014	0.0020
B	-	<0.0003	0.0004	<0.0003	<0.0003	<0.0003
W	-	0.006	0.052	0.001	<0.002	<0.002
Pb	0.00075	0.00003	0.00003	0.0001	0.0014	0.0020
N:Al [19]	1.135	2.120	1.674	3.60	28.4	14.4
MJ-F [116]	345	159	104	134	201	237
TIL [93]	0.0597	0.0462	0.0529	0.0433	0.0644	0.0486

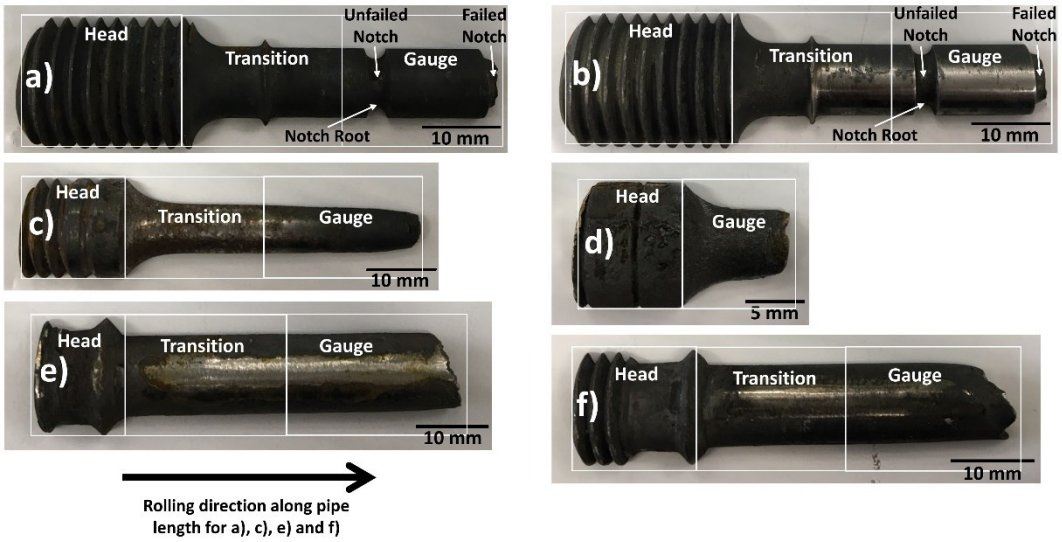

Figure 3.2: Photographs of the failed post-creep tested bars in the as-received state; double notch (a) Es-P (b) Es-F, smooth bars (c) ORNL-P (d) ORNL-F (e) Euro-Pi (f) Euro-P2. Head, transition and gauge sections are labelled, white boxes signify where metallographic sections were prepared as described in section 3.2.

For steels Es-P and Es-F, double notched creep test bars *(Figure 3.2)* were machined from the plain sections (non-weld regions) from the ex-service header and were tested at 625 °C with a net section stress of 100 MPa at the notch root. By comparison, the net stress in the gauge section was ~ 50 MPa. Es-P performed poorly in the accelerated creep tests, the reduction of area (ROA) measured was 26.5% which was significantly lower than the 70% ORNL 6303 development program aim [13]. The time to failure was also low, only 1,408 hours compared to that of 6,714 hours by steel Es-F. Steel Es-F had an ROA of 83% which is well above ORNL 6303 guidelines. With regards to impurity composition *(Table 3.4)*, steel Es-P contained a significant amount of tramp elements, the MJF was calculated at 345, whereas for steel Es-F this was calculated at 159. The N:Al ratios of Es-P and Es-F are 1.135 and 2.120, respectively, both of these values fall well below the recommendation of > 4, and Es-P is below the critical threshold of 2 as detailed in the EPRI guidelines for this material [19]. These 2 steels were selected for this project for a number of reasons; i) some of these materials may still be in current fossil-fuelled power plants, ii) they are service exposed steels so represent actual conditions typical Gr. 91 steels would be subjected to, iii) they possess very interesting properties with regards to creep performance, steel Es-P showed poor creep strength and ductility, whilst steel Es-F showed the expected

creep strength and ductility, iv) steel Es-P contained an MJF of 345, whilst steel Es-F contained an MJF of 159 therefore, comparing the differences would be interesting (i.e., inclusion contents).

For steels ORNL-P and ORNL-F smooth bar creep specimens *(Figure 3.2)* were machined and tested at 625 °C / 100 MPa and 649 °C / 75.8 MPa, respectively. Steel ORNL-P performed poorly in the creep test, only lasting 1,259 hours, it did show some ductility, however the ROA of 47.5% is still below the ORNL 6303 guidelines. Steel ORNL-F had a much longer time to failure than ORNL-P (29,363 hours compared to 1,259 hours), however steel ORNL-F showed little ductility with an ROA of just 13% *(Table 3.3)*. It should be noted that these steels were creep tested to different stresses and temperatures, which can significantly affect the time to failure and type of failure [197] where higher stresses and temperatures are known to reduce ROA and time to failure [15]. The MJF of both steels was also the lowest of all 6 steels in this project at 104 and 134 for ORNL-P and ORNL-F, respectively. The N:Al ratios were also measured as 1.674 and 3.60 for steels ORNL-P and ORNL-F, respectively *(Table 3.4)*. Both steels were selected for this project for a number of reasons; i) they were a part of the original ORNL development of modified Gr. 91 and were, therefore, manufactured to stringent guidelines, ii) Steel ORNL-P showed more creep ductility than steel ORNL-F, however it showed a relatively short time to failure in comparison, iii) both steels contained the lowest amounts of tramp elements from the steels in this project.

For steels Euro-Pi and Euro-P2 smooth bar creep specimens *(Figure 3.2)* were tested at 600 °C and at stresses of 100 MPa and 110 MPa, respectively. Steel Euro-Pi had a time to failure of 66,431 hours, compared to steel Euro-P2 which had a time to failure of 38,504 hours. The ROA for steel Euro-Pi was 7.5%, whereas the ROA for steel Euro-P2 was 30%, both these values were well below the ORNL 6303 guideline, with the steel Euro-Pi showing very little ductility *(Table 3.3)*. The MJF values for steels Euro-Pi and Euro-P2 were measured at 201 and 237 respectively, which meant they contain more impurity and inclusion-forming elements than steels ORNL-P and ORNL-F, less than steel Es-P (MJF 345), but more than steel Es-F (159). The N:Al ratios for both steels Euro-Pi and Euro-P2 are 28.4 and 14.4 respectively, this is due

to the very low and controlled Al contents in both steels *(Table 3.4)*. These 2 steels were selected for this project for a number of reasons; i) they are the most modern materials in this project and take advantage of a more controlled N:Al ratio and ii) they showed good creep strength yet very poor ductility.

3.2 Metallographic Sample Preparation

The post-creep tested samples provided by EPRI were sectioned in half along the longest length of the creep bars, including the failed notch, the un-failed notch, gauge section, transition and head *(Figure 3.2)*. For the majority of analysis techniques, samples were prepared using standard metallographic procedures by the following process (Buehler equipment and consumables), which is also shown in the flow diagram in *Figure 3.3*:

1. Further sectioning of the semi-cylinder creep bar into sub 30 mm sections using a (IsoMet High Speed Pro) precision cutter with a ferrous abrasive blade, creating 2/3 sections per sample (head, transition and gauge), which can be seen as the white boxes in *Figure 3.2*.
2. Mounting in conductive (KonductoMet) bakelite resin using a (SimpliMet 4000) compression mounting press, which formed 30 mm diameter samples. The flat face of each sample was mounted for analysis, which in *Figure 3.2* is flush with the surface in the image backgrounds.
3. Grinding samples (up to 6 samples at a time) until flat using progressively finer silicon carbide abrasive paper (320 and then 1200 grit) on an (AutoMet 300 Pro) automatic grinder/polisher.
4. Polishing samples (up to 6 samples at a time) using progressively finer finishing steps. This was done using a 9 µm diamond suspension and a (UltraPad) polishing cloth which was followed by a 3 µm diamond suspension and a (TriDent) polishing cloth. The final polishing step was performed with a 0.05 µm (MasterMet) colloidal silica suspension using a (ChemoMet) polishing cloth to ensure a deformation-free surface finish *(Figure 3.3)*.

Samples were thoroughly cleaned between each step, this also included the thorough cleaning of the automatic polisher/grinder holders and base plate, this was done to

eliminate any form of contamination between steps. Variation in preparation procedures were used when the polishing media were considered to have an influence on obtained results, these instances are as follows:

- For elemental mapping of the steel sections to find association between cavity and microstructural features. Polishing was only done down to the 3 µm step as seen in *Figure 3.3*, this was because some of the alumina/colloidal silica suspension used in the final polishing step could be retained within creep cavities on the prepared surface, with the likelihood of producing Al/Si-rich artefacts.

The flow diagram provided in *Figure 3.3* shows the variations in the metallographic sample preparations based on the analysis techniques performed.

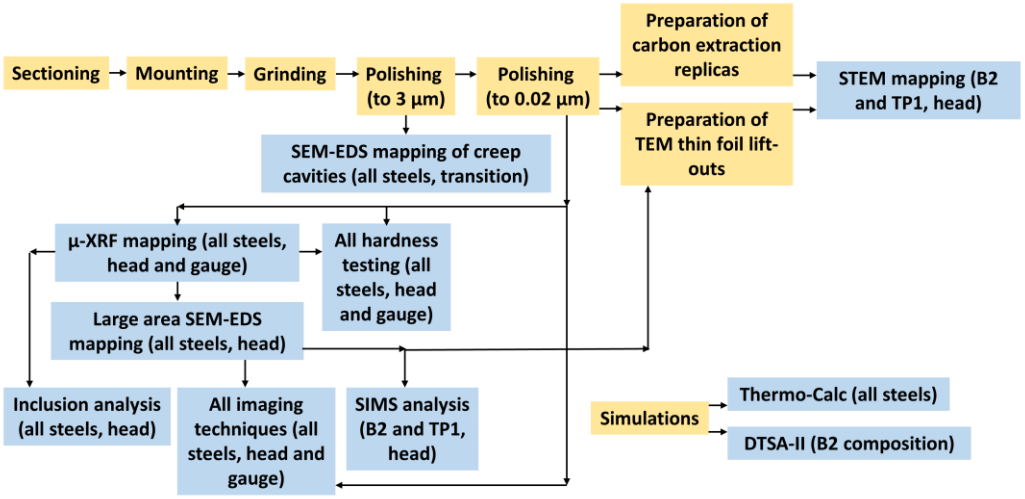

Figure 3.3: Flow diagram showing the metallographic sample preparation and analysis techniques performed on the steels in this project, as well as the simulation studies.

3.3 Hardness Testing

Vickers micro-hardness testing was performed using a Wilson VH1102 micro-hardness tester. Hardness indentations were completed to the ASTM-E384 standard [198] of keeping at least 2.5d spacing between indents (where d is equal to the diagonal distance in the indent for that particular steel tested and load used), this meant carrying out test indents to determine this distance. A load of 0.2 kgf was used as recommended by Siefert et al. [133] for micro-hardness testing/mapping, due to providing much

better precision than lower loads. An indentation dwell time of 10 seconds and a spacing of 100 µm was sufficient for 2.5d in X and Y directions (indents had a 35 - 40 µm diagonal measurement). Researchers at EPRI found a spacing of 1.6d is permissible when it is necessary to maximise the spatial resolution of micro-hardness maps without a significant effects on the overall micro-hardness measurements [133]. The Vickers micro-hardness is defined in *Equation (3.1)*, Where F = Force (i.e., 0.2 for 0.2 kgf) and d = mean diagonal distance (in mm).

$$HV = \frac{1.8544F}{d^2} \qquad \textit{Equation (3.1)}$$

Automated Vickers hardness testing was performed in three modes in the work using the specification above, which included:

- 10 x 10 grids of indents were performed which covered an area of 1 mm x 1 mm. These measurements were carried out on the head section of each steel and were used to obtain an average Vickers micro-hardness and standard deviation.
- Lines of indents were performed in the centre of each gauge section of each steel, starting from the failure and moving towards the head sections of each respective steel, for a distance of ~ 14 mm.
- Micro-hardness maps were performed using 40 x 10 grids of indents on steels Es-P and Es-F, these were done as an experiment to compare hardness variations across the head section of each steel. Hardness data were extracted and analysed using standard software packages.

3.4 Characterisation Techniques

A range of microstructural characterisation techniques was used in this project. The emphasis for most of the characterisation was to develop processes using a combination of techniques. These ranged from large scale cm-mm ‘macro’ techniques such as µ X-ray fluorescence elemental mapping, down to mm - µm ‘micro’ levels of analysis through SEM-EDS elemental mapping. Subsequently, even smaller level µm – nm ‘nano’ analysis such as SEM-BSE image quantification (as well as TEM-based techniques) was carried out. Such ‘macro’ to ‘micro’ to ‘nano’ procedures can be seen

in the flow diagram in *Figure 3.3*. The purpose of this work-flow was to assess the effects of micro-segregation on the quantification of microstructural features such as Laves phase, inclusions and $M_{23}C_6$ as well as mechanical properties. This is important because statistical extremes can be important with regard to variation in mechanical properties, damage accumulation and other factors, for example, a similar 'statistical extreme' approach is recommended in the ASTM E2283 standard for analysing inclusions [199]. A summary of all the different characterisation techniques used follows, it should be noted that all images, and SEM-EDS and μ-XRF maps were taken in the length axis of the creep specimens; for any steels which are a pipe, this is also consistent with their rolling direction, which can be clearly seen in the chemical maps.

3.4.1 Micro X-ray Fluorescence (μ-XRF)

At the cm - mm length-scale, the elemental distribution of all the steel samples in the head and gauge sections were evaluated using a Bruker M4 Tornado μ-XRF system. The system is equipped with two 30 mm^2 SD (silicon drift) Energy Dispersive Spectroscopy (EDS) detectors, the chemical maps were collected using a 20 μm step size, 50 kV accelerating voltage and a current of 600 mA all whilst under vacuum. An AlTi 100/25 filter was used to reduce diffraction peaks, quantitative data were collected using a quantification algorithm within the Bruker software, which implements a background subtraction from all spectra in the map. Each large/small map was collected with a pixel dwell time of 250 / 500 ms (respectively) to ensure that sufficient counts per peak could be extracted from even small areas of the maps. Raw data were extracted and plotted using standard software packages.

3.4.2 SEM–based Imaging of Microstructural Features

SEM–based image analysis (quantification) was required for the analysis of various microstructural features in this project, which included AlN precipitates, Laves phase particles and $M_{23}C_6$ precipitates, as well as cavities formed during creep exposure and/or testing. All these features had a size distribution large enough for effective SEM-based imaging [68], MX–type precipitates however are a good example of precipitates too small for effective SEM–based analysis, as studied and suggested by Hofer et al. [68]. The Laves phase, AlN precipitates and cavities were imaged using a JEOL 7800F Field Emission Gun Scanning Electron Microscope (FEG-SEM) with a

solid state back-scattered electron (BSE) detector. For imaging of $M_{23}C_6$ carbides, differentiation of these from other 2nd phase particles and matrix was difficult even whilst using a ≥ 5 kV voltage in SEM-BSE mode; this was because Fe is a major constituent of the $M_{23}C_6$ carbides and also for the steel matrix itself, so the Z contrast between the phases is not strong. Focussed Ion Beam (FIB-SEM) imaging was used in a FEI Scios dual beam system, with the application of XeF_2 gas. The effects of micro-segregation were investigated on the statistics of the Laves phase particles and $M_{23}C_6$ precipitates; these 2 phases were chosen because of their high alloying content in the steel (Cr) or a combination of relatively high alloying in the steel and also a large tendency to segregate (Mo).

3.4.2.1 Laves Phase

Laves phase particles and AlN precipitates have a significant difference in atomic number (Mo: 42, Al: 13 Fe: 26) or Z contrast compared with the steel matrix, which results in the Laves phase appearing bright and the AlN precipitates appearing dark, which is a phenomenon that has been long known amongst researchers [200]. An accelerating voltage of 5 kV was chosen for both quantification of the Laves phase and AlN precipitates. This voltage optimised the resolution of the images whilst maintaining limited depth penetration into the steel compared to higher voltages so that no truncation correction factor was required. Furthermore, at a lower kV the Z contrast often becomes larger between the steel matrix and precipitate phases. Laves phase particle characteristics were collected in 3 ways, the first was by using systematically collected random areas (SCRA), meaning an image was collected every millimetre along 2 horizontal lines separated by 10 mm (in the head and gauge sections) of each steel until 20 images were acquired. Images were also collected at least 1 mm away from the edge of any steel section (head or gauge). The area imaged was random with regard to the composition and Laves phase particle population characteristics. The 2nd and 3rd sets were taken from the positively and negatively segregated Mo areas respectively; these areas were located using the μ-XRF quant maps mentioned earlier and if neccesary the large area SEM-EDS if the segregation was very fine. 5 images were taken in each of these 2 areas.

3.4.2.2 Aluminum Nitride

These particles were analysed in the head sections of the steels, as no influence of ageing or creep on them is expected due to the relatively low testing temperature compared to the temperature for AlN precipitate formation, which is approximately 1100 °C. Therefore, cavity-free head sections were ideal. 60 images were taken at a spacing of 1 mm, at height intervals of 2 mm in the head sections of the steels, producing a 10 x 6 array of images. The sizes of AlN precipitates were generally larger than those of the Laves phase particles so images of larger horizontal field width (HFW) were used, *(Table 3.5).* The AlN precipitates had to be differentiated from Al_2O_3 inclusions due to a similar signal intensity because the atomic number of the phases are similar. This was done by manually deleting Al_2O_3 inclusions (using the ImageJ eraser tool) after results were obtained based on the spherical morphology of these inclusions compared to the angular and lenticular AlN precipitates.

3.4.2.3 Cavities

Cavities appeared dark compared to the matrix, however there was an overlap in Z contrast with other dark phases such as AlN precipitates and Al_2O_3 inclusions due to the black shadow effect created within the cavities. Al_2O_3 inclusions were eliminated as noted above, whilst the effects of AlN precipitates were eliminated by using 15 kV accelerating voltage due to the limited spatial resolution and magnification at 15 kV. The loss in resolution at the higher operating voltage meant that the fine AlN precipitates were not visible in images at the low magnification used for cavity imaging. As the cavitation found in these Gr. 91 steels was of irregular shape and could not be compared to a specific shape, no truncation correction factor was applied. Starting from the failure regions in the gauge sections of the smooth bar samples (Euro-Pi, Euro-P2, ORNL-P, ORNL-F) an image was taken every millimetre up until 14 mm from the failure. For notched bar samples (Es-P and Es-F), images were taken every 0.5 mm in the gauge section (unfailed notch) from one notch root to the other as seen in *Figure 3.2a and b*. Images with a 390 µm HFW were taken as a balance between capturing as many cavities as possible, whilst retaining suficient spatial resolution to detect and size them

3.4.2.4 $M_{23}C_6$ Carbides

A detailed procedure was used for the imaging of $M_{23}C_6$ carbides, after the imaging area was selected. Two passes of the FIB at 30 kV and 50 pA were scanned over the area at a pixel dwell time of 100 µs, this cleared the area of any surface contamination and oxidation. The image acquired also contained Laves phase particles as well as the $M_{23}C_6$ precipitates of interest. Therefore, a 3rd pass of the FIB was applied with flowing XeF_2 gas. This enabled the $M_{23}C_6$ and MX carbo-nitrides to be easily differentiated from the Laves phase particles and reduce the difffraction (grain) contrast from the matrix. These images were used to quantify the $M_{23}C_6$ carbides; any particles below 60 nm in diameter were eliminated as noise due to limited resolution (most MX are expected to be smaller than 60 nm). The imaging procedure was the same as with the Laves phase particle procedure, 20 SCRA fields, 5 fields in the solute positive region and 5 fields in the solute negative region. Images of 28 µm HFW were captured, which were later cropped down to 25.9 µm HFW during image processing to eliminate any edge illumination effects.

Table 3.5 summarises the parameters used and the statistics quantified in the 2 SEMs for imaging of the various microstructural features. After collecting the images an image analysis procedure was performed using ImageJ software [201]. This allowed the key information of the images to be collected in a consistent manner.

*Table 3.5: A summary of the settings used for the image analysis using any SEM-based techniques, per sample section investigated. *Steels Es-P and Es-F respectively.*

	Laves	AlN	Cavities	$M_{23}C_6$
Settings and parameters used				
Technique	BSE	BSE	BSE	FIB (w/ XeF_2)
Accelerating voltage (kV)	5	5	15	30
Working distance (mm)	~10	~10	~10	~20
HFW (µm)	20	40	390	25.9
Pixels (X x Y)	2560x1920	2560x1920	2560x1920	1432x951
Minimum diameter of quantified feature	40 nm	60 nm	2/1.5* µm	60 nm
Total images per steel section	30	60	15/12*	30
Total area sampled (μm^2)	9000	72000	1.708/1.367* (mm^2)	13,364
Statistics quantified				
Average size as equivalent circle diameter (µm)	Yes	Yes (as length)	Yes	Yes
Number per unit area ($/mm^2$)	Yes	Yes	Yes	Yes
Area coverage	Yes	Yes	No	Yes
Aspect ratio	No	Yes	No	No

3.4.3 Inclusion Analysis

For this analysis a JEOL 7800F FEG-SEM was used, which was equipped with an Ultimax 100 silicon drift detector (SDD) *(the subsequent section on EDS mapping (3.4.4)* was also performed on the same SEM with the same EDS detector). Inclusion analysis was performed using the feature analysis function of the Aztec software

version 4.2 to detect and classify the various inclusion types based on elemental concentration *(Table 3.6)*, these included S-, Al-, and Nb/Ti-rich type inclusions and large precipitates commonly found in Gr. 91 steels. The software collects SEM-BSE images, subsequently inclusions are detected by greyscale thresholding these images and then these thresholded features were then analysed using the EDS detector, in terms of the average size, area coverage, position in steel and composition.

Table 3.6: Classification system used for the inclusion analysis in this project.

Classification	Type of Inclusion
1	S-rich (i.e. MnS)
2	Al-rich (i.e. Al_2O_3)
3	Nb/Ti-rich (i.e. TiN)

The settings used for analysis included an accelerating voltage of 10 kV, current of 2 nA and a collection time of 1 second per inclusion. The choice of a 10 kV accelerating voltage is discussed in *Chapter 6*. Analysis regions were based on the Mn elemental segregation maps produced from the µ-XRF scans, Mn was of relatively high concentration in this grade of steel compared to other inclusion-forming elements, and readily formed MnS inclusions. It should also be noted the segregation behaviour of Mn was very similar to the segregation behaviour of Mo mentioned earlier. Although S is the other main constituent in the inclusion, the concentration of it was considerably lower than that of Mn, for example, steel Es-P nominally contained 0.010 wt % S but 0.40 wt % Mn. Two sets of inclusion analysis were performed as described:

- The first set (large) consisted of 4 sets of 2 mm x 2 mm areas placed in a square formation, with 1 of 4 areas containing a high amount of 'positively segregated' Mn and another 1 of 4 areas containing a high amount 'negatively segregated' Mn. The combined area this method covered was 16 mm^2. Although not time efficient, the reason for choosing 4 individual areas was to optimise the size of individual analysis fields so the smallest inclusion analysed was 0.5 µm instead of using larger fields and increasing the minimum size of inclusion detected. Furthermore, comparison of areas was enabled as

well as a lower drift factor in inclusion maps due to coverage of relatively small areas.

- The second set (small) of inclusion analysis was based on the first set, 2 areas were collected which were 1 mm x 1 mm each, these 2 areas were performed in the 2 compositional extremes as mentioned in the previous paragraph. However, with this analysis the field size was half that used in the first set, resulting in the smallest inclusion detectable reducing to 0.25 µm.

Both of these intricate inclusion analysis methods used have not been previously performed in literature for the analysis of steels. A summary of the settings used for each set of analysis is provided in *Table 3.7.*

Table 3.7: A summary of the settings and details used for the 2 sets on inclusions analysis.

Setting/Detail	Small	Large
Size of each area (mm ²)	1	4
Number of areas	2	4
Total area analysed (mm ²)	2	16
Magnification	X1000	x500
Size of each field (µm)	119 x 82	239 x 164
Total number of fields (per scan)	117	117
Smallest detectable feature (µm)	0.25	0.50
Acquisition time (s)	1	
Accelerating voltage (kV)	10	
Input counts per second	~200,000	

3.4.4 Energy Dispersive X-ray Spectroscopy (EDS) Mapping

FEG-SEM based EDS mapping was used for acquiring high spatial resolution elemental maps of the elements Fe, Cr, Mo, Mn, V, Nb, Al, O and S. This technique was utilised for 2 main purposes, the first was to produce large area maps to pinpoint areas of interest for SEM-based imaging. This was because, in some steels, the chemical banding was very fine (~20 µm banding) and sometimes difficult to locate in the SEM directly from a µ-XRF scan. This also enabled relative differences in chemical homogeneity of the steels to be identified and compared with µ-XRF measurements. The second reason was to perform high sensitivity EDS maps in gauge

and transition sections of the steel so any relationship between cavities and microstructural features could be determined. Details of the 2 procedures are as follows:

- Large area EDS maps (~1 mm horizontal field width (HFW)) were collected at 10 kV using a working distance of ~10 mm, these were performed in areas of interest detected in the μ-XRF maps. Extended exposure time periods (~8 hours) at high count rates (>200,000 input cps) were used to maximise the sensitivity of the SEM-EDS for elemental distribution mapping.
- Areas of ~260 μm HFW at a working distance of ~10 mm were used for EDS mapping systematically every mm in the gauge section (outside the necked region, which had too high a cavity number density). These were collected at 10 kV with a pixel dwell time of 500 ms at high count rates (>200,000 input cps). Simultaneously secondary electron SEM images were collected to make the association between cavities and EDS acquired microstructural features.

3.4.5 TEM–based Imaging and Elemental Mapping of Microstructural Features

An FEI Talos F200X FEG-(Scanning) transmission electron microscope ((S)TEM) equipped with a Super-X EDS system was used to analyse the FIB-prepared thin foil TEM samples as well as carbon extraction replicas (CERs). EDS maps in STEM mode were collected so that the second phase particles in the analysed volume could be studied. FIB-prepared thin foil samples only cover a small area (typically 25 μm^2) which is not an ideal sampling area, but CERs are non-site specific, so locations of analysis cannot be chosen. This is a crucial element in research with an objective of characterising statistical extremes. Therefore, TEM was used sparingly on head sections of steels Es-P and Es-F, with the three main purposes being:

- Performing STEM maps in positively and negatively segregated regions (prepared by FIB–SEM thin foil lift-out samples) to find the influence of micro– segregation effects on the MX and $M_{23}C_6$ precipitate populations.
- Investigating the overlap of size distributions between MX–type carbo-nitrides and $M_{23}C_6$ carbides using the CER technique which is detailed in *Section 3.5*.
- Analysis of fine Cu precipitates found near MnS inclusions in steel Es-P.

3.5 Preparation of TEM Thin-foil Samples

An FEI Versa 3D FIB–SEM was used for the preparation of thin foil samples for TEM investigations. This technique is particularly useful for quantifying differences in the MX–type carbo-nitrides and $M_{23}C_6$ carbides due to micro–segregation because site specific analysis is required. The key steps in the preparation procedure for the thin foil samples are shown in *Figure 3.4.* Once a suitable area of interest has been located, the first step is to deposit a Pt layer 20 µm long, 2 µm wide and 2 µm thick on the area *(Figure 3.4a)* in order to protect the area from the ion beam and enable homogenous thinning in later steps. The next step included creating trenches using a current of 65 nA next to the area of interest, which can also be seen in *Figure 3.4a*. A U–shaped cut was then made to semi-detach the thin section from the bulk, leaving a small section attached to ensure that the thin section remains in place. The sample was then lifted out by attaching to an EasyLift^{TM} (FEI) probe using Pt deposition. The remaining attached section was then cut off using the ion beam. The semi–finished TEM sample was then attached to a TEM grid (either Cu or Mo), again using Pt deposited connections; this can be seen in *Figure 3.4b and c*. A view of the TEM grid can be seen in *Figure 3.4d*, the final step of thinning was performed using the ion beam starting with a large current (1 nA) and the subsequent lower current as low as 300 pA, a thinned sample can be seen in *Figure 3.4e*.

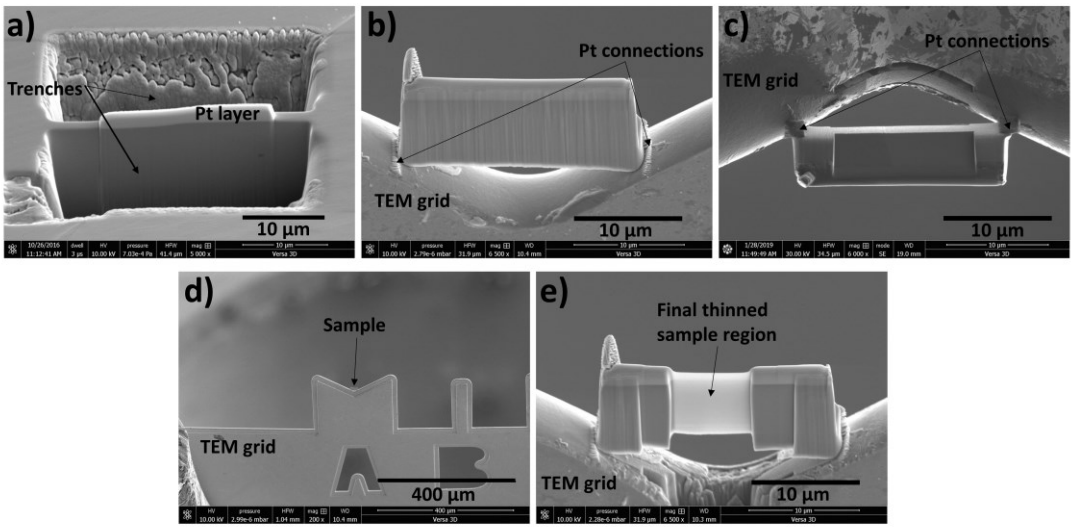

Figure 3.4: SEM images of the procedure of a TEM thin foil lift-out performed in a Versa 3D (FEI) FIB-SEM, showing the various steps (a) cutting the trenches, (b) and (c) attachment of thin foil to the TEM grid, (d) TEM grid and (e) final thinned sample ready for TEM analysis.

3.6 Preparation of Carbon Extraction Replicas (CERs)

CERs were used to create nano-scale thin carbon films with extracted precipitates attached onto them from the steels. These were then viewed in the FEI Talos F200X TEM for imaging or high-resolution elemental mapping (as mentioned earlier). CERs allow precipitates to be extracted from the matrix and deposited onto a thin carbon film. The obvious advantage of this technique would be the absence of the influence from the ferrite/martensite matrix which could influence the precipitate composition measurements, as well as saving time and cost over FIB-SEM thin foil sample preparation. However, the disadvantages include (i) the CERs are not site specific (unlike FIB-SEM techniques), and (ii) 100% precipitate pull-out rate is not guaranteed; for example, with a cluster (or a precipitate of excessive size) of precipitates not all may be extracted, as well as difficulty in extracting very fine precipitates. Overall, a complete representation of the precipitates may not be possible.

After polishing the samples using the metallographic sample preparation procedure described in *Section 3.2,* they were then etched using Villella's reagent for ~20 seconds to reveal the precipitates. The etched samples were then coated using a Safe-

Matic CCU-010 laboratory grade carbon coater, depositing a thin layer of carbon (10-20 nm), which was measured through the built-in sensors, onto the etched surface of the steel samples. A 2 mm by 2 mm mesh pattern was scored onto the coated samples; this allowed the carbon film to be extracted in small portions which made subsequent steps easier. The samples were then electrolytically etched with platinum wire in a solution of 10% HCl and 90% methanol, using a voltage of 3 volts and 50 mA current (for 30 seconds), this separated the carbon film from the surface. They were then quickly immersed in a beaker of methanol to wash off the etching solution and then were very slowly entered into a beaker of distilled water at an angle of about 45° with the face of the sample incident to the water, this allowed the carbon coating with the precipitates attached to be removed from the surface of the sample and float onto the water surface. The floating CER portions were extracted by a TEM copper mesh using a pair of tweezers. This process was done individually for each steel section sample one at a time, using fresh distilled water to avoid cross-contamination of the CERs.

3.7 Secondary Ion Mass Spectrometry (SIMS)

SIMS is an analytical tool which is capable of detecting most elements down to very low concentrations (parts per billion). This technique makes use of a primary ion beam (typically O^{-2} or Cs^{+}) to mechanically etch the sample in question. The ion beam impacts onto the sample surface and ejects positively and negatively charged ions (also known as positive or negative secondary ions) from the sample, via sputtering. The secondary ions are then analysed using mass spectrometry to produce data with regards to the depth profile. Therefore, it is possible to analyse the composition of samples with respect to the depth.

SIMS was performed by the Loughborough Surface Analysis team in the UK, for the respective work that is presented in this research project. SIMS Camecas 3f, 4f and 7f auto were used for the analysis, both O^{-2} (negative) and Cs^{+} (positive) ion beams were used for the primary ion bombardment, with secondary ion detection.

3.8 Thermo-Calc Thermodynamic Simulations

Thermodynamic predictions were performed using the Thermo-Calc software with the TCFE version 9 database, which is specifically adapted for steel alloys. This software

uses CALPHAD experimental approaches for simulations based on 2 assumptions; i) the Gibbs energy is at a minimum level and ii) functions are based on derivative equivalents, therefore, high order systems are predicted from lower order systems using extrapolation.

Chemical compositions were input from combinations of experimental results from SEM-EDS and those that were provided *(Table 3.4)* through ICP-OES/MS, to yield phase predictions at equilibrium conditions. Several impurity elements were not considered in these thermodynamic calculations due to the basic modelling ability of the software, these included Zr, As, Sn, Sb, Pb and Cu. Furthermore, certain phases that are not relevant in Gr. 91 steel, e.g. gas and diamond, were eliminated, and a temperature-range of 300 to 1600 °C was used.

This was a very useful tool for this project for investigating the effects of micro-segregation, this meant compositions used in simulations were varied based on the variable chemical compositions obtained experimentally. This provided simulated estimates of various microstructural features (such as Laves phase and MnS inclusions) depending on the concentration of the major alloying element, which was input into the software, results were used to compare to those acquired experimentally.

For the Scheil simulation performed in *Section 4.5* the composition input in Thermo-Calc was from the ICP-OES/MS provided for steel Es-P, this was because small variations in composition did not affect the simulation significantly. For the remaining simulations performed in *Chapter 5,* the SEM-EDS compositions were used for the elements Cr, V, Nb, Mo and Mn, and for the other elements the alloy compositions were used. It should be noted however, the Thermo-Calc software assumes a constant equilibrium partitioning coefficient (k_e) in its simulations, although in reality the value of k_e changes during solidification. Furthermore, Thermo-Calc does not include any back diffusion of elements, which also can be found experimentally.

3.9 Desk-top Spectrum Analyser 2 (DTSA-II) Simulations

The DTSA-II software has been developed by the Surface and Microanalysis Division (SMD) at the National Institute of Standards and Technology (NIST) and is freely available for download and use. The main purpose of the DTSA-II software is for

quantifying, simulating, visualising and manipulating energy dispersive X-ray spectra[202].

For this project a useful function of this software is the simulation of spectra using Monte-Carlo simulations. Upon chemically defining a unit of material with the elements present in it through the atomic weight percentage (e.g. Fe, Al, Mn, S, Cr and Mo), the Monte-Carlo simulation can predict the electron trajectories as they interact with the defined material, although the crystal structure of the compound cannot be defined. Based on these trajectories various information can be acquired, such as the depth and volume to which the electrons penetrate into the steel. This is useful for simulating the effect of different voltages on depth penetration for the steels characterised in this project.

Chapter 4 : Investigations of Sample Homogeneity

4.1 Introduction

In this section, the results and analysis from 3 distinct chemical mapping techniques will be studied; μ-XRF, SEM-EDS and SIMS. These techniques cover a range of sampling sizes and sensitivities, which in combination provide a detailed quantitative assessment of the chemical homogeneity of these steels.

4.2 μ - XRF: Centimetre-scale Chemical Homogeneity of Samples

μ-XRF was utilised to acquire macro (centimetre) scale chemical distribution maps in both the head and gauge sections of the steel creep tested bars. Initial maps were acquired from the entire head section of each of the 6 steels, which covered an area greater than 100 mm^2 for each steel. Examples of these maps can be seen in *Figure 4.1 and 4.2,* for steels Es-P and Es-F, respectively. The maps for steels ORNL-P, ORNL-F, Euro-Pi and Euro-P2 can be found in *Appendix A*. The major alloying elements (Mo, Cr, Mn, Nb, V), which are also the common precipitate and inclusion forming elements, are displayed in each figure along with a corresponding navigation camera image with a red rectangle to illustrate the area of the sample that was mapped. The purpose of these maps was to assess if the entire section of steel showed a consistent form of segregation.

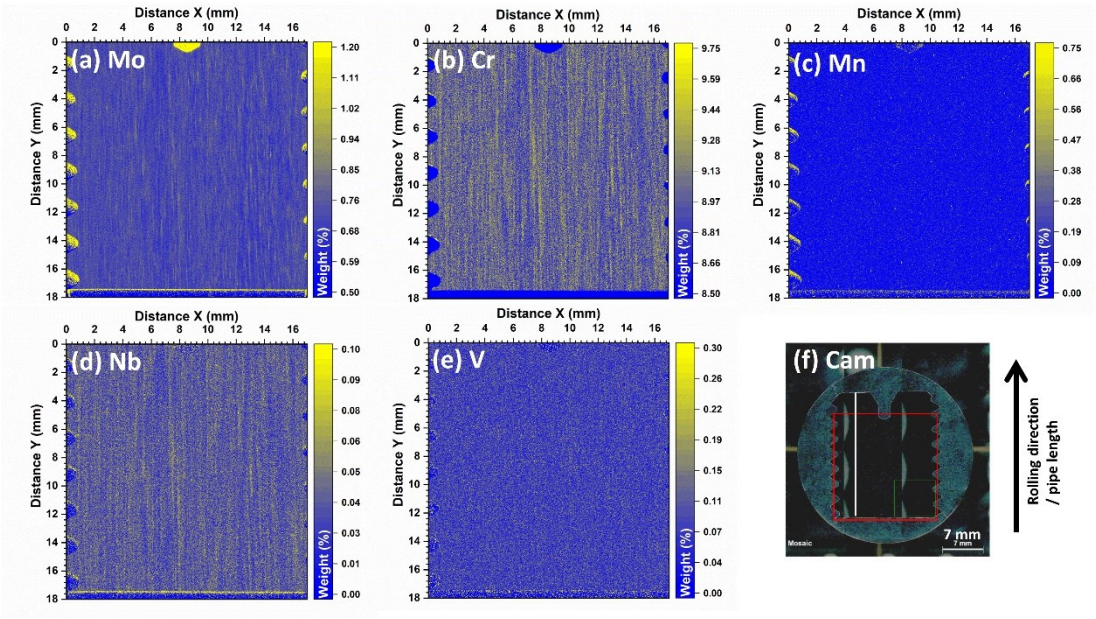

Figure 4.1: Centimetre-scale µ-XRF chemical distribution maps of steel Es-P from the head section, highlighting the chemical inhomogeneity in some of the major alloying elements (a) Mo (b) Cr (c) Mn (d) Nb (e) V (f) Navigation camera/mapped area photo (Red rectangle signifies mapped region).

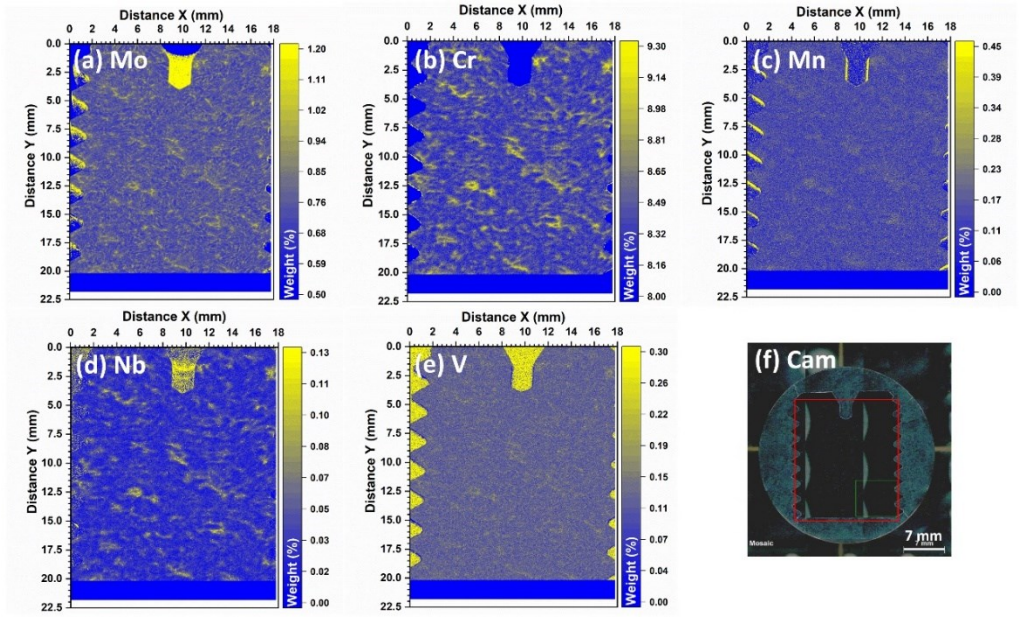

Figure 4.2: Centimetre-scale µ-XRF chemical distribution maps of steel Es-F from the head section, highlighting the chemical inhomogeneity in some of the major alloying elements (a) Mo (b) Cr (c) Mn (d) Nb (e) V(f) Navigation camera/mapped area photo (Red rectangle signifies mapped region).

After obtaining the initial centimetre scale assessment of each steel, the next step was to perform a smaller and more detailed µ-XRF scan focusing on a specific region for each head section, the purpose for this was to help define more clearly any scale and / or dimensions of the segregation effects as well as acquiring quantitative data on the variation in compositions of the elements of interest. These maps for all the steels are displayed in *Figures 4.3-4.8*. The type of segregation observed for all the steels was on the micron level, therefore the segregation in these steels will be referred to as micro-segregation as defined in literature for this scale [100][141].

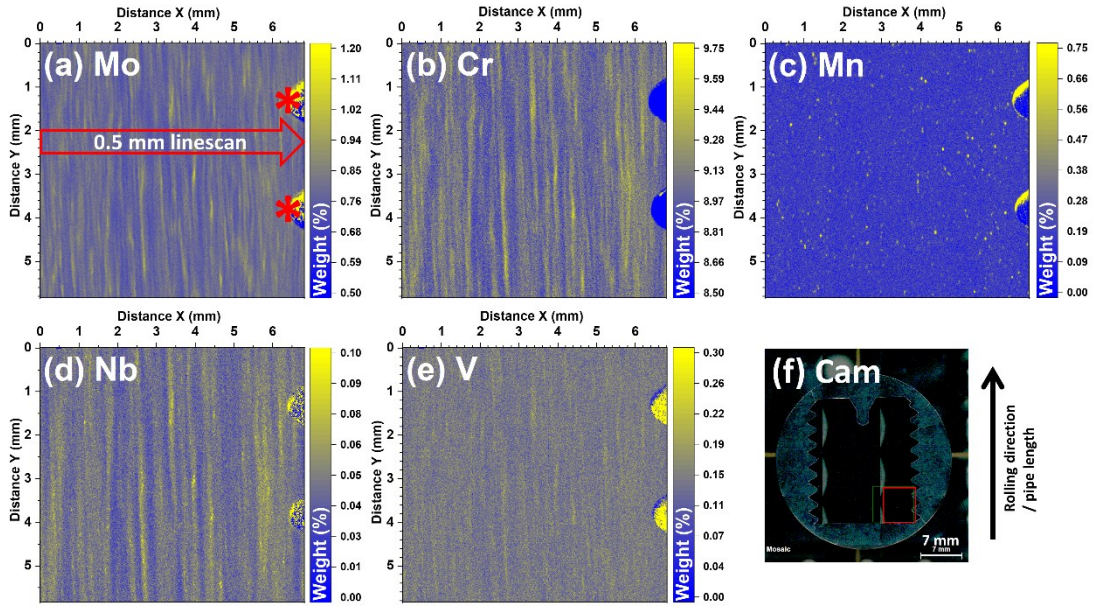

Figure 4.3: µ-XRF chemical distribution maps of steel Es-P from the head section, highlighting the chemical inhomogeneity in some of the major alloying elements (a) Mo (b) Cr (c) Mn (d) Nb (e) V (f) Navigation camera/mapped area photo (Red rectangle signifies mapped regions). (Asterisk marks the edges of the steel sample, these points were used as reference points for subsequent analysis in following chapters, red arrow marks the location, thickness and direction of the linescans).

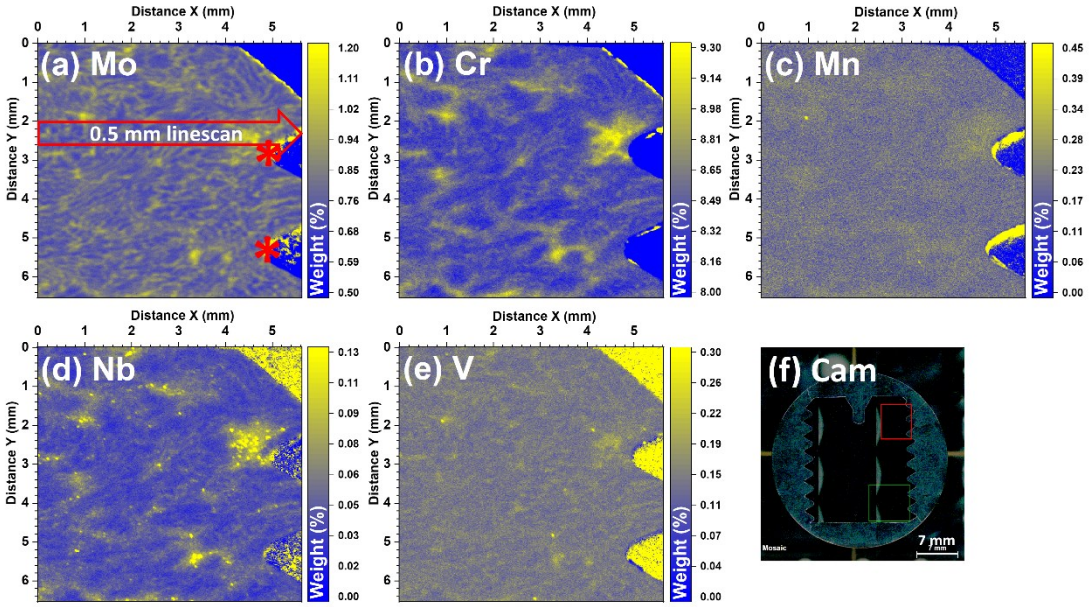

Figure 4.4: μ - XRF chemical distribution maps of steel Es-F from the head section, highlighting the chemical inhomogeneity in some of the major alloying elements (a) Mo (b) Cr (c) Mn (d) Nb (e) V (f) Navigation camera/mapped area photo (Red rectangle signifies mapped regions). (Asterisk marks the edges of the steel sample, these points were used as reference points for subsequent analysis in following chapters, red arrow marks the location, thickness and direction of the linescans).

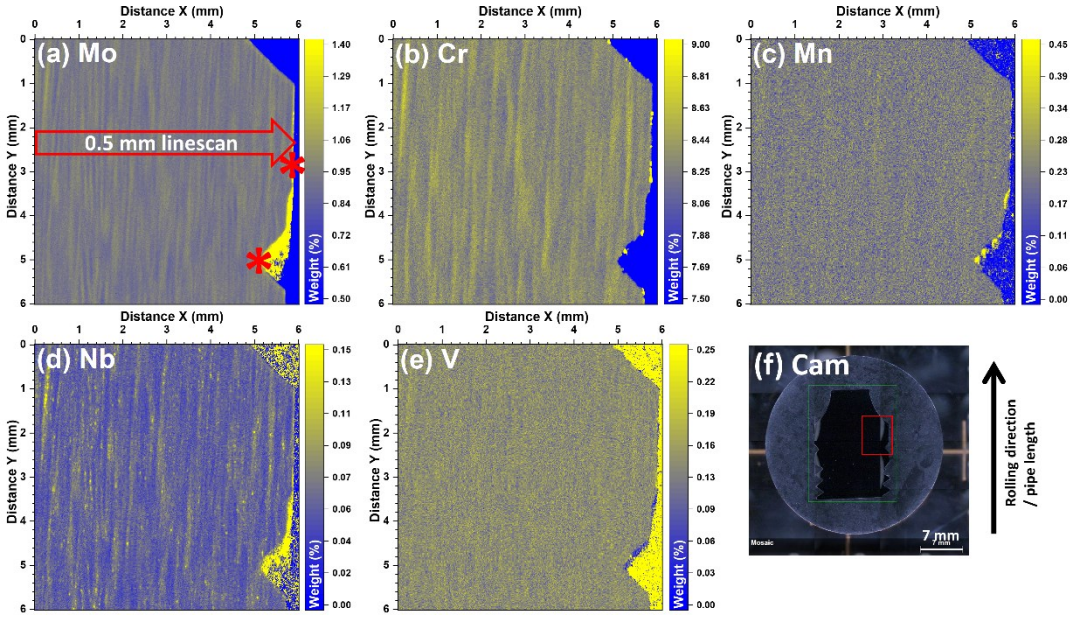

Figure 4.5: μ - XRF chemical distribution maps of steel ORNL-P from the head section, highlighting the chemical inhomogeneity in some of the major alloying elements (a) Mo (b) Cr (c) Mn (d) Nb (e) V (f) Navigation camera/mapped area photo (Red rectangle signifies mapped regions). (Asterisk marks the edges of the steel sample, these points were used as reference points for subsequent analysis in following chapters, red arrow marks the location, thickness and direction of the linescans).

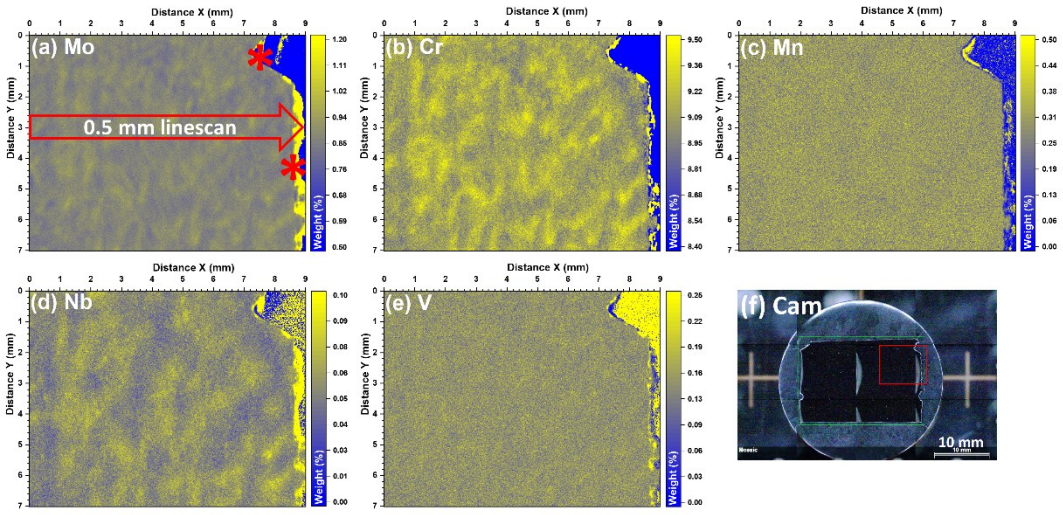

Figure 4.6: μ-XRF chemical distribution maps of steel ORNL-F from the head section, highlighting the chemical inhomogeneity in some of the major alloying elements (a) Mo (b) Cr (c) Mn (d) Nb (e) V (f) Navigation camera/mapped area photo (Red rectangle signifies mapped regions). (Asterisk marks the edges of the steel sample, these points were used as reference points for subsequent analysis in following chapters, red arrow marks the location, thickness and direction of the linescans).

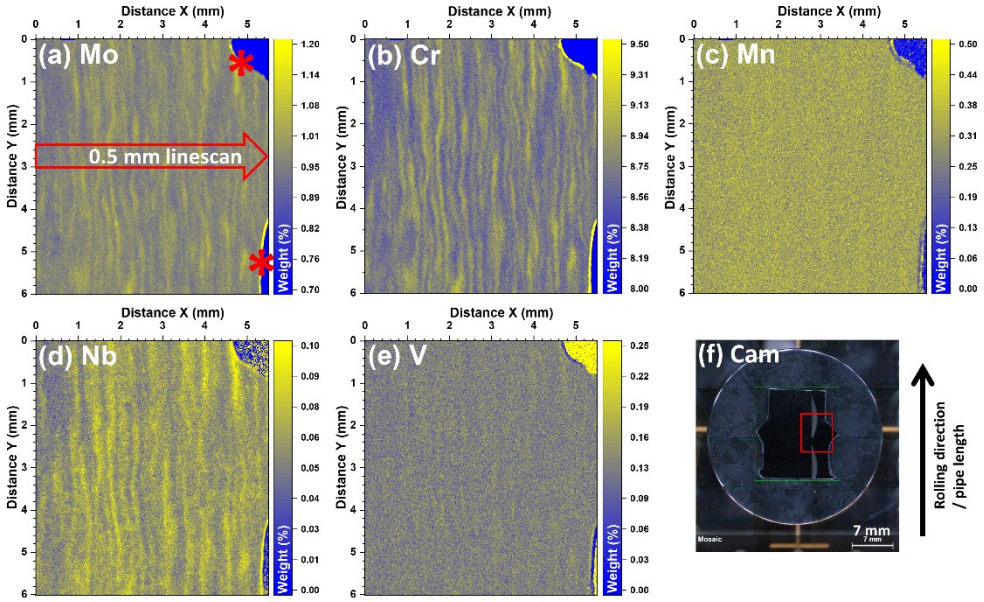

Figure 4.7: µ - XRF chemical distribution maps of steel Euro-Pi from the head section, highlighting the chemical inhomogeneity in some of the major alloying elements (a) Mo (b) Cr (c) Mn (d) Nb (e) V (f) Navigation camera/mapped area photo (Red rectangle signifies mapped regions). (Asterisk marks the edges of the steel sample, these points were used as reference points for subsequent analysis in following chapters, red arrow marks the location, thickness and direction of the linescans).

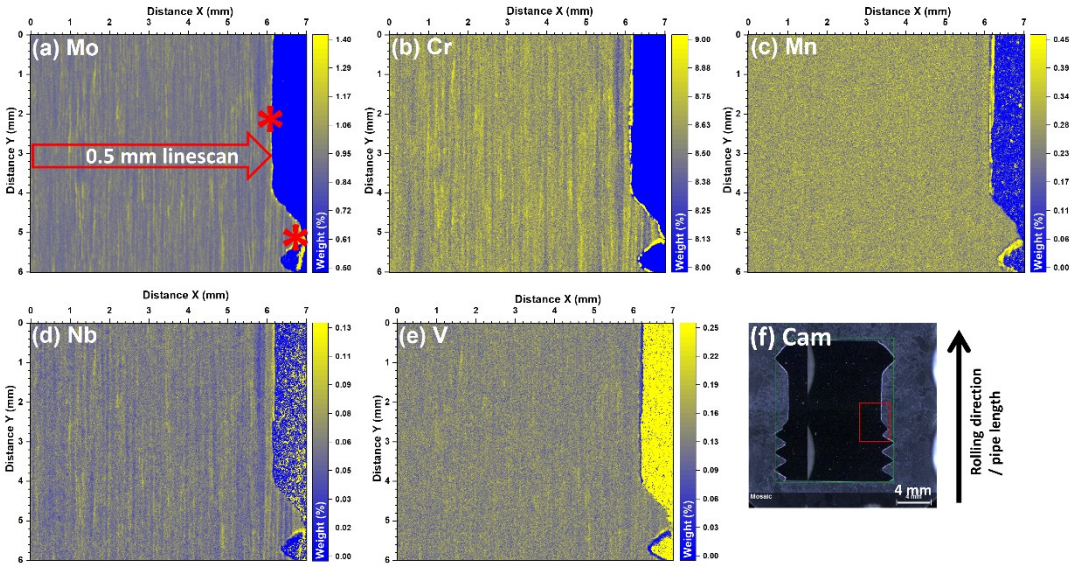

Figure 4.8: µ-XRF chemical distribution maps of steel Euro-P2 from the head section, highlighting the chemical inhomogeneity in some of the major alloying elements (a) Mo (b) Cr (c) Mn (d) Nb(e) V (f) Navigation camera/mapped area photo (Red rectangle signifies mapped regions). (Asterisk marks the edges of the steel sample, these points were used as reference points for subsequent analysis in following chapters, red arrow marks the location, thickness and direction of the linescans).

Although, chemical micro-segregation is observed in all of the steels, the chemical distributions showed 2 types of distinctive characteristics and dimensions. Examples of how these maps were analysed is shown in *Figure 4.9*, using the Mo µ-XRF maps for steels Es-P (rolled/drawn) and Es-F (forging), respectively. This analysis was performed for all steels using the same process as in *Figure 4.9*, with 5 measurements for each dimension per steel.

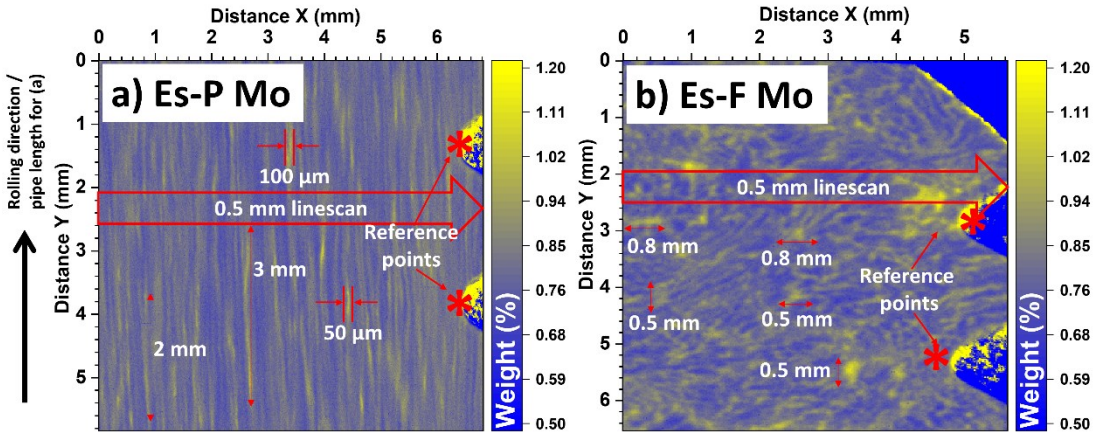

Figure 4.9: µ-XRF chemical distribution maps of Mo for steels (a) Es-P and (b) Es-F from the head sections. The asterisk marks the edges of the steel sample, these points were used as reference points for subsequent analysis in following chapters, red arrow marks the location, size and direction of the linescans.

- In steels Es-F and ORNL-F (*Figures 4.4 and 4.6* respectively) the segregation pattern exists in the form of diffuse "patches". For steel Es-F, the patches can vary from as large as 1 mm in X and Y directions, down to 100 µm, with an interconnectivity between regions. This can be clearly seen in the Mo map for Es-F. With regards to the plane of observation the chemical micro-structure is orientated in the X direction. For steel ORNL-F the patches range in the size of 1 - 2 mm in the X and Y directions, and the chemical micro-structure is orientated in the Y direction, with very closely connected regions. However, steel Es-F does seem to have a larger extreme of positively segregated regions, in terms of size distribution and magnitude.
- In steels Es-P, ORNL-P, Euro-Pi and Euro-P2 (*Figures 4.3, 4.5, 4.7 and 4.8* respectively) the segregation pattern exists as banding along the axis of the creep bars. These bands are typically between 0.5 to 4 mm in length and are approximately 20 to 200 µm wide, dimensions which are consistent with the reported literature for rolled/drawn interdendritic micro-segregation [25][40][103]. Steel Euro-P2 has the finest banding (20 µm), followed by steels Es-P and ORNL-P (50-100 µm). Steel Euro-Pi (150 - 200 µm) has the thickest banded microstructure, in all 4 steels the banding exists across the entire mapped region and band spacing appears to be the same throughout.

The following discussion will assess the segregation regions based on their size and shape; the micro-segregation compositions will be discussed in later sections. The spatial scale of the micro-segregation which has been defined for each steel is determined by the secondary dendrite arm spacing (SDAS) and the reduction ratio during the pipe-making or forging process [37]. The six steels in this project are most likely to have been produced from the ingot casting method rather than continuous casting, this is due to the low tonnage due to specific requirements or applications of Gr. 91 steels even in power generation.

For the ORNL steels the ESR process was used which is documented in the ORNL report [13]. Based on this and other literature studies it can be assumed that ESR processing was used for all of the steels in this project. This is due to a number of reasons, ESR processing is commonly used in critical applications where the quality of the finished product has a large effect on the performance of the component or system. Some examples include in Gr. 91 steels in the power generation industry [13] and other industries [119][120] where careful control of composition, impurities and inclusions are of importance. Furthermore, the TIL (total impurity level of O, N and S in wt %) proposed by Ali et al. [93] was similar for the known ESR processed steels (ORNL) and the remaining four steels (*Table 3.4)*. Although the TIL content was greater than those found in literature, this can be due to many other factors, such as the composition of the electrode, furnace atmosphere and the slag system [93]. One of the main factors which will determine the extent of micro-segregation is the melting rate during ESR [87][122]. The melting rate influences the solidification rate and therefore the SDAS, which determines the severity of micro-segregation during ESR processing. At higher melting rates the cooling is slower, which promotes the formation of coarse dendrites and larger SDASs. Zhu et al. [122] suggested that solute atoms aggregate within this interdendritic regions during ESR processing. The subsequent *Sections 4.3-4.5* will analyse the severities of micro-segregation in each of these steels using the μ-XRF and SEM-EDS based chemical mapping.

For Es-P a plug mill pipe-making method was used based on the thickness and outer diameter of the pipe (50 and 450 mm, respectively) as identified in the literature (JFE [94] and Vallourec [95]). The use of a plug mill meant that a longitudinal banded

microstructure was produced. For the Es-F steel, due to its complex geometry, the tee-piece was most likely to have been forged and then the internal hollow machined. This is likely to have had a lower reduction ratio during forging, which results in less modification to the chemical distribution relative to that during pipe fabrication. ORNL-P was a relatively thin-walled pipe (13 mm wall thickness) with a small outer diameter (76 mm) in comparison to the other pipes in this project it was produced via a hot rotary piercing route [13]. For ORNL-F a saddle forging method was used [13], which meant that a mandrel was used to maintain the shape of the cavity within the hollow forging. It is predicted that a greater reduction ratio was applied to ORNL-F than the other forging Es-F. This is because ORNL-F was not bored, but instead hot-worked to reduce its wall thickness. This explains why the micro-segregation spacing is a lot closer when compared to the Es-F steel. The two European supplier steels Euro-Pi and Euro-P2 were likely to have been produced from the same ingot size, based on their similar size and background. The plug mill was the most likely method of producing these two steels based on the outer diameters and thicknesses [94][95]; 355 and 219 mm in outer diameters and 35 and 26 mm in thicknesses for Euro-Pi and Euro-P2, respectively. The greater reduction ratio of Euro-P2 meant more hot deformation was carried out to make the pipe, when compared to Euro-Pi. This is shown via the finer micro-segregation banding as well as smaller spacing between positively segregated bands in Euro-P2.

The temperatures and stresses that the creep tests were conducted at were not sufficient to induce any homogenisation effects in the steels, this can be seen in the μ-XRF scans which were performed in the gauge sections of the steels, examples of these can be seen in *Figure 4.10 and 4.11,* for steels Es-P and Es-F respectively. The maps for steels ORNL-P, ORNL-F, Euro-Pi and Euro-P2 can be found in *Appendix B.*

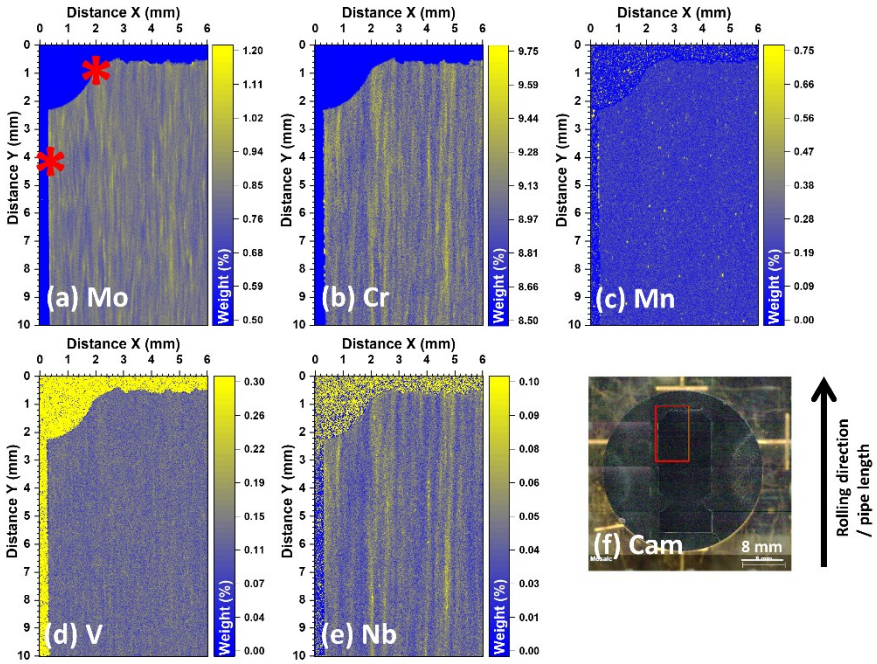

Figure 4.10: µ-XRF chemical distribution maps of steel Es-P from the gauge section, highlighting the chemical inhomogeneity in some of the major alloying elements (a) Mo (b) Cr (c) Mn (d) Nb (e) V (f) Navigation camera/mapped area photo (Red rectangle signifies mapped regions). (Asterisk marks the edges of the steel sample, these points were used as reference points for subsequent analysis in following chapters).

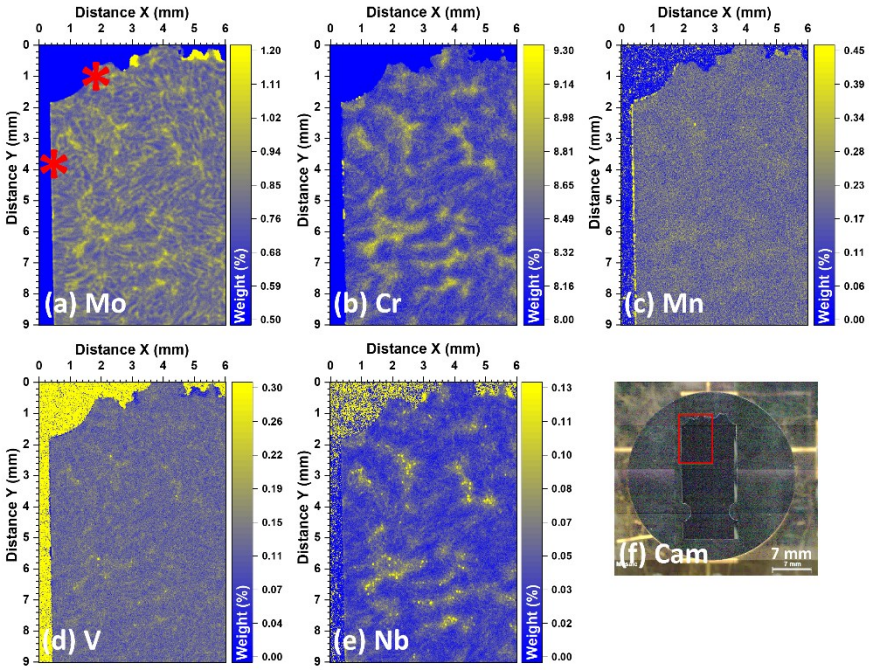

Figure 4.11: µ - XRF chemical distribution maps of steel Es-F from the gauge section, highlighting the chemical inhomogeneity in some of the major alloying elements (a) Mo (b) Cr (c) Mn (d) Nb (e) V (f) Navigation camera/mapped area photo (Red rectangle signifies mapped regions). (Asterisk marks the edges of the steel sample, these points were used as reference points for subsequent analysis in following chapters).

Figure 4.12 shows contour maps of the elements Cr and Mo for steels Es-P and Es-F derived from the µ-XRF maps for these 2 steels shown in *Figure 4.3 and 4.4*. Only the top 5% of composition is displayed in each map, i.e., the areas of positive micro-segregation (solute-rich regions). Following this *Figure 4.13* shows 2 overlaid maps, *Figure 4.13a* shows an overlay of Cr and Mo for steel Es-P and *Figure 4.13b* shows an overlap of Cr and Mo for steel Es-F. These maps indicate that micro-segregation of these elements is correlated in the steel but of course is not limited to just Cr and Mo as seen in the previous figures**.** The significance of this phenomenon is to stress the fact that as these elements are positively segregated in similar regions, it will also mean the effects on 2nd phase particles containing these elements will also be the same, for example the purple regions in *Figure 4.13* may see increased populations of carbides, carbo-nitrides and Laves phase particles; similar trends of 2nd phase particles/phases were found in a few other studies with CSEF steels [40][41].

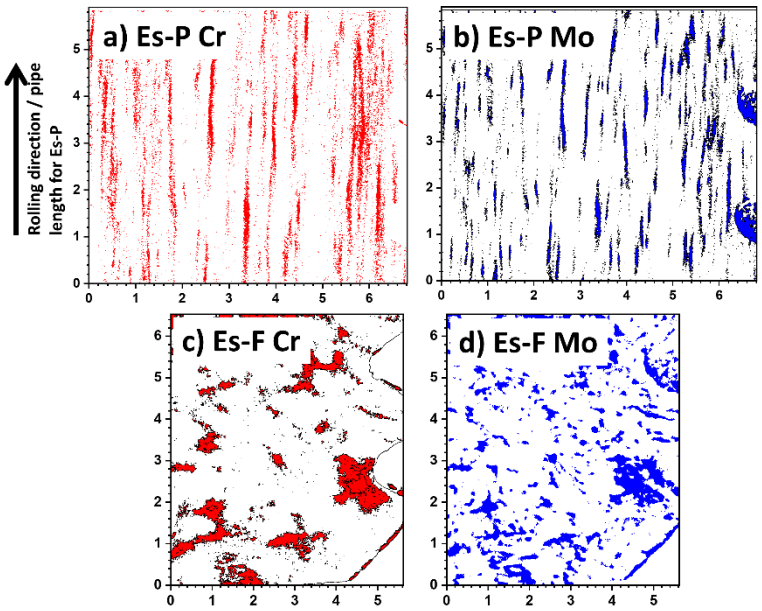

Figure 4.12: µ-XRF derived contour maps of the top 5 wt % in composition of Cr and Mo for the Es-P (a and b) and the Es-F (c and d), respectively, showing locations of positive micro-segregation.

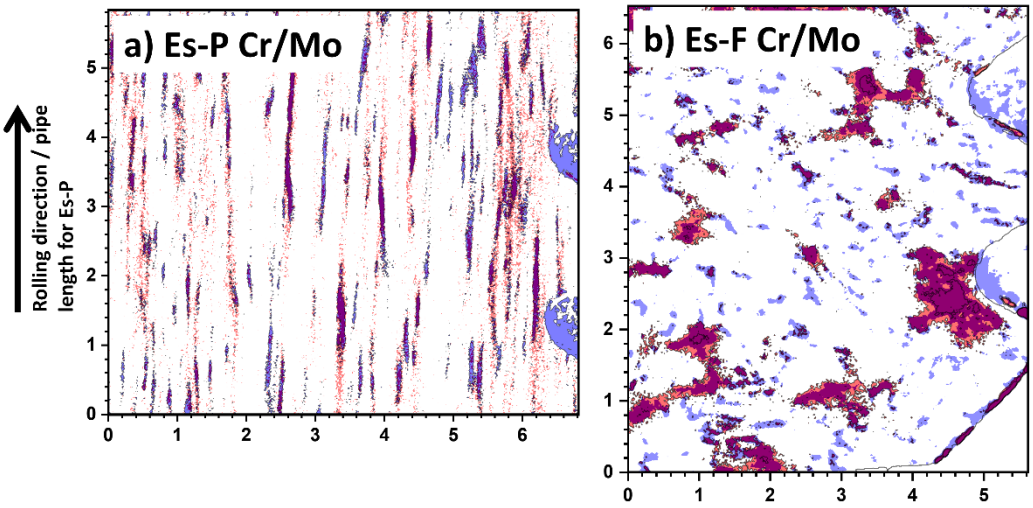

Figure 4.13: Overlaid µ-XRF derived contour maps of Cr and Mo from Figure 4.12, showing the same micro-segregation regions in the (a) Es-P and (b) Es-F steels.

4.3 Quantifications of Compositional Extremes from the µ-XRF

From the µ-XRF chemical maps *(Figure 4.3-4.8)* quantitative data were extracted which detailed the compositional variation across the mapped area. Compositional linescans (with a line thickness of 0.5 mm which equated to 25 data points in

thickness) were produced for each of the elements analysed for each of the steels (performed across the centre of the sample marked by the red arrows in *Figures 4.3 – 4.8*). These can be found in *Figure 4.14*, from which the maximum and minimum compositions for the elements Mo, Cr, Mn, Nb and V were extracted and are summarised in *Table 4.1*. It should be noted that, for steel Es-F there were large peaks at the same point (~ 4.5 mm), these were due to particularly high (positively) micro-segregated regions, this can be seen in *(Figure 4.4)* in the top right-hand side. The values were obtained by averaging the 3 highest peaks and the 3 lowest troughs for each of the 5 elements for each of the 6 steels (the peaks and troughs for each element coincided). The average XRF composition is also included in *Table 4.1* and was obtained from a 20 mm^2 scanned region in each μ-XRF map. It is noteworthy that the values for Cr and Mo obtained using the standard-less μ-XRF technique are close in absolute terms to the bulk composition measured by the commercial test house. The μ-XRF technique does not have the sensitivity to detect trace or tramp impurities in these steels due to diffraction effects or elements with a Z < Na due to X-ray absorption from the Be windows on the EDS detectors.

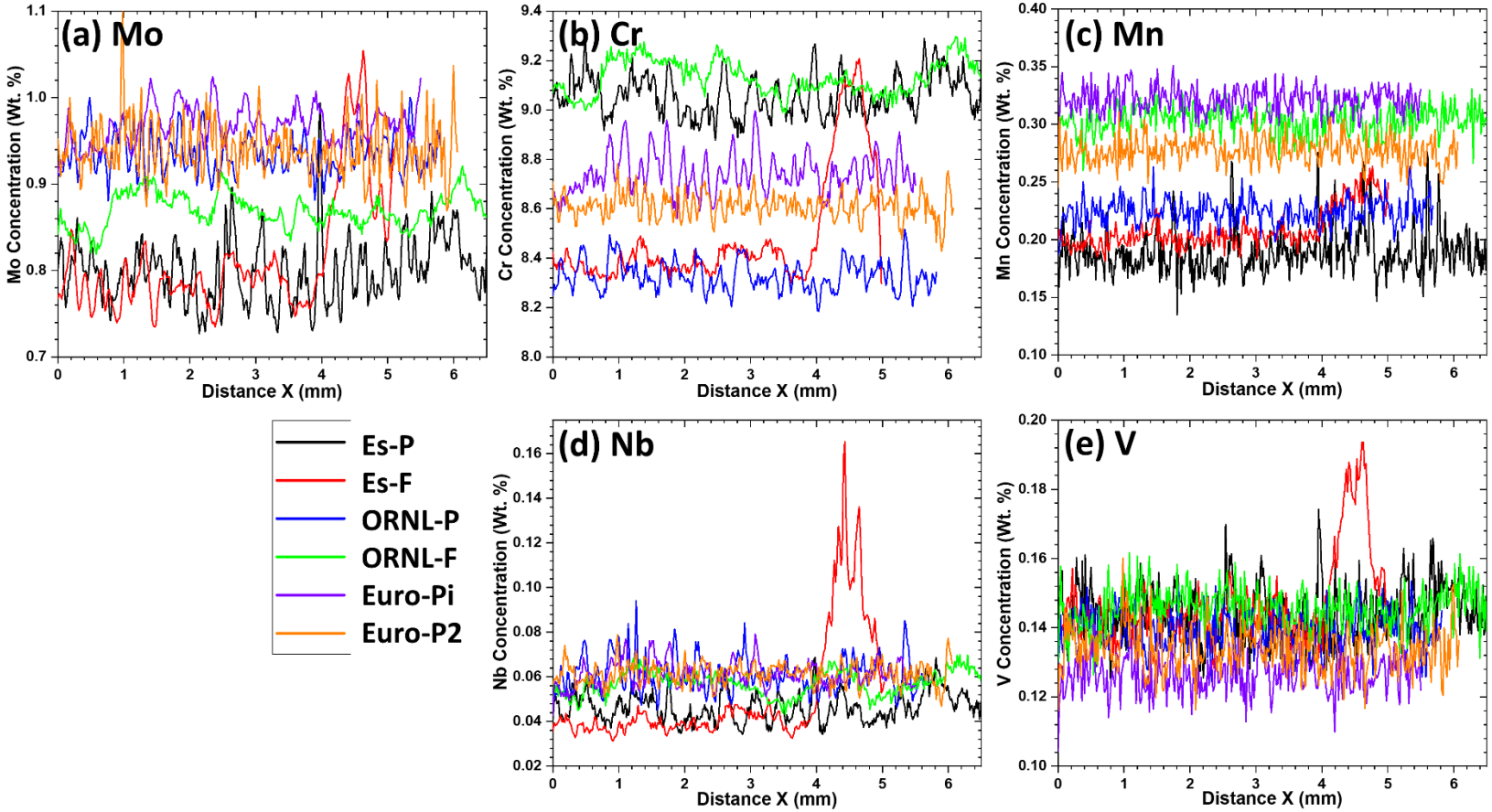

Figure 4.14: μ-XRF derived compositional linescans for the steels in this study showing variations in (a) Mo (b) Cr (c) Mn (d) Nb (e) V (Data used for Table 4.1).

Table 4.1: A summary of the maximum and minimum compositions obtained from the μ-XRF chemical maps, in comparison to the bulk composition measured and ICP/OES-MS composition provided (Section 3.1) in wt %.

Sample	Area	Concentration (Wt. %)				
		Mo	Cr	Mn	Nb	V
Es-P	High	0.93	9.28	0.27	0.07	0.17
	Low	0.73	8.89	0.14	0.03	0.12
	Average	0.80	9.06	0.19	0.05	0.14
	ICP-OES/MS	0.94	8.77	0.41	0.071	0.224
Es-F	High	1.02	9.06	0.26	0.14	0.19
	Low	0.74	8.31	0.18	0.03	0.13
	Average	0.81	8.49	0.21	0.05	0.15
	ICP-OES/MS	0.94	8.30	0.40	0.070	0.214
ORNL-P	High	0.99	8.48	0.26	0.09	0.15
	Low	0.88	8.20	0.20	0.05	0.13
	Average	0.94	8.33	0.22	0.06	0.14
	ICP-OES/MS	1.02	8.11	0.44	0.077	0.22
ORNL-F	High	0.91	9.28	0.33	0.07	0.16
	Low	0.82	9.00	0.27	0.04	0.13
	Average	0.87	9.13	0.30	0.06	0.15
	ICP-OES/MS	0.96	8.75	0.52	0.072	0.23
Euro-Pi	High	1.02	8.97	0.35	0.08	0.14
	Low	0.93	8.58	0.30	0.05	0.11
	Average	0.97	8.74	0.32	0.06	0.13
	ICP-OES/MS	1.06	8.548	0.53	0.072	0.195
Euro-P2	High	1.05	8.75	0.31	0.08	0.15
	Low	0.87	8.47	0.25	0.05	0.12
	Average	0.94	8.61	0.28	0.06	0.14
	ICP-OES/MS	1.02	8.411	0.50	0.071	0.199

A typical map spectrum is provided in *Figure 4.15a,* which shows the selection of the major elements which were included in the quantifications of the μ-XRF maps, it should also be noted that maximum peak height (Fe-k_α) for the map contains

approximately 1 x 10^9 counts. A spectrum for a single point is also displayed in *Figure 4.15b* which shows a statistically significant number of counts are available for quantification for every 20 µm spot. With regards to determining uncertainty in X-ray counts a recent study states that the Poisson standard deviation is approximately the amount of uncertainty in a series of measurements [203]. Therefore, a total count of 10^4 will only have a 1% uncertainty of the total counts, meaning even for a single pixel spectrum *(Figure 4.15b)* (20 µm x and y) the uncertainty for the spectra is below 1%.

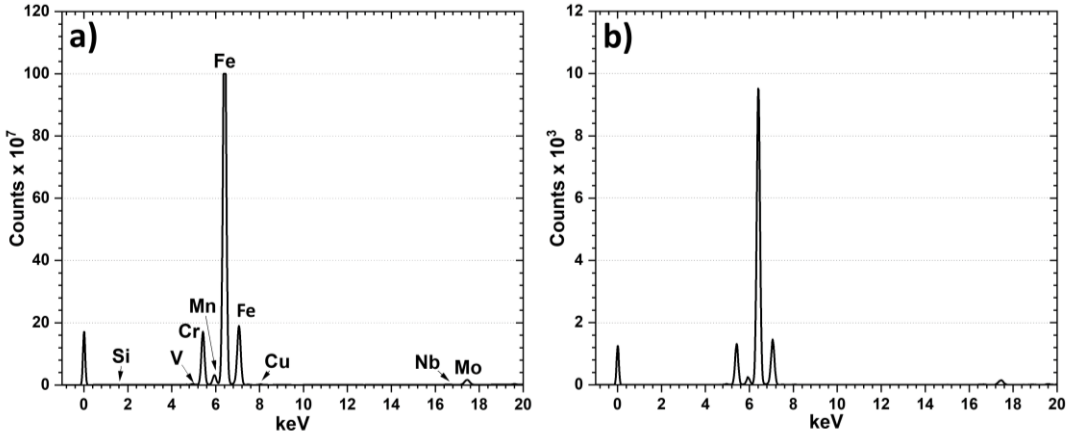

Figure 4.15: A typical map spectrum (from steel Es-P) acquired from the µ-XRF mapping (a) and a typical map spectrum for a single point from the µ-XRF mapping (b).

The compositional linescans in *Figure 4.14* show the variations in composition across each sample for the given elements. The forged steels (Es-F and ORNL-F) have less frequent peaks and troughs in comparison to the other samples, all of which exhibit chemical banding. *Figure 4.3* (for Es-P) showed a very frequent banded chemical microstructure, this is shown for the linescans in *Figure 4.14* where there are continuous variations in composition seen in the form of peaks and troughs. Another point worth noting is that *Figure 4.3* (for Es-P) shows peaks for Mn which can be seen as yellow dots in the figure, which could be due to coarse Mn-rich sulphides (MnS inclusions); this will be investigated in the *Chapter 6. Figure 4.4* (for Es-F) showed a few highly localized positively segregated regions, this is reflected in *Figure 4.14* where there is a large peak at the distance 4.5 mm for all of the elements examined. The remaining steels showed traces consistent with their chemical behaviour shown in *Section 4.2*, whether banded (ORNL-P, Euro-Pi, Euro-P2) or forged (ORNL-F).

Figure 4.16 uses the data from *Table 4.1* to calculate the percentage changes in compositions between the high and low measurements from the µ-XRF data, this shows the trend in segregation much more clearly for each of the elements analysed.

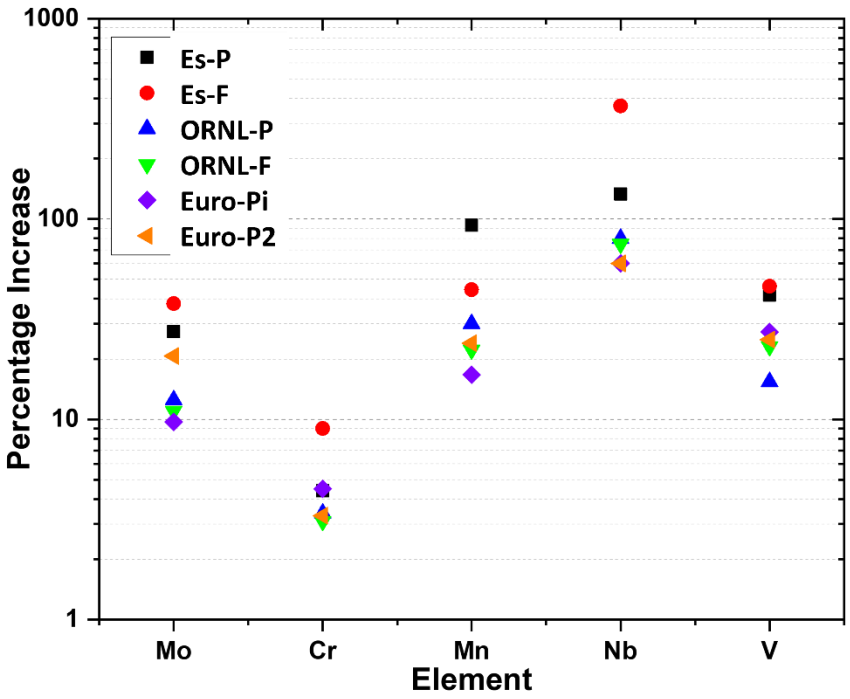

Figure 4.16: A graph showing the percentage increase from the lowest measurement made in the alloying elements Mo, Cr, Mn, Nb and V for all the steels in this project from the µ-XRF mapping from Table 4.1.

With regards to the individual steels, a ranking based assessment can be made which averages the rank of each steel for each of the 5 elements analysed. With this ranking system steel Es-F had the highest overall segregation with a ranking value of 1.2, which means it had the greatest percentage increase in 4 of the elements (Mo, Cr, Nb and V) and was second in Mn, therefore, (1 + 1 + 1 +1 + 2) / 5 = 1.2. Es-P ranked 2nd with 2.2, followed by ORNL-P (4.0), Euro-P2 (4.4), Euro-Pi (4.4) and lastly ORNL-F with 5. It is worth noting that the ex-service steels Es-P and Es-F were the 2 highest in the rankings for each individual element except Cr. In steel Es-F the non-strain oriented, localised micro-segregation allows an easily distinguishable enrichment to be quantified. Steel Es-P also has very clear positively segregated bands, which is reflected in its highest ranking among the banded steels. Steel ORNL-F meanwhile, which has a similar chemical distribution pattern to Es-F, showed the least percentage increase due to the weaker micro-segregation present.

4.4 Quantifications of Compositional Extremes from the SEM-EDS

SEM-based EDS maps were carried out in specific areas of interest that were defined by μ-XRF analysis (specific features were used to re-locate samples for the different techniques). These maps were performed to pinpoint locations of positive and negative micro-segregation as well as to compare the variation in compositions acquired from the μ-XRF technique. The chemical composition was obtained at a low magnification, long dwell time and high-count rate (> 200,000 input cps); more details can be found in *Section 3.4.5*. *Figures 4.17-4.19* show the SEM-derived EDS maps for all the steel head sections in the project for the selected elements (Cr, Mo, Nb). Gauge sections were also analysed and showed similar segregation behaviour, but are not shown as the creep testing increased complexity (e.g. creep cavitation and other damage associated with the fracture).

Figure 4.17a and b show the Cr and Mo SEM-EDS maps for Es-P, the positively segregated regions can be seen in the form of banding with a thickness of around 25 - 50 μm and a spacing that is also roughly 150 - 200 μm. Furthermore, coarse stringer inclusions can be seen within these positively segregated bands, which will be further discussed in *Chapter 6*. *Figure 4.17c to e* show the Cr, Mo and Nb maps for Es-F, the non-strain oriented localised micro-segregation can be seen in the maps which is defined by the dashed lines. In the Nb map a coarse Nb-rich phase can be seen in the positively segregated region, which is also consistent with Nb-rich phases found in positively segregated regions reported in Gr. 91 literature [40]. The positively segregated regions which are enriched in solute elements (such as Mo, Cr, V and Nb), lead to the nucleation and formation of more secondary phases.

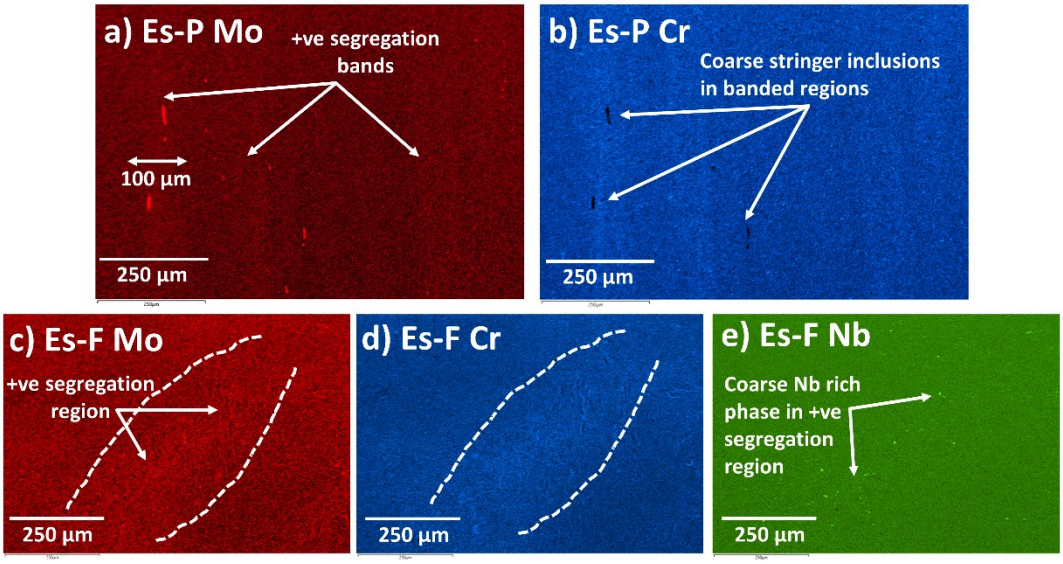

Figure 4.17: SEM-EDS derived intensity maps for steels Es-P (a and b) and Es-F (c-e) showing the micro-segregation effects for the elements Mo, Cr, and Nb.

Figure 4.18 shows the SEM-EDS maps for steels ORNL-P and ORNL-F which showed no significant changes in composition in the µ-XRF analysis *(Figure 4.16*). This is reflected in the maps where a large contrast differential is not present as compared to other ex-service steels. steel ORNL-F does not show any contrast differential in the SEM-EDS maps, this is also consistent with *Figure 4.16* which shows ORNL-F has one of the smallest degrees of micro-segregation from all the steels in the project. For steel ORNL-P banding was in the range of 100 µm with spacing of 200 - 250 µm between bands, and for steel ORNL-F a localised region of positive micro-segregation can be seen which is similar to that found in steel Es-F.

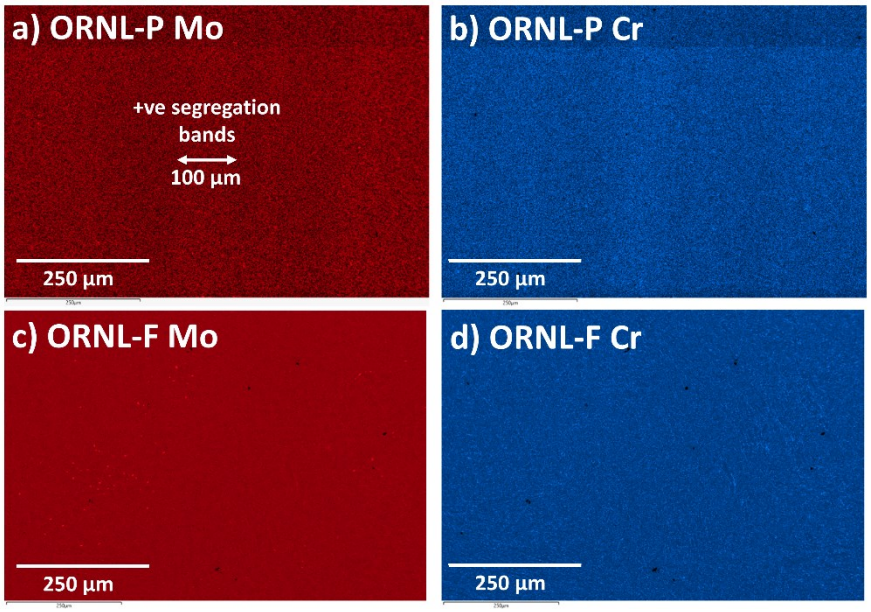

Figure 4.18: SEM-EDS derived intensity maps for steels ORNL-P (a and b) and ORNL-F (c and d) showing the micro-segregation effects in the elements Mo and Cr.

Figure 4.19 shows the Cr and Mo maps for steels Euro-Pi and Euro-P2, the banding is shown in these maps for both steels, although, a clear difference in the width and frequency of the chemical distribution can be seen very distinctly. In Euro-Pi it is ~100 - 150 µm in width with around 200 µm spacing between bands and for steel Euro-P2 the banding can be seen in the 20 µm scale but is very frequent, with 16 positively segregated bands can be seen within the 1 mm map.

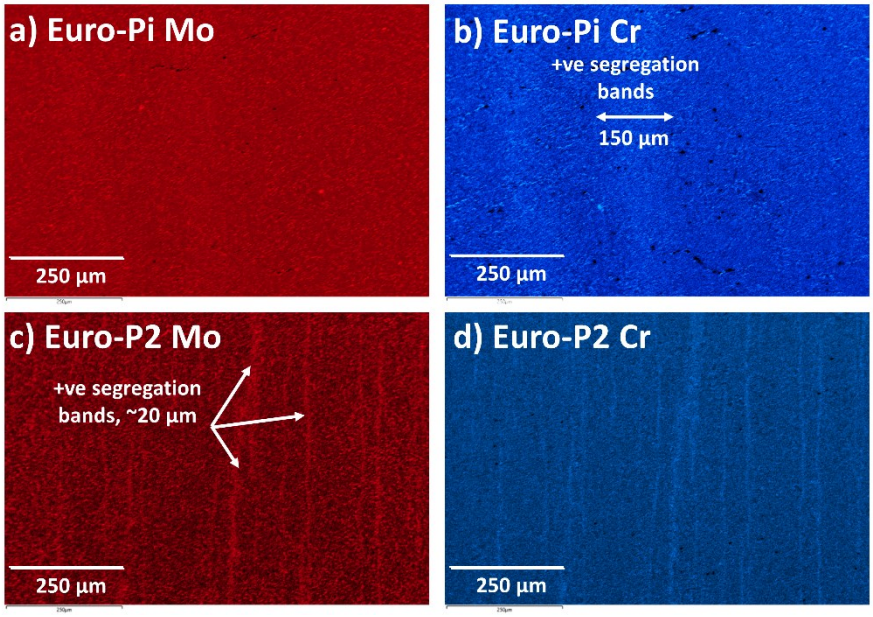

Figure 4.19: SEM-EDS derived intensity maps for steels Euro-Pi (a and b) and Euro-P2 (c and d) showing the micro-segregation effects in the elements Mo and Cr.

The maximum and minimum chemical compositions for the elements Mo, Cr, Nb, and V were extracted from these maps using the average of 3 different locations, which were taken from positively and negatively segregated regions respectively (from *Figures 4.17-4.19*). Mn was also discounted from the analysis because it did not show any variation in the SEM-EDS analysis. *Table 4.2* gives the extremes in compositions acquired, as well as the bulk composition from each map; the previous bulk compositions from the µ-XRF and ICP-OES/MS are also included for comparison. In all samples and all areas, the compositional extremes measured within the maps is lower in SEM-EDS than with µ-XRF. This is to be expected since the µ-XRF scans were performed over a much larger area providing many more positively and negatively segregated regions from which to select the highest and lowest areas. Even where the same area is studied from both techniques the much larger interaction volume of µ-XRF at 50 kV compared with SEM-EDS at 10 kV would be expected to yield result differences due to a larger sampling volume at 50 kV. Furthermore, from the µ-XRF mapping the incident X-ray beam is expected to penetrate much deeper than the electrons in the SEM-EDS beam, irrespective of the accelerating voltage.

Table 4.2: A summary of the maximum and minimum compositions obtained from the SEM-EDS chemical maps, in comparison to the bulk composition measured from the µ-XRF (Table 4.1) and ICP/OES-MS composition provided (Section 3.1) in wt %.

Sample	Area	Concentration (Wt. %)			
		Mo	Cr	Nb	V
Es-P	High	1.09	8.99	0.10	0.25
	Low	0.86	8.58	0.05	0.22
	Average	0.97	8.70	0.08	0.23
	µ-XRF	0.80	9.06	0.05	0.14
	ICP-OES/MS	0.94	8.77	0.071	0.224
Es-F	High	1.10	8.61	0.10	0.27
	Low	0.84	8.02	0.05	0.21
	Average	0.89	8.25	0.07	0.22
	µ-XRF	0.81	8.49	0.05	0.15
	ICP-OES/MS	0.94	8.30	0.070	0.214

ORNL-P	High	1.14	8.27	0.14	0.25
	Low	0.97	7.98	0.06	0.22
	Average	1.02	8.03	0.08	0.22
	μ-XRF	0.94	8.33	0.06	0.14
	ICP-OES/MS	1.02	8.11	0.077	0.22
ORNL-F	High	1.00	8.74	0.08	0.25
	Low	0.93	8.68	0.07	0.23
	Average	0.94	8.71	0.07	0.24
	μ-XRF	0.87	9.13	0.06	0.15
	ICP-OES/MS	0.96	8.75	0.072	0.23
Euro-Pi	High	1.21	8.54	0.10	0.26
	Low	1.00	8.29	0.09	0.22
	Average	1.03	8.29	0.09	0.23
	μ-XRF	0.97	8.74	0.06	0.13
	ICP-OES/MS	1.06	8.548	0.072	0.195
Euro-P2	High	1.14	8.71	0.10	0.24
	Low	1.00	8.29	0.07	0.21
	Average	1.07	8.41	0.08	0.23
	μ-XRF	0.94	8.61	0.06	0.14
	ICP-OES/MS	1.02	8.411	0.071	0.199

Figure 4.20 uses the data from *Table 4.2* to calculate the percentage changes in compositions between the high and low measurements from the SEM-EDS data, this shows the trend in segregation more clearly for each of the elements analysed. With regards to the individual elements, Nb had the greatest tendency to segregate, followed by Mo, V, and then Cr.

Similarly, to *Section 4.3* in the μ-XRF analysis, a ranking based assessment was made which averages the rank of each steel for each of the 5 elements analysed. These were

as follows, Es-F (1), Es-P (3), ORNL-P and Euro-Pi (3.5), Euro-P2 (4) and ORNL-F (5.75). Compared with the analysis performed with the µ-XRF data, a similar trend was found, in which steels Es-F and Es-P ranked the highest and steel ORNL-F ranked the lowest. Furthermore, steels ORNL-P, Euro-Pi and Euro-P2 ranked very closely in the SEM-EDS as they did in the µ-XRF analysis, the only difference being steels Euro-Pi and Euro-P2 were in reverse order. It should be noted however, for steels Euro-P2, with regards to elements Mo and V, the rankings are around the middle, however, for elements Cr and Nb, the rankings are at the bottom. In this analysis steels Es-P and Es-F were once again consistently the 2 highest in the ranks for each individual element. It should also be noted the degrees of segregation (percentage increase ranges) were much lower in the SEM-EDS analysis compared to the µ-XRF. Although nominally the same area was analysed using both techniques the sampling depth of µ-XRF is at least an order of magnitude greater than in SEM EDS. This means that the most segregated area in the sample defined by XRF may not be the most segregated area for SEM-EDS. In addition, the µ-XRF analysed the entire surface of the sample, which increased the likelihood of finding the most compositionally extreme area.

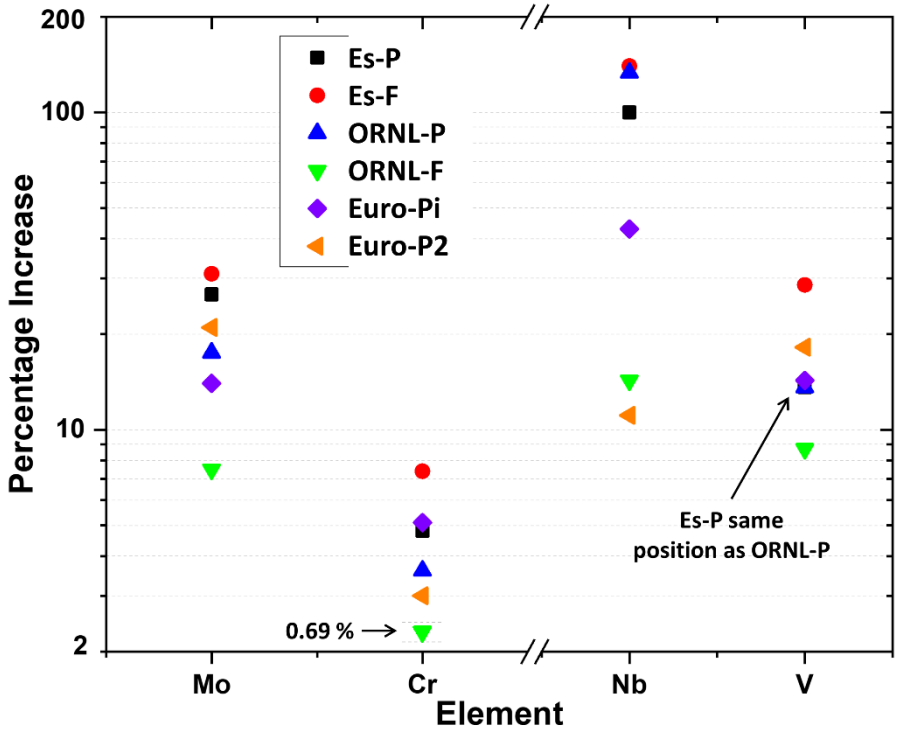

Figure 4.20: A graph showing the percentage increase from the lowest measurement made in the alloying elements Mo, Cr, Nb and V for all the steels in this project from SEM-EDS mapping from Table 4.2.

4.5 Comparisons of Equilibrium Partitioning Coefficients from the μ-XRF and SEM-EDS Composition Quantifications

Figure 4.21 shows a Scheil solidification calculation for a typical Gr. 91 steel composition performed using Thermo-Calc showing the elements Cr, Mo, Mn, Nb and V, in this case the ICP-OES/MS composition provided for steel Es-P was used as variations within Gr. 91 composition specification do not significantly affect the simulation. This example simulates how the partitioning of elements during the dendritic solidification of the steel from the melt influences the concentrations of some of the major alloying elements during the liquid to solid transformation based on their content and equilibrium partitioning coefficient (k_e). The k_e values based on this simulation can be calculated and are given as, 0.52, 0.26, 0.5, 0.13 and 0.19 for the elements Cr, Mo, Mn, Nb and V, respectively. It should be noted, the Scheil simulation is used to provide an upper limit on the amount of segregation that can occur and allows the elements to be ranked in terms of expected amount of segregation. However, these figures do not consider the back diffusion of elements during post-solidification cooling, nor the effects of any thermo-mechanical processing beyond the initial casting. Furthermore, a constant k_e during the solidification simulation is assumed, however, in reality, the k_e values will change during the solidification process due to composition changes. Therefore, the values obtained here are expected to be lower (lower k_e means greater partitioning) than those obtained from literature [101] and from the experimental studies in this chapter through μ-XRF and SEM-EDS.

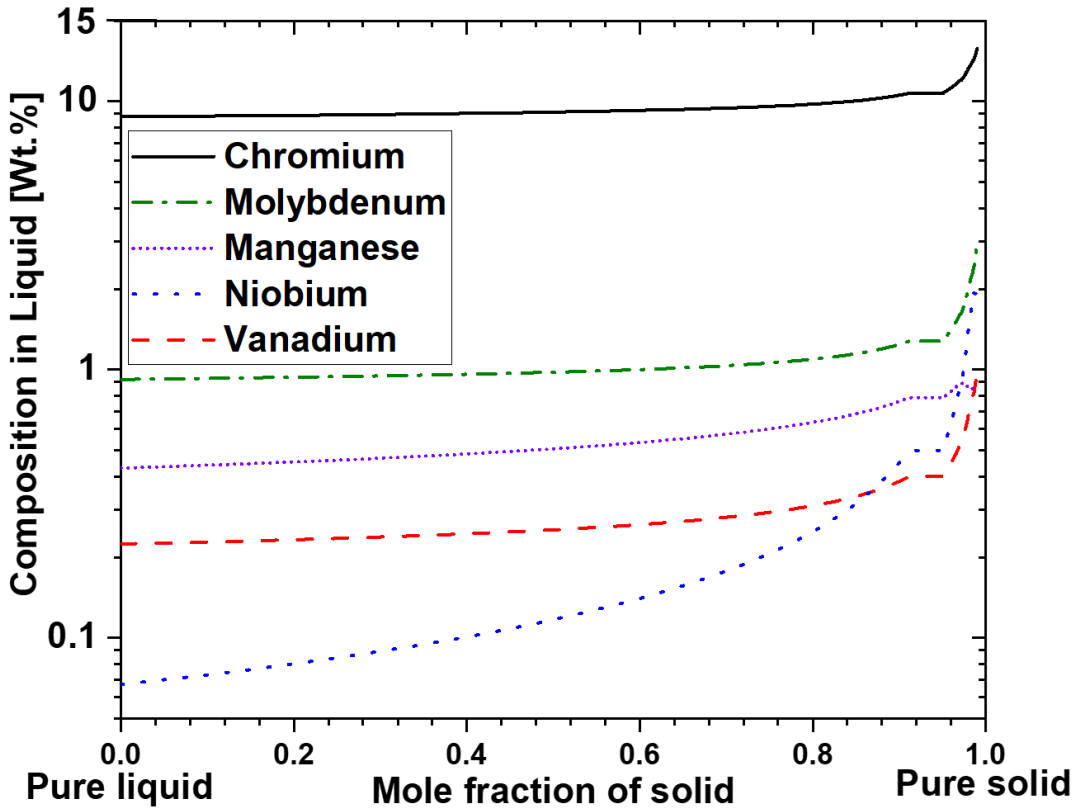

Figure 4.21: Thermo-Calc Scheil solidification simulation showing the change in concentration of the major alloying elements during dendritic solidification of a typical Gr. 91 steel composition (Es-P) (from ICP-OES/MS).

Figure 4.22 compares the k_e values found in the µ-XRF and SEM-EDS studies for the ex-service steels Es-P and Es-F against those found in the literature [39][101]. For both steels, there was good agreement between the ranking of the partitioning of elements with regards to the results found experimentally and those found in the literature (i.e., Nb largest partitioning and Cr the least). Cr was very consistent in both steels with the δ-ferrite values, this may have been due to the high content of Cr in these steels which increased the statistical accuracy of the data collected via the µ-XRF and SEM-EDS techniques. For Mo, there is good agreement between the δ-ferrite literature values and both the µ-XRF and SEM-EDS values, this was for both steels, Es-P and Es-F. With regards to Mn, the SEM-EDS values were not quantified, however, for both steels, a lower k_e for Mn was found experimentally through the µ-XRF than the literature reported values. This could be explained by the µ-XRF maps of Mn collected for Es-P and Es-F (*Figures 4.3c and 4.4c*, respectively), for Es-P spikes of Mn can be seen which may represent coarse Mn-rich inclusions which can also be seen as peaks in the µ-XRF linescans in *Figure 4.14c*. For steel Es-F it is a

similar reason, however *Figure 4.22* shows that Mn is not as significantly affected as in the case of Es-P, which may be due to the absence of coarse Mn-rich inclusions. For V, in both steels Es-P and Es-F the experimentally calculated k_e (µ-XRF and SEM-EDS) values are significantly greater than that of the k_e in austenite but less than that of in δ-ferrite, meaning that there could have been some back-diffusion of V during solidification of the steels. Lastly with regards to Nb, for Es-P both the µ-XRF and SEM-EDS techniques are largely consistent with the δ-ferrite k_e values. However, in Es-F the Nb does have a lower k_e in the µ-XRF than in the SEM-EDS, which could be due to the larger interaction volume of the µ-XRF, meaning there is more penetration so that compositional extremes can be found more effectively. When looking at the µ-XRF map of Nb for Es-F *(Figure 4.4d)*, highly enriched regions of Nb can be seen with spot-like features which may possibly represent coarse Nb-rich inclusions, similar to coarse Mn-rich inclusions in Es-P discussed earlier.

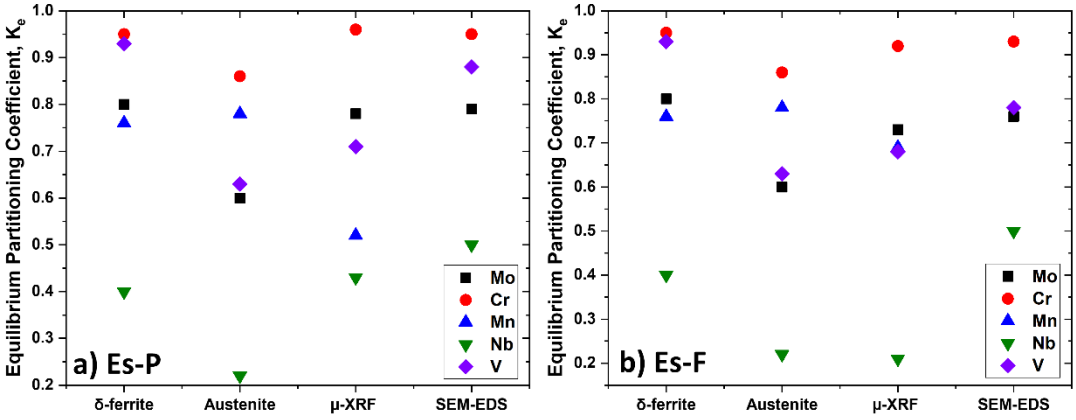

Figure 4.22: Comparison of the equilibrium partitioning coefficients acquired experimentally through µ-XRF and SEM-EDS compared with values found in literature (phase diagrams) for δ-ferrite and austenite [39][101] *for steels (a) Es-P and (b) Es-F.*

Figure 4.23 compares the k_e values found in the µ-XRF and SEM-EDS studies for the steels ORNL-P and ORNL-F against those found in the literature [101]. As for the ex-service steels, for ORNL-P and ORNL-F, there was an agreement between the ranking of the partitioning of elements with regards to the results found in the experiments and those from literature. The k_e values of Cr found experimentally (µ-XRF and SEM-EDS) were near those of the δ-ferrite k_e values, although they were slightly greater in both steels so less partitioning of Cr was found experimentally. There was also good agreement between the partitioning of Mo, from both experimental techniques for both

steels and the literature values of δ-ferrite. However, when comparing with steels Es-P and Es-F the experimental k_e values for steels ORNL-P and ORNL-F were considerably greater, meaning far less partitioning was calculated in Mo. For Mn, the experimental k_e (from the μ-XRF) values were marginally greater in both steels than those values found in the literature, signifying the likelihood of some back-diffusion. With regards to V, for steel ORNL-P (*Figure 4.23a*) both experimental values were near that of δ-ferrite, which was closer to 1, the same was found in steel ORNL-F *(Figure 4.23b)* however, a discrepancy between techniques was found in which the μ-XRF showed a lower k_e than the SEM-EDS. The Nb k_e value in both steels was consistent in the μ-XRF and was greater than both literature values, however in the SEM-EDS the partitioning was calculated to be greater in steel ORNL-P but far less in steel ORNL-F compared to the consistent value found in the μ-XRF. For the SEM-EDS partitioning in steel ORNL-F, all the elements are very closely spaced and close to 1 (0.85 - 1), whereas in the μ-XRF the same order is found with a much wider spread (0.55 - 1). This trend was also consistent with steels Es-P and Es-F but not to the same extent. Therefore, the greater partitioning of Nb for steel ORNL-P found in the SEM-EDS must be due to the detection of an abnormally high positively segregated regions.

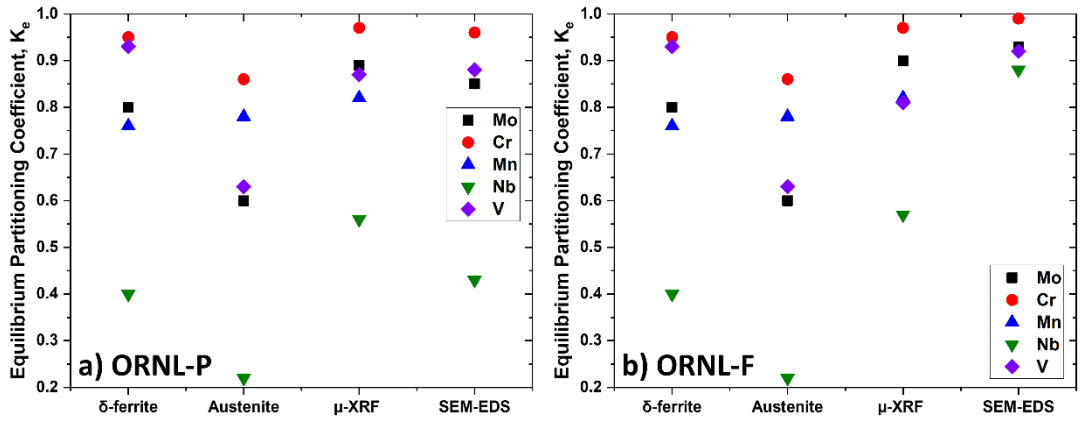

Figure 4.23: Comparison of the equilibrium partitioning coefficients acquired experimentally through μ-XRF and SEM-EDS compared with values found in literature (phase diagrams) for δ-ferrite and austenite [39][101] *for steels (a) ORNL-P and (b) ORNL-F.*

Figure 4.24 compares the k_e values found in the μ-XRF and SEM-EDS studies for the steels Euro-Pi and Euro-P2 against those found in the literature [101]. Like the previous steels already studied, there was largely a good agreement between the ranking of partitioning found experimentally and in literature. However, there was an

exception for Nb in steel Euro-Pi *(Figure 4.24a)*, the SEM-EDS k_e value was greater than the V and Mo values, which is the opposite to the literature. This could suggest in the SEM-EDS a representative positively segregated region was not found, the remaining experimental values for Nb in both steels showed the same trend as the other steels in this project. The k_e values of Cr found experimentally (µ-XRF and SEM-EDS) were consistent with the δ-ferrite k_e values, for both steels. With regards to Mo, the average k_e values in both Euro-Pi and Euro-P2 were greater than those found in the ex-service steels Es-P and Es-F, with little variation between the respective µ-XRF and SEM-EDS k_e values. It should be noted in Euro-Pi *(Figure 4.24a)* the Mo k_e value calculated through the µ-XRF was greater than the Mn, V and Nb, which would mean it is abnormally homogenous compared to the other elements and steels. For Mn, in both steels the partitioning was slightly less in the experimental µ-XRF compared to the literature values, this trend was the same for V in both steels, the experimental k_e values were greater than the austenite literature value but lower than the δ-ferrite k_e value.

When comparing the 6 steels, there are clearly 2 categories, the ex-service steels (Es-P and Es-F) and the remaining 4 non-service steels. For ex-service steels Es-P and Es-F, the experimental k_e values for Cr were marginally lower than those for the remaining steels, this was also true for V. With regards to Mn, Mo and Nb, a clear difference was seen between the 2 categories of steels. Steels Es-P and Es-F had considerably lower experimental k_e values for these 3 elements compared to steels ORNL-P, ORNL-F, Euro-Pi and Euro-P2. This means a greater degree of micro-segregation was found in the ex-service steels, as compared to the non-service steels.

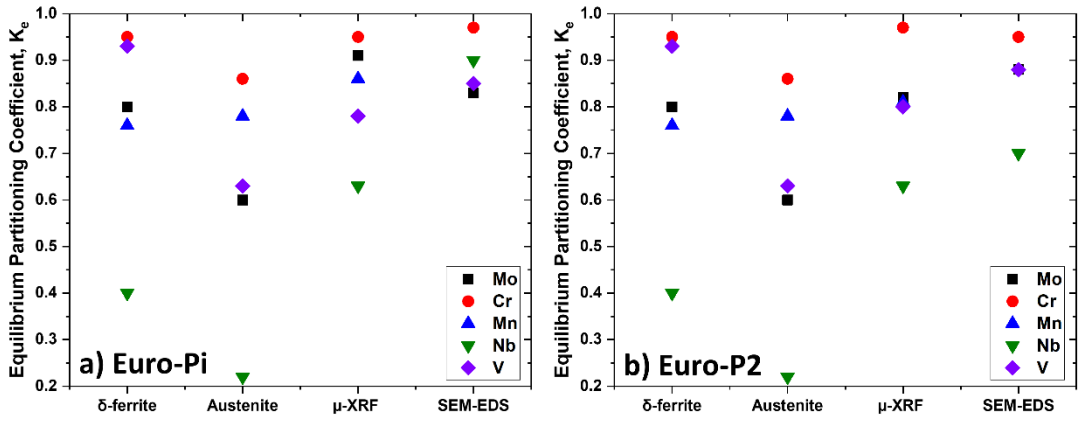

Figure 4.24: Comparison of the equilibrium partitioning coefficients acquired experimentally through µ-XRF and SEM-EDS compared with values found in

literature (phase diagrams) for δ-ferrite and austenite [39][101] *for steels (a) Euro-Pi and (b) Euro-P2.*

4.6 SIMS Analysis on the Ex-service Steels

SIMS maps were collected from steels Es-P and Es-F. These 2 steels were selected based on their micro-segregation characteristics in which they consistently ranked with the highest amount of solute enrichment amongst all the steels for both μ-XRF and SEM-EDS chemical mapping techniques. Furthermore, the tramp element content in steel Es-P is the highest of all the 6 samples examined, possessing an MJ-F of 345 with a notably large amount of Cu (0.19 wt %). Steel Es-F possessed a MJ-F of 159 and a Cu content amounting to 0.05 wt % and was chosen as it had the greater level of micro-segregation of the two forged samples available in this project. The large, localised regions (of ~1 mm) of positive segregation (solute rich) of major alloying elements also make it significantly easier to analyse areas of compositional extremes defined using μ-XRF.

Figure 4.25 shows the traces from SIMS for various elements in steel Es-P. It is clear in analysis (Cr, Nb, Mo, V, Mn) that there is evidence for similar trends, as areas of positive segregation are consistently higher than areas of negative segregation. Regions of positive and negative micro-segregation were located through specific locations determined through the μ-XRF and SEM-EDS maps shown in *Sections 4.2 and 4.4*. With regards to the tramp elements, *Figure 4.25d* shows the traces for S, Cu, and Pb. Only Cu shows a distinct increase in the positive regions in comparison to the negative regions for steel Es-P, which contains 0.19 wt % Cu. Steel Es-F which in comparison contains 0.05 wt % Cu but did not show any variation *(Figure 4.26)*. In *Figure 4.26* the signal from selected elements from positively and negatively segregated areas are shown for Es-F. The key major alloying elements (Cr, Nb, Mo, V, Mn) show a consistently higher signal in the positively segregated areas compared with the negatively segregated areas. The largest difference is in the heavy elements Mo and Nb in *Figure 4.26b,* this agrees well with the partitioning coefficients studied in *Section 4.5* for steel Es-F.

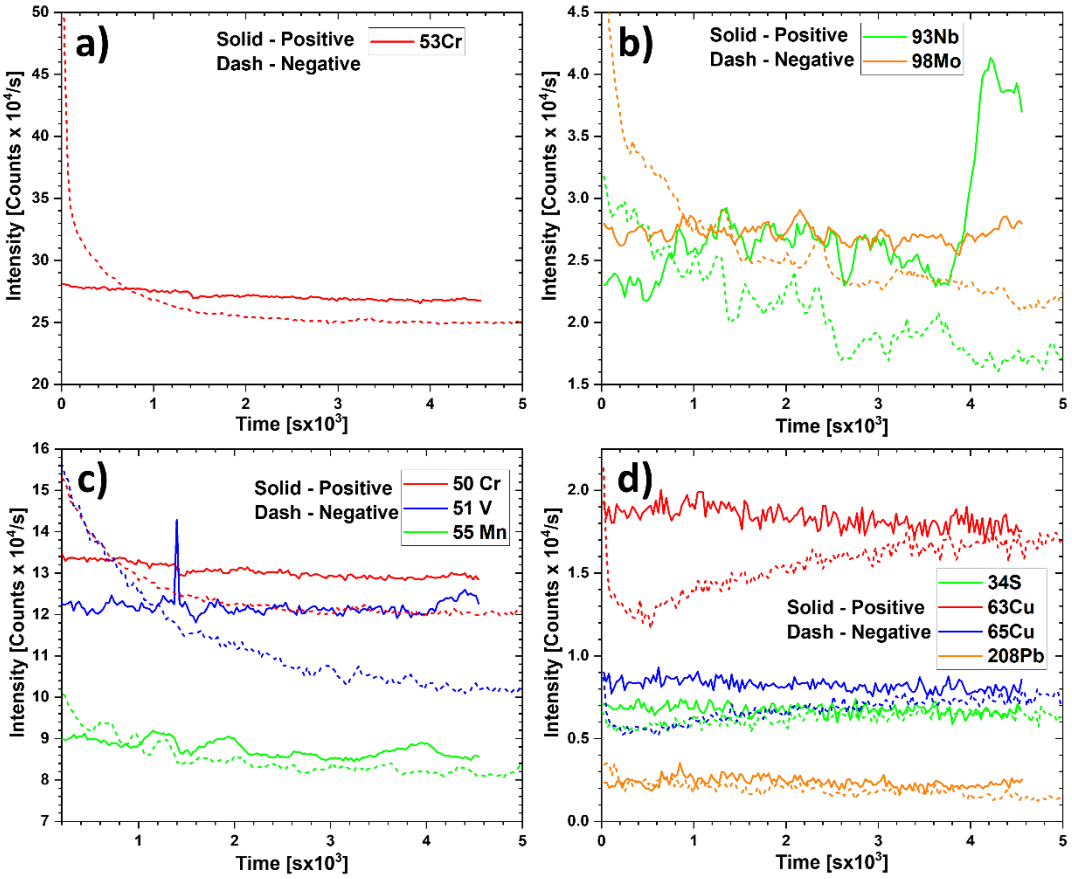

Figure 4.25: SIMS linescans showing traces of Cr, Nb, Mo, V, Mn, S, Cu and Pb isotopes for steel Es-P.

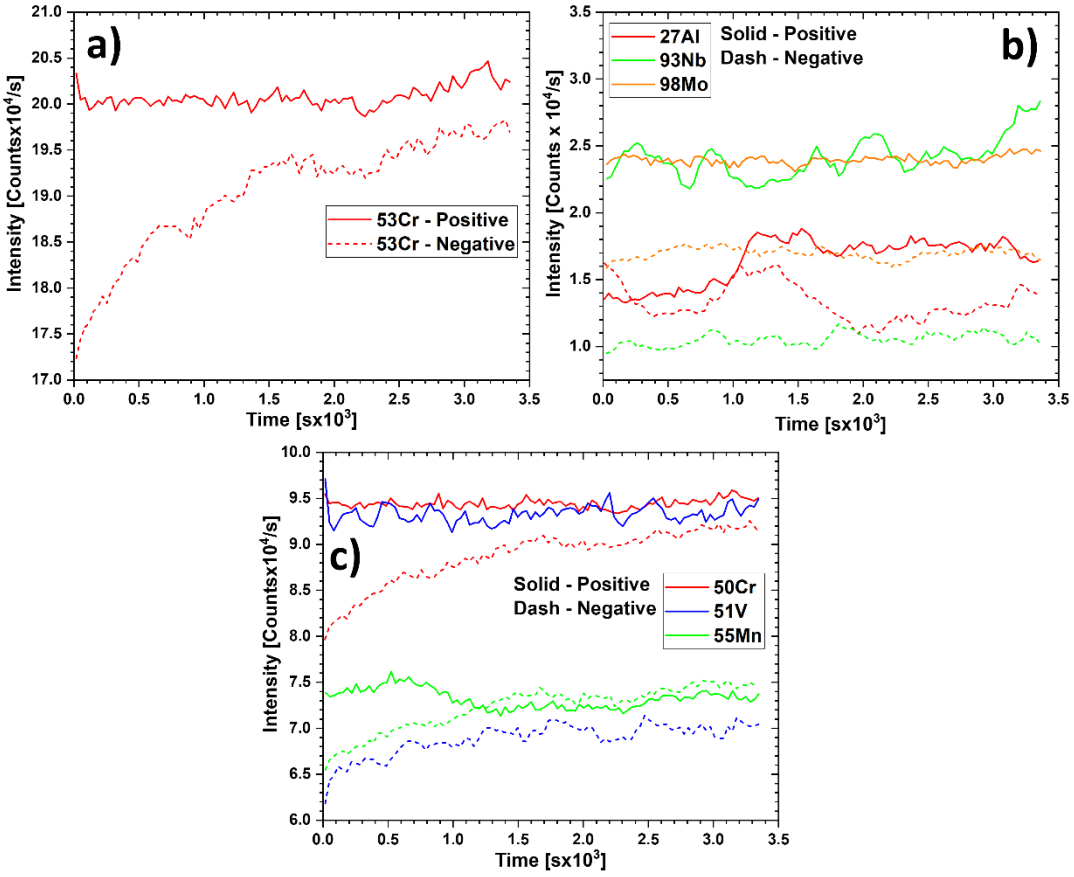

Figure 4.26: SIMS linescans showing traces of Cr, Nb, Mo, V, Mn, Al isotopes for steel Es-F.

4.7 Summary

Two experimental techniques (μ-XRF and SEM-EDS) were used to quantify the level of micro-segregation in the range of Gr. 91 steels for the major alloying elements. These techniques together enabled the micro-segregation in all the samples to be clearly defined. SEM-EDS was used for more site-specific chemical analysis with the benefit of a greater spatial resolution and better light element quantification compared with μ-XRF and consequently these values will be used in subsequent analysis. The SIMS analysis was complementary to the μ-XRF and SEM-EDS with regards to defining the micro-segregation, although, it was also beneficial in detecting the enrichment of Cu in steel Es-P.

The ex-service steels Es-P and Es-F were shown to have the greatest degree of micro-segregation. This was followed by the ORNL-P steel and then the two Euro steels, and finally the ORNL-F steel with the least degree of micro-segregation. All of the steels were thought to have had ESR processing due to their impurity levels and critical

nature in terms of their application where quality control of the component is of upmost importance. The ORNL steels also provided a guide in terms of the chemical composition since they were known to have had ESR processing performed [13]. In steel Es-P, chemical banding of 50-100 µm in width was found with up to 200 µm in spacing, these bands were up to 3 mm in length. In steel Es-F non-strain oriented localised regions of enrichment were found which are typically 0.2-1 mm in width and length. Steel Euro-P2 had the finest banding (20 µm), followed by ORNL-P (50-100 µm) and Euro-Pi (150-200 µm). Steel ORNL-F showed a forged chemical structure similar to that of Es-F, with a larger interconnected chemical distribution in the size range of 1-2 mm in width and length. For all steels a good agreement was found between the experimental and literature values for the k_e rankings of the key elements. A summary table (*Table 4.3*) is provided which compares the key micro-segregation characteristics, such as the dimensions and maximum and minimum composition measured.

Micro-segregation is a feature of the steelmaking process and is often difficult to eliminate through conventional thermo-mechanical heat treatments. The implications of this on the microstructure and therefore creep performance is not widely recognised amongst the CSEF steel community. *Chapters 5 and 6* will aim to build on the micro-segregation characteristics found in this chapter and quantify microstructural features in the steels based on the possible area to area variations.

Table 4.3: Summary table of the micro-segregation characteristics in each of the steels, including micro-segregation measurements and maximum and minimum compositions from µ-XRF and SEM-EDS in wt %.

Steel	Micro-segregation Structure [µm]			Element	Max. µ-XRF	Min. µ-XRF	Max. EDS	Min. EDS
	Width	Length	Spacing					
Es-P	50 to 100	3000	200	Mo	0.93	0.73	1.09	0.86
				Cr	9.28	8.89	8.99	8.58
				Mn	0.27	0.14	--	--
				Nb	0.07	0.03	0.10	0.08
				V	0.17	0.12	0.25	0.23
Es-F	200-1000		1500	Mo	1.02	0.74	1.10	0.84
				Cr	9.06	8.31	8.61	8.02

				Mn	0.26	0.18	--	--
				Nb	0.14	0.03	0.10	0.05
				V	0.19	0.13	0.27	0.21
ORNL-P	50 to 100	2000	300	Mo	0.99	0.88	1.14	0.97
				Cr	8.48	8.20	8.27	7.98
				Mn	0.26	0.20	--	--
				Nb	0.09	0.05	0.14	0.06
				V	0.15	0.13	0.25	0.22
ORNL-F	1000-2000		500	Mo	0.91	0.82	1.00	0.93
				Cr	9.28	9.00	8.74	8.68
				Mn	0.33	0.27	--	--
				Nb	0.07	0.04	0.08	0.07
				V	0.16	0.13	0.25	0.23
Euro-Pi	150 to 200	1800	250	Mo	1.02	0.93	1.21	1.00
				Cr	8.97	8.58	8.54	8.29
				Mn	0.35	0.30	--	--
				Nb	0.08	0.05	0.10	0.09
				V	0.14	0.11	0.26	0.22
Euro-P2	20	1200	100	Mo	1.05	0.87	1.14	1.00
				Cr	8.75	8.47	8.71	8.29
				Mn	0.31	0.25	--	--
				Nb	0.08	0.05	0.10	0.07
				V	0.15	0.12	0.24	0.21

Chapter 5 : The Effects of Micro-segregation on Microstructural Parameters

5.1 Introduction

The previous chapter provided an in-depth study into micro-segregation for a range of Gr. 91 steels, starting from macro-scale analysis (μ-XRF) down to micron level (SEM-EDS), but the implications have yet to be systematically researched for Gr. 91 and other CSEF steels. It is particularly important to link the micro-segregation levels to large area, relevant microstructural quantification since many studies continue to rely on 'basic' methods for investigating complex martensitic microstructures. Although, recently, a few studies have attempted to link segregation to properties such as creep life [40] in Gr. 91 steels, these have not been clear systematic approaches. In this chapter the effect of micro-segregation on hardness and the number and size of second phase particles (e.g., Laves, $M_{23}C_6$ and MX) is presented. The μ-XRF and SEM-EDS shown in the previous chapter allowed targeted local analysis of defined regions of interest.

5.2 Hardness Testing of the Grade 91 Steels

An initial assessment of the average Vickers micro-hardness was made using a 10 x 10 grid of indents at a load of 200 g for each of the steels *(Figure 5.1)* in the head section. A total of 100 indents were made per sample and covered a square millimetre of material (with a spacing of 100 μm between indents). *Figure 5.2* shows indentation maps collected from random areas within the head section from each of the steel samples. No systematic variation across the analysis area was observed in any of the samples. *Figure 5.3* shows the average values with standard deviations as error bars for each of the steels. For all steels there is less than a 5% variation between the extreme and average values. Significant differences in hardness between the steels are also observed. Steel Es-P has a significantly lower hardness (by ~20 - 30 HV) than the other pipe samples (Euro-Pi, Euro-P2 and ORNL-P), and a similar difference exists between the forged samples Es-F and ORNL-F. These differences are likely to be due to the in-service softening that occurred in the two ex-service materials (prior to creep testing these had been exposed to 570 °C at 16.5 MPa for 79,000 hours). In addition, product form has a clear effect on hardness with the pipe steels consistently ~20 - 30

HV harder than the forged steels (when the effects of service exposure are accounted for).

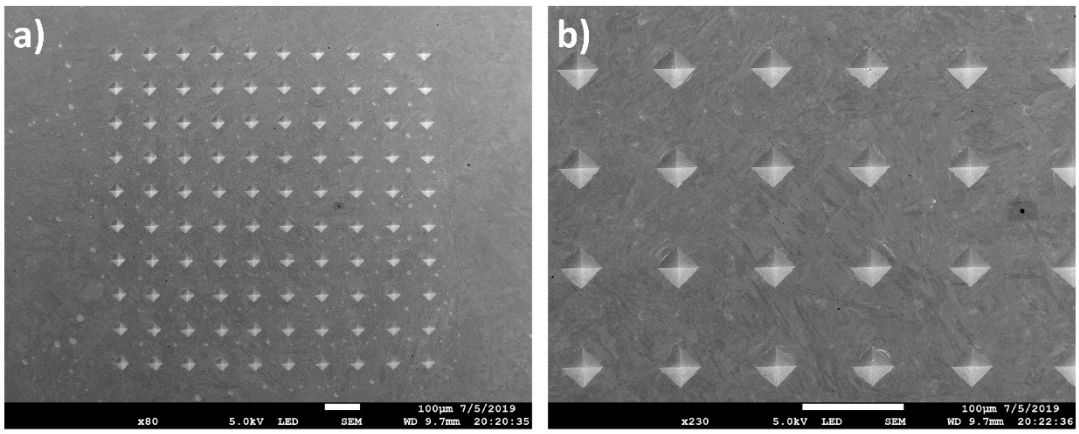

Figure 5.1: SEM images of a typical grid of 10 x 10 indents for obtaining the average Vickers micro-hardness in the head section of a Gr. 91 steel.

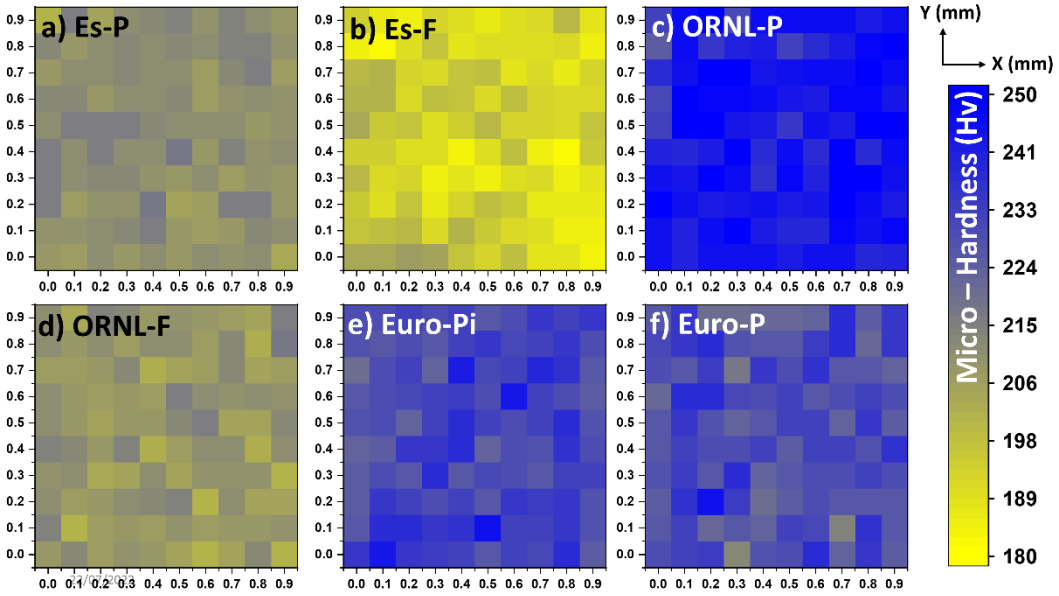

Figure 5.2: Plots showing the hardness of each indent in a 10 x 10 grid format for each of the 6 steels in this project (a) Es-P (b) Es-F(c) ORNL-P(d) ORNL-F (e) Euro-Pi (f) Euro-P2, a common scale bar is used for all 6 steels.

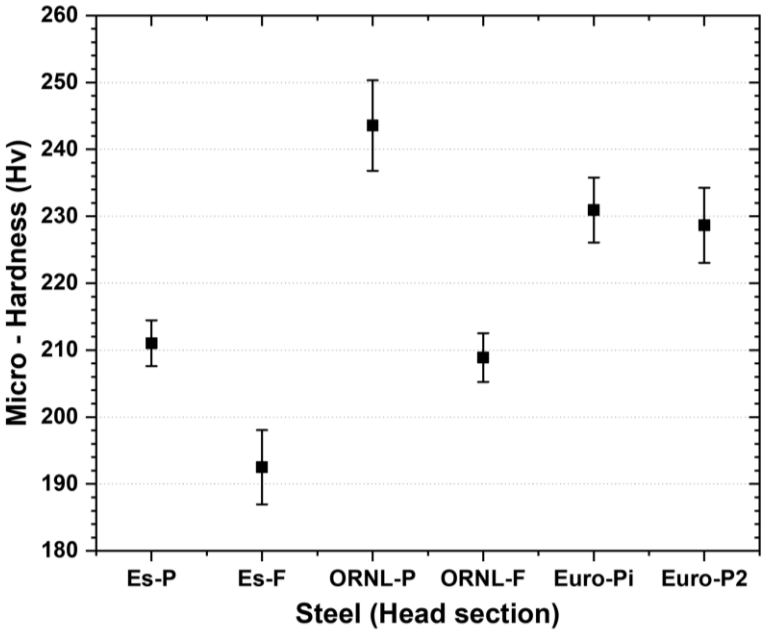

Figure 5.3: Graph showing the average hardness obtained for each of the 6 steels from the 10 x 10 grid of micro-hardness indentations.

In this section the effect of local composition caused by micro-segregation effects on micro-hardness will be investigated for both banded (Es-P) and non-strain oriented (Es-F) product forms. These steels were chosen because they exhibited the strongest micro-segregation of the materials available. *Figure 5.4a* shows a µ-XRF Cr map for steel Es-P, with a line scan (50 pixels / 1 mm) of interest expanded in *Figure 5.4b*; this region contained some clear positive Cr micro-segregation. Cr was chosen as an element of interest because it was the highest content alloying element in the steel and provides considerable precipitation strengthening by the formation of $M_{23}C_6$ carbides. A micro-hardness map *(Figure 5.4c)* was performed in the same region as *Figure 5.4b*, in order to determine the effect of micro-segregation on local hardness. A tentative correlation between positive segregation and increased micro-hardness can be observed. The highest microhardness values (225 HV) are found in the areas corresponding to the positive micro-segregation band and are ~ 6.5% higher than the average values displayed in *Figures 5.2 and 5.3*.

The same experiment was conducted with steel Es-F, a µ-XRF Cr map was performed initially, and an area of interest where a line scan was performed (50 pixels / 1 mm) showing a region of positive Cr micro-segregation *(Figure 5.5a and 5.5b)*. An indentation array was again performed, and a very clear pattern emerged which mirrored the micro-segregation of Cr in the area of interest. Where there was Cr

enrichment, the micro-hardness went up to values of 220 HV. This is a substantial increase of almost 15% in comparison to the material averages shown in *Figures 5.2 and 5.3.* A greater increase in micro-hardness was found for steel Es-F as compared to steel Es-P (15% compared to ~ 6.5%), also Es-F showed a much clearer correlation between the Cr concentration and micro-hardness, which was due to the coarser micro-segregation in Es-F, and finer banding in Es-P. The micro-hardness indentations will sample more than just the positively segregated regions, which is more important in steel Es-P due to the 50 – 100 µm banding. Therefore, a finer indent spacing can be implemented for steel Es-P such as 50 – 75 µm, which can better distinguish the micro-segregation. However, a smaller indent size/loading (approx. 0.1 kgf) would be required to ensure adequate spacing between the indentations. In this work, for the purpose of consistency the same spacing and loads were used for the two steels. The use of nano-indentation can also improve the resolution of the hardness-mapping and can more effectively isolate the effects of the micro-segregation in each steel; this can be considered for future work.

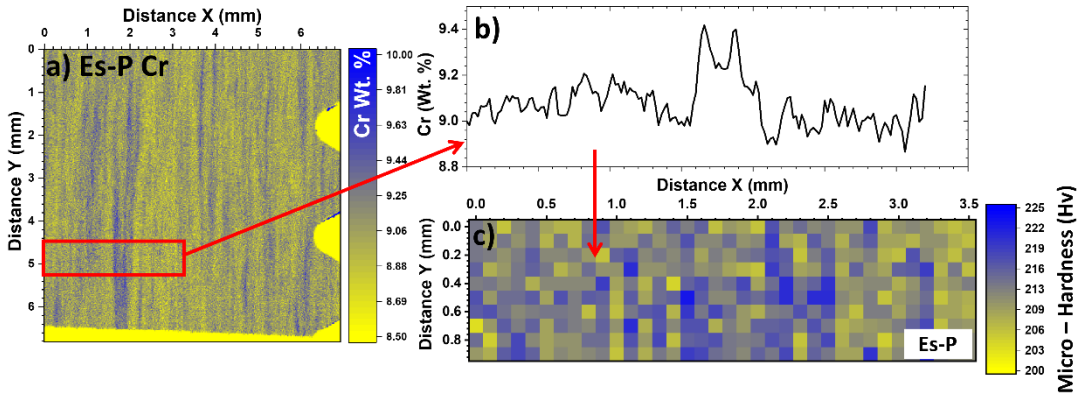

Figure 5.4: Diagram showing a) the µ-XRF map of Cr for steel Es-P with a Cr line scan from the indented section (b) and (c) Vickers micro-hardness indentation map of the same area from (b) Line scans were the same thickness as the red boxes in a) which was 50 pixels wide (1 mm).

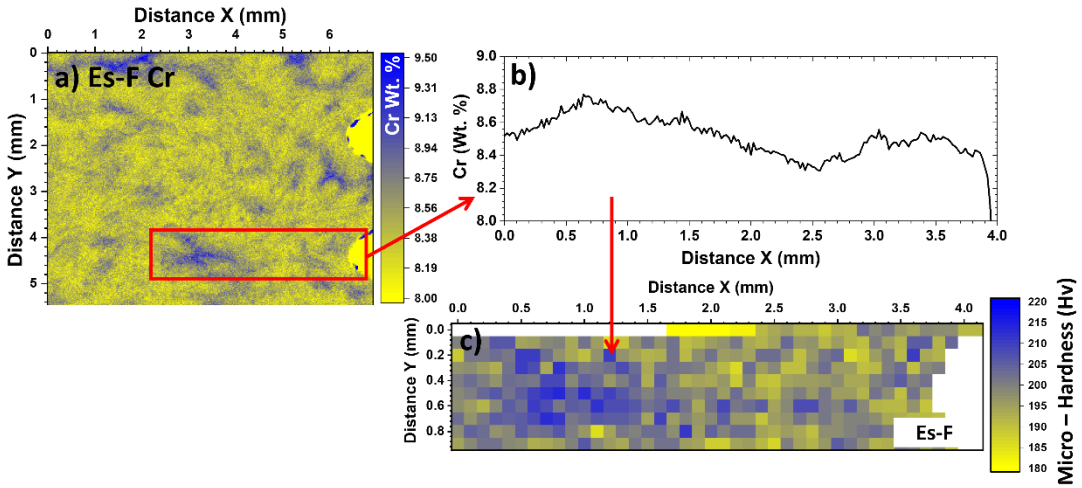

Figure 5.5: Diagram showing a) the µ-XRF map of Cr for steel Es-F with a Cr line scan from the indented section (b) and (c) Vickers micro-hardness indentation map of the same area from (b) Line scans were the same thickness as the red boxes in a) which was 50 pixels wide (1 mm).

Sawada et al. [41] concluded that the positive areas of Cr micro-segregation in a Gr.91 steel were greater in Vickers micro-hardness due to the extra $M_{23}C_6$ precipitation. Wang et al. also found similar results in a large cast of CB2 ferritic heat resistant steel; the hardness gradually increased from the edges to the centre of the cast structure due to macro-segregation, which was attributed to a greater amount of solute and formation of strengthening precipitates. Due to the larger scale of the macro-segregation, the hardness variations were much easier to detect [132]. It should be noted that the relationship between hardness and micro-segregation may be complex. This is because hardness depends on the characteristics of the second phase particle population, solid solution strengthening (e.g., from Mo) and grain size (including grain substructure) effects. The effects of micro-segregation on the second phase particle population will be studied in the remaining sections of this chapter.

5.3 Quantification of the Laves Phase using SEM-BSE Imaging

The intermetallic Laves phase precipitates in Gr. 91 and other CSEF steels at in-service temperatures, and is widely considered detrimental due to a loss of solid solution strengthening from W/Mo [12][204][205]. In this section the effect of segregation on the size and area fraction of Laves phase particles will be examined and compared with a standard sampling method often used in the literature for collecting quantitative Laves phase data. This is important as the effect of segregation

on Laves phase analysis has not been considered in any previous studies of 9Cr CSEF steels.

The detailed procedure for quantifying Laves phase is provided in *Section 3.4.2.1*, but in summary it consists of quantifying the Laves phase in 3 areas; i) a systematically collected random area (20 images), ii) in the positively segregated regions (5 images) and iii) the negatively segregated regions (5 images), using the SEM-EDS maps shown in *Figures 4.17-4.19*. An example of Laves phase particles in steel Es-P is shown in *Figure 5.6a*. The particles appear much brighter than the steel matrix, the other second phase which is visible in the image are the AlN precipitates, which appear as fine black particles; these will be analysed in *Section 6.6.* The energy dispersive spectra obtained from a typical Laves phase particle is shown in *Figure 5.6b*, which shows clear Si, Mo, Fe and Cr peaks. The former three elements are consistent with the composition of the Laves phase in Gr. 91 steels [65], and the presence of Cr can be explained by a combination of the interaction volume of the analysis exceeding the size of the particle to sample the significant amount of Cr in the steel matrix and possibly the attachment of $M_{23}C_6$ particles to the Laves phase particle. Quantification of the size distribution characteristics of the Laves phase particles was performed for all 6 of the steels in the head and gauge sections. The first step in the process was to identify regions of positive and negative micro-segregation, which are described in detail in *Chapter 4*. The micro-segregation was observed through the μ-XRF and SEM-EDS maps, images were taken immediately after the SEM-EDS maps were completed to ensure that the correct area was imaged. Low magnification BS SEM images, which show typical positively and negatively segregated regions for each of the steels are shown in *Figures 5.7-5.9*. It should be noted that these images were taken at x 2000 magnification with a HFW of ~ 60 μm for the purpose of a macro-scale visualisation, whereas the images used for quantification had a HFW of 20 μm in order to maintain over 100 pixels per μm as well as maintaining enough area to effectively image positively and negatively segregation regions of interest, such as that in *Figure 5.6a*. It is clear from all the images in *Figures 5.7-5.9* that there appears to be a greater number of Laves phase particles in the positive regions compared with the negative regions. It is also worth noting that steel ORNL-F has very few Laves phase particles, this could be due to the creep testing temperature, this sample was exposed to 649 °C,

which is the highest of the 6 steels in this project. This is discussed later in this chapter with regards to Thermo-Calc simulations in *Section 5.5*.

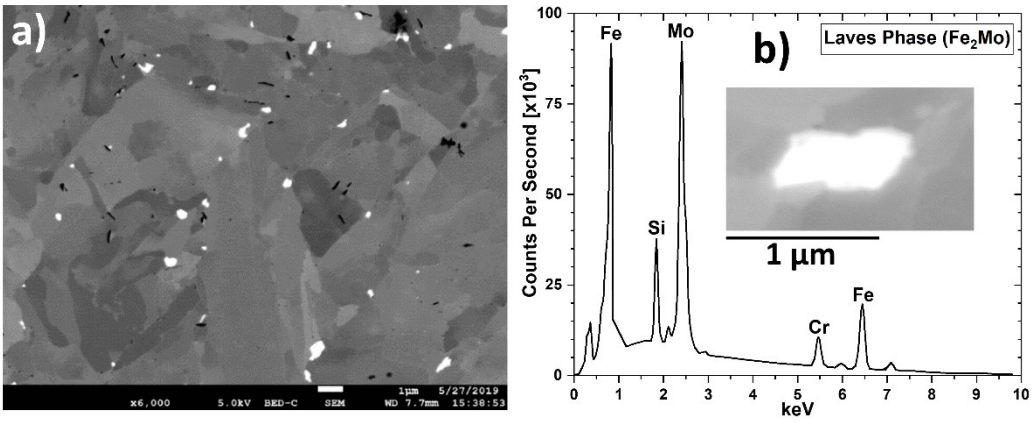

Figure 5.6: (a) SEM-BSE image of the steel Es-P's microstructure showing the Laves phase as bright features and (b) EDS spectra from the entire Laves phase particle with an accompanying SEM-BSE image of the Laves phase particle.

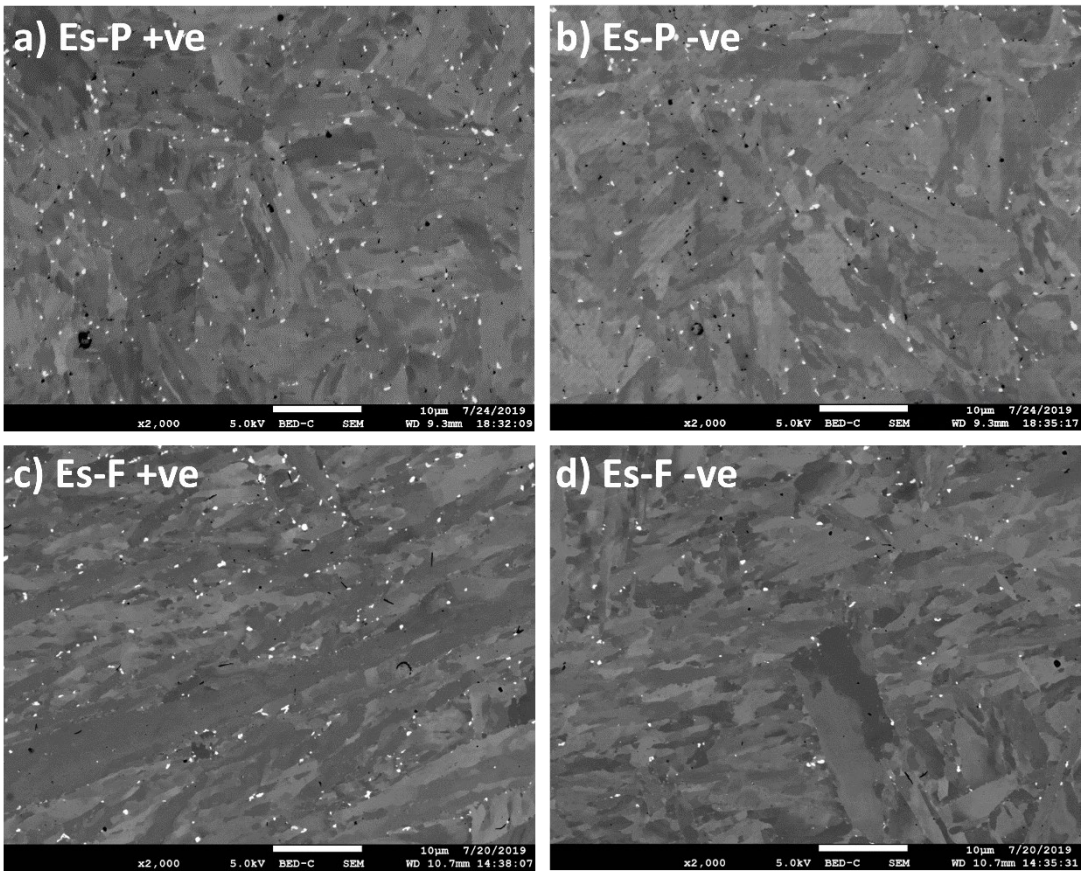

Figure 5.7: Macro-scale SEM-BSE images in (a) Es-P positively segregated region (b) Es-P negatively segregated region (c) Es-F positively segregated regions and d) Es-F negatively segregated region.

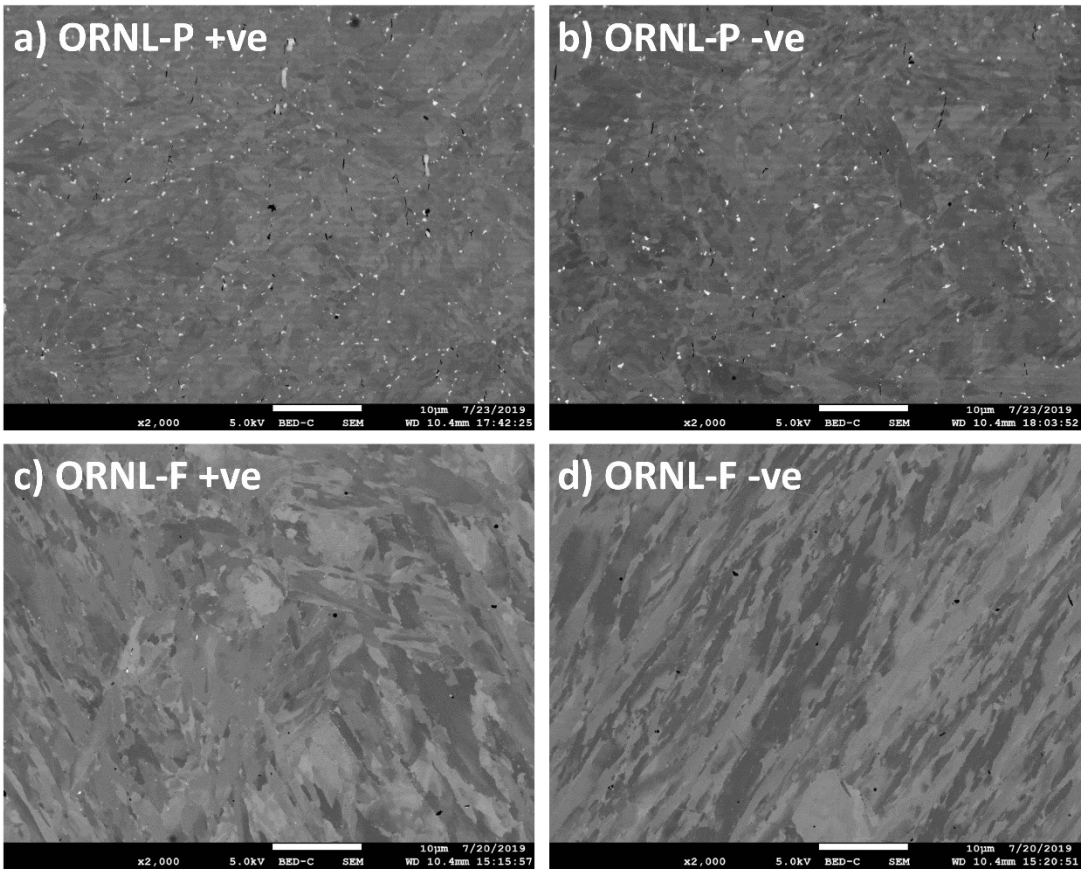

Figure 5.8: Macro-scale SEM-BSE images in (a) ORNL-P positively segregated region (b) ORNL-P negatively segregated region (c) ORNL-F positively segregated regions and (d) ORNL-F negatively segregated region.

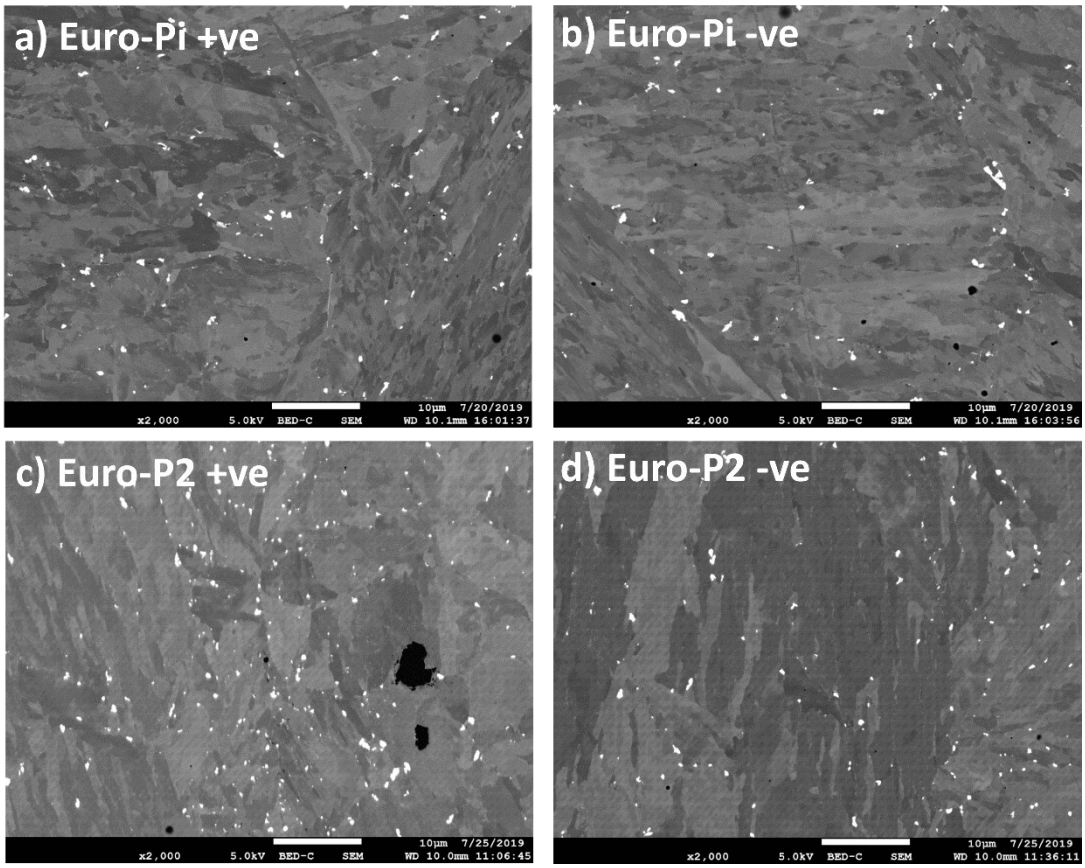

Figure 5.9: Macro-scale SEM-BSE images in (a) Euro-Pi positively segregated region (b) Euro-Pi negatively segregated region (c) Euro-P2 positively segregated regions and (d) Euro-P2 negatively segregated region.

The overlaid size distributions are shown in *Figures 5.10-5.15* for each of the 6 steels, Es-P, Es-F, ORNL-P, ORNL-F, Euro-Pi and Euro-P2, respectively. For steels Es-P and Es-F, the size distributions *(Figures 5.10* and *5.11)* are very similar in the head and gauge sections, this signifies a very similar average size due to the similar shape of the curves in both head and gauge. Furthermore, in the positively segregated regions in both steels (for both head and gauge), the positively segregated regions consistently contain a greater amount of the Laves phase than the negatively segregated and SCRA regions, although the shape of size distribution graphs appear similar. This is important because this clearly shows that local increases of Mo result in increased nucleation of Laves phase particles but not an increased growth rate. For steel Es-F, which has a large spatial segregation structure, the positively segregated region is more well defined in the size distribution *(Figure 5.11)* due to a combination of the ease of locating the (large) positively segregated regions as well as steel Es-F ranking high amongst the steels with regards to the degree of micro-segregation, as defined in *Chapter 4.*

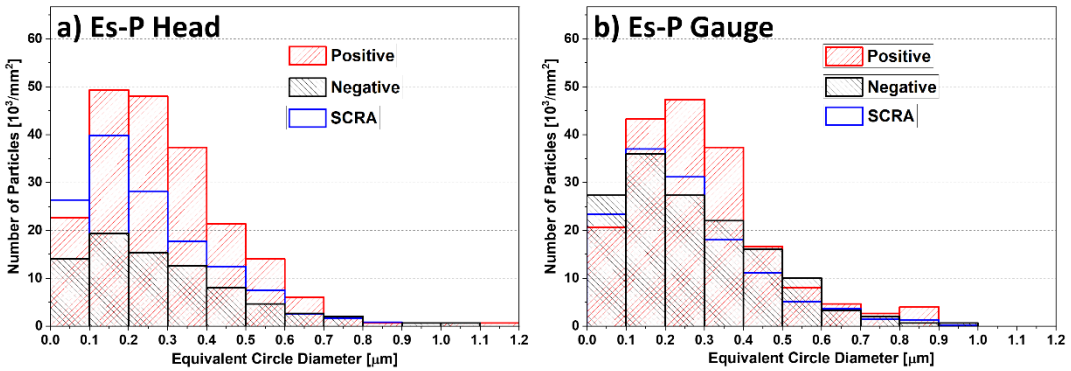

Figure 5.10: Size distributions for the Laves phase found in the steel Es-P (a) head section and (b) gauge section, with regards to the systematically collected random areas and positively and negatively segregated regions.

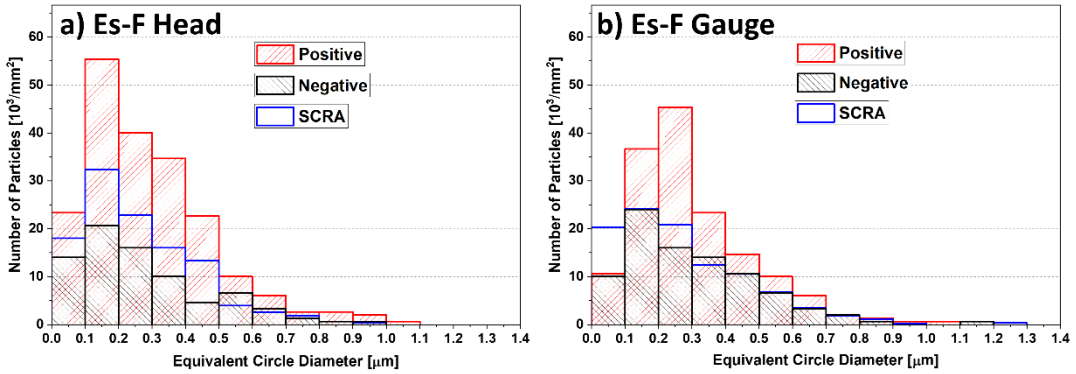

Figure 5.11: Size distributions for the Laves phase found in the steel Es-F (a) head section and (b) gauge section, with regards to the systematically collected random areas and positively and negatively segregated regions.

For steel ORNL-P *(Figure 5.12)* the size distribution and range of the Laves phase was found to be very similar to that of steels Es-P and Es-F. However, for steel ORNL-P the negatively segregated and SCRA regions are very similar in both the head and gauge, but the positively segregated region is much more pronounced in the head than in the gauge. The apparent reduced effect of segregation in the gauge section of the sample can be attributed to the large reduction in area (47.5%), which has made the segregation bands visually thinner *(Appendix B)*. In steel ORNL-F *(Figure 5.13)* there are far fewer Laves phase particles present in both the head and the gauge, as compared to steels Es-P, Es-F and ORNL-P. However, despite this, the same trend of increasing numbers of particles in the positively segregated compared with the negatively segregated areas is observed. In the gauge of the positively segregated region a significant increase in the number of small particles (i.e., particles < 0.1 μm) is

observed. This could be due to an increased nucleation of small Laves phase particles in this region.

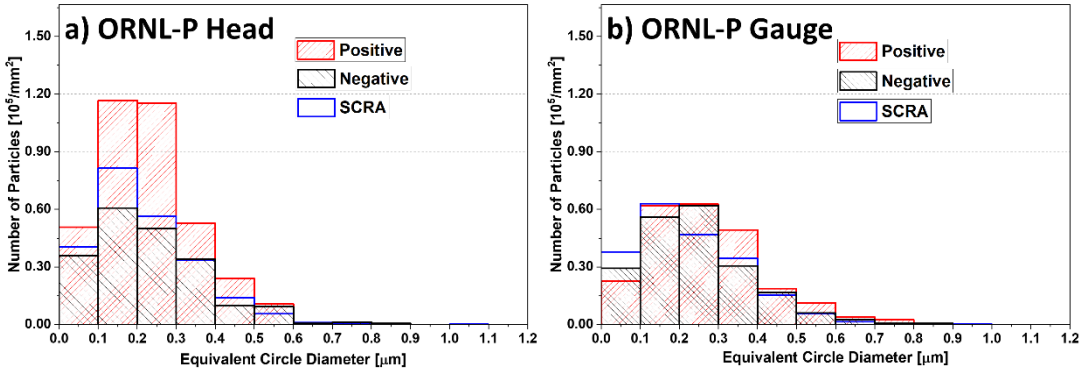

Figure 5.12: Size distributions for the Laves phase found in the steel ORNL-P (a) head section and (b) gauge section, with regards to the systematically collected random areas and positively and negatively segregated regions.

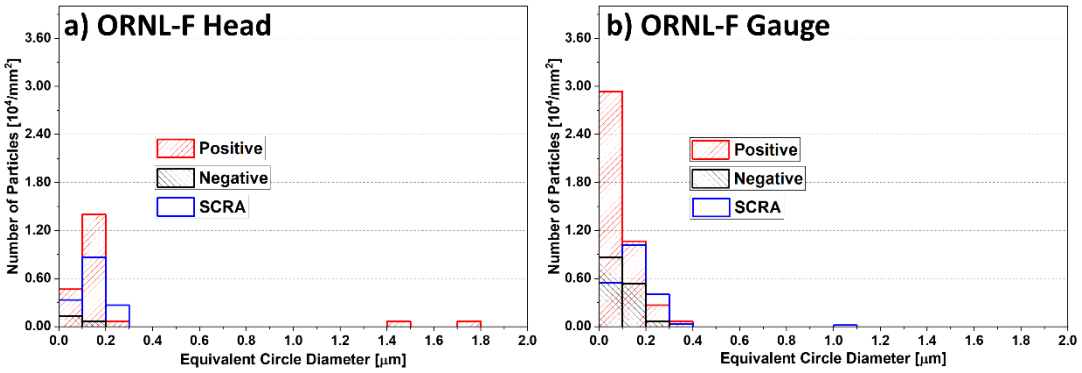

Figure 5.13: Size distributions for the Laves phase found in the steel ORNL-F (a) head section and (b) gauge section, with regards to the systematically collected random areas and positively and negatively segregated regions.

In steel Euro-Pi the size distributions of the Laves phase particles *(Figure 5.14)* show a distinct difference between the head and the gauge regions. The size range and distributions of the Laves phase particles are very similar to those found in the ex-service steels Es-P and Es-F. For steel Euro-P2 *(Figure 5.15),* the micro-segregation was very well defined (see Chapter *4),* in which the micro-segregation banding was very fine ~20 µm in width. This can be clearly seen in *Figure 5.9c*, where the Mo-rich Laves phase is clearly segregated along a thin band. This is reflected in the size distributions of the Laves phase particles, as the imaging was roughly ~20 µm in HFW. The positively segregated regions in both the head and gauge are distinctly greater than the negatively segregated and SCRA regions. Like steel Euro-Pi, the size ranges

of the Laves phase in Euro-P2 are also very similar to the ex-service steels Es-P and Es-F.

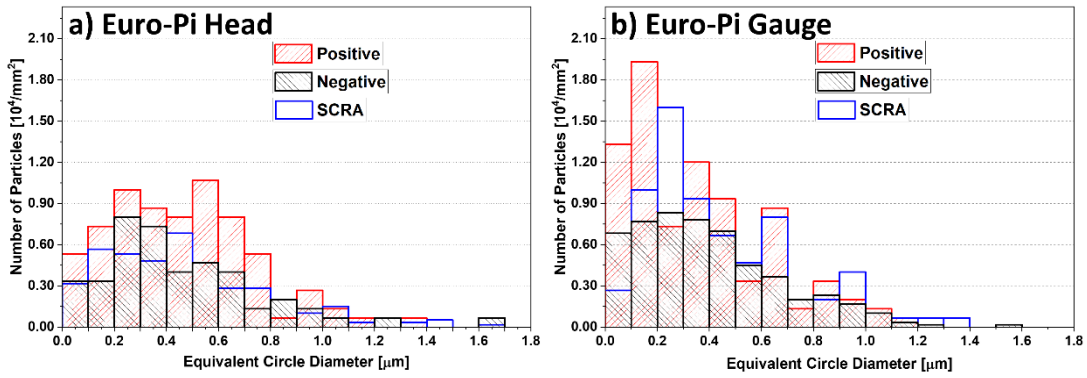

Figure 5.14: Size distributions for the Laves phase found in the steel Euro-Pi (a) head section and (b) gauge section, with regards to the systematically collected random areas and positively and negatively segregated regions.

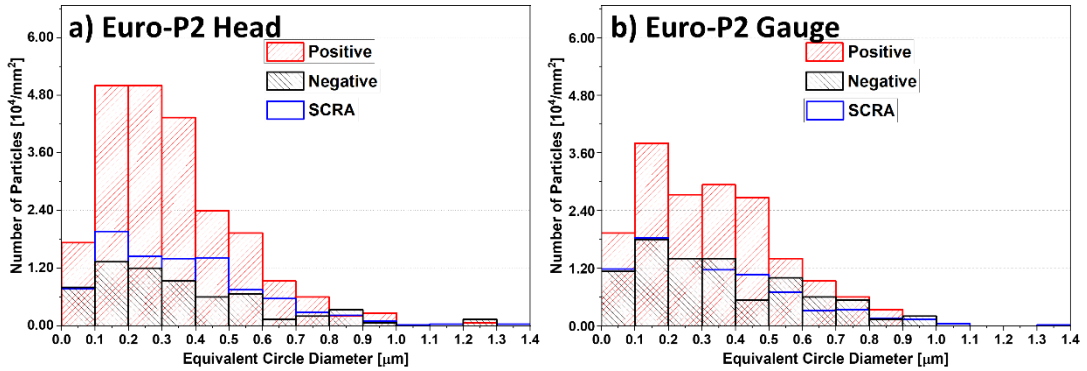

Figure 5.15: Size distributions for the Laves phase found in the steel Euro-P2 (a) head section and (b) gauge section, with regards to the systematically collected random areas and positively and negatively segregated regions.

The statistics from the size distribution graphs such as the average sizes, area coverages and number of particles are summarised in *Figures 5.16 to 5.18*. The average equivalent circle diameter (ECD) is shown in *Figure 5.16*, for steels Es-P and Es-F the average sizes are consistent amongst the head and gauge sections due to the same service exposure. For the non-service exposed steels ORNL-P, ORNL-F and Euro-P2 there is little variation between average sizes in the SCRA regions, except for in steel Euro-Pi in which the Laves phase particles were larger than in the gauge section. This may have been due to the randomised sampling procedure detecting larger particles. The other anomaly is that steel ORNL-F had an increased average size in the positively segregated region. This could have been due to the large bright particles being NbC rather than Laves phases (the detection of isolated NbC particles

is only significant in this sample where the number of Laves phase particles is relatively low).

Overall, the average sizes of the Laves phase particles presented in *Figure 5.16* show no significant change between the head and gauge sections. In a study by Hofer et al. on a 12 wt % Cr steel, TEM and EFTEM apparatus were used to investigate the effects of stress on the Laves phase evolution. The authors found no significant difference between the average size of the Laves phase particles in the head and gauge sections of that creep specimen, similar to what is found in the current work. Furthermore, other studies also found that stress had no effect on the size distributions of the Laves phase particles [36][69]. Coarse Laves phase particles can significantly reduce grain boundary pinning [36] and have also been considered sites for the nucleation of creep cavities by some researchers [34][36].

When coarsening (or showing an increase in area coverage (*Figure 5,17)*), the inter-particle spacing for the Laves phase particles can decrease which can increase the Orowan stress, which is defined by the *Equation (2.2)* [60].

$$\sigma_{or} = 0.8MGb/\lambda \qquad \textit{Equation (2.2)}$$

Where, λ is the mean interparticle spacing. M (= 3) is defined as the Taylor factor, G is defined as the shear modulus, b is defined as the magnitude of the Burgers vector. This theory, however must be applied to all pinning particles not just one type; thus, the mean interparticle spacing may be dominated by the finer precipitate types in the steel matrix, such as V-rich MX carbo-nitrides which do not coarsen rapidly and are often found under the size of 50 nm in virgin CSEF steels [79]. The Laves phase particles in this study have reached near micron sizes and so their contribution to strengthening is likely to be small compared with that from the combined MX and $M_{23}C_6$ precipitates. Although, a critical size is not determined for optimal creep strengthening via precipitation, comparisons can be made between the various precipitate sizes.

Figure 5.17 which compares the Laves phase area coverages shows a consistent trend of the positively segregated region having a greater amount in both the head and gauge for all the steels, although this is more prominent and consistent in the service exposed steels Es-P and Es-F, which may be due to the prolonged service exposure compared

to the relatively shorter creep tests for the remaining steels. *Figure 5.18* which shows the number of particles per unit area; quite clearly there is significant difference in these figures, the positively segregated regions consistently have a greater number of Laves phase particles than the negatively segregated and SCRA's in both head and gauge sections for all steels, once again like the area coverages a similar trend is found between the service exposed and non-service exposed steels.

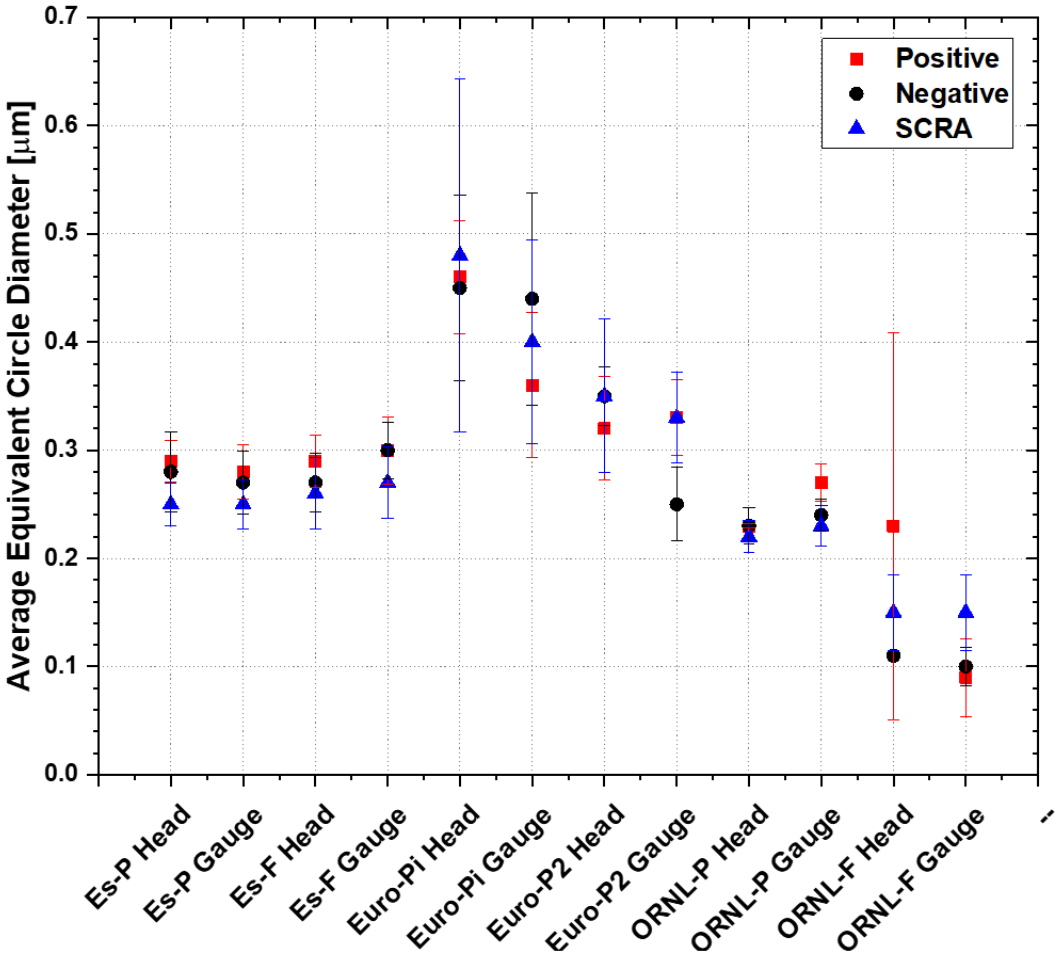

Figure 5.16: Graphs showing the average equivalent circle diameter of the Laves phase quantified in the 6 steels. With regards to the systematically collected random areas and positively and negatively segregated regions.

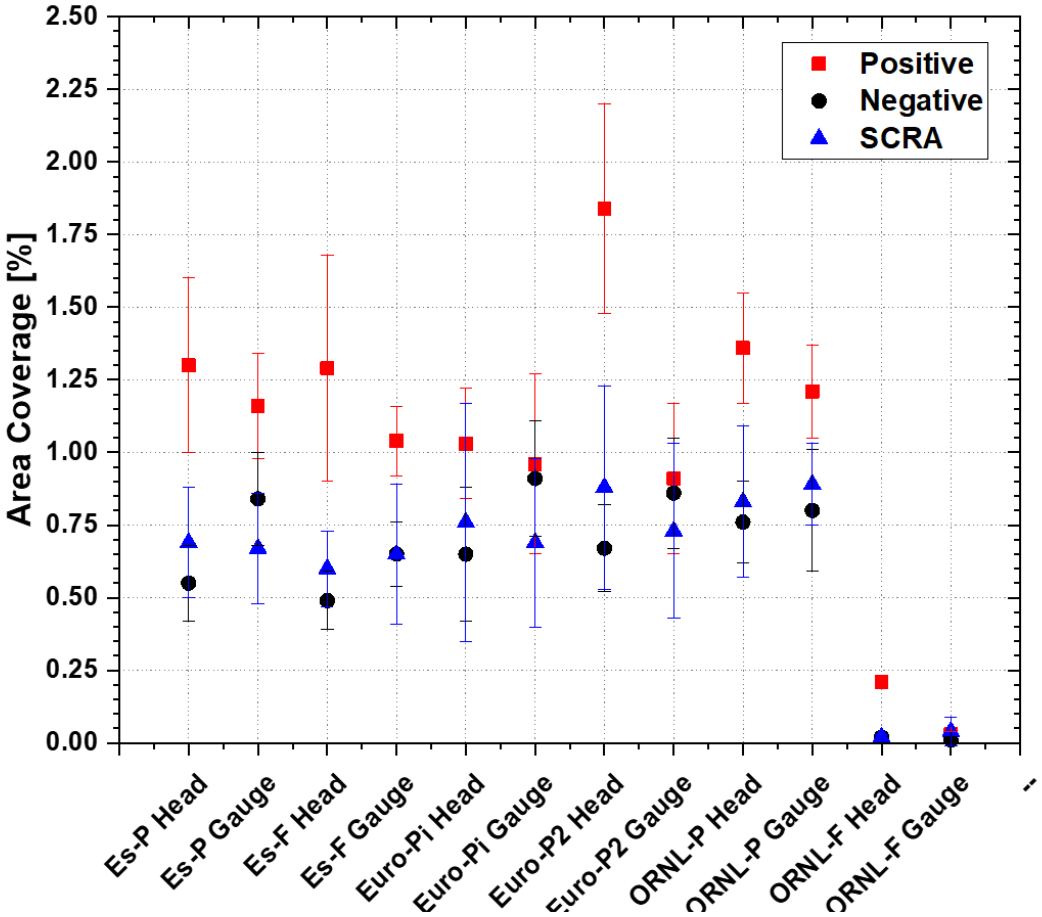

Figure 5.17: Graph showing the area coverage of the Laves phase quantified in the 6 steels. With regards to the systematically collected random areas and positively and negatively segregated regions.

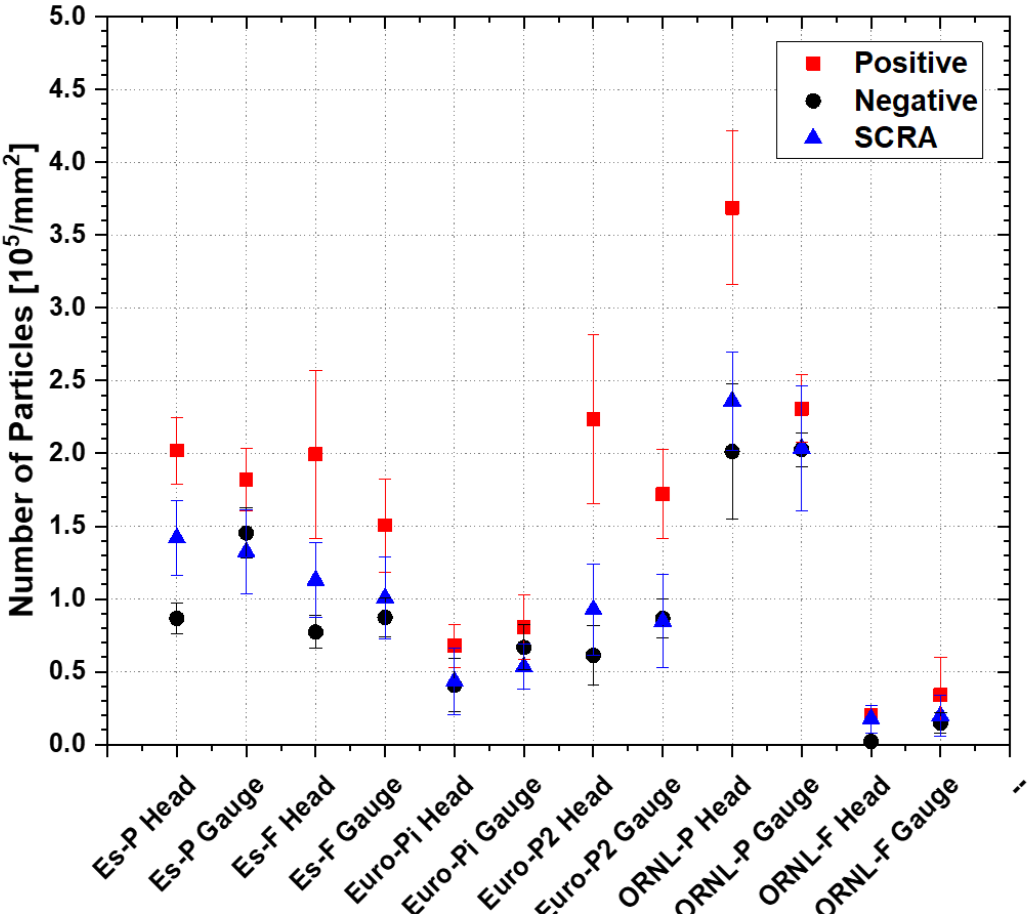

Figure 5.18: Graph showing the number density of particles of the Laves phase quantified in the 6 steels. With regards to the systematically collected random areas and positively and negatively segregated regions.

Figure 5.19 shows the area coverage of the Laves phase (from the head sections) of steels Es-P and Es-F with each area coverage plotted as an individual bar. The positively and negatively segregated regions can be easily distinguished in the form of their area coverages, more so in the forged steel Es-F due to the spatial scale of the micro-segregation. The data collected from SCRAs sit in between these extremes. For the Es-P steel, the data collected from SCRAs are at the mid-point between the extremes, whereas for Es-F they are located closer to the negatively segregated Mo point. This can be explained by the differences in the segregation characteristics of the samples, Es-F has non-strain oriented enriched Mo regions, whereas Es-P has a finer and much more ordered banded structure. For steels Es-P and Es-F Laves phase particle characteristics are very similar in the head and gauge sections, which can be seen in the size distributions (*Figures 5.10 and 5.11),* this is because the entire creep specimen was exposed to the same in-service exposure.

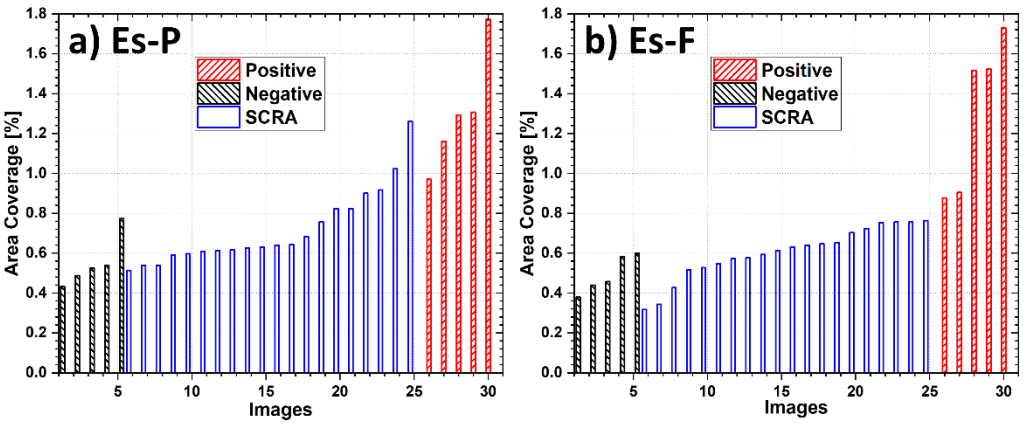

Figure 5.19: Bar charts showing the variation in area coverage of the Laves phase per image (from the head sections) in steels (a) Es-P and (b) Es-F. With regards to the systematically collected random areas and positively and negatively segregated regions.

5.4 Quantification of the $M_{23}C_6$ Carbides and MX Carbo-nitrides

The quantification of the $M_{23}C_6$ carbides and MX carbo-nitride population characteristics is widely studied in Gr. 91 and other CSEF steels [32][36][206]. These studies do not take into consideration the area-to-area variations due to micro-segregation, although recently Sawada et al. has published two papers which analyse the effects of segregation on Gr. 91 and 92 tubes, respectively [40][41]. However, in these studies a clear and systematic approach was not used, which leaves room for an improved site-specific method. The following section will explore this as well as attempting to overcome the difficulties in quantifying both the $M_{23}C_6$ carbides and MX carbo-nitride precipitates due to their overlapping size ranges. This will be done using both FIB-SEM ion beam imaging with XeF_2 gas as well as high resolution STEM chemical mapping in the TEM. Similarly, to *Section 5.2*, steels Es-P and Es-F are the focus of this study, as the magnitude of the micro-segregation is greatest for a pipe (Es-P) and forging (Es-F) in these steels.

5.4.1 Focused Ion Beam-based SEM $M_{23}C_6$ Quantification

The FIB-SEM procedure for the imaging of the $M_{23}C_6$ carbides is detailed in *Section 3.4.2.* In summary the procedure was similar to that detailed for quantifying the Laves phase in the previous section, with the main difference being locating the areas of positive and negative micro segregation, which were found using the Vickers micro-hardness indentions in the steel, *Figures 5.4 and 5.5*. Analysis was performed on head sections of steels Es-P and Es-F. Furthermore, the results for these 2 steel head sections

can be correlated with the hardness variations shown due to Cr micro-segregation in *Figures 5.4 and 5.5.* For example, in the micro-hardness indentation maps *Figures 5.4c and 5.5c,* for steels Es-P and Es-F respectively, the areas of blue and yellow corresponded to the positive and negative micro-segregation of Cr *(Figures 5.4b and 5.5b).* Therefore, the indentations were used to locate these specific areas, for example *Figure 5.20* shows SEM images of the micro-hardness indentations with small rectangular regions highlighted which show from where the FIB images were taken. In *Figure 5.20a* the cylinder in the left of the image is the nozzle for the XeF_2 gas, a valve was opened and closed for the application of the gas for when the FIB image was taken. Typical images for the quantification of the $M_{23}C_6$ carbides are shown in *Figure 5.21*, the carbides can be seen as dark particles in the steel matrix and can be readily quantified using image analysis techniques.

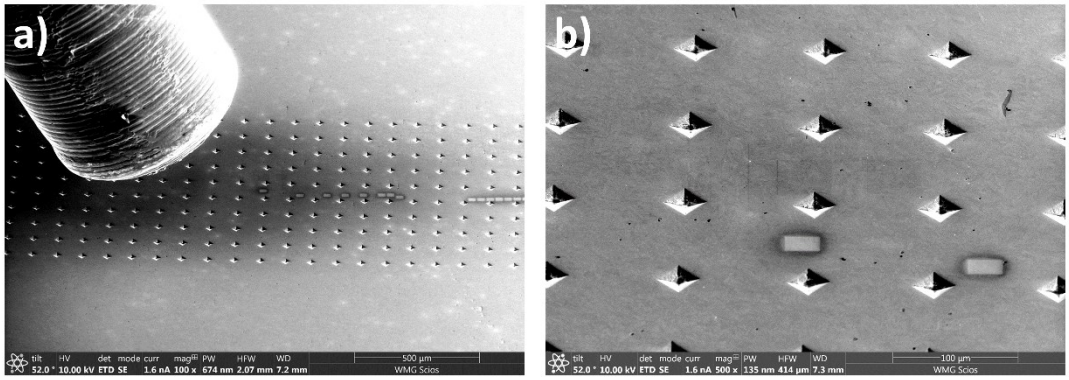

Figure 5.20: SEM images showing the placement of the FIB image locations for the head section of steel Es-P (a) large scale image with the view of the gas nozzle which supplied the XeF_2 gas and (b) higher magnification image showing individual indentations and FIB image locations.

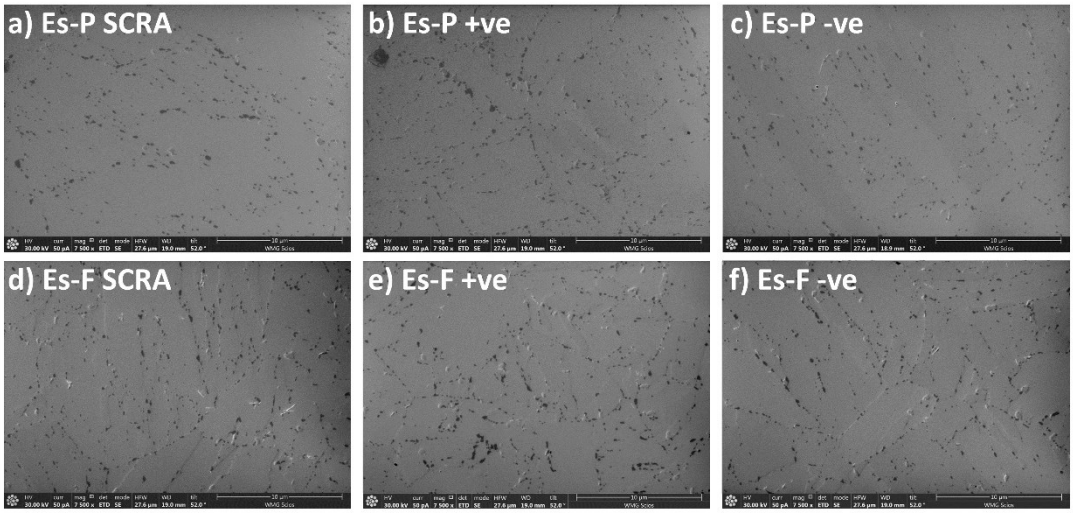

Figure 5.21: Typical FIB-SEM images used for the quantification of the $M_{23}C_6$ carbides for steels Es-P (a to c) and Es-F (d to f) from the head sections.

Figure 5.22 shows the size distributions for the $M_{23}C_6$ carbides in the Es-P and Es-F steels. In both steels the positively segregated regions show a greater number of particles in each size range across the entire size distribution. The SCRAs have a slightly, but consistently higher number of particles in each size range compared to the negatively segregated regions for both steels. The statistics for these size distributions are shown in *Figure 5.23.* The average sizes were quite consistent for each steel with regards to the SCRAs and positively and negatively regions, with a difference of roughly 20 nm for the $M_{23}C_6$ carbides in the Es-P and Es-F head sections. The area coverages for the $M_{23}C_6$ carbides in both steels were ~3.4 % in the positively segregated regions and ~ 2.0 % in the negatively segregated regions. Showing a difference of around 1.7 times. The number of particles was roughly 40 x 10^4/mm^2 more in the positively segregated regions compared to the negatively segregated regions in both the steel head sections. In a study by Sawada et al. [40] a greater number density of $M_{23}C_6$ carbides were reported in the inside of a Gr. 91 tube than on the outside, due to segregation effects from the steelmaking process. However, the study only mentioned that measurements were made from CER samples but did not provide any detail on how robust site-specific data were collected. The variation in the $M_{23}C_6$ carbides found in this study correlates with the variations in Vickers micro-hardness determined in *Section 5.2, Figures 5.4 and 5.5. Figure 5.24* compares the area coverage variations of the $M_{23}C_6$ carbides (from *Figure 5.23*) with the variations in micro-hardness (from *Figures 5.3-5.5).* The correlation between regions of positive and negative populations of the $M_{23}C_6$ carbides can be compared to regions of positive

and negative micro-hardness values. For steel Es-P, the differences in the range of micro-hardness between the positively and negatively regions correlate with the differences in $M_{23}C_6$ carbide area coverage. For steel Es-F the average and negative micro-hardness values are quite close in comparison to the SCRA and negative $M_{23}C_6$ carbide area coverage. However, a distinct increase can be seen for the positive regions for both micro-hardness and $M_{23}C_6$ carbides area coverage in steel Es-F. In comparison to the quantification of the Laves phase in the head sections of steels Es-P and Es-F (*Figures 5.10a and 5.11a*) the variations in the sizes of $M_{23}C_6$ carbides were not as significant as seen in *Figure 5.22* where the 3 size distributions are distinctly different but the difference between the positively and negatively segregated regions is not as pronounced as that for Laves phase particles. This correlates with the micro-segregation characteristics for Mo (main Laves phase constituent) and Cr (main $M_{23}C_6$ carbide constituent) which were quantified in *Chapter 4*. There Mo (~ 0.75) was found to have a significantly greater partitioning coefficient (k_e) than Cr (~ 0.95).

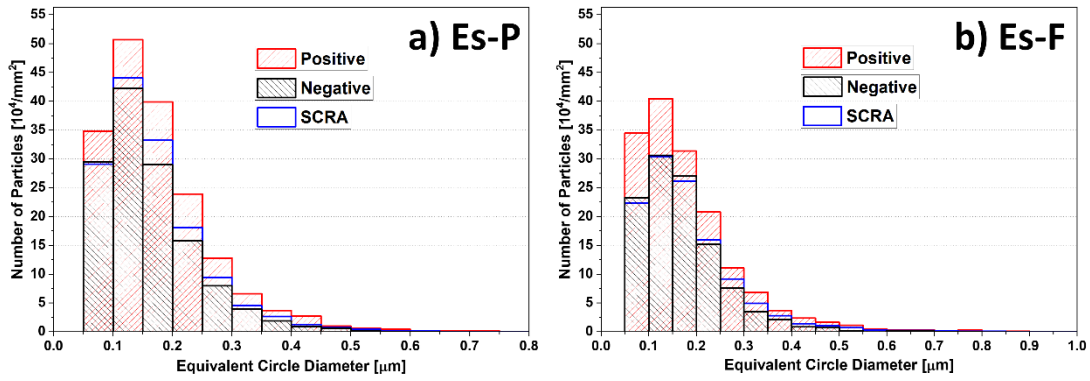

Figure 5.22: Size distributions for the $M_{23}C_6$ carbides quantified from the FIB imaging for the head sections of steels (a) Es-P and (b) Es-F. With regards to the systematically collected random areas and positively and negatively segregated regions.

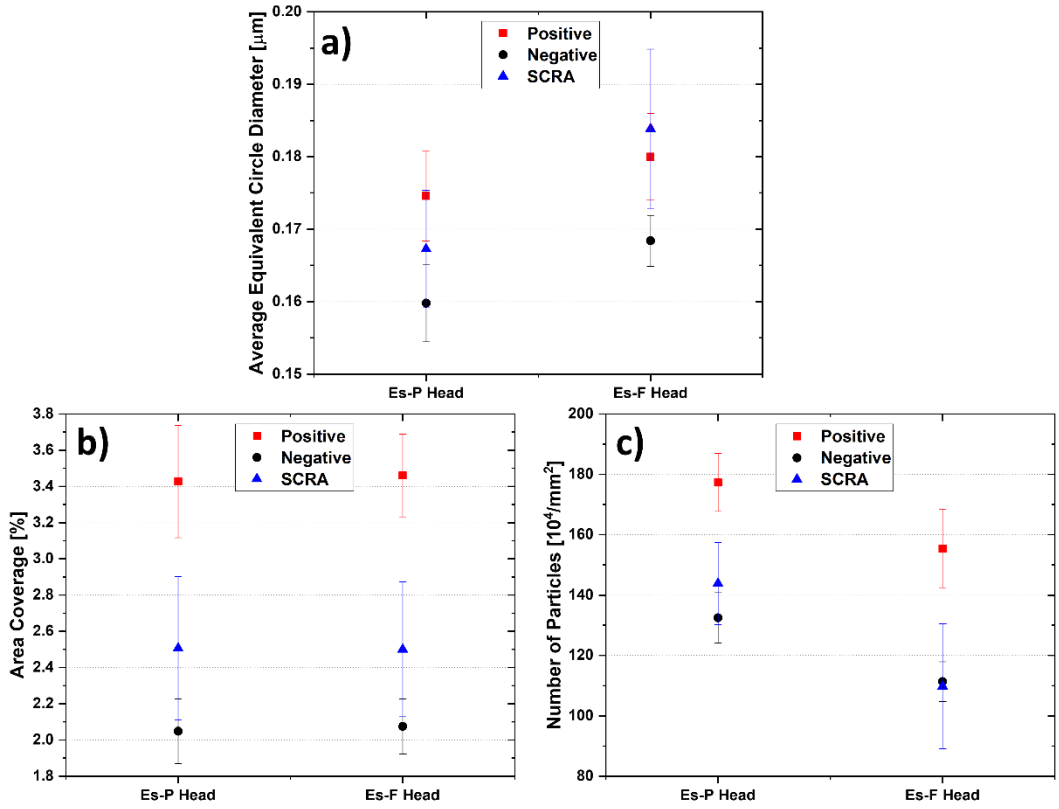

Figure 5.23: Statistics for the size distributions from quantifying the $M_{23}C_6$ carbides from the FIB imaging for the head sections of steels Es-P and Es-F showing (a) the average equivalent circle diameter (b) area coverage and (c) the number of particles. With regards to the systematically collected random areas and positively and negatively segregated regions.

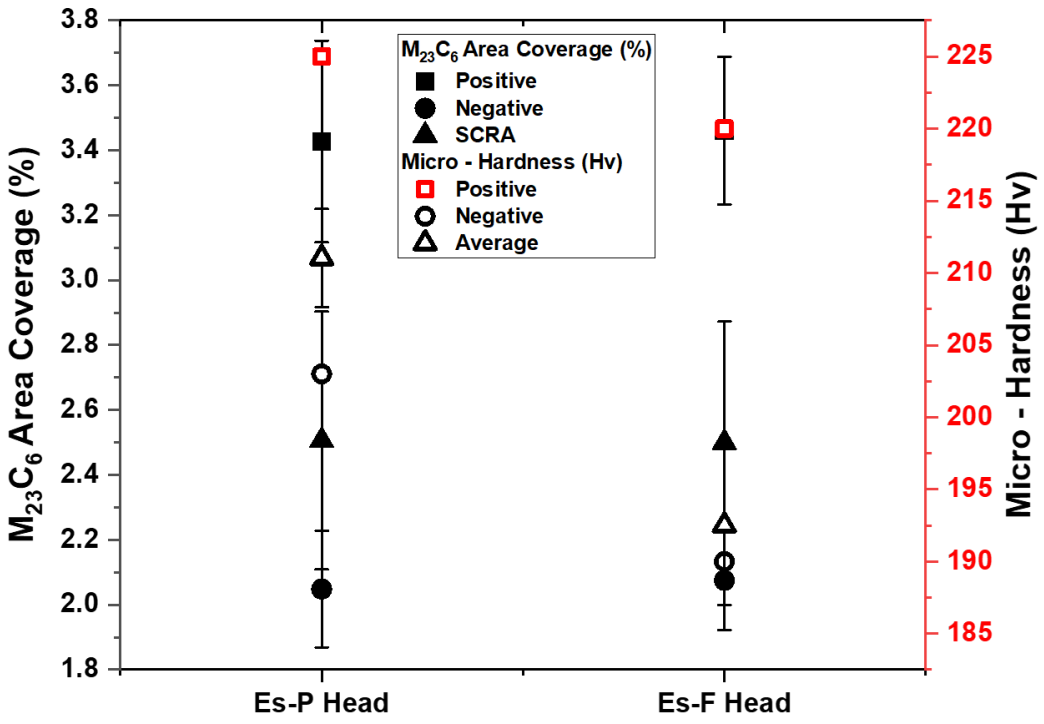

Figure 5.24: Comparison between the $M_{23}C_6$ carbides area coverage and Vickers micro-hardness for steels Es-P and Es-F, with regards to the positively and negatively segregated regions, as well as the SCRA and average. (Data taken from Figures 5.3, 5.4, 5.5 and 5.22).

5.4.2 Thin Foil Lift-out Based TEM $M_{23}C_6$ and MX Quantification

Further to the analysis performed using FIB imaging, site specific analysis was performed using the FIB thin foil lift-out procedure described in *Section 3.5*. The purpose for this analysis was to provide high resolution STEM chemical mapping for the quantification of the $M_{23}C_6$ carbides and the V-rich MX carbo-nitrides, with regards to the positively and negatively segregated regions. In the previous section the FIB imaging could not differentiate $M_{23}C_6$ particles from any coarse V-rich MX carbo-nitrides as the technique does not involve any compositional analysis. All the particles detected were assumed to be $M_{23}C_6$ because of the limited resolution of the FIB imaging which meant any precipitates below 60 nm in size were not detected. Energy Dispersive Spectroscopy spectra were acquired through STEM for these 2 phases (as well as Nb-rich carbides, which were only present in low quantities) in *Figure 5.25*.

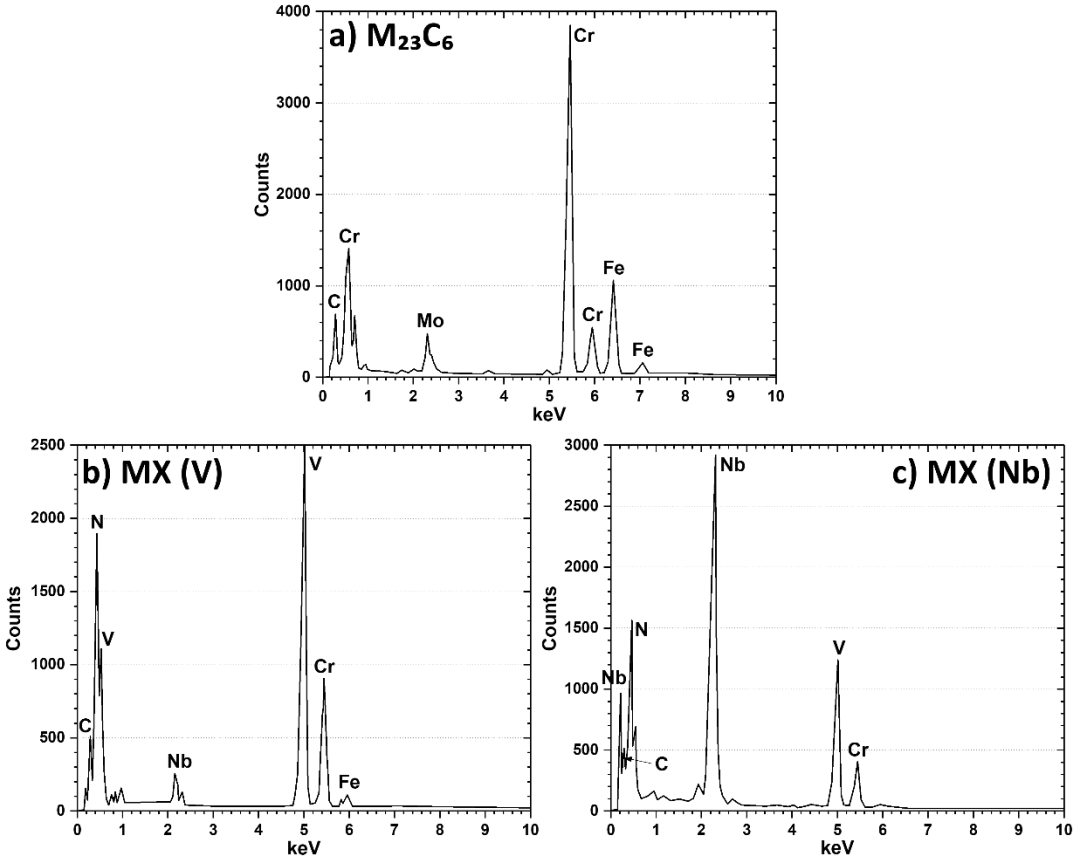

Figure 5.25: Energy dispersive spectra of the phases (a) $M_{23}C_6$ carbides (b) V-rich MX carbo-nitrides and (c) Nb-rich MX carbo-nitrides obtained from the head section of steel Es-P.

Images and maps from the thin foil lift-outs are shown in *Figures 5.26 and 5.27* for the positively and negatively segregated regions of steels Es-P and Es-F, respectively. For steel Es-P (*Figure 5.26)* the $M_{23}C_6$ carbides were quantified based on the Cr-STEM EDS map and the V-rich MX carbo-nitrides were quantified based on the V-STEM EDS map. The area quantified was not sufficiently large for useful statistical analysis of the Nb-rich MX, as seen in *Figures 5.26 and 5.27* and these particles were therefore omitted from the quantification. The size distributions for the 2 main precipitates in steel Es-P are shown in *Figures 5.28a and b,* for the $M_{23}C_6$ carbides and V-rich MX carbo-nitrides, respectively. The $M_{23}C_6$ carbides did not show a clear difference in the size distributions between positive and negative segregated regions. The V-rich MX carbo-nitrides meanwhile showed an increase in the number densities for the size distribution between 0.03 and 0.07 µm as well as a pronounced tail in the size distribution from the region of 0.15 to 0.18 µm in the positive compared with the negative segregated regions. For steel Es-F *(Figure 5.27)* the same process was used

to quantify the $M_{23}C_6$ carbides and V-rich MX carbo-nitrides, based on the STEM maps shown in *Figure 5.27.* The size distributions for the 2 particle types are shown in *Figures 5.28c and d.* Again, no significant difference in the number densities or size distributions of the $M_{23}C_6$ particles in positively and negatively segregated areas was observed. In addition, a similar trend to the Es-P sample was observed for the V-rich MX carbo-nitrides. Significant differences in the number and size distribution of the $M_{23}C_6$ particles was observed using the FIB imaging technique (*Figure 5.22*), this can be explained by the much larger total areas analysed in FIB method compared with the STEM-EDS method. It should be noted, due to time constraints, only 1 set of site-specific FIB thin foil lift-out samples were made for steels Es-P and Es-F.

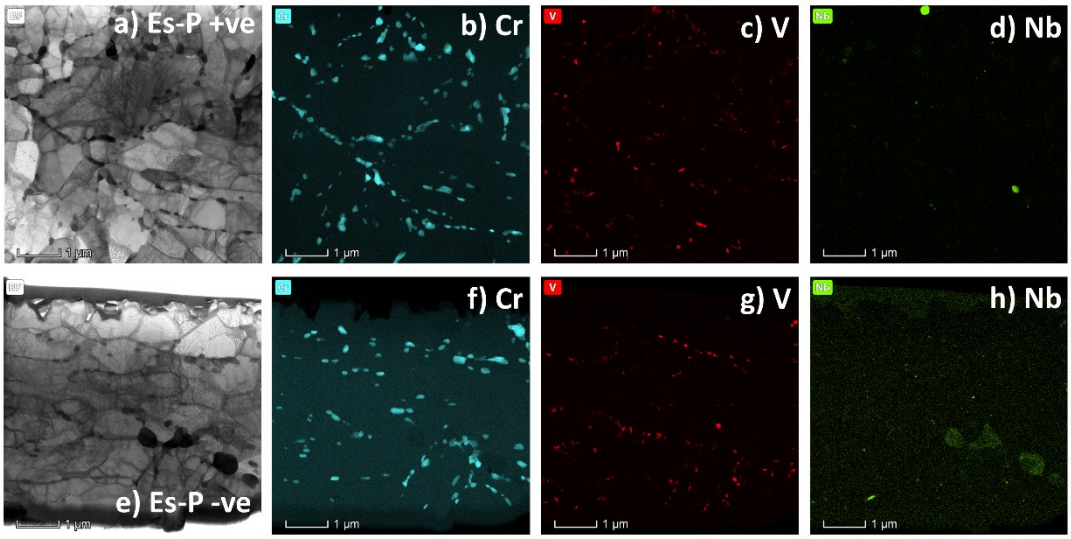

Figure 5.26: TEM bright-field images and corresponding STEM chemical maps of thin foil lift-outs produced from the FIB for a (a-d) positively segregated region and (e-h) a negatively segregated region for steel Es-P.

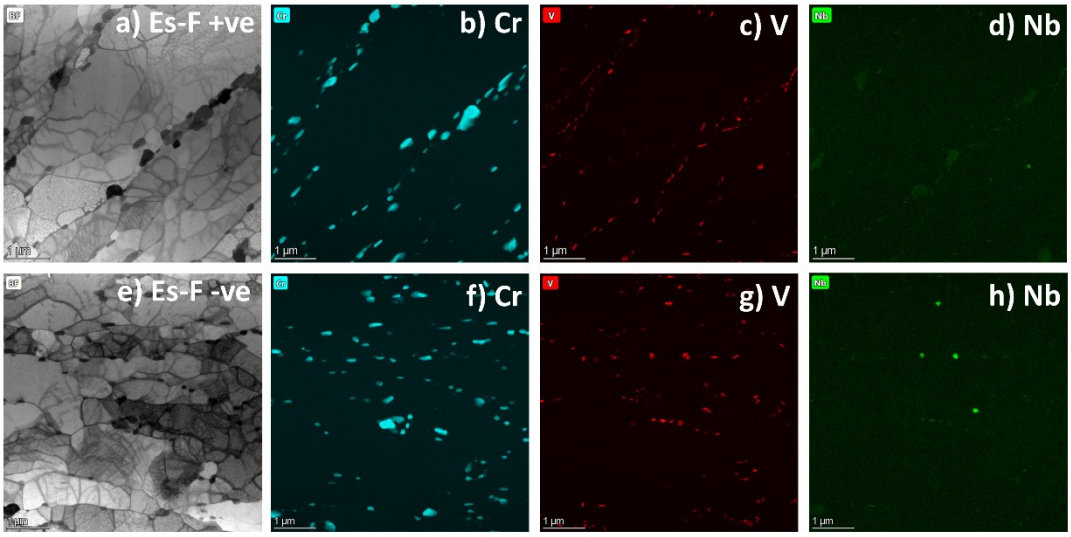

Figure 5.27: TEM bright-field images and corresponding STEM chemical maps of thin foil lift-outs produced from the FIB for a (a-d) positively segregated region and (e-h) a negatively segregated region for steel Es-F.

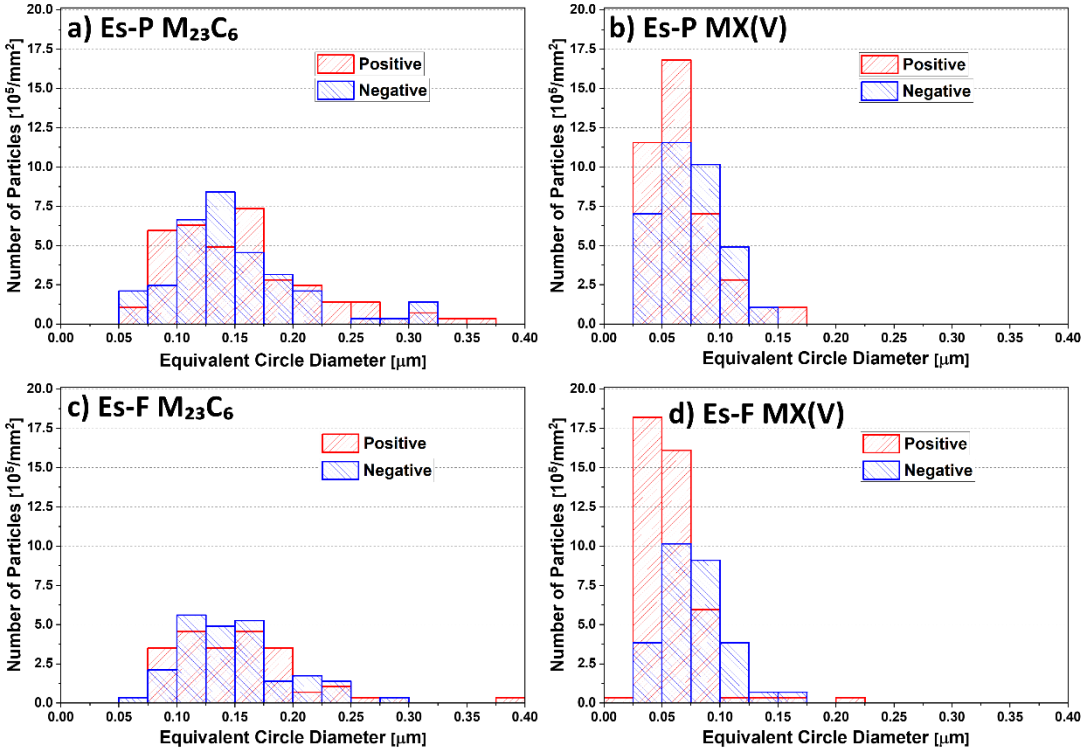

Figure 5.28: Size distributions for the $M_{23}C_6$ carbides and V-rich MX carbo-nitrides quantified from the STEM mapping using thin foil lift-outs from the head sections in steels (a and b) Es-P and (c and d) Es-F. With regards to the positively and negatively segregated regions.

The statistics for the size distributions are summarised in *Figure 5.29.* The average sizes (*Figure 5.29a)* of the $M_{23}C_6$ carbides are slightly greater in the positively segregated regions as compared to the negatively segregated regions for both steels. The average sizes were approximately 150 nm for both the ex-service steels; when comparing to literature studies, average sizes of 300 nm after 113, 431 hours of creep at 600 °C [36] and 250 nm after 50,000 hours at 600 °C [70] were reported in Gr. 91 steels. These literature sizes are significantly greater, but it should be noted the ex-service steels experienced most of their creep exposure at 570 °C for 79,000 hours, with relatively shorter creep tests at 625 °C (1,408 hours for Es-P and 6,714 hours for Es-F). Therefore, less coarsening was expected. The coarsening of the $M_{23}C_6$ carbides is detrimental to the creep rupture strength of the material due to the promotion of dislocation climb and redistribution at grain boundaries [59].

However, for the V-rich MX carbo-nitrides the average size was lower in the positively segregated regions as compared to the negatively segregated regions, which may have been due to the limited sampling area rather than an actual difference. This is because V-rich MX are more resistant to coarsening under creep conditions than $M_{23}C_6$ carbides [78][79]. In a study by Hofer et al. [68] on a 12 wt % Cr steel, the coarsening behaviours of the Laves phase, $M_{23}C_6$ carbides and V-rich MX carbo-nitrides were investigated using EFTEM. The average size of the V-rich MX carbo-nitrides only increased from 52 to 57 nm, compared to the $M_{23}C_6$ carbides which increased from 90 to 157 nm. Some researchers have also found that V-rich MX carbo-nitrides can dissolve during creep at the expense of the Z-phase, however Z-phase is not often reported in 9 wt % Cr steels, this is likely because it is only observed after extended creep or thermal aging times even at relatively high temperatures (e.g., 600 °C) [36][53][54]. It is however, more often reported in CSEF steels with a greater Cr content as Cr is the main constituent of the Z-phase (46.5 at %). Coarsening of precipitates during creep conditions increases the interparticle spacing, this is because coarsening occurs at a fixed volume fraction, therefore growth is accompanied by a reduction in number density. This is why emphasis has been put on developing CSEF steels which inhibit precipitation strengthening phases from coarsening, such as the addition of boron to 9 Cr wt % steels by Abe et al. [31] which is thought to inhibit coarsening of the $M_{23}C_6$ carbides.

With regard to the area coverage *(Figure 5.29b*), only the $M_{23}C_6$ carbides in steel Es-P showed an increase, the remaining precipitates amongst the 2 steels only showed a minor change in the form of a very small decrease in the positively segregated regions compared to the negatively segregated regions. *Figure 5.29c* shows the difference in the number densities of $M_{23}C_6$ carbides and V-rich MX carbo-nitrides between the positively and negatively segregated regions for both steels; it is clear that there is an increase in the number density of V-rich MX carbo-nitrides in the positively segregated regions for both steels, this is also shown in the size distributions from earlier *(Figure 5.28*). For the $M_{23}C_6$ carbides, a lower number density was found in the positively segregated regions for both steels. As mentioned previously, the sampling size from the thin foil lift-outs may have not been ideal for quantifying the $M_{23}C_6$ carbides but was ideal for the V-rich MX carbo-nitrides, which are smaller in size.

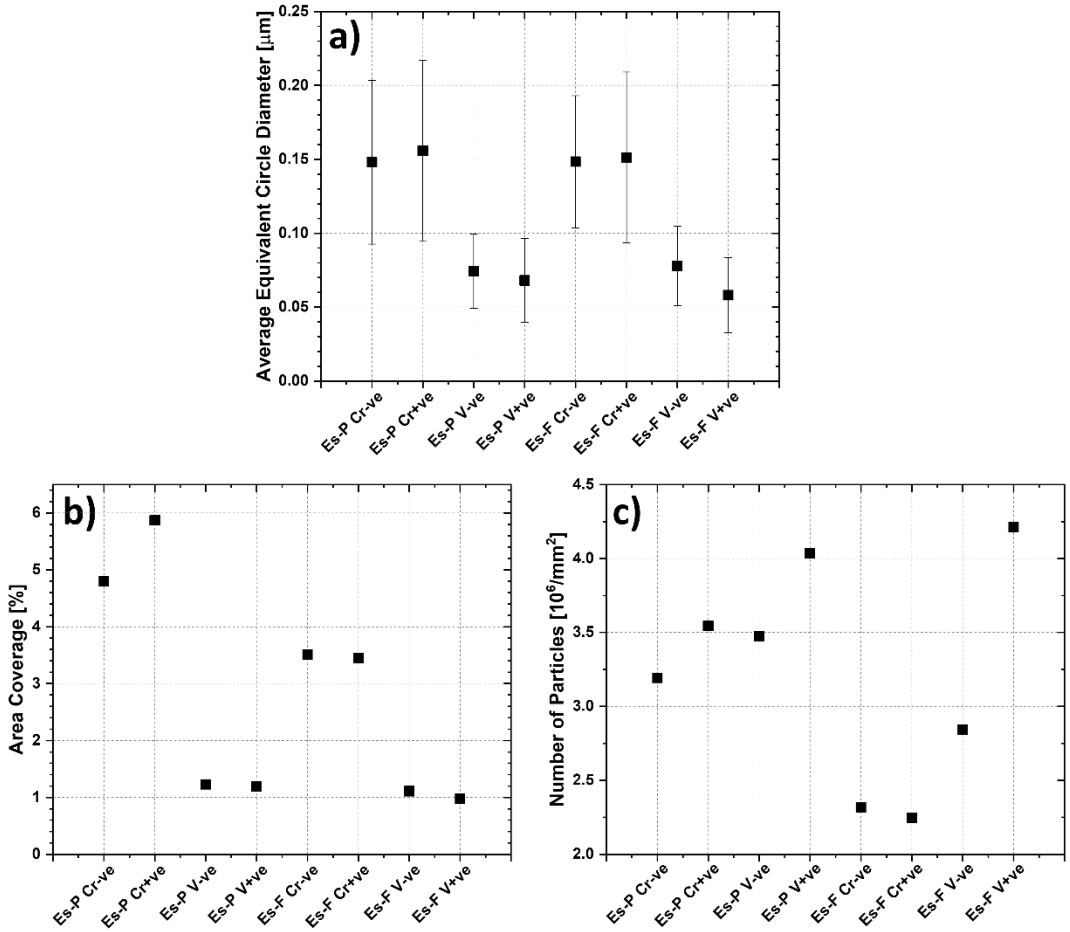

Figure 5.29: Statistics for the size distributions from quantifying the $M_{23}C_6$ carbides and V-rich MX from the STEM mapping using thin foil lift-outs for steels Es-P and Es-F head sections showing (a) the average equivalent circle diameter (b) area coverage

and (c) the number of particles. With regards to the positively and negatively segregated regions.

5.4.3 Carbon Extraction Replica-based TEM $M_{23}C_6$ and MX Quantification

CERs were used in this study for STEM-EDS chemical mapping of the nano precipitates in the steels, namely the $M_{23}C_6$ carbides and V-rich MX carbo-nitrides. The non-site-specific nature of this technique meant random sampling regions were selected each time. Head sections from steels Es-P and Es-F were used for the study in this section, with the purpose of investigating the overlap in the size distributions between the $M_{23}C_6$ carbides and V-rich MX carbo-nitrides. *Figure 5.30* shows the bright-field images for the steels Es-P and Es-F with the corresponding chemical maps, including Cr, V and Nb. The size distributions from the quantification of the $M_{23}C_6$ carbides and V-rich MX carbo-nitrides are shown in *Figure 5.31.* For both steels there is a distinct overlap in the size distributions where the larger V-rich MX carbo-nitride particles in the size distribution overlap with the smaller $M_{23}C_6$ particles, for example for Es-P (*Figure 5.31a*) between the sizes of 60 and 160 nm there is an overlap between the 2 precipitate types. For Es-F (*Figure 5.31b*), the size range between 60 and 260 nm shows the same overlap. Due to the analysis technique which utilises the chemical maps to quantify the precipitates, the different types can be easily distinguished, this means the only effective way of quantifying the V-rich MX carbo-nitrides would be through STEM chemical mapping. In a study by Hofer et al. [68] they concluded a distinct overlap between the $M_{23}C_6$ and MX carbo-nitrides, therefore suggesting that they can only be distinguished and quantified via energy filtered transmission electron microscopy (EFTEM). It should be noted that in *Section 5.4.,1* which was based on quantifying $M_{23}C_6$ carbides using FIB imaging, some overlap which included some of the MX precipitates in the 60 < nm size ranges were observed.

A direct comparison can be made between the thin foil lift-out method and CER method of quantifying the $M_{23}C_6$ carbides and V-rich MX carbo-nitrides with STEM chemical mapping. The main differences included the number densities of particles and size ranges quantified. In the CER method multiple replicas can be easily acquired and mapped in the TEM, whereas for the thin foil lift-outs the process is very time consuming (for 1 lift-out), in the same amount of time (approximately 3 hours) 10s of CERs can be made compared to 1 lift-out. The fact that the CER data *(Figure 5.30 and 5.31)* made use of 3 different sites means a more representative number of

particles were analysed which shows in the size distributions (*Figure 5.31),* where pronounced tails of the curves can be seen (past 0.4 µm for the $M_{23}C_6$ carbides). Compared to the thin foil lift-out data in *Figure 28* the size distributions are far narrower. The number of particles quantified per unit area with the thin foil lift-outs was far greater than with the CER data; this is seen in the size distributions and was due to the inefficiency of the CER technique to pull out all the precipitates, compared to the thin foil lift-outs which take the exact area out in preparation.

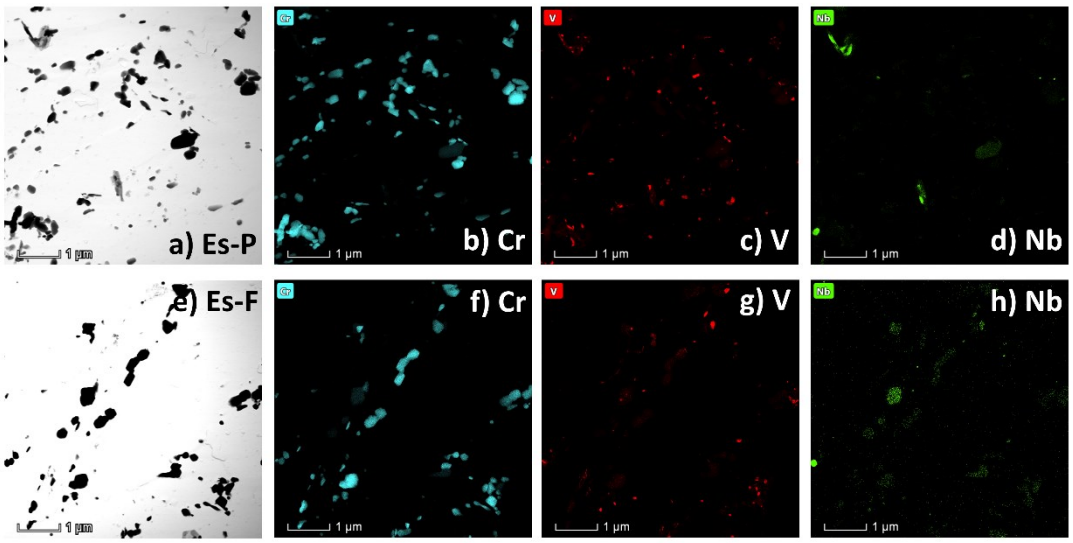

Figure 5.30: TEM bright-field images and corresponding STEM chemical maps produced from CERs for steels (a-d) Es-P and (e-h) Es-F.

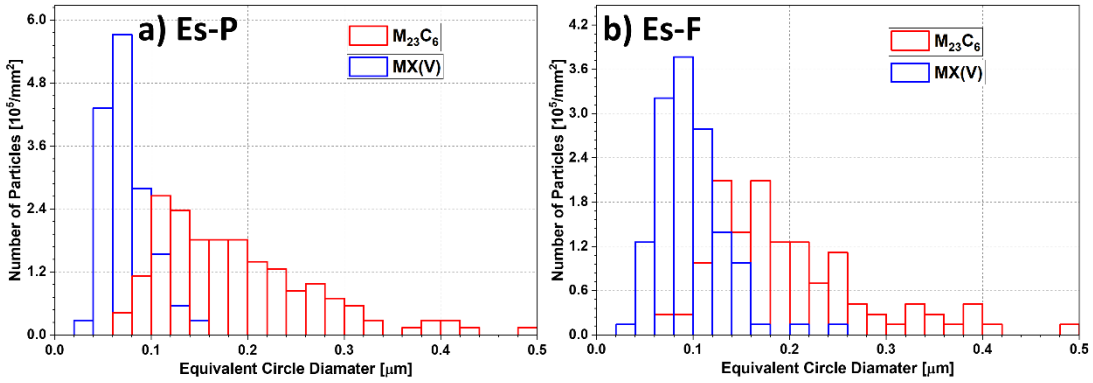

Figure 5.31: Size distributions for the $M_{23}C_6$ carbides and V-rich MX carbo-nitrides quantified from the CER STEM mapping for the head sections in steels (a) Es-P and (b) Es-F.

5.5 Simulating the Amount of Laves Phase, $M_{23}C_6$ Carbides and V-rich MX Carbo-nitrides using Thermo-Calc

Thermo-Calc simulations were performed in order to compare the experimental results found with those simulated by the software, based on the composition ranges (positive, negative and bulk) found in *Section 4.4* using the SEM-EDS technique. *Figure 5.32* shows the Thermo-Calc simulation results for the 6 steels used in this project based on the positive, negative and average compositions. Data are extracted from each curve depending on the creep testing temperature for the particular steel; for steels Euro-Pi, Euro-P2, ORNL-P and ORNL-F these temperatures are 600, 600, 625 and 649 °C. For steels Es-P and Es-F the in-service temperatures were used. This is because in-service the entire Es-P and Es-F creep bar (when it was formerly a Gr. 91 component) experienced 570 °C for 79,000 hours, whereas the creep testing temperatures were at 625 °C but for durations of only 1,408 and 6,714 hours respectively. At 625 °C no Laves phase was predicted to be formed in the negatively segregated regions for both steels Es-P and Es-F. It is clear that this last point is not consistent with the observations documented in this investigation, but the amount of Laves phase measured is consistent with the amount expected at thermal equilibrium at the service temperature. The relatively short creep tests at 625 °C do not seem to have affected the Laves phase content of these materials. This is important because the thermodynamic driving force is achieved on reaching the creep testing temperature, but the kinetics have been too slow to result in any noticeable dissolution.

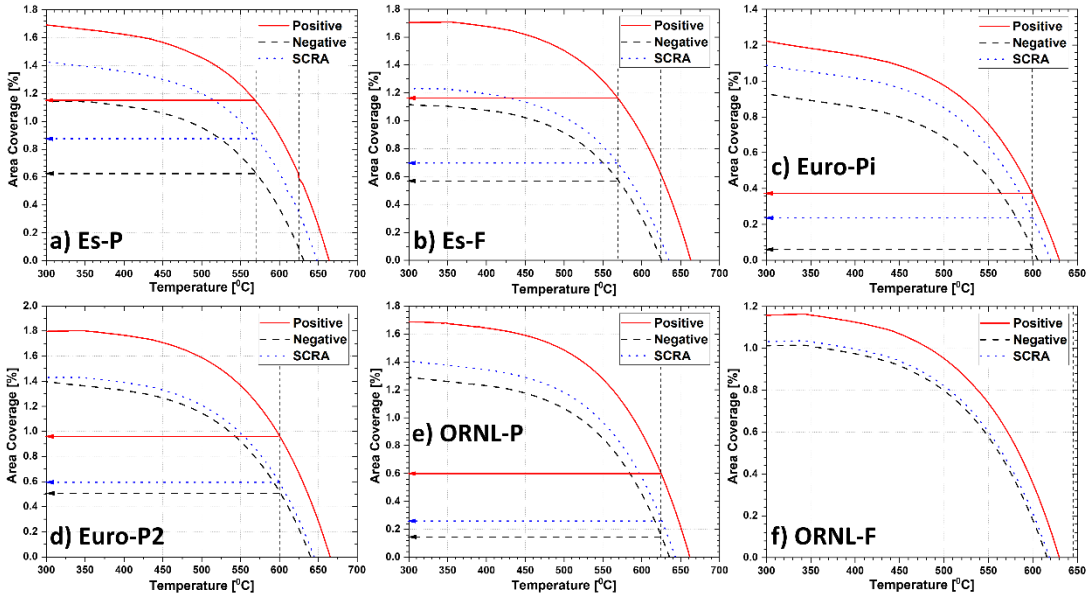

Figure 5.32: Thermo-Calc simulations showing the area coverage of Laves phase predicted in each of the steels in this project (a) Es-P (b) Es-F (c) Euro-Pi (d) Euro-P2 (e) ORNL-P and (f) ORNL-F. Comparisons made between the bulk composition and positively and negatively segregated regions.

Figure 5.33 compares the area coverage results from each of the 6 steel head sections with the Thermo-Calc values simulated. It is clear there are 2 distinct trends which relate to the ex-service steels (Es-P and Es-F) and the non-service exposed steels, ORNL-P, ORNL-F, Euro-Pi, Euro-P2. For steels Es-P and Es-F, the Thermo-Calc predictions at the SCRA (or average) compositions give good agreements with the respective range in the experimental work (SCRA for Es-P and Es-F). Therefore, the long-term in-service exposure has been sufficient in providing enough time (at the given temperature) for the equilibrium to be achieved with regards to the Laves phase. The relatively shorter exposure creep tests at the higher temperature did not result in significant dissolution, this is because the positively segregated experimental values exceed those predicted by Thermo-Calc, and the negatively segregated experimental values are below those predicted by Thermo-Calc. Some of the latter could come from dissolution of finer Laves phase precipitates, but not the former. The main differences between the experimental area coverages and those predicted by Thermo-Calc would be from experimental error, the Thermo-Calc predicted values fall within the error bars of those which were experimentally collected, which provides confidence that the experimental procedure is suitable for the ex-service steels Es-P and Es-F.

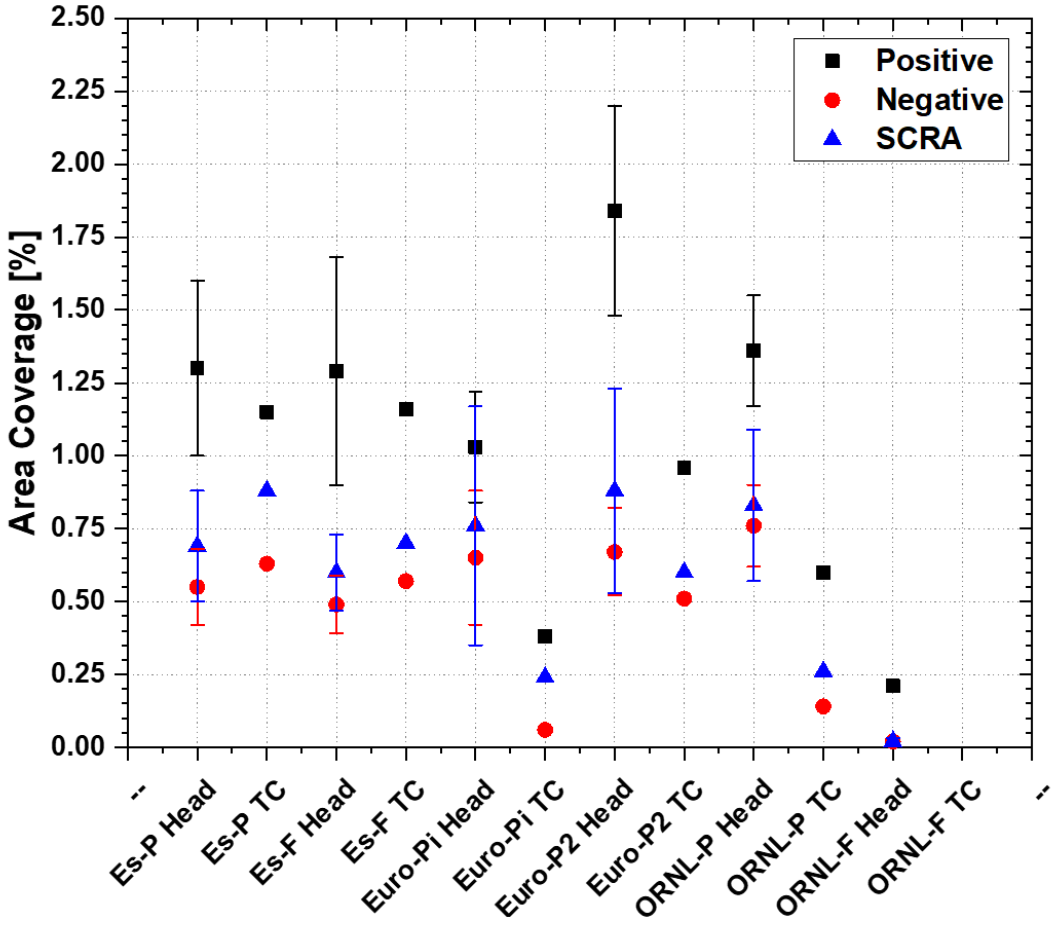

Figure 5.33: Summary figure comparing the area coverages of Laves phase predicted from Thermo-Calc (from a combination of ICP-OES/MS and SEM-EDS) and the area coverages acquired from the experimental results for the head sections of all the steels in this project. Comparisons made between the bulk composition and positively and negatively segregated regions.

For the non-service exposed steels, the Thermo-Calc predicted values are well below the experimental values with little to no overlap except in the experimental error bar SCRA region for steel Euro-P2 with the respective Euro-P2 SCRA Thermo-Calc region. For this there are a few possibilities, one of the main reasons is either or a combination of; i) there being abnormally high amounts of Laves phase quantified experimentally and ii) abnormally low levels of micro-segregation in these 4 steels (compared to steels Es-P and Es-F), meaning Thermo-Calc predictions would be abnormally low from the SEM-EDS data and the quantified Laves phase may be higher than expected and predicted. However, some error must be considered as more Laves phase was quantified in some of the non-service steels (Euro-P2 and ORNL-P) than in the ex-service steels. Many researchers have suggested an extended period of time is required for the Laves phase to reach thermal equilibrium [12][33], some of up

to 100,000 hours at elevated ageing/creep temperature ranges (550 - 600 °C) [36][65]. From *Figures 4.23 and 4.24,* for steels ORNL-P, ORNL-F, Euro-Pi and Euro-P2, the k_e values for the heavy elements (Mo and Nb) show some back-diffusion (through ESR or homogenisation) in comparison to the ex-service steels Es-P and Es-F; this could explain the abnormally low levels of micro-segregation which lead to lower extremes of Laves phase predicted in Thermo-Calc. Therefore, the difference in Thermo-Calc predictions and experimentally quantified results are difficult to explain for the non-service steels.

The Thermo-Calc predictions for the area coverages of $M_{23}C_6$ carbides and V-rich MX carbo-nitrides are shown in *Figure 5.34*. These were performed for comparative study with the area coverages of the $M_{23}C_6$ carbides and V-rich MX carbo-nitrides found in the FIB-SEM study of the $M_{23}C_6$ carbides in steels Es-P and Es-F *(Section 5.4.1)* as well as the thin foil lift-outs for the V-rich MX carbo-nitrides studies for steels Es-P and Es-F (*Section 5.4.2).* It should be noted that the FIB-SEM imaging technique for measuring the areas coverage of $M_{23}C_6$ was used to compare with the simulations rather than the thin foil lift-outs because of the much larger areas that were analysed and because multiple areas were analysed. Thermo-Calc simulations predicting the area coverage of $M_{23}C_6$ in both Es-F and Es-P as a function of temperature for both positive and negative compositions are shown in *Figure 5.34.* For both steels Es-P and Es-F no significant difference in $M_{23}C_6$ area coverage is predicted between positively and negatively segregated regions. The area coverage for both steels with regards to the compositional variations was around 1.55 %, whereas in the experimental work summarised in *Figure 5.23* a variation of area coverage in the range of 2 to 3.5 % was found with regards to the positively and negatively segregated regions. Therefore, the Thermo-Calc simulation predicted less $M_{23}C_6$ carbide for both steels as well as no variation due to compositional extremes. This may have been due to the same C content being used for each simulation which could have been the limiting factor, as C content could not be accurately quantified using SEM-EDS. With regards to the V-rich MX carbo-nitrides in both steels the Thermo-Calc curves in *Figures 5.34b and d* show that there is none of this phase present below 750 °C for either steel. This is because the MX carbo-nitrides in Gr. 91 steels form during holding at the tempering heat treatment stage which gives the phase enough time to nucleate in the temperature ranges of 730 - 780 °C and dissolve at increasingly high

temperatures shown in the graphs, this is why the MX carbo-nitrides are much more stable at creep temperatures than the $M_{23}C_6$ carbides. Although heat treatment details are not provided for steels Es-P and Es-F, a tempering temperature of 760 °C will be assumed which was the same temperature used for steels ORNL-P, ORNL-F, Euro-Pi and Euro-P2 *(Sections 3.1.2/3*), the area coverages of V-rich MX carbo-nitrides at this temperature for both steels are 0.25 and 0.34 % at the positively segregated composition, respectively. At the negatively segregated compositions these values are 0.23 and 0.31 %, respectively. Experimentally, the difference in area coverage was minimal between the positively and negatively segregated regions via the STEM chemical mapping quantification technique. All the area coverages were above 1 % for both steels for the V-rich MX carbo-nitrides, with regards to the compositional extremes. Therefore, once again the Thermo-Calc simulation has predicted far less than the experimental results. This may mean there is some error in the experimental area coverage quantification.

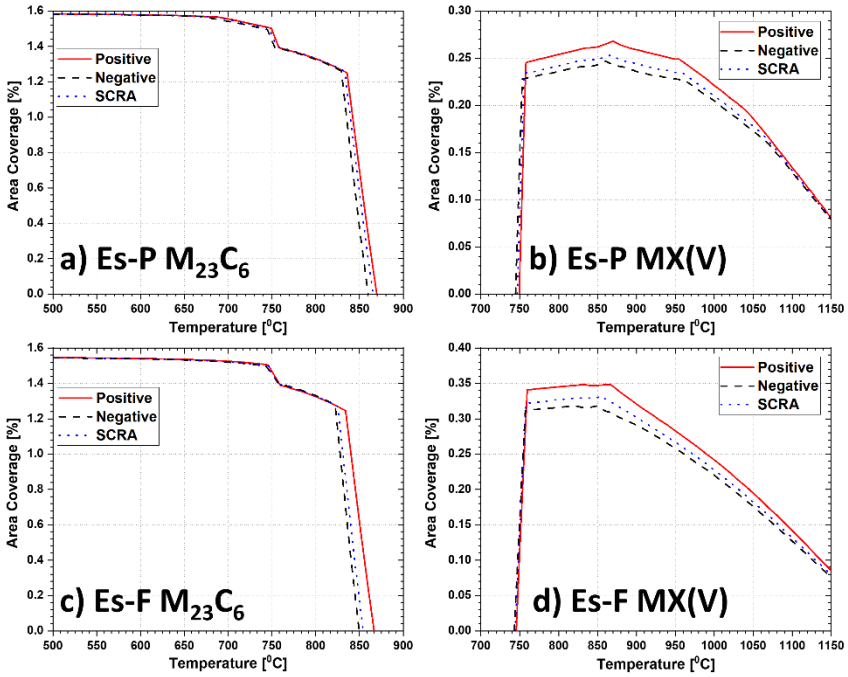

Figure 5.34: Thermo-Calc simulations showing the area coverage of $M_{23}C_6$ carbides and V-rich MX carbo-nitrides predicted in the steels a) Es-P and b) Es-F in this project. Comparisons made between the bulk composition and positively and negatively segregated regions.

5.6 Summary

This chapter studied in detail some of the effects of chemical micro-segregation on the hardness and microstructural parameters in the steel. Various parameters showed a

large influence due to micro-segregation of the major alloying elements in the steel. The Vickers micro-hardness of the steels Es-P and Es-F increased (~6.5 and 15 %) in positively segregated regions compared to the material averages. A combination of FIB-SEM imaging and STEM chemical mapping techniques studied the influence of micro-segregation on the $M_{23}C_6$ carbides and the V-rich MX carbo-nitrides which found a similar correlation with the micro-hardness, for example a larger population of $M_{23}C_6$ carbides in the positively segregated regions than in the negatively segregated and SCRAs. However, it should be noted that, for the quantification of the V-rich MX carbo-nitrides, the STEM mapping found a distinguishable difference whereas the variation in the $M_{23}C_6$ carbides was only found in the FIB-SEM, due to the thin foil lift-outs from the TEM providing an insufficient amount of area for the quantification of the carbides.

The quantification of Laves phase particles was performed in targeted areas for all steels and showed a distinct variation in the form of a greater number of particles and subsequently area coverage in the positively segregated regions as compared to the negatively segregated and SCRAs. The combined study of the experimental quantifications and Thermo-Calc predictions for the Laves phase showed there was a distinct difference between the ex-service steels Es-P and Es-F and the non-service steels ORNL-P, ORNL-F, Euro-Pi and Euro-P2.

Overall, this chapter shows special attention should be shown to area-to-area variations when quantifying a range of different phases, and properties (i.e., hardness) in Gr. 91 and possibly other CSEF steels. In-depth work such as this has not been produced before, with only a few publications which vaguely address the idea in CSEF steels [40][132]. The work presented in this chapter highlights multiple phases using a wide range of analytical techniques to show the importance of micro-segregation and its measurable effects on hardness and quantification of microstructural parameters. The next chapter will indeed attempt to also apply this to the quantification of inclusions in this project on Gr. 91 steels. It was quite clear that the implications can lead to variations in mechanical properties and precipitates.

Chapter 6 : Inclusions and Creep Cavitation

6.1 Introduction

This chapter sets out to investigate the effects of different accelerating voltages on quantification and characterisation of inclusions in Gr. 91 steels. The effects on quantification, spatial resolution and interaction volume will be studied; the use of simulations will also aid these experiments.

Furthermore, this chapter also aims to characterise and quantify the various types of inclusions in these steels which is often overlooked in studies of Gr. 91 and other CSEF steels. In order to do so an automated SEM-EDS inclusion analysis technique at an operating voltage of 10 kV and specific areas of interest has been developed and implemented, which includes paying attention to micro-segregation effects which have been previously highlighted in *Chapter 4*. As well as this, further detailed studies were carried out for steel Es-P which explored Cu association with inclusions, as well as quantification of the AlN precipitates in all steels. The cavitation and hardness profiles in each of the steels were also examined in order to find any substantive links between the damage, hardness and creep performance.

6.2 Effects of SEM Accelerating Voltages

Figures 6.1 and *6.2* show examples of MnS and Al_2O_3 inclusions respectively, comparing the acquired SEM images and corresponding energy spectra (and composition) for accelerating voltages of 5, 10 and 20 kV. The energy spectrum for each inclusion was acquired by tracing around the inclusion manually in each instance. *Figures 6.1a* and *ai* show the image, spectrum and composition of an MnS inclusion at 5 kV. The spectrum for the inclusion is limited in terms of the analytical range (only up to 5 keV); this means the quantification of the Mn content in the inclusion is difficult to determine because it is only based on the L_α X-ray peak, the K_α X-ray peak is located closer to 6 keV which is out of the 5 keV spectrum range. Furthermore, the quantification of the S K_α X-ray peak at 2.3075 keV cannot be solely used to quantify MnS-type inclusions due to possible overlap with the Mo K_α X-ray energy peak at 2.29 keV, it can be seen that 18 wt % of Mo is quantified without any Laves phase present. This is also problematic because Mo is the main constituent of the intermetallic Laves phase, which tends to form on grain boundaries and microstructural features such as inclusions. At 10 kV *(Figure 6.1bi)* less Mo is

quantified (2.8 wt %), this could be from nearby (sub-surface) Laves phase or error in measuring the S K_α X-ray peak, although if error, it is considerably less than at 5 kV and can be considered negligible error due to the possibility of it being from Laves phase. Based on the limited analytical range 5 kV is not suitable for analysing the inclusion population in these steels. *Figure 6.2a and ai* show the image, spectrum and composition for an Al_2O_3 inclusion, quantification for this inclusion is feasible with the 5 keV analytical range due to the Al and O X-ray energies being well below 5 keV, eliminating the Fe K_α X-ray peak. However, due to the lack of MnS inclusion quantification from an overlap in Mo and S K_α X-ray peaks and Mn L_α X-ray peak, 5 kV remains impractical for quantifying inclusions using an SEM-EDS automated system.

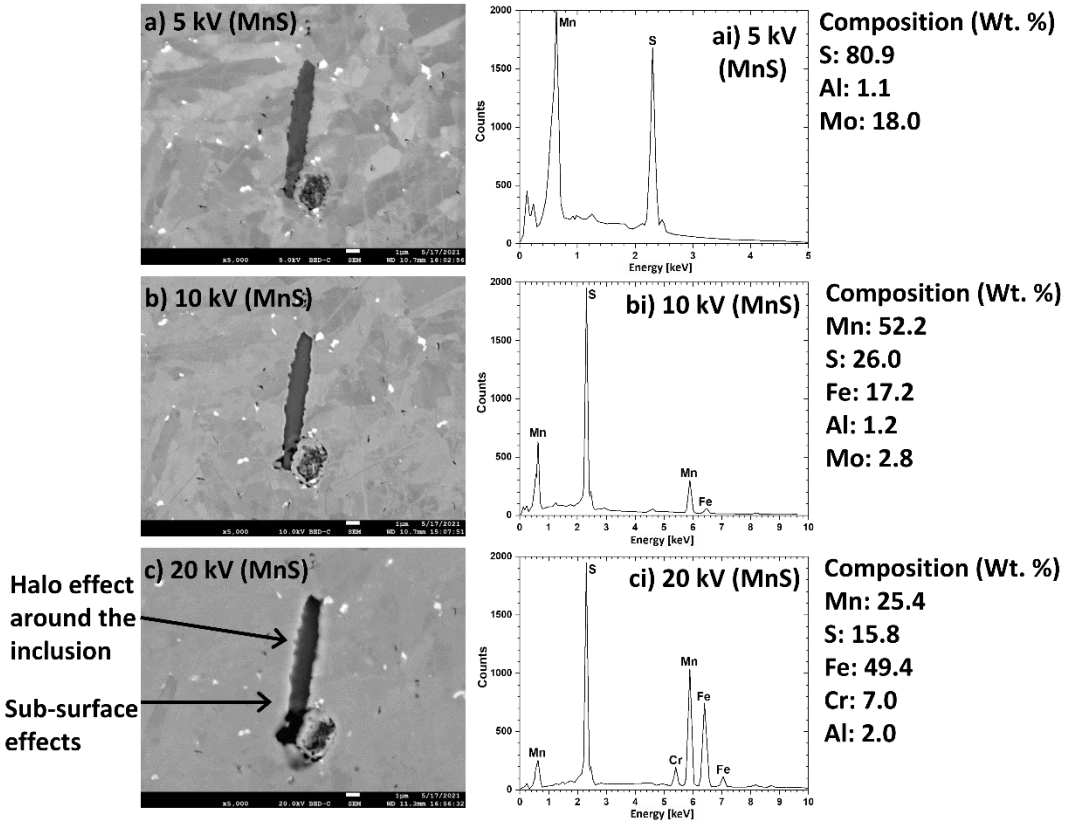

Figure 6.1: SEM images and accompanying chemical spectra and composition of an MnS inclusion at 3 different voltages (a) 5 kV (b) 10 kV and (c) 20 kV. Spectra: (ai) 5 kV (bi) 10 kV (ci) 20 kV.

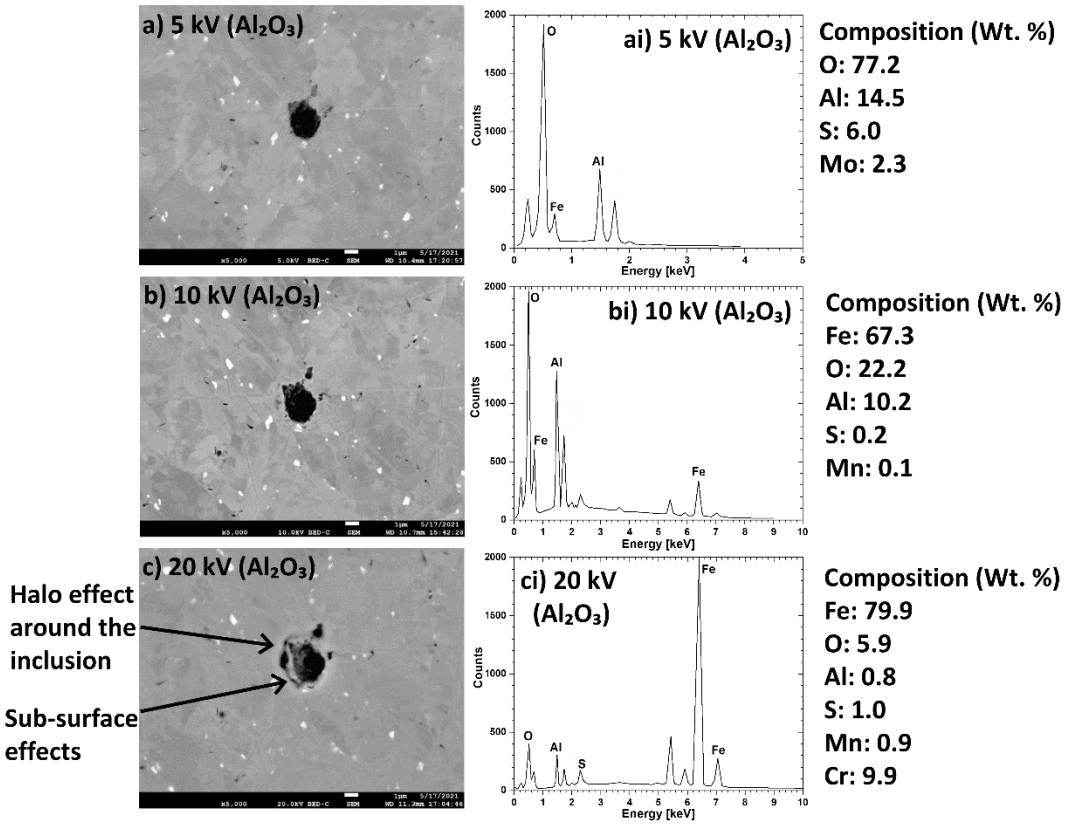

Figure 6.2: SEM images and accompanying chemical spectra and composition of an Al_2O_3 inclusion at 3 different voltages (a) 5 kV (b) 10 kV and (c) 20 kV. Spectra: (ai) 5 kV (bi) 10 kV (ci) 20 kV).

Figures 6.1b and *bi* show the image, spectrum and composition of an MnS inclusion collected at 10 kV. The spectrum for the inclusion is based on the analytical range of 0 - 10 keV, which means that the Mn K_α X-ray peak, located at 5.9 keV, can be used in the analysis, this is shown in the composition in which 52.2 wt % of Mn is measured. There is also the presence of the Fe K_α X-ray at 6.39 keV, however the Fe K_α X-ray peak is minimal in comparison to the other peaks, meaning not many counts are consumed by that specific peak; this is because the interaction volume of the electron beam does not penetrate the Fe matrix. The image resolution at 10 kV *(Figure 6.1b)* appears very similar to that of 5 kV due to a similar interaction volume (*Figure 6.1a*) (based on visual observations of other features in the images), as a result there are also very similar sub-surface effects. *Figures 6.2b* and *bi* show the image, spectrum and composition for an Al_2O_3 inclusion at 10 kV, the most significant difference between this image and spectrum compared to the 5 kV image and spectrum *(Figures 6.2a* and *ai*) is the increased analytical range, which includes the Fe K_α X-ray peak, although this peak is very small this does not affect the ratios of Al:O (as seen in the

compositions) in the quantification of Al_2O_3 inclusions as the quantification energies for Al_2O_3 are well below 5 kV.

Figures 6.1c and *ci* show the image, spectrum and composition of an MnS inclusion at 20 kV. The spectrum for the inclusion is based on the analytical range of 0 - 20 keV, although only the 0 - 10 keV is displayed in the figure because no important peaks for this material appear above this. The image for the 20 kV accelerating voltage is distinctly different to that of 5 and 10 kV (*Figures 6.1a and 1b*) in 2 major ways, firstly there is a halo effect around the edge of the inclusion which cannot be seen at the other voltages, this is due to the difficulty of acquiring high-quality SEM-BSE images at 20 kV (through brightness and contrast segmentation) in comparison to 5 and 10 kV. Furthermore, the 20 kV image is clearly showing some sub-surface effects, which show through in *Figure 6.1c,* e.g. a dark feature can be observed towards the bottom of the inclusion which can affect the quantification of the inclusion composition. This is due to the significantly greater interaction volume at 20 kV compared with 5 and 10 kV. The sub-surface effects will be further discussed in *Section 6.3* through the use of simulations. The other clear difference at 20 kV is the heightened Fe K_α X-ray peak at 6.39 keV, which means useful counts are going towards quantifying the Fe matrix rather than the inclusion (there is maximum total input counts that can be used). This is reflected in the higher measured Fe content (49.4 wt %), however this is a result of the increased voltage allowing electrons to penetrate deeper into the steel than at the lower voltages. *Figures 6.2c and ci* shows the image, spectrum and composition for an Al_2O_3 inclusion at 20 kV, similar to the MnS inclusion at 20 kV (*Figures 6.1c and ci)* the Fe K_α X-ray peak is heightened, which again means a lot of the useful counts are not being used for inclusion quantification (79.9 wt % Fe). In comparison to the MnS inclusion, this Al_2O_3 inclusion is much smaller, therefore, the exaggerated Fe K_α X-ray peak is a result of the sub-surface matrix effects from the 20 keV beam energy. This is also reflected in the image *(Figure 6.2c*), where other dark features can be seen next to or associated with the inclusion. These features cannot be easily distinguished at the lower voltages. In literature studies an accelerating voltage of 20 kV is widely used [167][179]–[181] for the purpose of attaining a full spectral range. However, it does inherently lower spatial resolution and an accelerating voltage of 10 kV is recommended with respect to inclusion analysis in Gr. 91 and other CSEF steels. This is because in creep applications the total number and full size distribution of inclusions

is important as they are potential sites for nucleation of creep cavities, compared to inclusions > 1 μm for strength and fatigue applications [184].

Further analysis will not include the use of 5 kV due to the insufficient analytical range in quantifying S-rich inclusions (namely MnS inclusions). This sub-section shows a comparison of MnS and Al_2O_3 inclusions in steel Es-P, these were randomly selected, and the same region was examined at 10 and 20 kV. After thresholding the inclusions from the matrix at the 2 voltages, the images and spectra were exported, and the length of each inclusion was quantified using Image-J. *Figure 6.3* compares the quantification of an MnS and an Al_2O_3 inclusion through automated SEM inclusion analysis at 10 kV and 20 kV. The MnS inclusion (*Figure 6.3a*) measures 9.4 μm in length at 10 kV, and out of the 5200 total counts for the inclusion spectrum, only 200 counts are in the Fe K_α X-ray peak. In comparison, the same MnS inclusion *(Figure 6.3c)* measures 10.7 μm at 20 kV, and almost 1/3 of the counts (3000 out of a total of 9100) are consumed by the Fe K_α X-ray peak. The size of the MnS quantified is approximately 15 % larger at 20 kV compared with 10 kV, and the efficacy of the counts is significantly decreased at 20 kV. As shown in *Figures 6.1 and 6.2* the amount of Fe measured is far greater at 20 kV than at 10 kV, for both inclusion types, meaning some inclusions may not be measured due to a loss of Mn, S, Al and O characteristic X-rays at 20 kV.

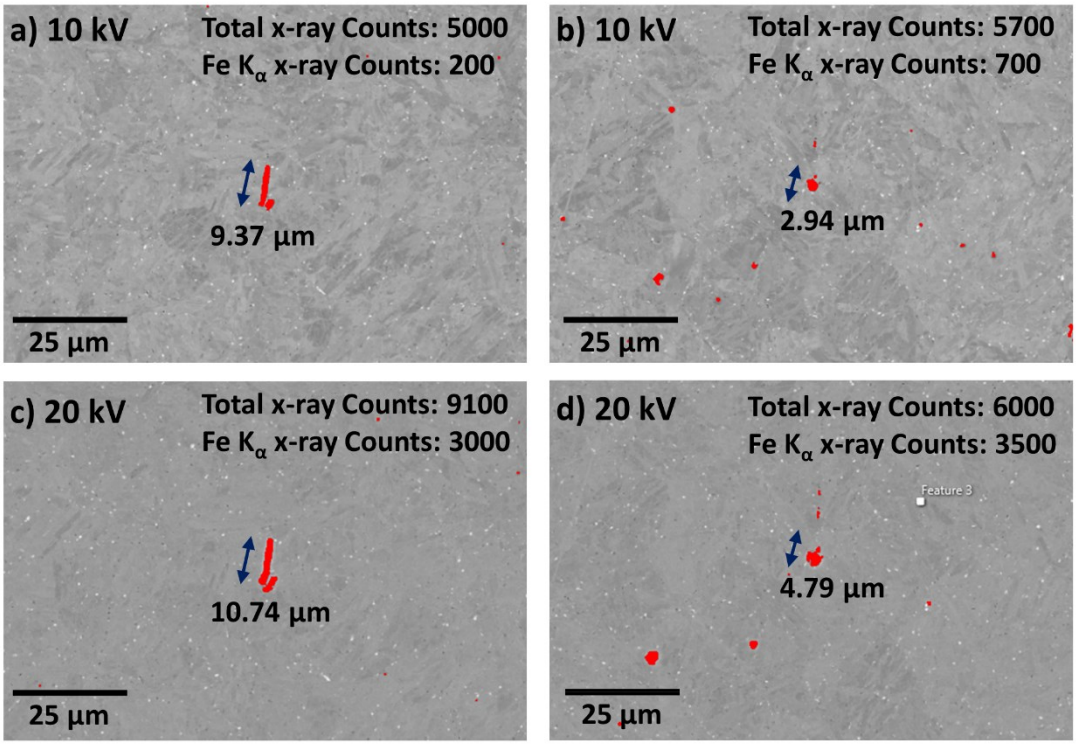

Figure 6.3: SEM images of an MnS (a and c) and an Al_2O_3 (b and d) inclusion at 10 kV (a and b) and 20 kV (c and d), respectively. Showing the differences in the acquired size, total x -ray count and Fe K_α X-ray counts.

For an Al_2O_3 inclusion (*Figure 6.3b)* the quantified size measured at 2.9 µm in length at 10 kV, and of the total 5700 counts in the inclusion spectrum, only 700 quantify the Fe K_α X-ray peak. Whereas, at 20 kV the same Al_2O_3 inclusion (*Figure 6.3d)* measured at 4.8 µm in length, the total counts in the inclusion spectrum are of 6000, and a significant 3500 are consumed by the Fe K_α X-ray peak. Once again, similarly to the MnS inclusion a significant number of counts are essentially wasted to the Fe K_α X-ray peak, furthermore the effective size of the Al_2O_3 inclusion is 63% larger at 20 kV than at 10 kV. These differences in size are associated with the reduced image resolution at 20 kV due to the increased interaction volume (depth and lateral). This effect become increasingly pronounced as the size of the inclusions decrease. This results in a greater number of inclusions being detected at 10 kV compared with 20 kV. An example of this is provided in *Figure 6.3 (b and d)* where in the same analysis area additional smaller inclusions are thresholded by the software at the lower accelerating voltage. In addition, at 20 kV a significant fraction of the useful counts are consumed by the Fe K_α X-ray peak, this reduces the number of counts that are

contained in useful areas of the spectra (the total maximum input counts that the detector can analyse is fixed).

Another factor to consider is the overvoltage ratio requirement for quantification of inclusions. The overvoltage ratio is the ratio of the voltage in the primary electron beam (i.e., the accelerating voltage, 10 kV, 20 kV), compared to the critical ionisation energy of the element of interest (i.e., Mn and S for MnS inclusions). The voltage suggested for conventional quantitative electron probe analysis is x 2 of the critical ionisation energy, although as low as x 1.5 [207] or as low as x 1.3 [208] is suggested for the generation of a useful X-ray signal for characteristic X-rays. For example, the highest energy X-ray in the inclusion analysis in the study is the Mn K_{α} X-ray peak at 5.7 keV, therefore, if a voltage of 10 kV is used for inclusion analysis, then the overvoltage ratio requirement will be satisfied (10 / 5.7 = x 1.75).

6.3 Simulating the Effect of Accelerating Voltages on a Grade 91 Steel

The Desk-Top Spectrum Analyser 2 (DTSA-II) is a commercially available software for simulating electron beam trajectories in a given sample / composition using a Monte Carlo style method of computation; more details on this are given in the *Section 3.9.* Simulations for both an MnS and an Al_2O_3 inclusion were performed at the 2 voltages of interest; 10 kV and 20 kV, as well as using the steel matrix composition to simulate the electron beam interaction volume. 5 kV was not considered as it has an insufficient analytical range to study the inclusions of interest in this work effectively. *Figure 6.4* shows visual representations of the electron beam interaction within a volume of MnS and Al_2O_3 inclusion at 10 kV (*Figure 6.4a, ai, b, bi*) and 20 kV (*Figure 6.4c, ci, d, di*), respectively.

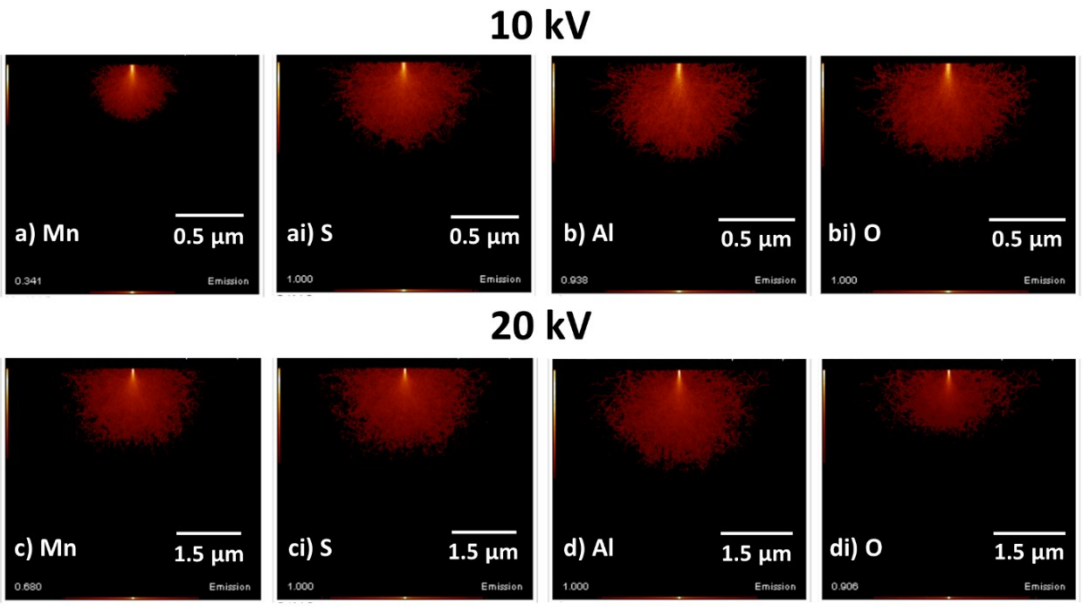

Figure 6.4: Visual plots from simulation results for MnS inclusions at 10 kV (a and ai), and 20 kV (c and ci), Al_2O_3 inclusion at 10 kV (b and bi), and 20 kV (d and di).

The simulations show that at 10 kV the interaction depth of MnS (*Figure 6.4a and ai*) is roughly 1/3 of the interaction depth of MnS (*Figure 6.4c and ci*) at 20 kV. This is similar to the Al_2O_3 inclusion, which shows roughly triple the interaction depth at 20 kV (*Figure 6.4d and di*), as compared to 10 kV (*Figure 6.4d and bi*). These diagrams are quantified numerically and displayed in *Figure 6.5* in the form of depth penetration (50 and 90%) and lateral penetration (100%). *Figure 6.5a* shows 50% of the electron beam reaches a maximum depth of 0.24 µm for the elements Mn, S, Al, O (K_α X-ray peaks) for 10 kV, compared to 20 kV (*Figure 6.5b*) where the maximum depth for the same 4 elements is 0.75 µm. With regard to 90% of the electron beam, at 10 kV the maximum depth is 0.44 µm for the 4 elements, in comparison, at 20 kV this maximum depth figure increases to 1.45 µm. For both 50% and 90% this shows a rough increase of a factor of 3 in depth. With regards to the lateral distance, the beam spreads to a maximum distance of 1.19 µm at 10 kV for the 4 elements, however at 20 kV this distance is 3.75 µm for the 4 elements, again roughly a threefold increase.

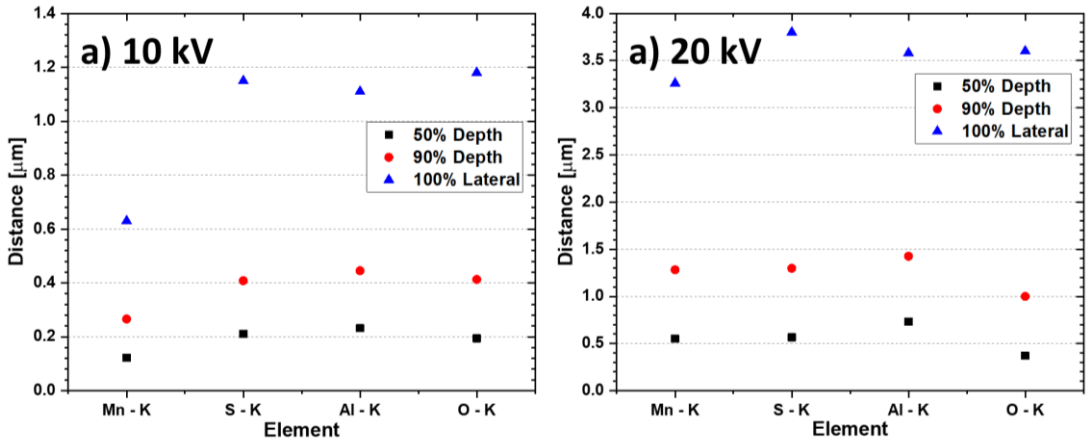

Figure 6.5: Graphical plots of data acquired from Figure 6.4 showing the distance for depth and lateral penetration of an electron beam for MnS and Al_2O_3 inclusion alloying element constituents at (a) 10 kV and (b) 20 kV.

In order to compare the effects of resolution at 10 kV and 20 kV in the steel matrix, simulations were performed using the steel matrix' composition (using the composition of steel Es-P). At 10 kV (*Figure 6.6a and ai*), 50% of the beam penetrates 0.06 µm and 90% of the beam penetrates 0.14 µm and laterally the beam spreads to 0.35 µm. At 20 kV, 50% of the beam penetrates 0.3 µm and 90% of the beam penetrates 0.6 µm and laterally the beam spreads to 1.75 µm (*Figure 6.6b and bi*). When comparing the penetration depth for the 2 voltages, for 90% of the beam, at 10 kV the distance is only 0.14 µm, whereas at 20 kV, this distance is over 4 times as much (0.6 µm). Laterally, the beam spreads over 4 times as much at 20 kV than at 10 kV, this explains why such inclusions and microstructural features appear much larger at 20 kV in previous figures such as *Figures 6.1, 6.2 and 6.3*. Although experimentally a significance of 4 times was not found, this indicates the software may over-estimate the penetration (depth and laterally), however, qualitatively the software does agree with the experimental work performed in *Section 6.2.*

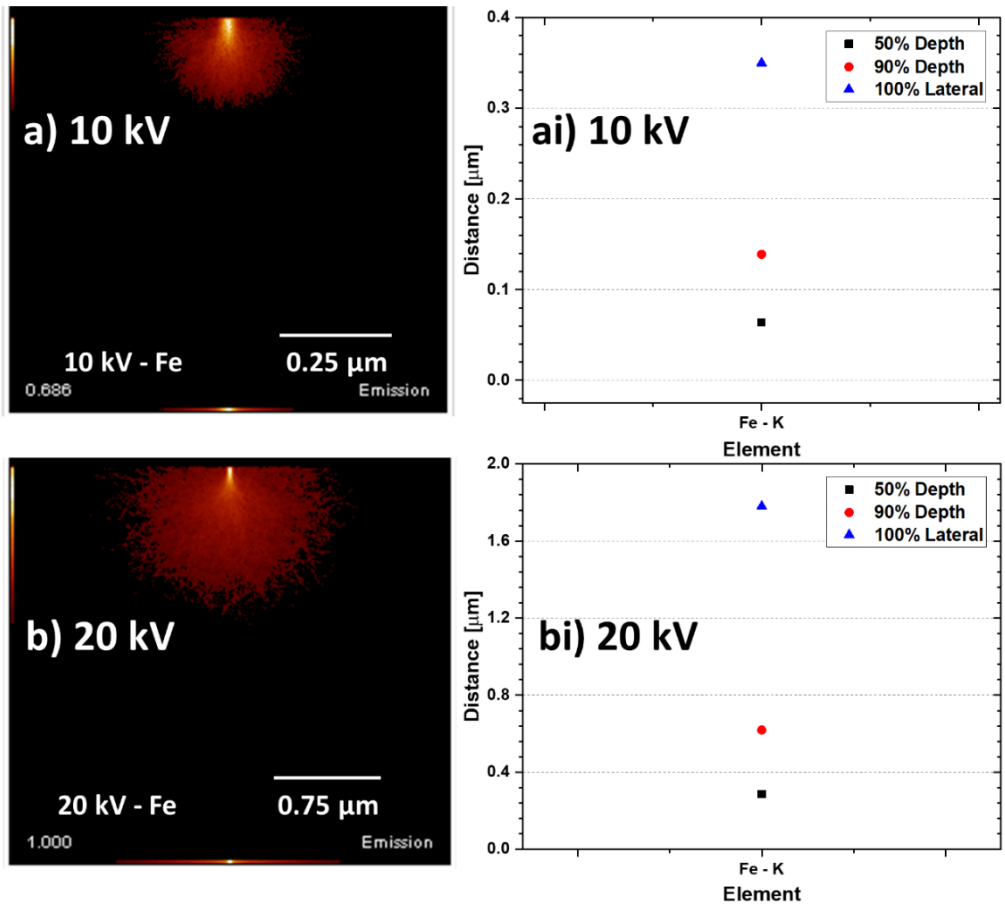

Figure 6.6: Visual and graphical plots of the depth and lateral penetration of an electron beam at (a and ai) 10 kV (b and bi) 20 kV.

6.4 Inclusion Analysis

6.4.1 Typical Inclusions Found in the Gr. 91 Steels

Examples of typical inclusions found in the 6 Gr. 91 steels in this project with accompanying spectra are displayed in *Figure 6.7.* Among these there were 3 distinct types found in the steels studied, the most common of which were MnS inclusions, which can be seen in *Figure 6.7a* and in previous sections in this chapter. The other main type of inclusion found was Al_2O_3, as seen in *Figure 6.7b* and in previous sections. The third type of inclusion found in these steels was hybrid Nb/Ti nitrides (*Figure 6.7c),* the hybrid term is to signify the Nb and Ti content within the nitride. Another common precipitate found in Gr. 91 steels is AlN, some authors regard AlN as an inclusion. This phase is also dark/black, in contrast to the steel matrix, and therefore, it can be detected in automated inclusion analysis. In order to eliminate this phase from the inclusion quantifications, 2 processes were utilised. The first is based

on size, since most AlN precipitates are smaller than the 0.25 µm detection limit, most were removed automatically. Those that remained were filtered out using a classification system based on composition. Finely sized Al-rich particles which contained N with no other elements (O, Mn, S) were excluded using the classification system. It should be noted that the size of AlN precipitates were quantified using a separate image analysis process *(Section 6.6)*.

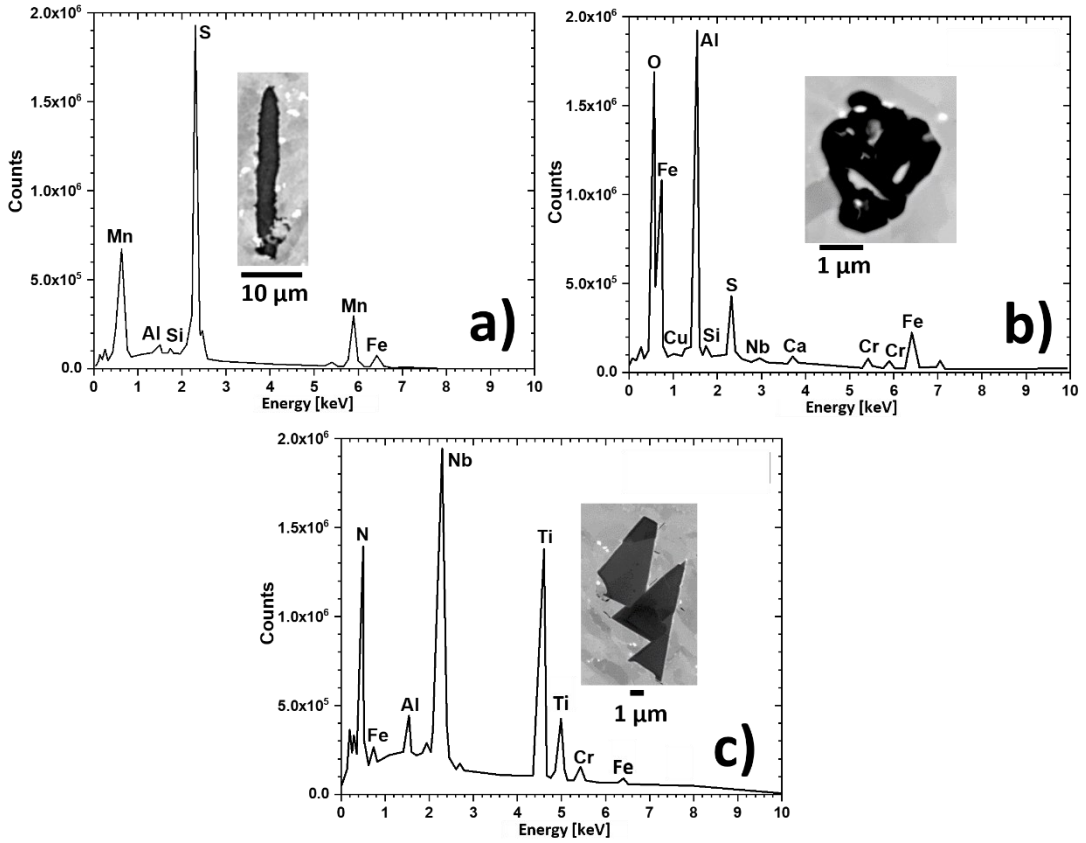

Figure 6.7: Typical SEM images and energy spectra for the inclusions found in the Gr. 91 steels in this project (a) MnS (b) Al_2O_3 and (c) Nb/Ti Nitrides.

Al_2O_3 inclusions were at times associated with MnS inclusions. This can be attributed to the solidification process of liquid steel, in which the MnS inclusions form on the already solid Al_2O_3 inclusions in the liquid steel. Therefore, when classifying these inclusions, the different types were based on composition of inclusions from the most common to the least common. For example, (S-type) MnS inclusions were the most common, therefore, these were class 1, with subclasses that included Mn (i.e., MnS inclusions) and Al (for Al_2O_3-MnS complexes), and subsequent types were class 2 Al-type (i.e., Al_2O_3), and class 3 (i.e., Ti/Nb-type).

All the inclusion types appeared dark relative to the steel matrix due to the much lower atomic number *(Figure 6.7)* and could therefore easily be differentiated from the matrix based on the grayscale threshold (*Figure 6.3*). This allows large data sets to be collected automatically. The size characteristics of the particle or inclusion are calculated via a rotating chord algorithm, which draw chords (lines) from the centre of the particle / inclusion at constant intervals. EDS composition data are acquired through the use of horizontal lines from the top to the bottom of the inclusion [180]. It should be noted, the smaller the particle/inclusion detected, the larger the iron content will be in the acquired composition, due to more X-rays from the steel matrix itself, this means smaller particles/inclusions are more inaccurate when quantifying composition. However, as discussed in *Section 6.3,* the use of a 10 kV accelerating voltage can alleviate this problem of quantifying fine inclusions (down to 0.25 μm) in size as it was simulated 50% of the electrons penetrate as little as 0.24 μm (*Figure 6.5a*).

6.4.2 Sample Homogeneity and Areas of Interest

The chemical homogeneity of Mn in the steels was assessed as an initial step in the inclusion analysis procedure. Mn was chosen because it is one of the main alloying elements which forms inclusions as it readily binds with S to create MnS. *Figures 6.8 and 6.9* show the Mn μ-XRF derived chemical distribution maps, each map consisting of at least 30 mm^2 of mapped area. *Figures 6.8a, 6.8d, 6.9a and 6.9b* show the steels which had chemical banding in the longitudinal axis of the creep sample, which included steels Es-P, ORNL-P, Euro-Pi and Euro-P2. It is also worth noting that in steel Es-P *(Figure 6.8a)* the blue dots represent coarse MnS inclusions, which were detected in the μ-XRF scans due to their size being close to that of the 20 μm spot size. *Figures 6.1 and 6.7a. Figures 6.8b and c* show the steels Es-F and ORNL-F respectively, which display a different form of segregation which formed as a result of the forged production route. More details on the micro-segregation behaviour and quantification can be found in *Chapter 4.*

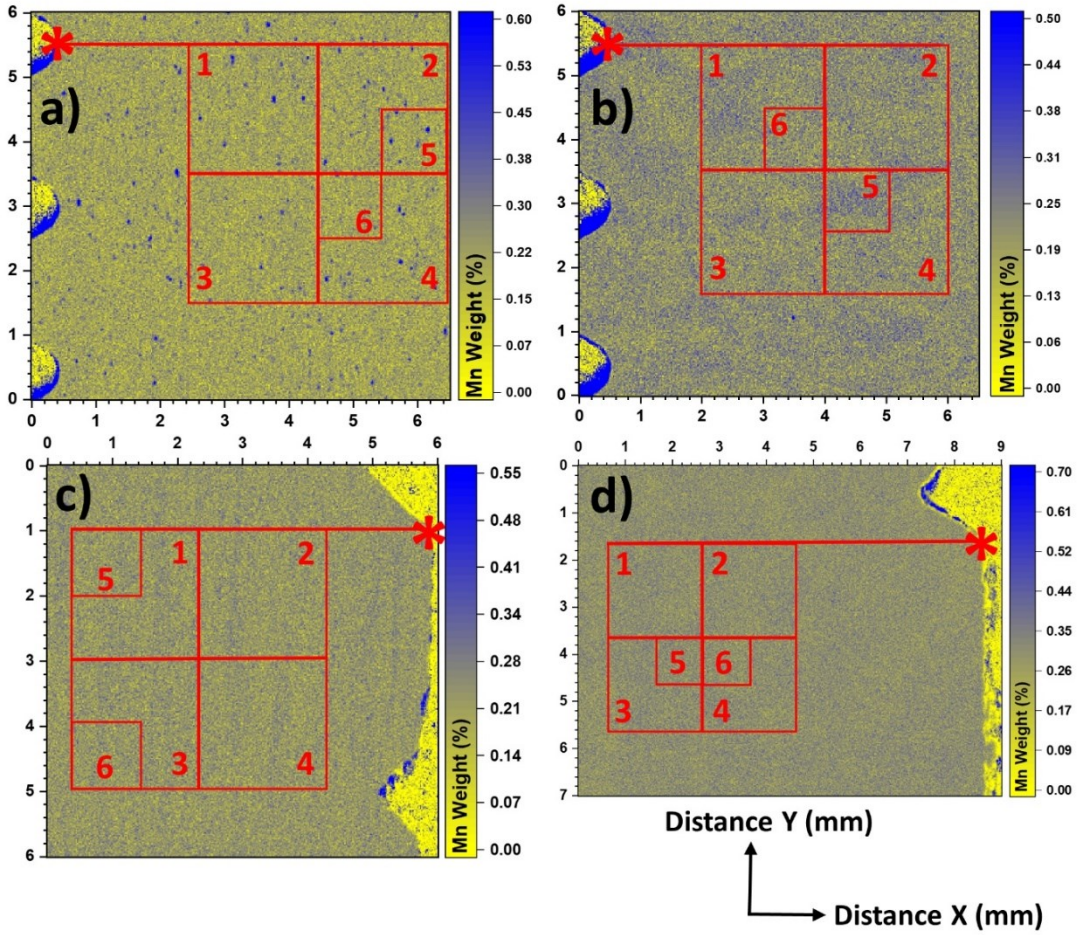

Figure 6.8: µ-XRF chemical distribution maps of steels (a) Es-P (b) Es-F (c) ORNL-P and (d) ORNL-F highlighting the chemical inhomogeneity of Mn. (Asterisk marks the edge of the steel from which the locations for the inclusion analysis were selected shown by the red boxes)

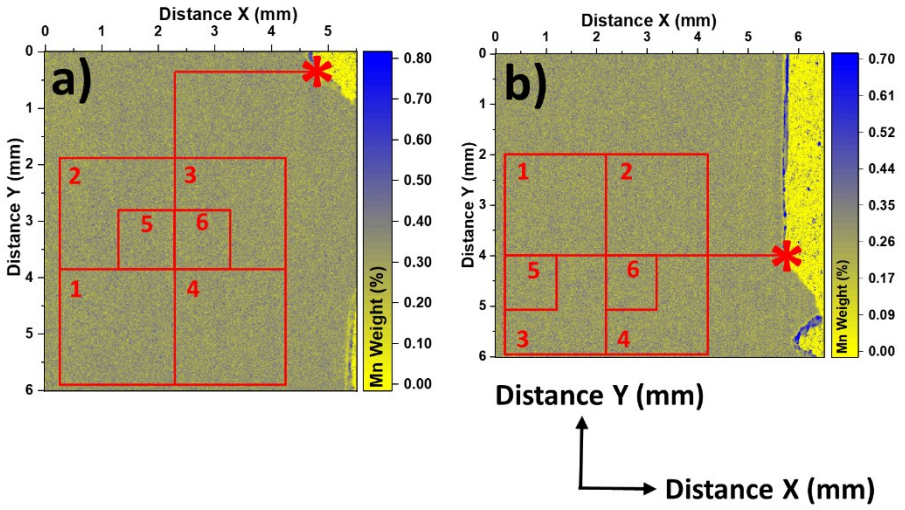

Figure 6.9: µ-XRF chemical distribution maps of steels (a) Euro-Pi and (b) Euro-P2 highlighting the chemical inhomogeneity of Mn. (Asterisk marks the edge of the steel from which the locations for the inclusion analysis were selected shown by the red boxes)

The next step in the procedure was based on the Mn µ-XRF maps shown in *Figures 6.8 and 6.9*, regions of inclusion analysis maps were selected based on the chemical distribution maps. For each Mn µ-XRF map the asterisk marks the edge of the sample which provided a starting point for the location of each of the automated SEM-based inclusion mapping regions (1-6). Large maps (1-4) were selected in a square formation to map a total square area of 16 mm^2, this provided an overview of the inclusion characteristics in the steel, with the smallest inclusion being detected at a size of 0.5 µm. A range of steel compositions were covered in these 4 maps, which can be seen in *Figures 6.8 and 6.9*, denoted by the darker shades (blue) and lighter shades (yellow). Small maps (5-6) were performed in largely positively and negatively segregated regions respectively within the previously mapped large regions (1-4). These were chosen based on the Mn wt % variation found in the µ-XRF maps, the purpose of these 2 (smaller) maps was to investigate the effect of Mn micro-segregation on inclusion characteristics with the smallest inclusion detected being 0.25 µm. This automated technique of inclusion mapping is very effective in finding the absolute numbers and variations of inclusions from area to area. In comparison to the more conventional methods, such as imaging and image analysis, (due to the acquisition of a more representative region on the sample / steel) [176][194] or scanning large regions of samples in order to achieve a representative total area [177][179]–[181].

6.4.3 Quantification of the Inclusions in the Gr. 91 Steels

This sub-section will focus on the 4 large inclusion maps for each steel in which inclusions are quantified down to the size of 0.5 μm. This will provide an overview of the inclusion populations, the 2 smaller inclusion maps for each steel will be discussed later in *Section 6.4.4* with regards to micro-segregation effects. *Table 6.1* shows the number of inclusions detected according to their inclusion types and provides the average sizes in brackets. Steel Es-P contains the highest number of inclusions in total, with an average of 210 per mm^{-2}, steel Es-F contained 114 per mm^{-2}, steels Euro-Pi and Euro-P2 contained 83 per mm^{-2}, steel ORNL-P contained 48 per mm^{-2}, and steel ORNL-F contained 20 per mm^{-2}. This rank is also mostly consistent with the MJF value for each steel, which is provided in *Table 6.1*. Es-P had the highest MJF of 345, steels Euro-Pi and Euro-P2 had an MJF of 201 and 237, respectively, Es-F had 159. Steels ORNL-P and ORNL-F which were found to be cleaner had MJFs of 104 and 134, respectively. When comparing the individual inclusion types, steel Es-P had the most MnS inclusions from all the steels, steel ORNL-P had the most Al_2O_3 inclusions.

Table 6.1: Quantification table of the number of inclusions per mm^2 (and types) and the average sizes (μm), for the steels used in this project. (For the 4 large areas per steel).

Es-P (MJF:345)				
	Area 1	Area 2	Area 3	Area 4
Inclusion Type	Number (mm^2), (Average Size (μm))			
Sulphide	202 (1.61)	175 (1.67)	186 (1.57)	182 (1.62)
Aluminate	18 (1.72)	25 (1.65)	17 (1.74)	18 (1.62)
Nb/Ti Type	6 (1.06)	5 (1.11)	3 (0.93)	3 (0.97)
Es-F (MJF:159)				
	Area 1	Area 2	Area 3	Area 4

Inclusion Type	Number (mm^2), (Average Size (μm))			
Sulphide	105 (1.16)	103 (1.12)	89 (1.31)	111 (1.20)
Aluminate	8 (2.48)	8 (1.74)	11 (2.28)	7 (2.12)
Nb/Ti Type	3 (1.93)	3 (2.43)	5 (2.50)	3 (1.43)
ORNL-P (MJF:104)				
	Area 1	Area 2	Area 3	Area 4
Inclusion Type	Number (mm^2), (Average Size (μm))			
Sulphide	29 (2.07)	20 (2.13)	24 (1.94)	19 (2.05)
Aluminate	31 (1.83)	20 (2.02)	24 (1.99)	23 (1.95)
Nb/Ti Type	--	--	1 (0.77)	1 (0.64)
ORNL-F (MJF:134)				
	Area 1	Area 2	Area 3	Area 4
Inclusion Type	Number (mm^2), (Average Size (μm))			
Sulphide	6 (2.44)	9 (2.82)	4 (2.56)	9 (2.76)
Aluminate	13 (2.52)	15 (2.15)	4 (3.03)	16 (2.37)
Nb/Ti Type	--	--	--	--
Euro-Pi (MJF:201)				
	Area 1	Area 2	Area 3	Area 4

Inclusion Type	Number (mm^2), (Average Size (μm))			
Sulphide	62 (2.29)	66 (1.99)	65 (2.44)	61 (2.69)
Aluminate	20 (1.68)	18 (1.73)	16 (1.86)	22 (1.88)
Nb/Ti Type	--	--	--	--
Euro-P2 (MJF:237)				
	Area 1	Area 2	Area 3	Area 4
Inclusion Type	Number (mm^2), (Average Size (μm))			
Sulphide	29 (2.12)	34 (2.13)	38 (2.17)	32 (2.16)
Aluminate	63 (2.47)	44 (2.28)	47 (2.28)	46 (2.30)
Nb/Ti Type	--	--	--	--

Steels Es-P and Es-F contained notably high MnS inclusion number densities (186 and 102 per mm^2 respectively) in comparison to the other inclusion types and compared to steels Euro-Pi and Euro-P2 (63 and 33 per mm^2 respectively) and steels ORNL-P and ORNL-F (23 and 7 per mm^2 respectively). Since the amount of Mn in each of the steel samples far exceeds that of S, the S content is expected to control the amount of MnS inclusions present. The amounts of S in steels Es-P and Es-F are 0.010 and 0.002 wt %, respectively, whereas in steels Euro-Pi, Euro-P2, ORNL-P and ORNL-F the S content is much lower at 0.0025, 0.001, 0.001 and <0.001 wt % respectively. It is worth noting a discrepancy in which steel Euro-Pi contained marginally more S than steel Es-F (0.0025 to 0.002 wt %), but Es-F contained more MnS inclusions. The average sizes for the MnS inclusions for each steel remained consistent across the 4 regions per sample, although the largest were in steel ORNL-F (2.65 μm ECD) and the smallest were in the ex-service steel Es-F (1.20 μm ECD) based on the averages from the 4 regions of sample. It is interesting that the ex-service steels had the smallest

average sized MnS inclusions, compared the 4 non-service steels, however the ex-service steels also contained the most S which, suggests a greater number density of MnS inclusions at a finer average size. This may suggest the ex-service steels had a faster cooling rate during solidification, leading to a larger number of finer MnS inclusions as compared to the non-service steels.

The amount of Al in each of the steels is much less than the amount of O, therefore the amount of Al will control the oxide inclusion numbers. The amount of O (in wt %) is provided for steels in the highest to lowest rank, Euro-Pi (0.0051), Euro-P2 (0.0044), Es-P (0.0043), ORNL-F (0.0027) and Es-F (0.0018). In relation to the amount of Al_2O_3 inclusions steel Euro-P2 contained the most at 50 per mm^2, steels Es-P and ORNL-P contained 20 and 25 per mm^2, respectively and steel Euro-Pi contained 19 per mm^2. Although ORNL-F has more O in it than Es-F, Es-F contained noticeably more Al_2O_3 inclusions, which may be a discrepancy or possibly due to the fact Es-F's Al content is almost double that of steel ORNL-F's (0.02 versus 0.011 wt %, respectively). The average sizes for the Al_2O_3 inclusions for each steel remained consistent across the 4 regions per sample, although the largest were in steel ORNL-F (2.52 µm ECD) and the smallest were in steel Es-P (1.70 µm ECD) based on the averages from the 4 regions sampled.

The final type of inclusions found in these steels was Nb/Ti rich nitrides, these are large enough in size to be detected and quantified in the inclusion analysis software as well as being large enough to act as potential creep cavitation nucleation sites. An example of this inclusion in steel Es-F is shown in *Figure 6.7c.* Only steels Es-P and Es-F contained this type of inclusion, on average Es-P contained 4 per mm^2 and Es-F contained 3 per mm^2. The average size of these particles varied drastically between Es-P and Es-F, in the former the average ECD is 1.00 µm, whereas in the latter it is 2.1 µm.

6.4.4 The Effects of Micro-segregation on Inclusion Quantifications

Further to the inclusion analysis discussed earlier, smaller inclusion maps were also collected. These inclusion mapping areas are denoted as Areas 5 and 6 in *Figures 6.8 and 6.9* and are 1 mm by 1 mm areas that represent the most positively and negatively micro-segregation areas available. Within these areas (5 and 6) inclusions were quantified down to a size of 0.25 µm.

Table 6.2 shows the number of inclusions detected for the smaller areas of interest for all steels according to their inclusion types and provides the average sizes. This section will focus on steels Es-P and Es-F because these 2 steels showed the largest degree of micro-segregation of all the steels studied and had the highest inclusion contents. MnS inclusions down to a size of 0.25 µm have formed during solidification and will be formed in or pushed into the interdendritic regions.

The forged chemical structure of steel Es-F meant differences in inclusion populations could be distinguished much more easily than in a banded chemical microstructure, in comparison to Es-P however, it does contain far fewer inclusions and is a cleaner steel (MJF of 159). Steel Es-P is the highest inclusion-containing steel and also the most impure (MJF of 345). *Figure 6.10* compares the mapped areas 5 and 6 (positive and negative segregation, respectively) for steel Es-P. The Es-P Mn µ-XRF map *(Figure 6.10a)* shows blue dots which can be seen represent coarse MnS inclusions in *Figure 6.10b*; these dots are consistent with the micro-segregation banding and with other elements such as Cr, Mo, Nb as seen in *Chapter 4.* Therefore, the effect of these on inclusion quantifications is to be investigated.

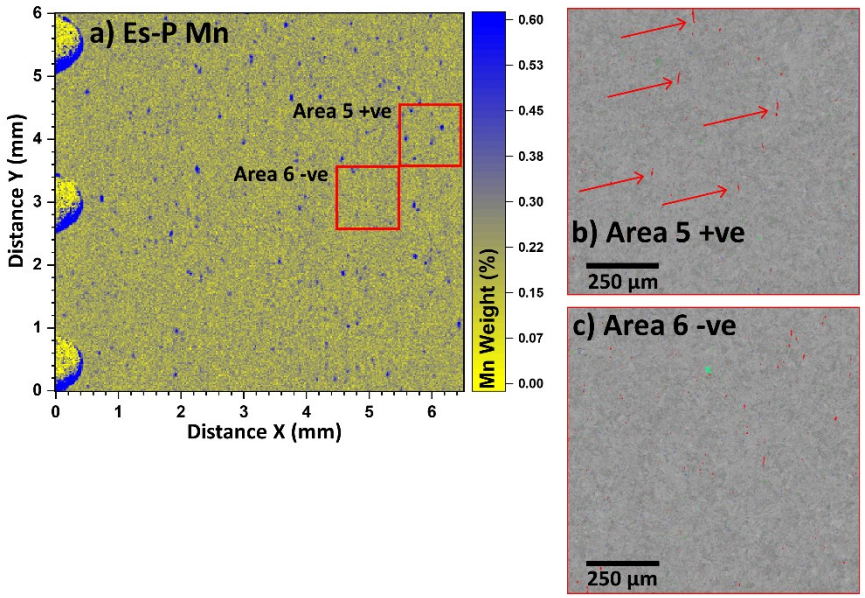

Figure 6.10: µ-XRF chemical distribution maps of steel (a) Es-P highlighting the chemical inhomogeneity of Mn with areas 5 and 6 highlighted. Inclusion analysis maps of areas 5 (b) and 6 (c) showing the distribution of MnS inclusions in red.

Steels ORNL-F, Euro-Pi and Euro-P2 did not show a significant difference between the positively and negatively micro-segregated areas as seen in *Table 6.2,* although

this difference is difficult to quantify in Euro-Pi and Euro-P2 due to the thin banding (20 to 200 µm wide). For steel ORNL-P a difference was found in the number density and size of the MnS inclusions between the positively and negatively segregated regions, 91 per mm^2 and 1.14 µm to 69 per mm^2 and 0.90 µm, respectively, which is a difference of 27 % in the number per mm^2. With regards to the Al_2O_3 inclusions, the same number density was found in the positive and negative regions, 68 per mm^2, although the size did decrease from 1.38 to 1.07 µm, respectively. 31 Nb/Ti rich particles were found in the positive region versus only 18 in the negative region, the average size remained consistent. These differences were found because steel ORNL-P showed sufficient micro-segregation but also contained banding which was on the scale of ~ 150 µm in thickness *(Figure 6.8c)*, it should be noted, only one positively and negatively area was mapped, therefore, in order to improve the statistical significance more areas will need to be mapped. In comparison steel Es-P's micro-segregation banding was roughly ~ 50 µm in thickness *(Figure 6.8a)* which means in the subsequent paragraphs when analysing steels Es-P and Es-F the effect of steel Es-P's banding is not as representative in the inclusion quantifications comparing positively and negatively segregated regions.

Table 6.2: Quantification table of the number of inclusions per mm^2 (and types) and the average sizes (µm), for the steels used in this project. (For the 2 small areas per steel, positive and negative).

Es-P		
	Area 5 (+ve)	Area 6 (-ve)
Inclusion Type	Number (mm^{-2}), (Average Size (µm))	
Sulphide	619, (0.88)	608, (0.83)
Aluminate	72, (1.01)	47, (0.94)
Nb/Ti Type	54, (0.31)	43, (0.32)
Es-F		
	Area 5 (+ve)	Area 6 (-ve)
Inclusion Type	Number (mm^{-2}), (Average Size (µm))	

Sulphide	404, (0.80)	316 (0.75)
Aluminate	15, (1.05)	16, (1.61)
Nb/Ti Type	31, (0.51)	13, (0.81)
ORNL-P		
	Area 5 (+ve)	Area 6 (-ve)
Inclusion Type	Number (mm^{-2}), (Average Size (μm))	
Sulphide	91, (1.14)	69, (0.90)
Aluminate	68 (1.38)	68 (1.07)
Nb/Ti Type	31 (0.40)	18 (0.41)
ORNL-F		
	Area 5 (+ve)	Area 6 (-ve)
Inclusion Type	Number (mm^{-2}), (Average Size (μm))	
Sulphide	8, (1.28)	8, (1.80)
Aluminate	26, (0.94)	35 (1.51)
Nb/Ti Type	11, (0.40)	3 (0.32)
Euro-Pi		
	Area 5 (+ve)	Area 6 (-ve)
Inclusion Type	Number (mm^{-2}), (Average Size (μm))	
Sulphide	186 (1.41)	225 (0.94)
Aluminate	144 (0.66)	132 (0.47)
Nb/Ti Type	--	--
Euro-P2		
	Area 5 (+ve)	Area 6 (-ve)
Inclusion Type	Number (mm^{-2}), (Average Size (μm))	

Sulphide	113 (0.92)	134 (0.97)
Aluminate	201 (0.84)	167 (0.90)
Nb/Ti Type	--	--

With regards to the ex-service steels Es-P and Es-F, when comparing the quantifications of inclusions in *Table 6.2* steel Es-P did not show any significant differences with regards to the number of MnS inclusions per mm^2, a similar number were found in the positive and negative regions (619 and 608 respectively) the average size also remained consistent. However, a greater number density of Al_2O_3 inclusions was found in the positive region compared to the negative region of interest (72 and 47 respectively) with similar averages sizes. With regard to Nb/Ti nitrides no significant differences were found in the number per mm^2 or the average size. For steel Es-F, there was a large difference in the number density of MnS inclusions between the positively and negatively segregated regions, 404 and 316 per mm^2 respectively, although the average sizes were very similar (0.80 and 0.75 µm respectively). The number density of Al_2O_3 inclusions remained consistent between the 2 regions; however, the average size did increase from 1.05 to 1.61 µm. The number density of Nb/Ti type particles was more than double in the positive region compared to the negative (31 to 13 per mm^2), the average size was 0.51 µm in the positive region and 0.81 µm in the negative region for those inclusions. It should be noted that the number density of inclusions for each steel in the large areas (*Section 6.4.3)* are much lower than the small areas, this discrepancy is due to the small areas being able to detect inclusions half the size of those in the larger areas, 0.25 to 0.5 µm respectively, this effect was also found in quantifying cavities by Siefert et al.[27]

The size distributions of MnS inclusions in the 1 x 1 mm inclusion scans for Es-P and Es-F are shown in *Figure 6.11,* with respect to the positive and negative regions of interest. The size distributions for Es-P are very similar, however, *Figure 6.11b* shows a magnified region of steel Es-P's size distribution (from 5 µm to 12 µm). It is clear there are a greater number density of MnS inclusions within this size range, the positively segregated region contains 9 versus 5 for the negatively segregated region; this explains the large blue dots in the Mn µ-XRF maps for steel Es-P *(Figure 6.8a)* which is also shown in *Figure 6.10.* With regard to steel Es-F, the size distributions

clearly show more MnS inclusions in the 0.5 - 1.0 µm size range *(Figure 6.11c)*. As found in *Chapter 4*, the extent of micro-segregation was greater in steel Es-F than in steel Es-P, this is reflected in the larger difference between positively and negatively segregated regions. *Figure 6.12* shows the size distributions for the Al_2O_3 inclusions, in line with the *Table 6.2* of inclusion quantifications steel Es-P shows more inclusions in the positive region versus the negative region. For steel Es-F, there are equal numbers in both regions, however the negative region does show some Al_2O_3 inclusions in the larger size distribution (3 between 2 and 6 µm) *(Figure 6.12b)*.

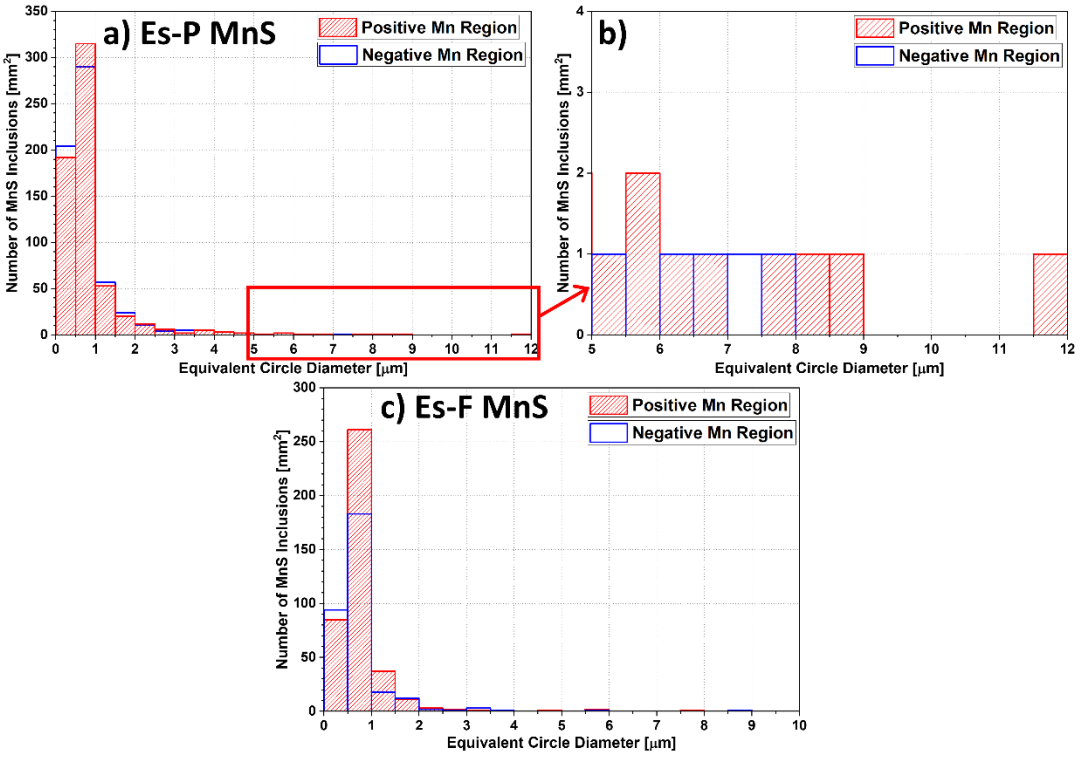

Figure 6.11: Size distributions for the MnS inclusions in the positively and negatively Mn segregated regions for steels Es-P (a and b, b is magnified from the red box in a) and Es-F (c).

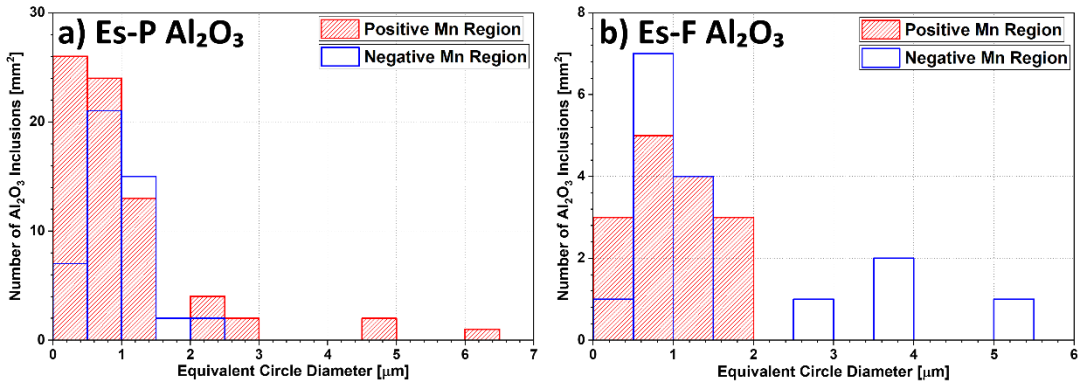

Figure 6.12: Size distributions for the Al_2O_3 inclusions in the positively and negatively Mn segregated regions for steels Es-P (a) and Es-F (b).

6.5 Copper Association with MnS Inclusions in steel Es-P

Inclusion analysis in CSEF steels is not often reported, further to that the association of impurities (such as Cu) with inclusions has not previously been studied. In order to carry out this assessment steel Es-P was chosen, this was because Es-P contained the largest amount of Cu (0.19 wt %) from all the steels in this project. Steel Es-P also possessed the largest number of MnS inclusions from all the steels in this project. The first step in the process was to chemically map a number of MnS inclusions using the SEM-EDS system to detect any inherent Cu in or around the inclusion-matrix interface. An example of this is shown in *Figure 6.13*, where an MnS inclusion with some Al_2O_3 association can be seen mapped. *Figure 6.13b* shows a bright red spot at the top of the inclusion which signifies a higher intensity of Cu and the EDS spectrum in *Figure 6.13c* shows the Cu L_α X-ray peak at 0.93 keV. After mapping a total of 30 randomly located and sized MnS inclusions it was found that there was an average of 1.20 wt % Cu within the inclusions (with a standard deviation of 0.85 wt % Cu), which is considerably more than the 0.19 wt % in the bulk composition of steel Es-P.

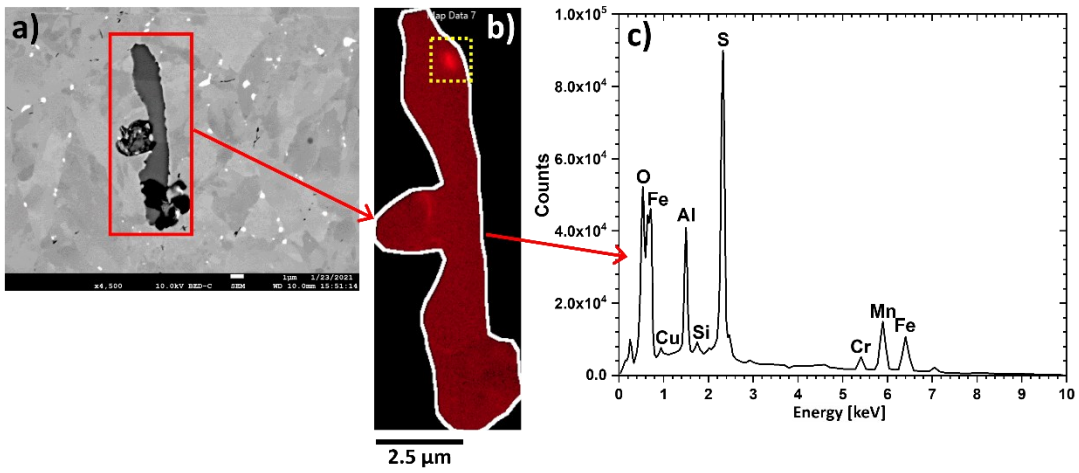

Figure 6.13: An SEM micrograph of an MnS inclusion from steel Es-P (a), corresponding EDS mapped region (b) and EDS spectrum from the mapped region (c).

In order to investigate the form in which Cu was associated with these inclusions a TEM study was performed. This involved the preparation of thin foil samples using the dual beam FIB-SEM. For this particular application a planar thin foil sample was created so the entirety of the inclusion cross section could be directly viewed and chemically mapped. Rather than a traditional thin foil sample which is created perpendicular to the sample surface a planar thin foil is created parallel to the sample surface, this can be seen in *Figure 6.14a,* where the entire length of the inclusion in in the field of view of the bright field TEM image. The Cu map of the area is shown in *Figure 6.14b and 6.14d,* at low and high magnifications, respectively. Fine Cu particles can be seen in the STEM-EDS maps, at the approximate size range of 0 - 50 nm. An association of Al at the inclusion-matrix interfaces, can be seen in *Figure 6.14c*, which is consistent with the nucleation of AlN precipitates on the already formed MnS inclusions (and Al_2O_3 inclusions). In similar TEM work, AlN precipitates were found attached to MnS inclusions in a rapidly quenched low carbon steel [209]. The higher resolution Cu map is shown in *Figure 6.15a* with the 3 main Cu particles highlighted as 1, 2 and 3. Point analysis within the particles was performed on these 3 locations and the results are shown in the corresponding spectra in *Figure 6.15b, 6.15c, and 6.15d.* Fe, Mn, and Al peaks were present in all 3 spectra; however, these were due to the MnS inclusion, steel matrix and AlN precipitates. From the spectra the Cu L_α X-ray peaks at 0.93 keV and 8.05 keV suggests the presence of high Cu concentrations. These CuS precipitates can be identified as spherical nano-sized Cu_2S

as reported by Liu et al. [153], the low solubility of Cu_2S in γ-Fe whilst cooling creates a super saturation of this precipitate therefore, large amount of fine Cu_2S precipitates form [153], this is also evident in the examples shown for steel Es-P. This analysis was complicated by the signal from the grid material (only Cu or Mo options were available). In this case a Mo grid was used, and this resulted in an overlap between Mo from the grid and S. However, it was possible to deconvolute the contributions from both S and Mo.

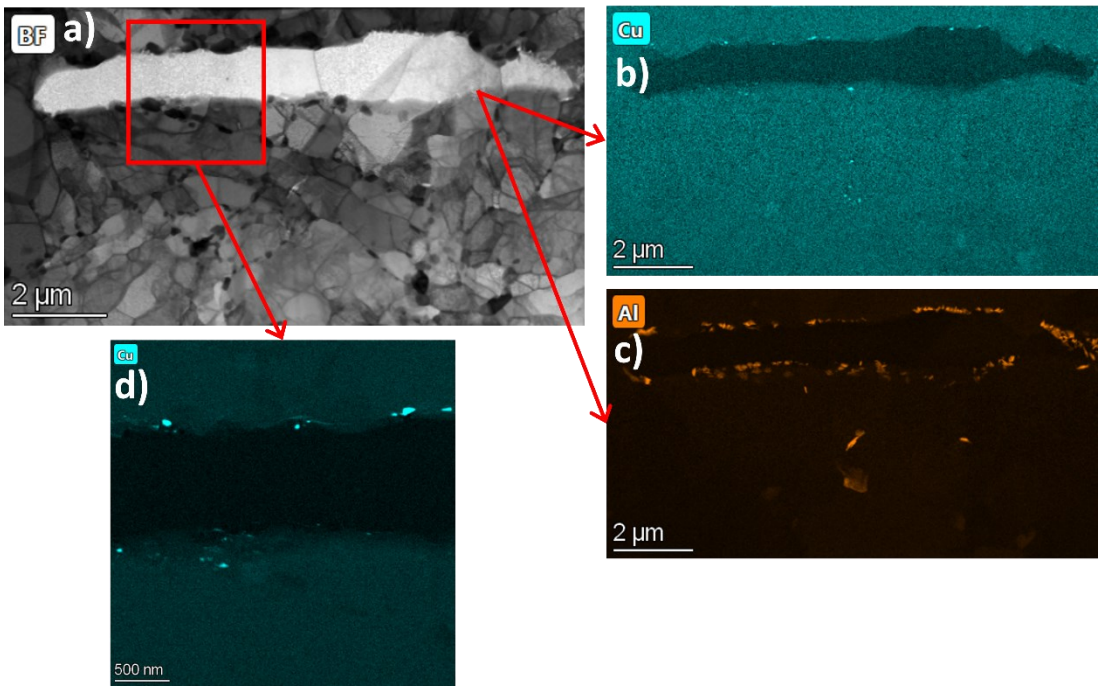

Figure 6.14: STEM micrograph of an MnS inclusion from steel Es-P showing a) BF image and chemical maps for Cu (b and d) and Al (c).

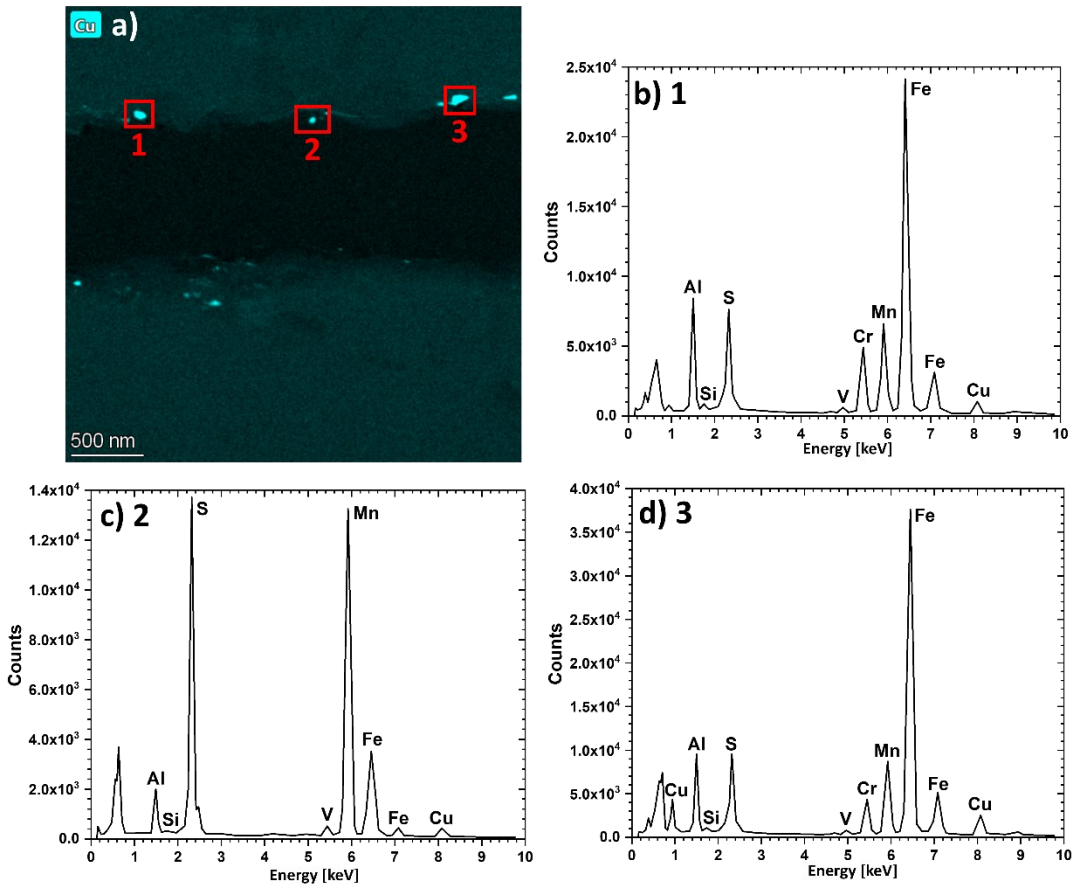

Figure 6.15: STEM Chemical map of Cu (a) with corresponding energy dispersive spectra from regions 1 (b), 2 (c) and 3 (d).

6.6 Quantification of the Aluminium Nitride Precipitates

The N:Al ratio is an important criterion to consider during the steelmaking process of Gr. 91 steels; this is to ensure a minimum amount of AlN precipitates are formed during the solidification of the steel and a maximum amount of N is available for MX-type nano precipitates for precipitation strengthening. In order to quantify the amount of AlN precipitates in each of the steels a series of 40 BSE-SEM images were taken across each of the 6 steels head sections, further details on the procedure can be found in *Section 3.4.2.* An example of an AlN precipitate can be seen in *Figure 6.16c,* with the accompanying chemical spectrum *(Figure 6.16b),* in which the Al and N peaks can be seen. *Figure 6.16a* shows an example of the size distribution of the AlN precipitates, in this case from steel Es-P, as compared to the size distribution ranges (with regards to micro-segregation) of the Laves phase particles and $M_{23}C_6$ precipitates from *Chapter 5.* When comparing ECDs the AlN precipitates are not as large as the Laves phase particles, however, the ECD is not the best representation as

the AlN precipitates are very fine and needle-like, rather than equiaxed like the Laves phase particles.

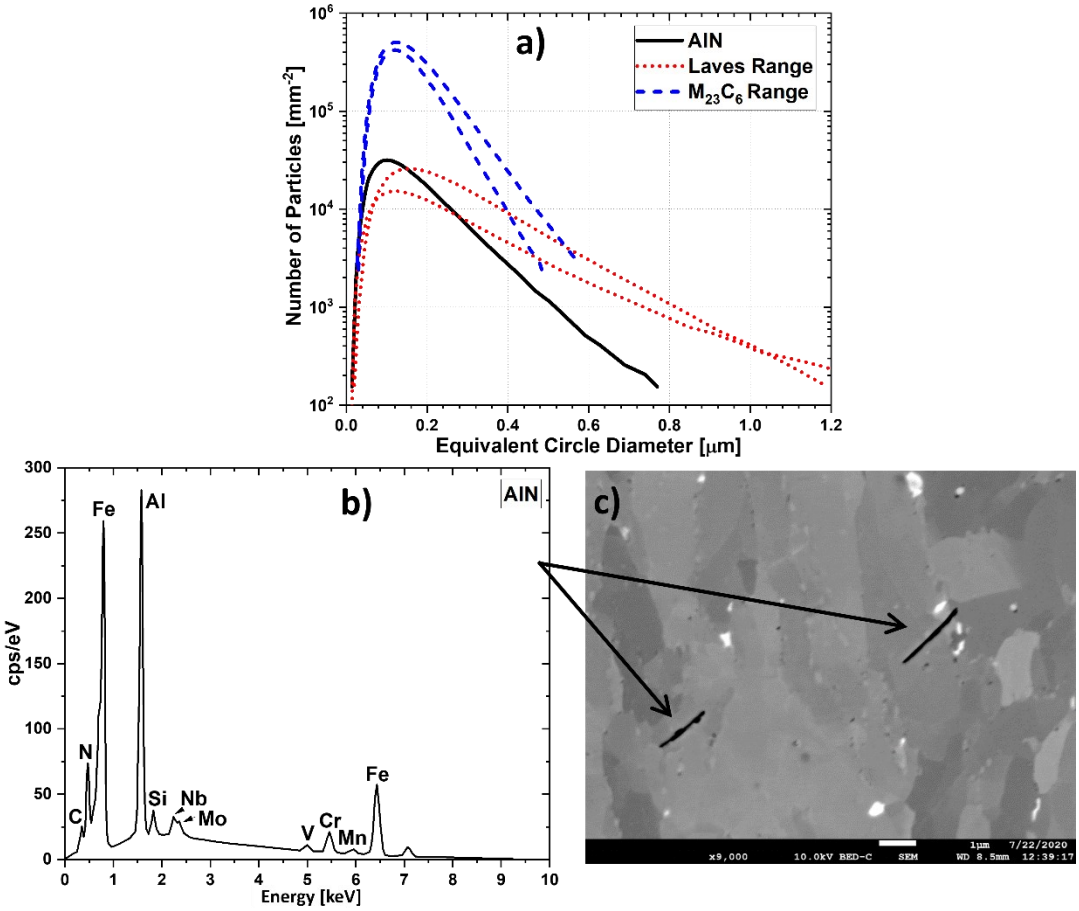

Figure 6.16: Size distribution of the AlN precipitates, Laves phase and $M_{23}C_6$ carbides for steel Es-P (a), and a typical energy dispersive spectrum of an AlN precipitate (b) with a high magnification image of the AlN precipitates from steel Es-F (c).

In steels Euro-Pi and Euro-P2 no AlN precipitates were found. These 2 steels had N:Al ratios of 28.4 and 14.4 respectively, the Al content in each of the steels was also very low in relation to the other 4 steels in this project at 0.002 and 0.003 wt % for Euro-Pi and Euro-P2, respectively. This was because these 2 steels were produced after regulations of reducing the amount of Al and increasing the N:Al in Gr. 91 steels were made [11].

In steels Es-P, Es-F, ORNL-P and ORNL-F, the N:Al ratios for each of the these were 1.135, 2.120, 1.674 and 3.60. The amounts of Al in each of the 4 steels was 0.04, 0.02, 0.031 and 0.011 w. %. Typical images used for each of the 6 steels can be seen in *Figure 6.17*. The statistics for the quantification of the AlN precipitates for steels Es-P, Es-F, ORNL-P and ORNL-F can be seen in *Figure 6.18*. *Figure 6.18c* also

compares the Thermo-Calc predictions for the area coverage of the AlN precipitates against that which was experimentally quantified. It should be noted, Thermo-Calc predicted the maximum formation of the AlN phase (for which no AlN was predicted for steel ORNL-F), this is because the AlN is known to form during solidification of the steel and does not re-dissolve during any normalising and / or tempering heat treatments [18].

The rankings of Thermo-Calc area coverages were consistent with the values found experimentally for the 3 steels (Es-P, Es-F and ORNL-P). The area coverage and number of particles per mm^2 *(Figures 6.18c and 6.18d)* were the greatest for steel Es-P, steel Es-P also contained the highest amount of Al and also had the lowest N:Al ratio of the 4 steels studied. When comparing the Thermo-Calc area coverage predictions for steel Es-P with the experimental value, a large difference is found, this may be due to the nucleation of the AlN precipitates on pre-existing MnS and Al_2O_3 inclusions, this is due to Es-P having the greatest number of (MnS and Al_2O_3) inclusions from all the steels as seen in *Tables 6.2 and 6.1*.

Steel ORNL-P contained the second largest area coverage and number of particles per mm^2, ORNL-P had the second highest amount of Al and the second lowest N:Al ratio (after Es-P), the Thermo-Calc area coverage predictions for ORNL-P agreed with the value found experimentally. Steels Es-F and ORNL-F both contained a low area coverage and number of particles per mm^2 of the AlN precipitates, due to their lower Al content and greater N:Al ratio versus steels Es-P and ORNL-P.

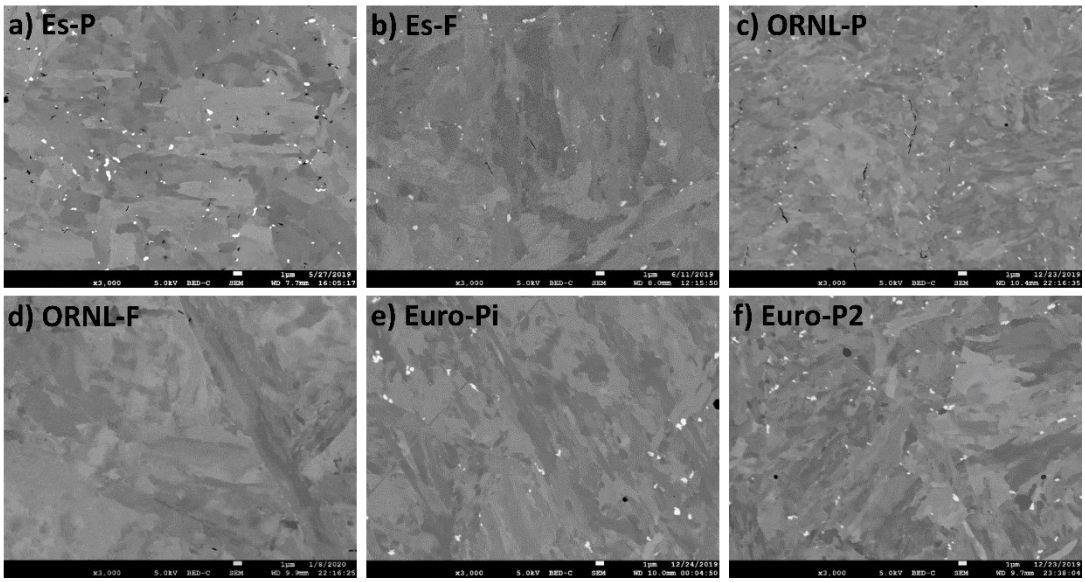

Figure 6.17: Typical SEM-BSE images used for the quantification of the AlN precipitates for steels (a) Es-P (b) Es-F (c) ORNL-P (d) ORNL-F (e) Euro-Pi and (f) Euro-P2.

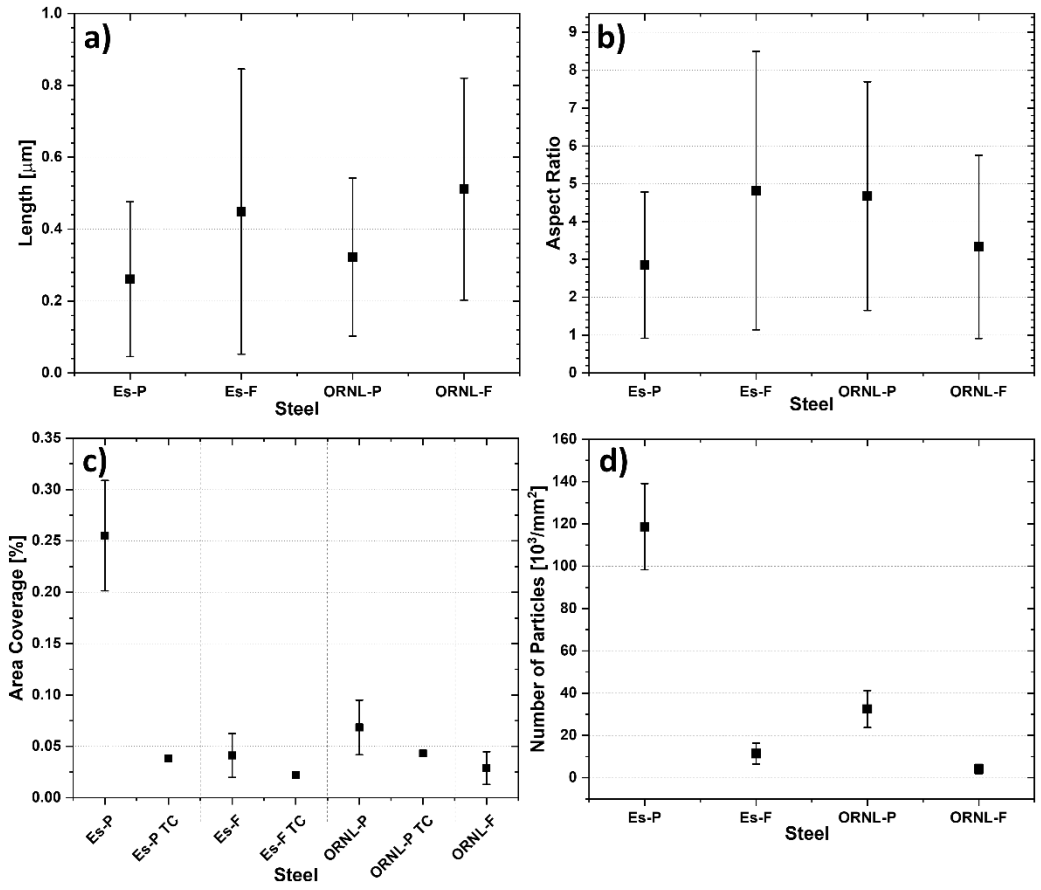

Figure 6.18: Statistics for the quantifications of the AlN precipitates from the SEM-BSE imaging of steels Es-P, Es-F, ORNL-P and ORNL-F showing (a) the average length (b) the average aspect ratio (c) the area coverage (with Thermo-Calc comparisons) and (d) the number of particles.

Figure 6.18a shows steel ORNL-F contained the longest AlN precipitates at an average length of 0.55 μm, followed by steel Es-F. These 2 steels had the lowest number densities of AlN precipitates; but they were larger in size compared to those found in steels Es-P and ORNL-P. This is also supported in the images, which can be seen in the examples of images for analysis in *Figure 6.17,* where steels Es-P and ORNL-P have many but fine AlN precipitates, but steels Es-F and ORNL-F have very few, elongated AlN precipitates. As mentioned previously for steel Es-P, the association of AlN precipitates to MnS and Al_2O_3 inclusions was also common, an example of this was shown earlier in *Figure 6.14c* where the AlN precipitates are present on the MnS / matrix interface in steel Es-P. Furthermore, *Figure 6.19a* shows examples of the association of AlN precipitates with other inclusion types (MnS and Al_2O_3), which is due to the nucleation of the AlN precipitates on other inclusions which had already formed in the steel. This increases the effective size of inclusions as well as increasing their stress concentrating effect (which can increase the susceptibility of crack initiations) through the angular morphologies [146]. The Thermo-Calc simulation in *Figure 6.19b* shows that Al_2O_3 inclusions nucleate upon solidification followed by MnS inclusions at ~1350 °C, AlN then precipitates at ~1100 °C. As Al_2O_3 and MnS inclusion are already present in the steel they can act as nucleation sites for AlN precipitates.

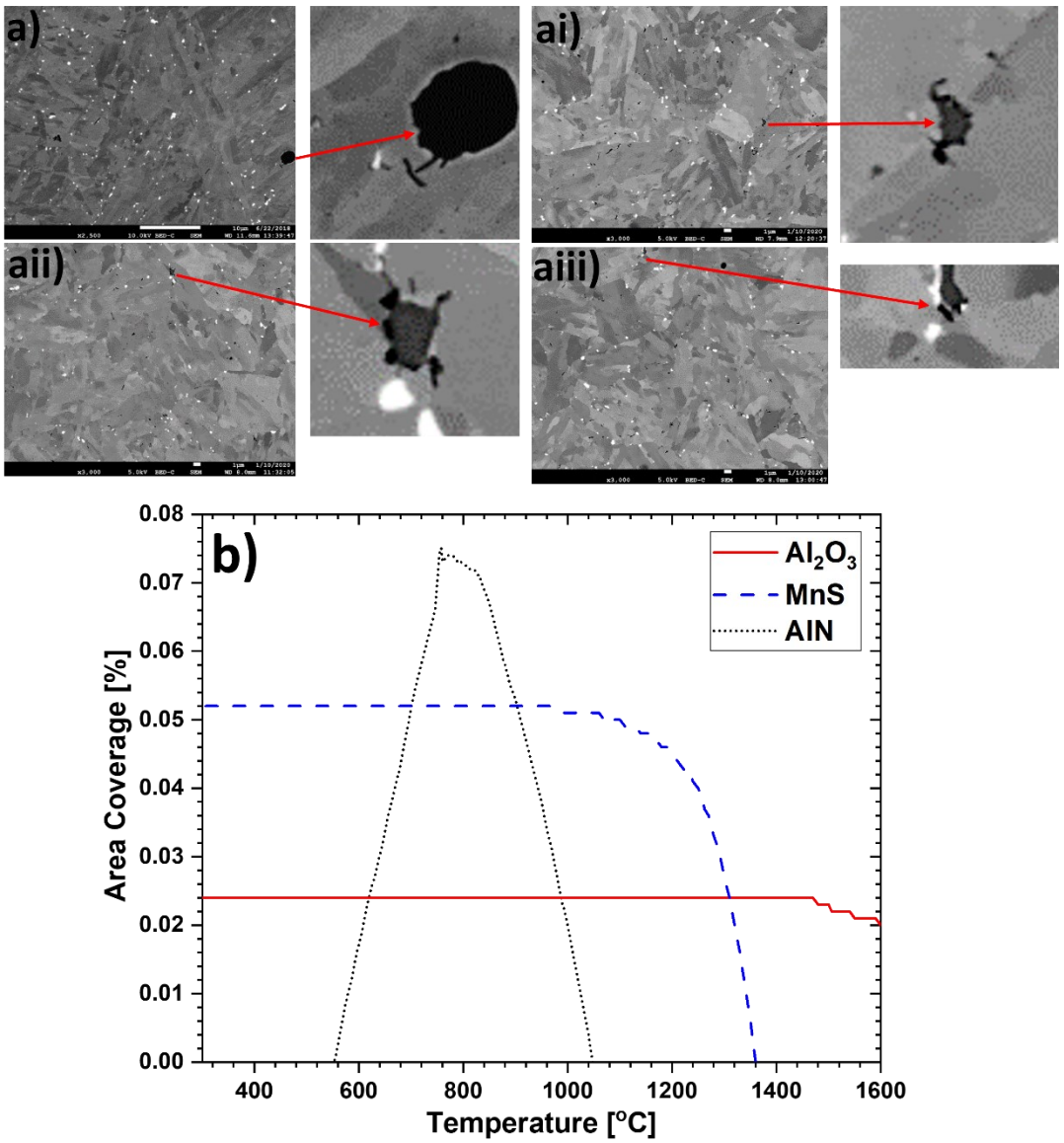

Figure 6.19: Examples of AlN precipitate association with other inclusions in the steel for steels Es-P (a and ai) and ORNL-P (aii and aiii) and b) a phase formation prediction from Thermo-Calc for the inclusions Al_2O_3, MnS and AlN, using the Es-P steel composition.

6.7 Simulating the Amount of MnS and Al_2O_3 Inclusions using Thermo-Calc

Figure 6.20 compares the differences in area coverage between MnS and Al_2O_3 inclusions with regards to the experimental values from the positively and negatively segregated regions (of the smaller area analysis *Section 6.4.4*) and those predicted by Thermo-Calc simulations using the steel compositions provided in *Chapter 3, Table 3.3* for each of the steels in this project. For the MnS inclusions, there is good agreement with the Thermo-Calc prediction rankings for each steel when compared with the experimental area coverages. For Al_2O_3 inclusions there is also good

agreement between rankings for steels Es-P, Es-F and ORNL-F. It should be noted that the amount of O for steel ORNL-P was not provided, therefore, the Thermo-Calc simulation for Al_2O_3 was omitted for that steel.

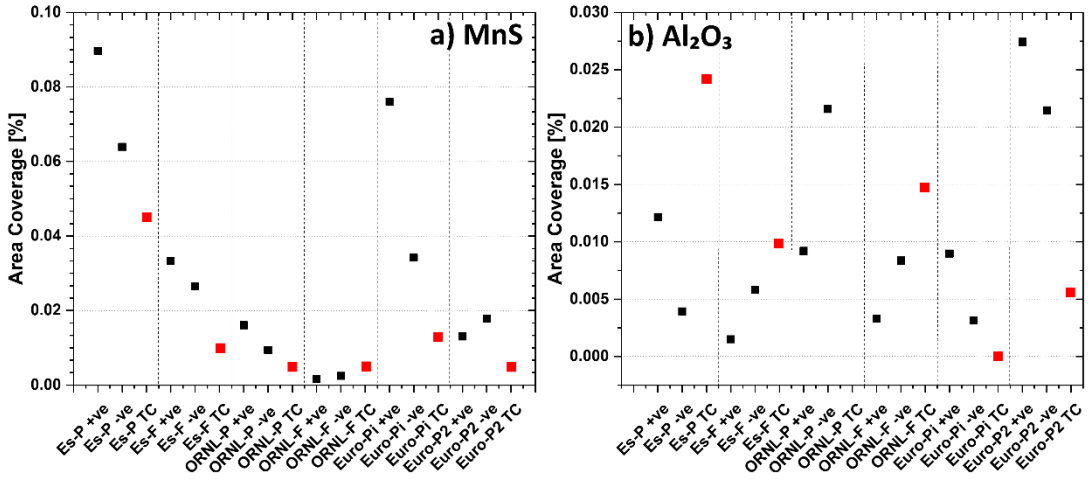

Figure 6.20: Graphs comparing the amount of area coverage of the MnS (a) and Al_2O_3 (b) inclusions acquired experimentally and predicted by Thermo-Calc (from Figure 6.20).

There are distinct trends for the quantification of area coverages for the MnS and Al_2O_3, respectively. With regards to the Al_2O_3 inclusions *(Figure 6.20b)*, the area coverage was consistently overpredicted compared with the experimental values (for steels Es-P, Es-F and ORNL-F), this is because Al_2O_3 inclusions form first upon solidification, which is also explained in *Figure 6.19b* and subsequent inclusion types such as MnS form later in solidification ~1350 °C often using the Al_2O_3 inclusions as sites for nucleation, which results in the Al_2O_3 inclusions being covered up. This effect is why a smaller area fraction of Al_2O_3 was quantified experimentally versus that predicted by Thermo-Calc. However, for steels Euro-Pi and Euro-P2 the amount of Al_2O_3 predicted by Thermo-Calc was below that which was quantified through the inclusions analysis. Conversely, more area coverage of MnS inclusions were quantified experimentally than predicted in Thermo-Calc, due to the same reason of the MnS inclusions forming around the pre-existing Al_2O_3 inclusions. However, there was 1 discrepancy, which was with regard to steel ORNL-F, in which Thermo-Calc did predict more MnS inclusions than what was quantified experimentally. This may have been due to sampling regions due to the very low numbers of MnS inclusions compared with the other steels in this project.

6.8 Cavitation Association with Inclusions

In order to investigate the association of cavities with inclusions, a series of images and chemical maps were taken in the transition sections for each of the 6 steels. The transition section, which is between the head and gauge sections was chosen because the number of cavities per unit area was very low for all the steels. Therefore, this was where cavitation was in its initial stages. It should be noted that the samples were not polished using the final step of colloidal silica for this analysis to avoid any contamination of the cavities with the colloidal silica solution. The statistics for the inclusion association with cavities are provided in *Table 6.3* and examples of typical images and SEM-EDS data acquired are provided in *Figure 6.21. Figure 6.21a* shows an image taken for steel Es-P with the corresponding EDS maps showing MnS and Al_2O_3 inclusions associated with the cavities and *Figures 6.21b* and *c* show Al_2O_3 inclusions associated with cavities in steels Euro-P2 and ORNL-F respectively. *Table 6.3* summarises for steel Es-P, of 73 cavities mapped 16 were associated with MnS inclusions and 7 with Al_2O_3 inclusions, one in every 3.2 cavities was associated with an observed inclusion. Steel ORNL-F had the lowest cavity to inclusion ratio (of 1.5) which meant 2/3 of the cavities were associated with an inclusion, steel Euro-Pi however had the largest cavity to inclusion ratio (of 9.6), which mean roughly 1 in 10 cavities were associated with an inclusion. The cavity to inclusion ratio has a rough trend with the inclusions quantified in the large area analysis (*Table 6.1).* Most of the cavity - inclusion associations were with the Al_2O_3 inclusions, the exception being the ex-service steel Es-P which had a strong association with MnS inclusions, this may have been due to the coarse MnS inclusions identified in *Figure 6.10*, or the total number of MnS inclusions which steel Es-P contained being considerably more than the other steels. When comparing the remaining 5 steels, inclusion to cavity ratios with just the Al_2O_3 inclusions quantified in *Table 6.3,* no significant correlation is found. The cavitation to inclusion ratios could be even greater than what was measured, which may have been due to inclusion fallout as well as sectioning effects during the metallographic sample preparation (i.e., grinding and polishing steps).

Table 6.3: Summary table of the statistics of the inclusion to cavity association from the gauge and transition sections of all the steels in this project.

Steel	No. of Cavities Mapped	Inclusion Association		Cavity to Inclusion ratio
		MnS	Al_2O_3	
Es-P	73	16	7	3.2
Es-F	28	4	4	3.5
ORNL-P	102	2	23	4.1
ORNL-F	62	3	38	1.5
Euro-Pi	173	1	17	9.6
Euro-P2	147	--	51	2.9

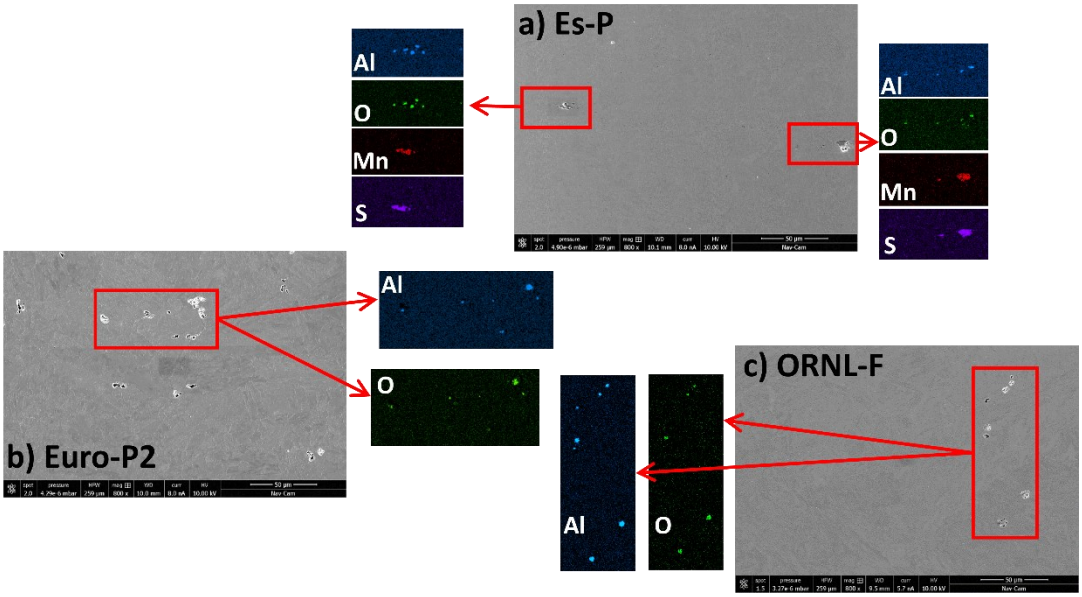

Figure 6.21: Examples of inclusion to cavity association showing SEM images and corresponding chemical maps performed in the SEM-EDS for steels (a) Es-P(b) Euro-P2 and (c) ORNL-F.

6.9 Cavitation and Hardness Profiles in the Gauge Sections

Quantifying cavitation in steels Es-P and Es-F was carried out in the region of the gauge section around the un-failed notch. As these two steels were creep tested as double notched bar samples, the nucleation of cavitation and cracking and then eventual failure was expected to occur in one of the notched regions. The purpose of the double notch was to accelerate the failure by providing a fixed stress concentration at each notch, as well as revealing damage prior to failure at the un-failed notch after 1 of the 2 fails and the test is stopped. Images for cavity quantification were taken

every 0.5 mm from one notch root across to the other notch root, the notch roots can be seen in *Figure 3.3*. The number of cavities for each of the steels per mm^2 and average size are shown in *Figure 6.22.* The number density of cavities is significantly higher in steel Es-P than in steel Es-F; it can be seen in *Figure 6.22a* that the number density of cavities in Es-P increases up to 6000 - 7000 per mm^2 at the notch roots and decreases to around 2500 per mm^2 at the central region between notches, whereas in Es-F the number of cavities per mm^2 stays consistently around the ~500 range from one notch root to the other. This suggests that steel Es-F has a higher resistance to creep damage in the form of creep cavitation and is reflected in its higher creep ductility than steel Es-P (ROA of 83.0 % in Es-F, versus 26.5 % in Es-P, *Table 3.2).* *Figure 6.22b* shows the average sizes of the creep cavities measured in the 2 steels, steel Es-F consistently contained coarser creep cavities, which may have been due to the longer time to rupture than steel Es-P (6,714 to 1,408 hours, respectively). The greater number density and finer creep cavities in steel Es-P could indicate continued nucleation of cavities with little growth, which could be due to the considerably greater numbers of inclusions (also including AlN precipitates) in the steel compared with Es-F.

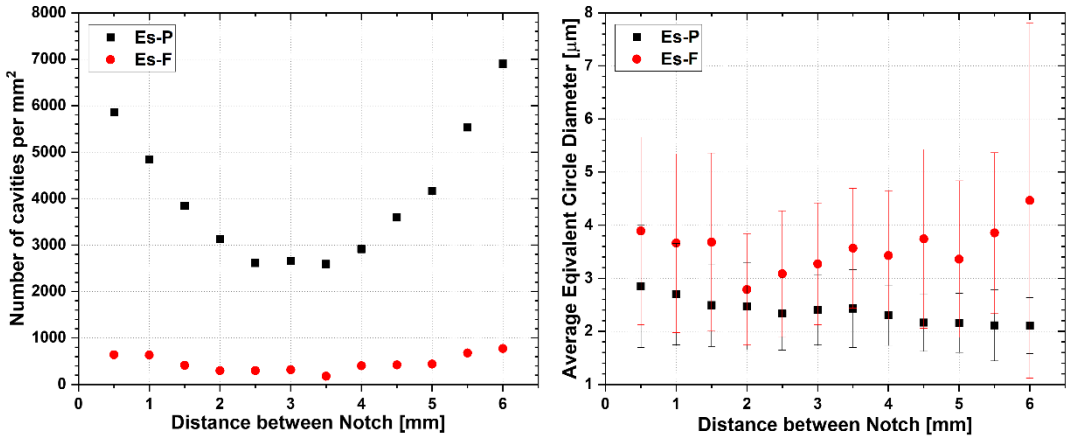

Figure 6.22: Graphs showing the number of cavities (a) and average size of cavities (b) between the un-failed notches of steels Es-P and Es-F.

For steels ORNL-P, ORNL-F, Euro-Pi and Euro-P2, the statistics *(Figure 6.23)* for the number density of cavities and respective average sizes were taken along the gauge length of the smooth bar, starting from 1 mm away from the fracture up until the transition region of the creep bar. Steel ORNL-P showed the greatest number density of cavities of the 4 steels *(Figure 6.23a);* it can be seen that close to the fracture surface

the number of cavities is close to 2000 per mm^2 and even at distances of 8 - 14 mm away from the fracture there are still ~1000 cavities per mm^2. In comparison the other ORNL steel ORNL-F contained very little creep cavitation in its gauge section, the number of cavities were consistently between 0 - 150 per mm^2. This trend did not correlate with the creep ductility figures, in which steels ORNL-P and ORNL-F possessed ROAs of 47.5 and 13.0 % respectively *(Table 3.2)*. However, the considerably greater number density of inclusions (also including AlN precipitates) in ORNL-P may explain why so many more creep cavities were quantified. Steels Euro-Pi and Euro-P2 contained 250 - 650 cavities per mm^2 across their gauge length, these values were in between those of ORNL-P and ORNL-F. The steel with the lowest number density of cavities (ORNL-F) did, however, possess the highest average size *(Figure 6.23b)* with cavities up to 25 µm close to the failure region. Steel ORNL-P contained the finest cavities with steels Euro-Pi and Euro-P2 in between ORNL-F and ORNL-P with regard to the average size.

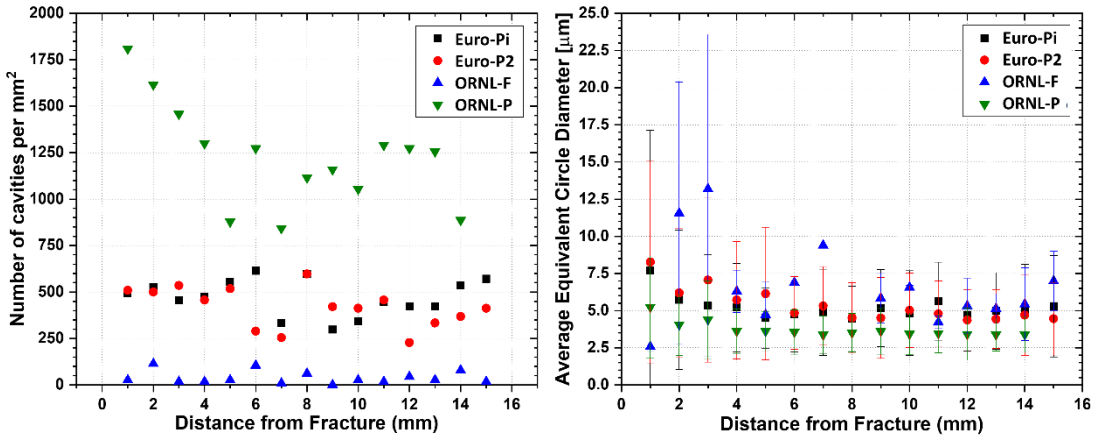

Figure 6.23: Graphs showing the number of cavities (a) and average size of cavities (b) from the gauge sections (starting from fracture) of steels ORNL-P, ORNL-F, Euro-Pi and Euro-P2.

The hardness profiles are provided in *Figures 6.24 and 6.25. Figure 6.24* shows the profiles for steels Es-P and Es-F, the profiles were taken from the centre of the un-failed notch along the gauge length of the creep bar towards the transition section. A decrease in hardness between the un-failed notch and the failure point of the creep specimens can be seen for both of the steels; for both the steels this value is approximately 175 HV. It should be noted that the decrease in hardness in the gauge section versus the head sections may well have been due to creep cavitation as the values were much lower than the micro-segregation ranges shown in *Section 5.2*. For

steel Es-P this was 211 HV and for steel Es-F 192.4 HV, therefore, the decrease in hardness for Es-F was much lower compared to that in Es-P, by approximately 20 HV. The changes in the micro-hardness can be associated with the microstructural evolution in the stressed regions of the creep specimens. It is clear that steel Es-P underwent more microstructural evolution than steel Es-F. As mentioned in the literature review *Section 2.4* the main mechanisms which contribute to softening are the formation of creep cavities, recovery of the martensite matrix, secondary phase evolution, and coarsening of the $M_{23}C_6$ carbides and MX carbo-nitrides. It was found that steel Es-P was much more susceptible to creep cavitation then steel Es-F, but the remaining characteristics were not studied in this project.

For steels ORNL-P, ORNL-F, Euro-Pi and Euro-P2 the hardness profiles were taken in the gauge section from the failure towards the head section of the steel, these can be seen in *Figure 6.25*. For steels ORNL-P and ORNL-F *Figure 6.25a* shows the hardness profiles; for ORNL-P the hardness starts at ~150 HV at the failure regions and reaches 180 HV at the end of the gauge section, this is a notably large decrease as the average micro-hardness from the head section for ORNL-P was 243.6 HV. For steel ORNL-F the micro-hardness begins at 160 HV at the failure region and quickly climbs to 200 - 210 HV, which is roughly the average micro-hardness obtained for the steel. It should, however, be noted steel ORNL-P had a very long gauge section (about 25 mm) compared with that ORNL-F which was ~ 10 mm. Large differences in the micro-hardness changes were found between the two ORNL steels, ORNL-P showed a large change which was most likely due to far greater creep cavitation, this is because ORNL-P only lasted for 1, 259 hours during the creep test so microstructural evolution may have not been very significant. However, these results are difficult to explain because ORNL-P showed a large amount of creep cavitation but an ROA of 47.5 %, whereas ORNL-F had an ROA far lower at 13 % but less creep cavitation.

Figure 6.25b shows the profiles for steels Euro-Pi and Euro-P2; the average micro hardness values for both steels were quite similar, 230.9 and 228.6 HV respectively. From the profiles it can be seen that although there is a large variation in the data a trend does exist. For steel Euro-Pi the micro-hardness starts at roughly 180 HV and goes up to 210 HV along the length of the gauge and for Euro-P2 it also starts around 180 HV but only reaches around 200 HV towards the end of the gauge section. The biggest differences between these 2 steels in terms of microstructure are the lower

N:Al ratio in Euro-Pi (28.4 versus 14.4 in Euro-P2) and Euro-Pi having considerably less Laves phase as discussed in *Chapter 5*. The microstructural evolution can be considered quite similar in these two steels, this is also due to similar levels of creep cavitation in these steels.

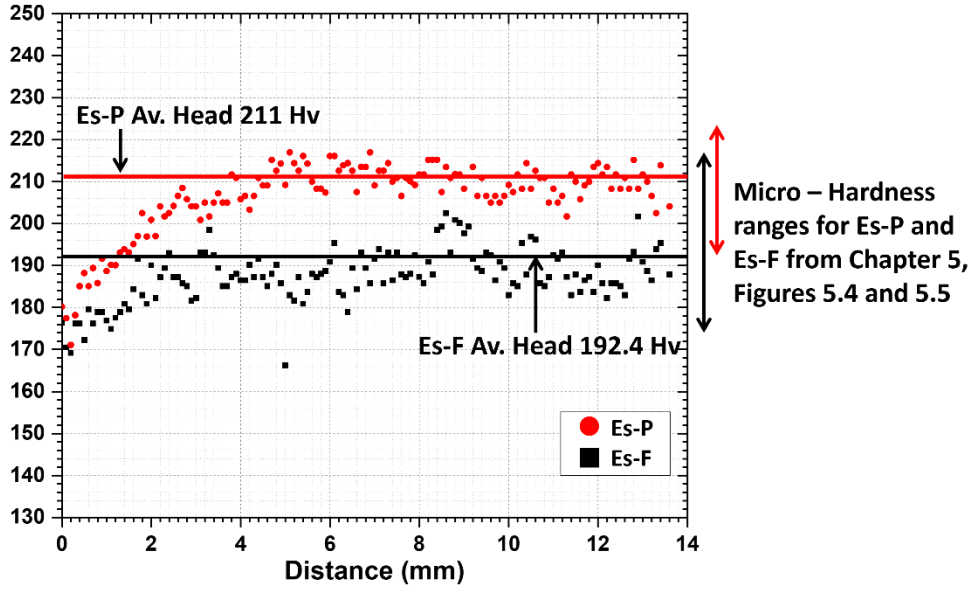

Figure 6.24: Vickers micro-hardness profiles of the gauge sections of steels Es-P and Es-F, point 0 mm signifies the failure point. (The average micro-hardness and micro-hardness variations from the head sections is also provided)

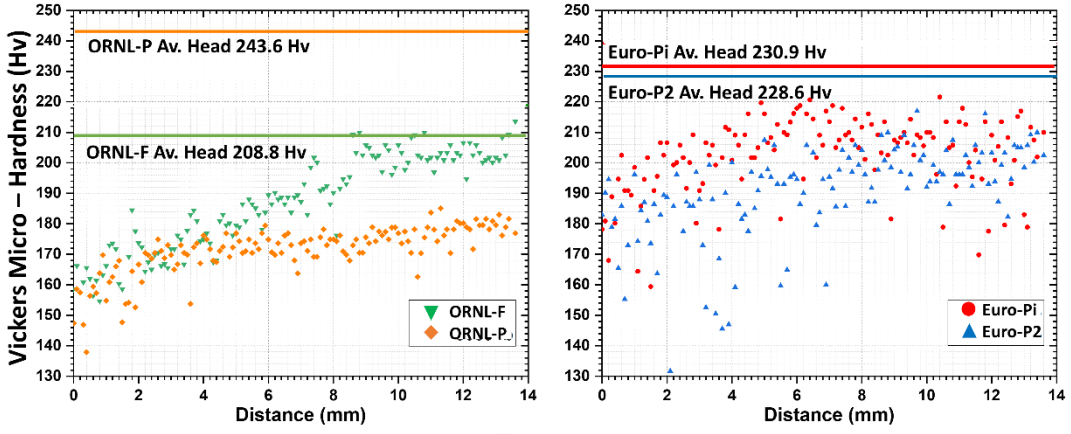

Figure 6.25: Vickers micro-hardness profiles of the gauge sections of steels (a) ORNL-F and ORNL-P and (b) Euro-Pi and Euro-P2, point 0 mm signifies the failure point. (The average micro-hardness from the head sections is also provided)

6.10 Summary

Investigations into the effect of accelerating voltages on automated inclusion analysis were undertaken. An accelerating voltage of 10 kV was shown to be advantageous

when used for inclusion analysis with regards to improved resolution and a significantly lower interaction volume compared with 20 kV.

Experimental and simulated inclusion analysis was performed which was largely consistent with the MJF rankings. A technique suggested for locating sampling regions was also implemented which utilised chemical mapping by μ-XRF to ensure compositional extremes are represented in order to include variations in the inclusion populations from area to area. Significant variations were only found in steel Es-F due to the localised behaviour of micro-segregation, which was easier to detect. AlN precipitates were strongly associated with other microstructural features, namely other inclusions (MnS and Al_2O_3) which had already formed in the steel during solidification, effectively increasing their size and potential stress concentrating action.

Creep cavitation was considerably reduced in steel Es-F versus steel Es-P, with regards to the ex-service steels. This can be linked to the creep ductility figures for each of the two steels for which Es-F possessed an 83 % ROA and Es-P 26.5 %. For the remaining non-service steels, the quantification of creep cavities was performed in the smooth bar gauge section. The ORNL steel ORNL-P contained considerably more cavities than the ORNL-F forging, however, this did not correlate with their creep ductility figures, for which ORNL-P possessed 47.5 % ROA and ORNL-F 13 % ROA, although the excessive cavitation in ORNL-P can be linked to the much greater number of inclusions and AlN precipitates. The two European steels Euro-Pi and Euro-P2 showed similar cavitation characteristics in their gauge section, although Euro-Pi has a longer time to failure (66,431 hours) and lower ROA (7.5 %) versus Euro-P2, 38,504 hours and 30 % ROA, respectively. The creep test results do not show any significant correlations between for the Euro steels.

Chapter 7 : Discussion

The following discussion will discuss the results acquired in *Chapters 4* to *6* in further detail.

7.1 Processing routes and Micro-segregation in the Steels

In *Chapter 4* the chemical microstructures were investigated for each of the steels, the production routes and assumed post-casting refining / heat treating and shaping largely influenced the chemical homogeneity (size / scale and severity) of each steel. The observed chemical heterogeneities are a result of solidification segregation and the subsequent cooling and thermo-mechanical treatments. It should be noted that due to the low tonnage and very specific applications of Gr. 91 and other CSEF steels, ingot casting is typically used as continuous casting only becomes a cost-efficient process when hundreds of tonnes of steel are being produced. The following discussions will use the literature review in this thesis as well as information on the ORNL steels to link the post-casting processing routes and micro-segregation characteristics of the steels.

7.1.1 ESR processing

The ESR process is commonly used for many critical applications where the refinement of steel composition and inclusions is important [113]. This is evident in the case of Gr. 91 steels, for which two of the steels in this study, ORNL-P and ORNL-F have been ESR processed [13]. Furthermore, the ORNL steels were produced in the mid-1970s, with the other four steels in this study (Ex-service and Euro) being produced at later dates. Therefore, the importance and practice of steel refinement for Gr. 91 steels was already well established. Furthermore the release of several initiatives such as Code Case 2864 [24] and EPRI recommendations [19] have further emphasised the importance of composition control. ESR processing is likely to have been used for the Ex-service and Euro steels, for a number of reasons, as given below.

i. The control and refinement of the chemical composition is an important criterion for Gr. 91 and other CSEF steels, therefore ESR processing is likely to have been employed for all the Gr. 91 components which require creep resistance. Some examples of the critical applications in which ESR processing is used are steam turbines [120], die steels [119], ultra-high strength steels [93], bearing steels [121] and Gr. 91 products [13].

ii. Although the MJF values are quite varied between each of the six steels (*Table 7.1*), the only steel which showed a distinct difference was steel Es-P, with an MJF of 345. This could be due to an abnormally high amount of impurity and inclusion-forming elements in the original cast, as well as little removal of the impurity elements during ESR processing. The final product after ESR processing is a result of many initial conditions and parameters [93], e.g., the inclusion and impurity content in the electrode, furnace atmosphere and type of slag system being used.

iii. The TIL (total impurity level) content (*Table 7.1*), which is a measure of the total N, S and O, proposed by Ali et al. [93] can also be compared for the six steels. The reduction of the TIL content due to the ESR processing cannot be compared in this study, however the TIL content for the known ESR processed (ORNL) steels can be compared with that of the remaining steels. The TIL contents of the ORNL steels were 0.0529 and 0.0433 wt % for ORNL-P and ORNL-F, respectively. It should be noted, a marginally larger value for ORNL-P would be expected because the O content of ORNL-P was unavailable (typical O content is around 0.0001-0.0005 wt %). The TIL contents for the four remaining steels fell within or were very close to these two values, which can be seen in *Table 7.1*. A similar TIL content implies that all the steels underwent ESR processing.

iv. With regard to the inclusion content, the same inclusion types were found across all the steels, which consisted of MnS and Al_2O_3 inclusions. Wang et al. [119] found that many exogenous complex inclusions which formed during the refining process were modified to less harmful inclusions such as Al_2O_3 during ESR processing. Therefore, the presence of these types of inclusions (see *Section 6.4.1*) implies that all the steels did indeed undergo ESR processing. Furthermore, since the known ESR steels (ORNL) have the same inclusion types as the remaining steels, that too also implies ESR was performed for all of the steels.

7.1.2 Micro-segregation due to pipe-making or forging

Chapter 4 investigated the micro-segregation characteristics of the steels in this study. Information on this is summarised in the *Table 7.1*. The μ-XRF and SEM-EDS mapping both found similar trends in terms of a ranking system for the micro-

segregation severities (*Sections 4.3-4.5)*, the order was as follows from highest to lowest. Es-F, Es-P, ORNL-P, Euro steels, ORNL-F. For the pipe steels (Es-P, ORNL-P, Euro-Pi and Euro-P2), the micro-segregation spacing is on a similar scale to that of a large ESR processed steel ingot, i.e. as shown in *Figure 2.23* from Yan et al. [121]. It should be noted, however, that the pipe steels did also have reduction ratios applied, which can explain the smaller micro-segregation spacing.

From the possible pipe or tube production methods identified in the literature (JFE [94] and Vallourec [95]), a plug mill was most likely to have been used for the Es-P due to its large diameter. Due to this pipe-making process, the steel's microstructure was stretched and reduced in thickness based on the reduction ratio, however, the original ingot size and reduction ratio are not known. Typically, the rolling elongation can be 4 to 7 times the original ingot length and the cross-section reduction can be up to 85 % [98]. For the Es-F steel, which is part of a geometrically complex tee-piece section, a closed-die forging process was most likely to have been used, with subsequent machining into a hollow component. Therefore, it can be assumed that an aggressive reduction ratio was not applied to this steel. This can explain the large spacing between the large positively segregated regions, which has been summarised in *Table 7.1*. The micro-segregation severities were the greatest in these two ex-service steels, compared with the other steels studied in this project. Based on the literature studies on ESR, it can be assumed a high melting rate was used for processing the ingot, this would have led to a high solute enrichment in the interdendritic regions [87][122].

Similarly, to the Es-P steel the ORNL-P showed chemical banding along the length of the creep specimen. This was from the mandrel mill pipe-making process, which is commonly used for smaller diameter pipes (25 – 180 mm outer diameter) [94][95]. Much like the Es-P steel, the reduction ratio is unknown for the pipe-making process, therefore cannot be compared to the other pipe steels. For ORNL-F, a saddle forging process was used, which involves the use of a mandrel (piercer) to help keep open and maintain the shape of the cavity. Since no material was predicted to have been machined out from the steel like it was for Es-F, a greater reduction ratio can be assumed, this is reflected in the spacing between positively segregated regions. When compared to the Es-F steel, the ORNL-F steel shows closer spacing of positively segregated regions. Micro-segregation severities (positive and negative) were found

to be far less significant in these ORNL steels (compared to the Ex-service steels). The micro-segregation levels of ORNL-P were less than those of Es-P but more than the Euro steels, whereas ORNL-F had the lowest micro-segregation levels from all the six steels. However, since the micro-segregation were far less in the ORNL-F steel this may have meant a much slower melting rate.

For the Euro steels, the plug mill is the most likely method used for producing these pipes, based on their outer diameters and thicknesses [94][95], 355 and 219 mm in outer diameters and 35 and 26 mm in thicknesses for Euro-Pi and Euro-P2, respectively. Both steels showed banded micro-segregation along the length of the creep specimen, however the band spacing was different for each of the steels. For Euro-Pi the band spacing and thickness was quite coarse (similar to that of Es-P and ORNL-P), whereas the Euro-P2 has a much finer band thickness and spacing. It is assumed that the original ingot sizes were the same for both steels, the difference can be attributed to the SDAS as well as the reduction ratios for each steel. Euro-P2 has a finer SDAS as well as larger reduction ratio, which can be assumed due to its lower wall thickness. The Euro steels also showed a lesser degree of micro-segregation than the ex-service steels, but more similar to the ORNL steels. These two pipe steels had the lowest extent of micro-segregation from the four pipe steels in this thesis, this can be attributed to a slow melting rate during ESR processing, which lead to a finer dendritic microstructure. This may explain the fine size and spacing of micro-segregation in Euro-P2 but does not consider the reduction ratio.

*Table 7.1: A summary of the key sample details including the sizes, fabrication methods, impurity levels, micro-segregation severities and spatial distributions. *O content unavailable*

Steel	Ex-service?	Melting Practice	Product	Product Size OD /thickness (mm)	Fabrication Method	MJF (impurity index)	S content	TIL content	Micro-segregation severity (relative)	Micro-segregation size and spacing (μm)		
							Wt. %			Width	Length	Spacing
Es-P	Yes	ESR (assumed)	Pipe	450/50	Plug Mill (assumed)	345	0.010	0.0597	High	60	2500	200
Es-F	Yes	ESR (assumed)	Tee-Piece Forging	210/54	Hot Forged then Bored (assumed)	159	0.002	0.0462	High	200-1000		1500
ORNL-P	No	AOD-ESR	Pipe	76/13	Hot Rotary Pierced	104	0.001	0.0529*	Medium-High	90	2000	300
ORNL-F	No	AOD-ESR	Saddle Forging	781/166	Hot Forged	134	0.001	0.0433	Low	1000-2000		500
Euro-Pi	No	ESR (assumed)	Pipe	355/35	Plug Mill (assumed)	201	0.0025	0.0644	Medium	150	1800	250
Euro-P2	No			219/26		237	0.001	0.0486	Medium	20	1200	100

7.2 Quantifying Phases and Micro-hardness with regards to Micro-segregation

A range of imaging and chemical mapping techniques were used for quantification of microstructural phases in the Gr. 91 steels. Variations in the local mechanical properties were also investigated through Vickers micro-hardness testing.

The effects of Cr micro-segregation found in the µ-XRF studies were compared to the variation in Vickers micro-hardness for the ex-service steels Es-P and Es-F in the head sections away from any creep cavitation, which could have also affected the results. These steels were selected based on the results in *Chapter 4* which defined them as the most severely micro-segregated steels from the six in the project. *Figures 5.4* and *5.5* presented these results; for steel Es-P a ~ 6.5 % increase was found and for steel Es-F a ~ 15 % increase was found, this was between the most negatively and positively segregated regions for each steel, for which the Cr µ-XRF maps were used. An indent spacing of 100 µm was used, this spacing was not very effective for differentiating micro-segregated regions in the banded Es-P steel. However, in the large localised micro-segregated regions in the Es-F steel, it was much more effective as multiple indents could be placed within the negatively and positively segregated regions. Two studies exist in the literature by Sawada et al. [40][41] described micro-hardness variations due to chemical segregation in these steel types. In the study on Gr. 92 steels [41], the micro-segregation was compared within the positively segregated regions and outside of them. On average from the three steels investigated an average micro-hardness of 258.9 HV was measured inside the micro-segregation band, whereas 235.3 HV was measured outside the micro-segregation band. This shows an increase of approximately 10 %, which was in between the values found in this project for steels Es-P and Es-F. Sawada et al. concluded that the difference was due to the increase in number density of the $M_{23}C_6$ carbides and MX carbo-nitrides. Furthermore, throughout the tube thickness, layered micro-segregation banding was also found along the longitudinal direction of the steels, similar to those found in the µ-XRF and SEM-EDS studies in *Chapter 4*.

Based on the Vickers micro-hardness mapping, which was performed on the ex-service steels, FIB-SEM based imaging was performed in site-specific regions. This imaging technique was used to quantify the $M_{23}C_6$ carbides in the high and low micro-hardness regions, which were found to be correlated with the Cr-rich regions (found in the µ-XRF mapping) in the steels. Cr is the main constituent element in the $M_{23}C_6$

carbides and also precipitation strengthening from these carbides is considered one of the main strengthening mechanisms. The MX carbo-nitride phase was also quantified in the high and low micro-hardness regions, however thin foil lift-outs were created for these with subsequent STEM chemical mapping. This is because the MX carbo-nitrides were very fine in size and could not be accurately quantified in SEM-based imaging. The $M_{23}C_6$ carbides were also quantified from the same thin foil lift-outs, however the small area relative to the larger $M_{23}C_6$ carbides was not sufficient in providing a good representation. Therefore, data from the FIB-SEM imaging of the $M_{23}C_6$ carbides were used to compare to the micro-hardness variations.

Figure 5.22 compares the size distribution for the $M_{23}C_6$ carbides in the ex-service steel head sections, locations for the imaging were defined by the position of micro-hardness indentations (*Figure 5.20*). Large differences were found between the positively and negatively (Cr) segregated regions (or high and low micro-hardness regions). With regards to area coverage, which is a quantitative measure of total particle population, the positively segregated regions in both steels contained ~ 3.4 % and the negatively segregated regions ~ 2.0 %. *Equation (2.2)* from *Section 2.3.3* defines the effect of precipitation strengthening [60].

$$\sigma_{or} = 0.8MGb/\lambda \qquad \textit{Equation (2.2)}$$

λ is defined at the mean interparticle spacing. Since it was concluded that the positively segregated regions contained more of the $M_{23}C_6$ carbides (and area coverage) the λ value would be smaller, therefore σ_{or} would be greater. This explains (at least in part) why the micro-hardness was greater in the Cr-rich regions which contained more $M_{23}C_6$ carbides. It should also be noted that the V-rich MX carbo-nitrides were quantified and presented in *Figures 5.28b, d* and *5.29*. A significant increase in the number per unit area and area coverage were also found. The size distribution in *Figure 5.28* showed that there was a pronounced increase in the number of V-rich MX carbo-nitrides in the size range of 25 to 75 nm. Similarly, to the quantification of the $M_{23}C_6$ carbides, the V-rich MX carbo-nitrides showed a similar trend in terms of differences between positively and negatively segregated regions. Sawada et al. [41] also found similar differences in the populations of the $M_{23}C_6$ carbides and V-rich MX carbo-nitrides. The increased amount of these precipitates in specific location affected the martensitic microstructure. It was found that in these positively segregated regions,

that the prior austenite grain, packet and block sizes were much finer. The amount of high angle boundary within the segregation zone was 1.61 μm per μm^2 and 1.30 μm per μm^2 outside of the segregation zones. In both of the studies by Sawada et al. [40][41] the authors concluded that the presence of micro-segregation banding was detrimental to the creep rupture strength of the steel. In solute-depleted material, less precipitation strengthening, lower total high angle boundaries and lower dislocation density would reduce the overall strength. The recovery of the martensitic matrix was believed to be accelerated in regions of lower Cr content. Sawada et al. [40] did however recommend a heat treatment regime of renormalising / homogenising at 1200 °C and tempering at 760 °C, followed by the typical normalising and tempering for Gr. 91/92 steels. This recommendation is similar to those suggested as homogenisation heat treatments in *Section 2.4.8* [129][130].

The formation of Laves phase during aging or creep exposure is widely studied in Gr. 91 and other CSEF steels [33][36][69]. All previous quantification of the phase has not accounted for area-to-area variation due to the effects of micro-segregation. In *Chapter 4* the extent of micro-segregation was quantified for the major alloying elements in all the steels present in the project. The micro-segregation of Mo and Nb were consistently the greatest in all steels, which was due, in part, to their large atomic size, meaning a greater tendency to partition to the liquid phase and slower diffusion in the solid phase. Initial chemical mapping which was performed using μ-XRF and SEM-EDS in *Chapter 4* was used as a basis to locate and image specific areas of positive and negative micro-segregation in both the head and gauge sections of all steels; systematically collected random areas (SCRA) were also quantified as a 'material average'. *Figures 5.10-5.18* present the size distributions and statistics for the Laves phase particle quantifications. Thermo-Calc simulations were also performed using micro-segregation compositions acquired from the SEM-EDS in order to compare the simulated and experimental area coverage values acquired.

For the ex-service steels, a similar size distribution shape was observed both in the head and gauge sections which indicated a similar overall average size of the Laves phase particles. For both steels the positively segregated regions showed an increase in the number density of Laves phase particles in both the head and gauge sections. When comparing the experimental and simulated area coverages the in-service conditions of 570 °C for 79,000 hours were representative of the simulation, because,

at the creep test temperature of 625 °C, Thermo-Calc did not predict any Laves phase. The relatively short creep tests clearly did not have much influence on the Laves phase precipitation. Overall, the simulated area coverages fell within the error bars of the experimental quantification which showed good agreement, with little error likely in the experimental process.

With regards to the non-service steels the same general trends in the positively segregated, negatively segregated and SCRA results were found as in the ex-service steels and were in good agreement in terms of sample ranking with the Thermo-Calc predictions. However, in terms of the area coverages, all of the Thermo-Calc predictions were well below the values found experimentally. This difference may have been due to abnormally high Laves phase in these steels which led to abnormally high quantifications. This does not agree with literature which often states an extended period of time is required for the Laves phase to reach thermal equilibrium [12][33], some of up to 100,000 hours at elevated ageing/creep temperature ranges (550 - 600 °C) [36][65]. Therefore, there was either error in the quantification or Laves phase was already present in the virgin material. The behaviour of the Laves phase in the non-service steels is difficult to explain unlike that of the ex-service steels and needs further study.

7.3 Inclusions and Creep Cavitation

Chapter 6 investigated various topics, including inclusion analysis, the association of creep cavities to inclusions and the micro-hardness and creep cavitation profiles in the gauge sections of the steels.

The effects of accelerating voltage on the quantification of inclusions were investigated. It was found that a 10 kV accelerating voltage not only improved the spatial resolution, but also reduced the interaction volume compared with 20 kV, which reduced the effect of sub-surface features. Furthermore, the apparent size of inclusions was significantly greater at 20 kV and a large portion of the input counts were consumed by the Fe K_{α} X-ray peak, which meant longer durations of chemical analysis would be required to achieve similar quantifications to those achieved at 10 kV.

A standardised SEM-EDS inclusion analysis procedure was used to quantify the main inclusions found in the Gr. 91 steels, which consisted of mainly MnS and Al_2O_3

inclusions. This procedure utilised an accelerating voltage of 10 kV and quantified the type, number density and size distributions using automated SEM-EDS detection software. The inclusions were quantified in all steels with positively and negatively segregated regions being identified from the μ-XRF-derived Mn maps. In the ex-service steel Es-F a clear trend between positive segregation and increased MnS inclusion content was observed. The high levels of micro-segregation as well as the localised form of micro-segregation made it easier to detect any area-to-area variations in this steel. A good agreement was found between the MJF values and inclusion contents; the ex-service steels (Es-P and Es-F) contained the most inclusions (and had the greatest MJF) and the cleanest steels (ORNL-P and ORNL-F) contained the least number of inclusions. Steels Euro-Pi and Euro-P2 which possessed MJF values in between those of the two aforementioned sets also sat in between the two sets in terms of number density of inclusions. This suggests that the ex-service steels were produced in a less controlled environment, which may also suggest why they contained much higher impurity levels (MJF). Thermo-Calc simulations were used to predict the area coverages of the MnS and Al_2O_3 inclusion types, which suggested that the experimental area coverage values were over-quantified for the MnS inclusions and under-quantified for the Al_2O_3 inclusions, consistent with the nucleation of MnS inclusions on pre-existing Al_2O_3 inclusions. AlN precipitate quantification was also performed; for the Euro steels, which had N:Al ratios in excess of 10, no AlN precipitates were found which is consistent with thermodynamic simulation calculations. The Euro samples are believed to be more modern materials than either the ex-service steels and the ORNL development steels and therefore, took advantage of a greater N:Al ratio; the specification for which was introduced more recently [24]. The extent of AlN precipitation (area coverage and number) in steels Es-P, Es-F, ORNL-P and ORNL-F was in line with their respective N:Al ratio, in which they ranked Es-P, ORNL-P, Es-F, and ORNL-F. The AlN precipitates were found to be strongly associated with other inclusion types (MnS and Al_2O_3); this is consistent with them nucleating on these pre-existing inclusions during post-solidification cooling. STEM chemical mapping of an MnS inclusion in steel Es-P also showed the strong association of the AlN precipitates with the MnS / matrix interface as well as spherical nano-sized Cu_2S precipitates, which have not been studied in Gr. 91 steels before.

A summary for the quantification of various microstructural features from this project is provided in *Table 7.2*. When comparing the steels Es-P and Es-F, the former possesses much lower creep strength and ductility (time to rupture and ROA, respectively). As *Table 7.2* shows, many differences were found between Es-P and Es-F. Es-P contained at least double the number density of inclusions and a much greater cavity count between the notches. This may explain why the cavity to inclusion ratio was smaller for steel Es-P, 3.2 than for steel Es-F, 3.5. There were also a number of other differences which may have accounted for the increased creep cavitation, or lower creep ductility which is often associated with excessive creep cavitation [15]. This included the lower N:Al ratio in Es-P (1.14) which meant more AlN precipitates (~ 119 x 10^3/mm^2), compared to a higher N:Al ratio in Es-F (2.12) and fewer AlN precipitates (~ 16 x 10^3/mm^2). Furthermore Es-P also contained more Laves phase particles and a significantly higher amount of tramp elements (measured as the MJF). Overall, the reduction of creep strength and ductility between Es-P and Es-F is difficult to narrow down to a single factor but may well be a combination of the reasons mentioned above.

The ORNL steels showed interesting behaviour, this is because ORNL-P has a lower creep strength but higher creep ductility than ORNL-F. Based on *Table 7.2* when comparing the number of inclusions per mm^2, steel ORNL-P has considerably more than ORNL-F, 225 versus 50, respectively. The creep cavitation is also much greater in ORNL-P than in ORNL-F. A big difference is the cavity to inclusion ratio; for ORNL-F this is close to 1 (1.5), which means most the cavities were associated with inclusions, whereas for ORNL-P this was 4.1. That means roughly only 1 in 4 cavities were associated with inclusions. This could be due to the low N:Al ratio in ORNL-P (1.67) which means a relatively large number of the detrimental AlN precipitates were present. The level of impurities for both steels were quite low when compared to those calculated in the ex-service steels, due to a better control of composition. Another important factor to consider for the differences in creep strength and creep ductility between the two ORNL steels is the creep testing conditions, a 24 °C difference would have had a profound effect on the performance data. For example, Parker [15] found that the ROA decreased from 49.2 % to 9.2 % and then to 4.5 % for creep tests performed at 550 °C, 600 °C, and 650 °C. This test was performed on a Gr. 91 steel for similar durations and stresses between tests. Furthermore, Parker and Siefert [30],

also found that at higher stress levels specimens are more likely to rupture in a ductile manner. Therefore, these differences in creep test conditions for ORNL-F (649 °C at 75.8 MPa) and ORNL-P (625 °C at 100 MPa) may explain why ORNL-F has an ROA of just 13 % and ORNL-P of 47.5 %. This shows the temperature and stress could have a large effect on the creep ductility.

For the Euro steels the same creep testing temperature 600 °C was used, however Euro-Pi was under less stress than Euro-P2 (100 versus 110 MPa, respectively). This difference in stress may have had an effect on the creep ductility measured. For which Euro-P2 did show an improved amount of 30 % against 7.5 % shown by Euro-Pi. The time to rupture for Euro-Pi was far greater, although when comparing the number density of inclusions and number of creep cavities in the gauge section similar numbers were found (*Table 7.2*). The cavity to inclusion ratio was far greater for Euro-P2 than for Euro-Pi, it was found that more inclusions were associated with the Al_2O_3 inclusions, for which steel Euro-P2 contained considerably more of this inclusion type. Both steels possessed high N:Al ratios, and no AlN precipitates were found. However, steel Euro-Pi did contain less Laves phase as well as a slightly lower MJF. The shorter time to rupture in steel Euro-P2 may be due to the presence of a larger number of Al_2O_3 inclusions (which were commonly associated with creep cavities in the gauge section for Euro-P2), more Laves phase and slightly higher tramp element contents.

Table 7.2: A summary of some of the sample details and key microstructural quantifications from this project.

Sample	Creep Conditions [°C/MPa]	Time to Failure [Hours] / ROA	Inclusions [per mm^2]	Cavities [per mm^2]	Cavity to inclusion ratio	N:Al	AlN [$10^3/mm^2$]	Laves [$10^3/mm^2$]	MJF (impurity index)
Es-P	625/100 (50 MPa @ notch)	1,408/ 26,5	801	High	3.2	1.14	~119	~137	345
Es-F		6,714/ 83	392	Low	3.5	2.12	~16	~107	159
ORNL-P	625/100	1,259/ 47.5	225	~1250	4.1	1.67	~32	~220	104
ORNL-F	649/75.8	29,363/ 13	50	~50	1.5	3.60	~3	~19	134
Euro-Pi	600/100	66,431/ 7.5	394	~450	9.6	28.4	--	~49	201
Euro-P2	600/110	38,504/ 30	376	~450	2.9	14.4	--	~89	237

Chapter 8 : Conclusions and Future Work

The key findings from results *Chapters 4, 5 and 6* as well as suggestions for future work based on the findings from this project are concluded in the following sections.

8.1 Conclusions

This thesis analysed a range of very different and complex Gr. 91 as-received creep specimens, of which there were three distinct material backgrounds, a number of key conclusions can be made based on this project.

Micro-segregation was quantified in a range of Gr.91 steels using μ-XRF and SEM-EDS chemical mapping. The steels included ex-service, developmental (ORNL) and more recently produced steels from a European supplier. Micro-segregation was found to be the most severe in the ex-service steels as compared to the non-service steels, with the exception of the ORNL-P steel showing relatively high amounts of micro-segregation. Post-casting processing routes such as ESR processing and then shaping were likely to have had a large influence on the micro-segregation structures and severity as well as the steel composition and inclusion contents. Due to the two ex-service steels having the greatest amount of micro-segregation, more ex-service steels need to be analysed to increase understanding of micro-segregation behaviour in complex alloy steels.

Since the presence of micro-segregation was found in all steels, it is important to assess and address micro-segregation in Gr. 91 and other CSEF steels for potential effects on creep performance.

The effects of micro-segregation are of key significance when quantifying microstructural parameters in Gr. 91 and other CSEF steels. This project investigated the effects of micro-segregation on various microstructural features and mechanical properties such as the Laves phase in all of the steels, the $M_{23}C_6$ carbides and MX carbo-nitrides for the ex-service steels and the Vickers micro-hardness for the ex-service steels. All of these parameters are important to quantify in these steels, therefore, the impact of the results is quite novel and has the potential to influence future characterisation of these types of steels.

Site-specific micro-hardness testing of steels Es-P and Es-F showed a significant variation based on the positively and negatively segregated regions determined from

μ-XRF mapping due to the enrichment and depletion of the major alloying elements. More specifically, Cr micro-segregation was used as a basis because of the role of Cr in forming $M_{23}C_6$ carbides that provide precipitation strengthening. These results correlated with the site-specific analysis of the precipitation strengthening of the $M_{23}C_6$ carbides and V-rich MX carbo-nitrides. Note: V was also segregated similarly to Cr (in the same regions), so the V-rich MX was expected to behave similarly to the $M_{23}C_6$ carbides. This can have important implications on hardness testing, which is used extensively in industrial creep applications, as well as the quantification of nano-precipitates for creep strengthening mechanisms. Varying populations of strengthening precipitates can increase or decrease the mechanical properties depending on the location being tested or quantified.

The intermetallic Laves phase was quantified for the set of steels in this project, both in the head and gauge sections, with regards to the effects of micro-segregation using a novel procedure based on targeting specific locations using μ-XRF and then SEM-EDS chemical mapping techniques. Average sizes of the Laves phase particles were consistent between positively and negatively segregated regions, whereas the number density of Laves phase particles was consistently greater in the positively segregated regions; this suggested that the localised increases in Mo only increased the nucleation of Laves phase particles but not the growth of them. Thermo-Calc simulations were used to predict the area coverage of the Laves phase based on SEM-EDS composition variations and compared with the area coverage results found experimentally, the ex-service steels showed good agreement, but the non-service steels did not. This suggests room for further work. The precipitation of the Laves phase is considered detrimental to creep strengthening due to loss in solid solution strengthening [36] and some also consider that Laves phase particles act as sites for cavity nucleation [34].

Similarly, for the quantification of inclusions a process which started with μ-XRF mapping to locate site-specific regions was used. Furthermore, the accelerating voltage, which is the most important parameter in automated SEM-EDS inclusion analysis was investigated. Overall, 10 kV was found to be optimal, based on the improved spatial resolution and reduced interaction volume which reduced sub-surface effects. This allowed for finer inclusions to be quantified which improved upon other literature studies and standards. The rankings of inclusion contents closely mirrored the steel cleanliness (MJF), for which the ORNL steels were the cleanest and

the ex-service steels had the highest MJF and number density of inclusions values. The Euro steels fell somewhere in between the two aforementioned sets (in terms of MJF and inclusion content) but took advantage of a more controlled N:Al ratio, which meant that they were the only steels that did not contain any AlN precipitates.

When linking the creep performance, time to rupture or ROA, to microstructural features it is difficult to make any conclusions. This is because of various microstructural features that were present in every steel, therefore making it difficult to narrow down any single phase or reason. Furthermore, the varying creep specimen geometries and test conditions could also influence creep strength and ductility. Although creep cavitation was commonly associated with inclusions, narrowing down any specific cause of loss in creep strength or ductility was very debatable. A combination of many factors needs be considered such as the loss in strengthening, e.g. by nano-precipitate coarsening; formation of Laves phase which causes loss in solid solution strengthening; and recovery of the martensite matrix. Coupled with these are factors such as the amount of tramp elements and inclusions present in the steel, as well as AlN precipitation. Furthermore, micro-segregation can influence all of these microstructural parameters.

8.2 Future Work

The current project has highlighted a few aspects that can be considered for further work, which are as follows:

- Parallel production of Gr. 91 steels with the same composition and thermo-mechanical treatments but in different scales of production, e.g.., industrial casts as well as laboratory casts can be produced, and the morphologies and degrees of micro-segregation can be quantified (and compared) and correlated to specific differences within the steelmaking process. The quantification of micro-segregation can be carried out using both μ-XRF and SEM-EDS chemical mapping techniques. The use of both techniques will also allow for comparative studies on the results found by the two techniques.
- For the ex-service steels Es-P and Es-F the Laves phase results showed good agreement with Thermo-Calc, however, this was not the case with the non-service steels. Therefore, extended creep test exposure times should be applied to investigate why the Laves phase experimental quantifications did not match

those predicted by Thermo-Calc as they did with the ex-service steels. Interrupted aging or creep tests at different time durations may be ideal for studying this.

- The effects of micro-segregation on microstructural evolution of creep specimens can be analysed. More specifically, the changes in the martensite matrix, and coarsening of nano-precipitates in the positively and negatively segregated regions in various locations of the gauge length of creep specimens.
- Nano-indentation can be used to aid the micro-hardness mapping of the steels in order to detect variations due to local composition. In the case of steel Es-P, the size of the microhardness indents used in this study was not ideal to distinguish the micro-segregation, therefore, nano-indentation can be implemented for future work.

References

[1] R. Viswanathan, K. Coleman, and U. Rao, “Materials for ultra-supercritical coal-fired power plant boilers,” *Int. J. Press. Vessel. Pip.*, 2006, doi: 10.1016/j.ijpvp.2006.08.006.

[2] F. Masuyama, “History of power plants and progress in heat resistant steels,” *ISIJ Int.*, vol. 41, no. 6, pp. 612–625, 2001, doi: 10.2355/isijinternational.41.612.

[3] GE, “Ultra-Supercritical & Advanced Supercritical Technology,” 2021. [Online]. Available: https://www.ge.com/steam-power/coal-power-plant/usc-ausc. [Accessed: 01-Jan-2022].

[4] P. J. Ennis and A. Czyrska-Filemonowicz, “Recent advances in creep-resistant steels for power plant applications,” *Sadhana - Acad. Proc. Eng. Sci.*, vol. 28, no. 3–4, pp. 709–730, 2003, doi: 10.1007/BF02706455.

[5] F. Masuyama and J. P. Shingledecker, “Recent status of ASME code on creep strength enhanced ferritic steels,” in *Procedia Engineering*, 2013, doi: 10.1016/j.proeng.2013.03.260.

[6] F. Abe, “Development of creep-resistant steels and alloys for use in power plants,” in *Structural Alloys for Power Plants: Operational Challenges and High-Temperature Materials*, 2014, pp. 250–293.

[7] T. Wang, “Global electricity generation by energy source 2017,” 2017. [Online]. Available: https://www.statista.com/statistics/269811/world-electricity-production-by-energy-source/. [Accessed: 16-Jun-2020].

[8] F. Starr, “High temperature materials issues in the design and operation of coal-fired steam turbines and plant,” in *Structural Alloys for Power Plants: Operational Challenges and High-Temperature Materials*, 2014, pp. 36–68.

[9] D. Oberhaus, “China Is Still Building an Insane Number of New Coal Plants,” 2019. [Online]. Available: https://www.wired.com/story/china-is-still-building-an-insane-number-of-new-coal-plants/. [Accessed: 16-Jun-2020].

[10] J. A. Siefert, “The Influence of the Parent Metal Condition on the Cross-weld Creep Performance in Grade 91 Steel,” Loughborough University, 2019.

[11] A. American, N. Standard, and ASTM International, “Standard Specification for Seamless Ferritic Alloy-Steel Pipe for High-Temperature,” *Society*, no. October 2002, pp. 1–11, 2003, doi: 10.1520/A0335.

[12] X. Z. Zhang, X. J. Wu, R. Liu, J. Liu, and M. X. Yao, “Influence of Laves phase on creep strength of modified 9Cr-1Mo steel,” *Mater. Sci. Eng. A*, vol. 706, no. August, pp. 279–286, 2017, doi: 10.1016/j.msea.2017.08.111.

[13] R. W. M. and W. K. S. Distefano, J.R., V. K. Sikka, J. J. Blass, C. R. Brinkman, J. M. Corum, J. A. Horak, R. L. Huddleston, J. F. King, “Summary of Modified 9Cr-1Mo Steel Development Program: 1975-1985,” Oak Ridge, TN (US), 1987.

[14] M. J. Cohn, J. F. Henry, and D. Nass, “Fabrication, construction, and operation problems for Grade 91 fossil power components,” *J. Press. Vessel Technol. Trans. ASME*, vol. 127, no. 2, pp. 197–203, 2005, doi: 10.1115/1.1904054.

[15] J. Parker, “Creep ductility considerations for high energy components manufactured from creep strength enhanced steels,” *Mater. High Temp.*, vol. 34, no. 2, pp. 109–120, 2017, doi: 10.1080/09603409.2016.1270720.

[16] J. Parker and S. Brett, “Creep performance of a grade 91 header,” *Int. J. Press. Vessel. Pip.*, vol. 111–112, pp. 82–88, 2013, doi: 10.1016/j.ijpvp.2013.05.003.

[17] D. Kalisz and S. Rzadkosz, “Modeling of the Formation of A1N Precipitates During Solidification of Steel,” *Arch. Foundry Eng.*, vol. 13, no. 1, pp. 63–68, 2013, doi: 10.2478/afe-2013-0012.

[18] J. Liu, M. Strangwood, C. L. Davis, and J. Parker, “Non-destructive characterisation of N/Al level in P91 steels using electromagnetic sensors,” *Mater. Sci. Technol. (United Kingdom)*, vol. 31, no. 9, pp. 1042–1050, 2015, doi: 10.1179/1743284714Y.0000000642.

[19] EPRI, “Guidelines and Specifications for High-Reliability Fossil Power Plants, 2nd Edition: Best Practice Guideline for Manufacturing and Construction of Grade 91 Steel Components,” p. 110, 2015, doi: 3002006390.

[20] J. Parker and J. Siefert, “Metallurgical and Stress State Factors Which Affect the Creep and Fracture Behavior of 9% Cr Steels,” *Adv. Mater. Sci. Eng.*, vol.

2018, 2018, doi: 10.1155/2018/6789563.

[21] J. D. Parker and J. A. Siefert, “The creep and fracture behaviour of tempered martensitic steels,” *Mater. High Temp.*, vol. 35, no. 6, pp. 491–503, 2018, doi: 10.1080/09603409.2017.1389441.

[22] F. G. Wilson and T. Gladman, “Aluminium nitride in steel,” *Int. Mater. Rev.*, vol. 33, no. 1, pp. 221–286, 1988, doi: 10.1179/imr.1988.33.1.221.

[23] F. Abe, “Effect of boron nitrides and aluminium nitrides on long-term creep life and rupture ductility of martensitic 9 to 12Cr steels,” *Jt. EPRI-123HiMAT Int. Conf. Adv. High-Temperature Mater.*, pp. 145–154, 2019.

[24] “Code Case 2864, 9Cr-1Mo-V Material, Section I, ASME Boiler and Pressure Vessel Code, Approval Date: September 21, 2016.,” 2016.

[25] K. Kimura, K. Sawada, “Influence of chemical composition and materials processing on creep strength of Grade 91 steels.,” in *4th International ECCC Conference*, 2017.

[26] K. Kimura, K. Sawada, H. Kushima, and Y. Toda, “Influence of chemical composition and heat treatment on long-term creep strength of grade 91 steel,” *Procedia Eng.*, vol. 55, pp. 2–9, 2013, doi: 10.1016/j.proeng.2013.03.211.

[27] J. A. Siefert and J. D. Parker, “Evaluation of the creep cavitation behavior in Grade 91 steels,” *Int. J. Press. Vessel. Pip.*, vol. 138, pp. 31–44, 2016, doi: 10.1016/j.ijpvp.2016.02.018.

[28] J. A. Siefert, J. D. Parker, and R. C. Thomson, “Linking performance of parent Grade 91 steel to the cross-weld creep performance using feature type tests,” in *Advances in Materials Technology for Fossil Power Plants - Proceedings from the 8th International Conference*, 2016.

[29] G. Eggeler, J. C. Earthman, N. Nilsvang, and B. Ilschner, “Microstructural study of creep rupture in a 12% chromium ferritic steel,” *Acta Metall.*, 1989, doi: 10.1016/0001-6160(89)90265-4.

[30] J. Parker and J. Siefert, “Creep fracture in tempered martensitic steels,” *Int. J. Petrochemical Sci. Eng.*, 2018, doi: 10.15406/ipcse.2018.03.00068.

[31] F. Abe, T. Horiuchi, M. Taneike, and K. Sawada, “Stabilization of martensitic microstructure in advanced 9Cr steel during creep at high temperature,” *Mater. Sci. Eng. A*, vol. 378, no. 1-2 SPEC. ISS., pp. 299–303, 2004, doi: 10.1016/j.msea.2003.11.073.

[32] J. Hald and L. Korcakova, “Precipitate stability in creep resistant ferritic steels - Experimental investigations and modelling,” *ISIJ Int.*, vol. 43, no. 3, pp. 420–427, 2003, doi: 10.2355/isijinternational.43.420.

[33] I. Fedorova, A. Belyakov, P. Kozlov, V. Skorobogatykh, I. Shenkova, and R. Kaibyshev, “Laves-phase precipitates in a low-carbon 9% Cr martensitic steel during aging and creep at 923K,” *Mater. Sci. Eng. A*, vol. 615, pp. 153–163, 2014, doi: 10.1016/j.msea.2014.07.046.

[34] J. S. Lee, H. Ghassemi Armaki, K. Maruyama, T. Muraki, and H. Asahi, “Causes of breakdown of creep strength in 9Cr-1.8W-0.5Mo-VNb steel,” *Mater. Sci. Eng. A*, vol. 428, no. 1–2, pp. 270–275, 2006, doi: 10.1016/j.msea.2006.05.010.

[35] K. Sawada, K. Suzuki, H. Kushima, M. Tabuchi, and K. Kimura, “Effect of tempering temperature on Z-phase formation and creep strength in 9Cr-1Mo-V-Nb-N steel,” *Mater. Sci. Eng. A*, vol. 480, no. 1–2, pp. 558–563, 2008, doi: 10.1016/j.msea.2007.09.031.

[36] C. G. Panait, W. Bendick, A. Fuchsmann, A. F. Gourgues-Lorenzon, and J. Besson, “Study of the microstructure of the Grade 91 steel after more than 100,000 h of creep exposure at 600 °C,” *Int. J. Press. Vessel. Pip.*, vol. 87, no. 6, pp. 326–335, 2010, doi: 10.1016/j.ijpvp.2010.03.017.

[37] M. C. Flemings, “Solidification processing,” *Metall. Trans.*, 1974, doi: 10.1007/BF02643923.

[38] G. Krauss, “Solidification, Segregation, and Banding in Carbon and Alloy Steels,” *Metallurgical and Materials Transactions B: Process Metallurgy and Materials Processing Science*. 2003, doi: 10.1007/s11663-003-0084-z.

[39] A. Ghosh, “Segregation in cast products,” in *Sadhana - Academy Proceedings in Engineering Sciences*, 2001, doi: 10.1007/BF02728476.

[40] K. Sawada *et al.*, “Effect of initial microstructure on creep strength of ASME grade T91 steel,” *Tetsu-To-Hagane/Journal Iron Steel Inst. Japan*, vol. 105, no. 4, pp. 23–32, 2019, doi: 10.2355/tetsutohagane.TETSU-2018-066.

[41] K. Sawada, K. Sekido, and K. Kimura, “Segregation and its effect on creep rupture strength in Grade 92 steels,” *Mater. Charact.*, vol. 169, no. May, p. 110581, 2020, doi: 10.1016/j.matchar.2020.110581.

[42] C. G. Panait, “Metallurgical evolution and creep strength of 9-12% Cr heat resistant steels at 600 C and 650 C,” Paris Institute of Technology, 2010.

[43] L. Li, “Microstructural evolution in 9 wt.% Cr power plant steels,” Loughborough University, 2013.

[44] Y.Gu, “Microstructural investigation of creep behaviour in Grade 92 power plant steels,” Loughborough University, 2017.

[45] J. J. Sanchez-Hanton, “Microstructural evolution in Grade 91 (9Cr-1MoVNb) Power Plant Steels,” Loughborough University, 2007.

[46] J. D. Verhoeven, *Steel Metallurgy for the Non-Metallurgist*. 2019.

[47] A. A. K. Haarmann, J. C. Vaillant, B. Vandenberghe, W. Bendick, *The T91/P91 Book*. 2002.

[48] G. Krauss, “Steels: heat treatment and processing principles,” *ASM Int. 1990,* 1990.

[49] S. J. Sanderson, “Mechanical Properties and Metallurgy of 9%Cr 1%Mo Steel.,” 1983.

[50] H. Bhadeshia and R. Honeycombe, *Steels: Microstructure and Properties*. 2006.

[51] D. A. Porter, K. E. Easterling, and M. Y. Sherif, *Phase transformations in metals and alloys, third edition*. 2009.

[52] M. Taneike, K. Sawada, and F. Abe, “Effect of carbon concentration on precipitation behavior of M23C6 carbides and MX carbonitrides in martensitic 9Cr steel during heat treatment,” *Metall. Mater. Trans. A Phys. Metall. Mater. Sci.*, vol. 35 A, no. 4, pp. 1255–1262, 2004, doi: 10.1007/s11661-004-0299-x.

[53] J. Hald, “Microstructure and long-term creep properties of 9-12% Cr steels,” *Int. J. Press. Vessel. Pip.*, 2008, doi: 10.1016/j.ijpvp.2007.06.010.

[54] M. Ortolani and P. Mariani, “Microstructural evolution of ASTM grade 91 after long-term creep testing,” *Mater. High Temp.*, vol. 33, no. 6, pp. 604–608, 2016, doi: 10.1080/09603409.2016.1201332.

[55] J. Orr and D. Burton, “Improving the Elevated Temperature Strength of Steel 91(9% CrMoNbVN),” in *Materials for Advanced Power Engineering 1994*, 1994.

[56] H. K. D. H. Bhadeshia, “Design of Heat Resistant Alloys for the Energy Industries,” in *Proceedings of the Fifth International Charles Parsons Turbine Conference*, 2000, pp. 3–40.

[57] A. and C.-F. Ennis, PJ., Zielifiska-Lipiec, “Comparison of the Microstructures of High Chromium Steels for Advanced Power Stations, in Microstructural Stability of Creep Resistant Alloys for High Temperature Plant Applications,” *Microstruct. Stab. Creep Resist. Alloy. High Temp. Plant Appl.*, pp. 135–145, 1998.

[58] T. Shrestha, S. F. Alsagabi, I. Charit, G. P. Potirniche, and M. V. Glazoff, “Effect of heat treatment on microstructure and hardness of grade 91 steel,” *Metals (Basel).*, vol. 5, no. 1, pp. 131–149, 2015, doi: 10.3390/met5010131.

[59] F. Abe, “Precipitate design for creep strengthening of 9% Cr tempered martensitic steel for ultra-supercritical power plants,” *Sci. Technol. Adv. Mater.*, vol. 9, no. 1, 2008, doi: 10.1088/1468-6996/9/1/013002.

[60] K. Maruyama, K. Sawada, and J. I. Koike, “Strengthening mechanisms of creep resistant tempered martensitic steel,” *ISIJ International*. 2001, doi: 10.2355/isijinternational.41.641.

[61] H. Kitahara, R. Ueji, N. Tsuji, and Y. Minamino, “Crystallographic features of lath martensite in low-carbon steel,” *Acta Mater.*, 2006, doi: 10.1016/j.actamat.2005.11.001.

[62] A. Orlová, J. Buršík, K. Kuchařová, and V. Sklenička, “Microstructural development during high temperature creep of 9% Cr steel,” *Mater. Sci. Eng.*

A, 1998, doi: 10.1016/S0921-5093(97)00708-9.

[63] Y. Qin, G. Götz, and W. Blum, "Subgrain structure during annealing and creep of the cast martensitic Cr-steel G-X12CrMoWVNbN 10-1-1," *Mater. Sci. Eng. A*, vol. 341, no. 1–2, pp. 211–215, 2003, doi: 10.1016/S0921-5093(02)00215-0.

[64] K. Rodak, A. Hernas, and A. Kiełbus, "Substructure stability of highly alloyed martensitic steels for power industry," *Mater. Chem. Phys.*, vol. 81, no. 2–3, pp. 483–485, 2003, doi: 10.1016/S0254-0584(03)00047-6.

[65] M. I. Isik, A. Kostka, and G. Eggeler, "On the nucleation of Laves phase particles during high-temperature exposure and creep of tempered martensite ferritic steels," *Acta Mater.*, vol. 81, pp. 230–240, 2014, doi: 10.1016/j.actamat.2014.08.008.

[66] K. Sawada *et al.*, "Effect of W on recovery of lath structure during creep of high chromium martensitic steels," *Mater. Sci. Eng. A*, 1999, doi: 10.1016/s0921-5093(99)00066-0.

[67] J. Hald, "Metallurgy and creep properties of new 9-12%Cr steels," *Steel Res.*, 1996, doi: 10.1002/srin.199605503.

[68] P. Hofer, H. Cerjak, B. Schaffernak, and P. Warbichler, "Quantification of precipitates in advanced creep resistant 9-12% Cr steels," *Steel Res.*, 1998, doi: 10.1002/srin.199805562.

[69] G. Dimmler, P. Weinert, E. Kozeschnik, and H. Cerjak, "Quantification of the Laves phase in advanced 9-12% Cr steels using a standard SEM," *Mater. Charact.*, vol. 51, no. 5, pp. 341–352, 2003, doi: 10.1016/j.matchar.2004.02.003.

[70] L. Cipolla, A. Di Gianfrancesco, D. Venditti, G. Cumino, and S. Caminada, "Microstructural evolution during long term creep tests of 9%Cr steel grades," in *2007 Proceedings of the ASME Pressure Vessels and Piping Conference - 8th International Conference on Creep and Fatigue at Elevated Temperatures - CREEP8*, 2008, doi: 10.1115/CREEP2007-26030.

[71] K. Sawada, H. Kushima, M. Tabuchi, and K. Kimura, "Effect of creep

deformation on z phase formation in Gr.91 steel," *Energy Mater. Mater. Sci. Eng. Energy Syst.*, vol. 9, no. 2, pp. 12–16, 2014, doi: 10.1179/1743284713Y.0000000309.

[72] K. Sawada, H. Kushima, K. Kimura, and M. Tabuchi, "TTP diagrams of Z phase in 9-12% Cr heat-resistant steels," *ISIJ Int.*, vol. 47, no. 5, pp. 733–739, 2007, doi: 10.2355/isijinternational.47.733.

[73] K. Kaneko *et al.*, "Characterization of carbides at different boundaries of 9Cr-steel," *Mater. Sci. Eng. A*, 2004, doi: 10.1016/j.msea.2003.12.065.

[74] C. Wagner, "Theory of precipitation aging by resolving (Ostwald ripening)," *J. Electrochem. reports Bunsen Soc. Phys. Chem.*, vol. 65, no. 7–8, pp. 581–591, 1961.

[75] I. M. Lifshitz and V. V. Slyozov, "The kinetics of precipitation from supersaturated solid solutions," *J. Phys. Chem. Solids*, 1961, doi: 10.1016/0022-3697(61)90054-3.

[76] A. Umantsev and G. B. Olson, "Ostwald ripening in multicomponent alloys," *Scr. Metall. Mater.*, 1993, doi: 10.1016/0956-716X(93)90191-T.

[77] J. Ågren, F. H. Hayes, L. Höglund, U. R. Kattner, B. Legendre, and R. Schmid-Fetzer, "Applications of computational thermodynamics," *Zeitschrift fuer Met. Res. Adv. Tech.*, 2002, doi: 10.3139/146.020128.

[78] M. Taneike, M. Kondo, and T. Morimoto, "Accelerated Coarsening of MX Carbonitrides in 12%Cr Steels during Creep Deformation," *ISIJ Int.*, 2001, doi: 10.2355/isijinternational.41.Suppl_S111.

[79] K. Sawada, K. Kubo, and F. Abe, "Contribution of coarsening of MX carbonitrides to creep strength degradation in high chromium ferritic steel," *Mater. Sci. Technol.*, vol. 19, no. 6, pp. 732–738, 2003, doi: 10.1179/026708303225010687.

[80] M. Hättestrand and H. O. Andrén, "Evaluation of particle size distributions of precipitates in a 9% chromium steel using energy filtered transmission electron microscopy," in *Micron*, 2001, doi: 10.1016/S0968-4328(00)00086-X.

[81] F. Masuyama and J. P. Shingledecker, "Recent status of ASME code on creep

strength enhanced ferritic steels," *Procedia Eng.*, vol. 55, pp. 314–325, 2013, doi: 10.1016/j.proeng.2013.03.260.

[82] K. Sawada, K. Maruyama, Y. Hasegawa, and T. Muraki, "Creep life assessment of high chromium ferritic steels by recovery of martensitic lath structure," *Key Eng. Mater.*, 2000, doi: 10.4028/www.scientific.net/kem.171-174.109.

[83] "Argon Oxygen Decarburization," 2022. [Online]. Available: https://www.lindeus.com/industries/metal-production/argon-oxygen-decarburization-aod. [Accessed: 23-Aug-2022].

[84] S. K. Sarna, "Stainless Steel Manufacturing Processes," 2014. [Online]. Available: https://www.ispatguru.com/stainless-steel-manufacturing-processes/.

[85] S. Louhenkilpi, "Continuous Casting of Steel," in *Treatise on Process Metallurgy*, 2014.

[86] Michael Vynnycky, "Continuous casting," *Metals (Basel).*, vol. 9, no. 643, 2019.

[87] C. Shi, X. Zheng, Z. Yang, P. Lan, J. Li, and F. Jiang, "Effect of Melting Rate of Electroslag Rapid Remelting on the Microstructure and Carbides in a Hot Work Tool Steel," *Met. Mater. Int.*, vol. 27, no. 9, pp. 3603–3616, 2021, doi: 10.1007/s12540-020-00717-6.

[88] S. K. Sarna, "Steel ingots and their Casting during Steelmaking," 2018. [Online]. Available: https://www.ispatguru.com/steel-ingots-and-their-casting-during-steelmaking/. [Accessed: 23-Aug-2022].

[89] S. K. Sarna, "Electroslag Remelting Process," 2020. [Online]. Available: https://www.ispatguru.com/electroslag-remelting-process/. [Accessed: 23-Aug-2022].

[90] E. J. Pickering, "Macrosegregation in Steel Ingots," University of Cambridge, 2014.

[91] A. Mitchell, "Solidification in remelting processes," *Mater. Sci. Eng. A*, 2005, doi: 10.1016/j.msea.2005.08.157.

[92] A. Scheriau, “Special Metallurgical Production Processes of Ingots,” 2019.

[93] M. Ali, D. Porter, J. Kömi, M. Eissa, H. El Faramawy, and T. Mattar, “The effect of electroslag remelting on the microstructure and mechanical properties of CrNiMoWMnV ultrahigh-strength steels,” *Metals (Basel).*, vol. 10, no. 2, pp. 381–395, 2020, doi: 10.3390/met10020262.

[94] JFE Steel Corporation, “Products - Commodity & Pipe and Tubes - Manufacturing Process,” 2003. [Online]. Available: https://www.jfe-steel.co.jp/en/products/pipes/seizoukoutei.php. [Accessed: 05-Jun-2020].

[95] “INTERNATIONAL WORKSHOP ON FABRICATION & PROCESSING OF GRADE 91 MATERIAL (FAB 91),” Tiruchirappalli, 2011.

[96] P. Smith, *Piping Materials Guide*. Elsevier, 2005.

[97] Werner Sölken, “Steel Pipe and Manufacturing Processes,” 2008. [Online]. Available: http://www.wermac.org/pipes/pipemaking.html. [Accessed: 05-Jun-2020].

[98] R. Li, X. Zhang, C. Zhang, J. Wang, and J. Huang, “Preparation of High-Precision Dimension Seamless Thick-Walled Pipe by New Cold Rolling Process,” *Metals (Basel).*, vol. 12, no. 10, 2022, doi: 10.3390/met12101761.

[99] M. L. Lobanov *et al.*, “Tensile Deformation and Fracture Behavior of API-5L X70 Line Pipe Steel,” *Materials (Basel).*, vol. 15, no. 2, 2022, doi: 10.3390/ma15020501.

[100] M. C. Flemings, “Solidification processing,” *Metall. Trans.*, vol. 5, no. 10, pp. 2121–2134, 1974, doi: 10.1007/BF02643923.

[101] D. Zhang, “Characterisation and Modelling of Segregation in Continuously Cast Steel Slab,” University of Birmingham, 2015.

[102] D. G. R. William D. Callister, Jr., “8.6 Fracture Toughness Testing,” *Mater. Sci. Eng. an Introd.*, vol. 1, pp. 250–255, 2010, doi: 10.1017/CBO9781107415324.004.

[103] C. Slater, A. Mandal, and C. Davis, “The Influence of Segregation of Mn on the Recrystallization Behavior of C-Mn Steels,” *Metall. Mater. Trans. B*

Process Metall. Mater. Process. Sci., 2019, doi: 10.1007/s11663-019-01603-2.

[104] E. A. Brandes and G. B. Brook, Eds., *Smithells Metals Reference Book*, 7th Editio. London, 1998.

[105] P. J. Alberry and C. W. Haworth, "Interdiffusion of Cr, Mo, and W in Iron," *Met. Sci.*, vol. 8, no. 1, pp. 407–412, 1974, doi: 10.1179/msc.1974.8.1.407.

[106] L. Gui *et al.*, "Effects of Inclusion Precipitation, Partition Coefficient, and Phase Transition on Microsegregation for High-Sulfur Steel Solidification," *Metall. Mater. Trans. B Process Metall. Mater. Process. Sci.*, vol. 49, no. 6, pp. 3280–3292, 2018, doi: 10.1007/s11663-018-1401-x.

[107] M. Daamen, P. Von Schweinichen, S. Richter, G. Hirt, and D. Senk, "Strip casting and ingot casting : comparison of different cooling conditions regarding the as- cast quality," *8th Eur. Contin. Cast. Conf. , Graz , Austria , ECCC 2014*, no. June, 2014.

[108] C. Zhang, A. Loucif, M. Jahazi, R. Tremblay, and L. P. Lapierre, "On the effect of filling rate on positive macrosegregation patterns in large size cast steel ingots," *Appl. Sci.*, vol. 8, no. 10, 2018, doi: 10.3390/app8101878.

[109] S. K. Choudhary and S. Ganguly, "Morphology and segregation in continuously cast high carbon steel billets," *ISIJ Int.*, vol. 47, no. 12, pp. 1759–1766, 2007, doi: 10.2355/isijinternational.47.1759.

[110] M. Alizadeh, "Correlation between the continuous casting parameters and secondary dendrite arm spacing in the mold region," *Mater. Lett.*, vol. 91, pp. 146–149, 2013, doi: 10.1016/j.matlet.2012.09.108.

[111] D. Zhang and M. Strangwood, "Interdendritic microsegregation development of high-strength low-alloy steels during continuous casting process," *Mater. Sci. Technol. (United Kingdom)*, vol. 35, no. 11, pp. 1337–1346, 2019, doi: 10.1080/02670836.2019.1624016.

[112] A. Suzuki, T. Suzuki, Y. Nagaoka, and Y. Iwata, "On Secondary Dendrite Arm Spacing in Commercial Carbon Steels with Different Carbon Content," *Journal of the Japan Institute of Metals*, vol. 32, no. 12. pp. 1301–1305, 1968, doi: 10.2320/jinstmet1952.32.12_1301.

[113] E. J. Pickering, “Macrosegregation in steel ingots: The applicability of modelling and characterisation techniques,” *ISIJ Int.*, vol. 53, no. 6, pp. 935–949, 2013, doi: 10.2355/isijinternational.53.935.

[114] M. Wu, A. Ludwig, and A. Kharicha, “Simulation of As-Cast Steel Ingots,” *Steel Res. Int.*, vol. 89, no. 1, 2017, doi: 10.1002/srin.201700037.

[115] G. Lesoult, “Macrosegregation in steel strands and ingots: Characterisation, formation and consequences,” *Mater. Sci. Eng. A*, vol. 413–414, pp. 19–29, 2005, doi: 10.1016/j.msea.2005.08.203.

[116] M. Kohno, M. Miyakawa, S. Kinoshita, and A. Suzuki, “Effect of Chemical Composition on Properties of High Purity 3. 5 NiCrMoV Steel Forging,” in *Advances in Material Technology for Fossil Power Plants*, 1987, pp. 81–88.

[117] E. Entezari, B. Avishan, H. Mousalou, and S. Yazdani, “Effect of Electro Slag Remelting (ESR) on the microstructure and mechanical properties of low carbon bainitic steel,” *Kov. Mater.*, vol. 56, no. 4, pp. 253–263, 2018, doi: 10.4149/km_2018_4_253.

[118] C. Bin Shi, X. C. Chen, H. J. Guo, Z. J. Zhu, and H. Ren, “Assessment of oxygen control and its effect on inclusion characteristics during electroslag remelting of die steel,” *Steel Res. Int.*, 2012, doi: 10.1002/srin.201100200.

[119] Q. Wang, X. J. Wang, G. Q. Li, and Y. Liu, “Investigation on Band Segregate Formation during the Electroslag Remelting of H13 Die Steel,” *IOP Conf. Ser. Mater. Sci. Eng.*, vol. 529, no. 1, 2019, doi: 10.1088/1757-899X/529/1/012064.

[120] Y. Liu, Z. Zhang, G. Li, Q. Wang, L. Wang, and B. Li, “The structural evolution and segregation in a dual alloy ingot processed by electroslag remelting,” *Metals (Basel).*, vol. 6, no. 12, pp. 1–11, 2016, doi: 10.3390/met6120325.

[121] W. Yan, Y. Zhang, W. Chen, and J. Li, “Characteristics and formation tendency of freckle segregation in electroslag remelted bearing steel,” *Metals (Basel).*, vol. 10, no. 2, 2020, doi: 10.3390/met10020246.

[122] Q. T. Zhu, J. Li, J. Zhang, C. Bin Shi, J. H. Li, and J. Huang, “Precipitation Mechanism and Reduction of Amount of Primary Carbides During Electroslag Remelting of 8Cr13MoV Stainless Steel,” *Metall. Mater. Trans. B Process*

Metall. Mater. Process. Sci., vol. 50, no. 3, pp. 1365–1377, 2019, doi: 10.1007/s11663-019-01573-5.

[123] T. Xuwei and Z. Rong, "Study of Cleanliness of High Nitrogen Steel in ESR," in *Energy Materials CONFERENCE PROCEEDINGS 2014*, 2019, pp. 343–351.

[124] A. Di Gianfrancesco and R. Blum, "A-USC programs in the European Union," in *Materials for Ultra-Supercritical and Advanced Ultra-Supercritical Power Plants*, Elsevier, 2017, pp. 773–846.

[125] M. S. Garcia, "EFFECT OF MATERIALS HETEROGENEITIES ON MECHANICAL PROPERTIES AT INITIAL STATE," 2018.

[126] T. Hardin, "Carbon Macrosegregation in Large Forgings," Rockville, 2017.

[127] H. Li, H. Yang, and Z. Zhang, "Hot Tube-Forming," in *Comprehensive Materials Processing*, vol. 5, 2014, pp. 321–350.

[128] G. Alves dos Santos *et al.*, *Engineering design applications 2: Structures, materials and processes*, vol. 113. 2020.

[129] P. D. Jablonski and J. A. Hawk, "Homogenizing Advanced Alloys: Thermodynamic and Kinetic Simulations Followed by Experimental Results," *J. Mater. Eng. Perform.*, vol. 26, no. 1, pp. 4–13, 2017, doi: 10.1007/s11665-016-2451-3.

[130] K. Li, M. A. Klecka, S. Chen, and W. Xiong, "Wire-arc additive manufacturing and post-heat treatment optimization on microstructure and mechanical properties of Grade 91 steel," *Addit. Manuf.*, vol. 37, no. June 2020, p. 101734, 2021, doi: 10.1016/j.addma.2020.101734.

[131] Y. Fukuda, Y. Kado, T. Yoshikawa, K. Oishi, and Y. Mae, "Diffusion distances of the constituent atoms in the metallurgical phenomena such as recovery, recrystallization, grain growth, and aging in aluminum and copper alloys," *J. Mater. Eng. Perform.*, vol. 11, no. 5, pp. 544–550, 2002, doi: 10.1361/105994902770343809.

[132] B. Wang *et al.*, "Thermal simulation study on the solidification structure and segregation of a heavy heat-resistant steel casting," *Metals (Basel).*, 2019, doi:

10.3390/met9020249.

[133] J. A. Siefert, J. P. Shingledecker, and J. D. Parker, “Optimization of Vickers Hardness Parameters for Micro- And Macro-Indentation of Grade 91 Steel,” *J. Test. Eval.*, vol. 41, no. 5, p. 20120290, 2013, doi: 10.1520/jte20120290.

[134] M. L. Santella, R. W. Swindeman, R. W. Reed, and J. M. Tanzosh, “Martensite transformation, microsegregation, and creep strength of 9 Cr-1 Mo-V steel weld metal,” *ASM Proc. Int. Conf. Trends Weld. Res.*, pp. 713–718, 2002.

[135] F. Wang, C. Davis, and M. Strangwood, “Grain growth on reheating for an as-cast Al-Nb-containing steel with segregated composition,” *Mater. Sci. Technol. (United Kingdom)*, 2019, doi: 10.1080/02670836.2019.1577533.

[136] S. Zheng, C. Davis, and M. Strangwood, “Elemental segregation and subsequent precipitation during solidification of continuous cast Nb-V-Ti high-strength low-alloy steels,” *Mater. Charact.*, 2014, doi: 10.1016/j.matchar.2014.06.008.

[137] D. Chakrabarti, M. Strangwood, and C. Davis, “Effect of bimodal grain size distribution on scatter in toughness,” *Metall. Mater. Trans. A Phys. Metall. Mater. Sci.*, 2009, doi: 10.1007/s11661-009-9794-4.

[138] S. K. Sarna, “Inclusions, Inclusion Engineering and Clean Steels,” 2021. [Online]. Available: https://www.ispatguru.com/inclusions-inclusion-engineering-and-clean-steels/. [Accessed: 25-Aug-2022].

[139] Q. Chen, E. Shao, D. Zhao, J. Guo, and Z. Fan, “Measurement of the critical size of inclusions initiating contact fatigue cracks and its application in bearing steel,” *Wear*, vol. 147, no. 2, pp. 285–294, 1991, doi: 10.1016/0043-1648(91)90186-X.

[140] Z. G. Yang *et al.*, “On the critical inclusion size of high strength steels under ultra-high cycle fatigue,” *Mater. Sci. Eng. A*, vol. 427, no. 1–2, pp. 167–174, 2006, doi: 10.1016/j.msea.2006.04.068.

[141] G. Kraus, “Primary Processing Effects on Steel Microstructure and Properties,” *Steels Process. Struct. Perform.*, pp. 149–175, 2005.

[142] L. Zhang, B. G. Thomas, X. Wang, and K. Cai, “Evaluation and control of steel

cleanliness - Review," *Steelmak. Conf. Proc.*, vol. 85, pp. 431–452, 2002.

[143] B. G. Thomas, "Modeling of the continuous casting of steel - Past, present, and future," *Metall. Mater. Trans. B Process Metall. Mater. Process. Sci.*, vol. 33, no. 6, pp. 795–812, 2002, doi: 10.1007/s11663-002-0063-9.

[144] E. S. Persson, A. Karasev, A. Mitchell, and P. G. Jönsson, "Origin of the inclusions in production-scale electrodes, esr ingots, and pesr ingots in a martensitic stainless steel," *Metals (Basel).*, vol. 10, no. 12, pp. 1–16, 2020, doi: 10.3390/met10121620.

[145] T W Miller, J. Jimenez, A. Sharan, and D. A. Goldstein, "The Making, Shaping and Treating of Steel, 11th Edition Steelmaking and refining Volume.," *AISE Steel Found.*, 1998, doi: 10.1017/CBO9781107415324.004.

[146] A. L. V. Da Costa E Silva, "The effects of non-metallic inclusions on properties relevant to the performance of steel in structural and mechanical applications," *J. Mater. Res. Technol.*, vol. 8, no. 2, pp. 2408–2422, 2019, doi: 10.1016/j.jmrt.2019.01.009.

[147] L. Zhang and B. G. Thomas, "State of the art in evaluation and control of steel cleanliness," *ISIJ Int.*, vol. 43, no. 3, pp. 271–291, 2003, doi: 10.2355/isijinternational.43.271.

[148] L. Zhang and B. G. Thomas, "State of the art in the control of inclusions during steel ingot casting," *Metall. Mater. Trans. B Process Metall. Mater. Process. Sci.*, vol. 37, no. 5, pp. 733–761, 2006, doi: 10.1007/s11663-006-0057-0.

[149] C. E. SIMS and F. B. DAHLE, "Effect of Aluminium on the properties of medium carbon cast steel," *Trans. Am. Foundrym. Soc*, vol. 46, pp. 65–132, 1938.

[150] X. jing Shao, X. hua Wang, C. xi Ji, H. bo Li, Y. Cui, and G. sen Zhu, "Morphology, size and distribution of MnS inclusions in non-quenched and tempered steel during heat treatment," *Int. J. Miner. Metall. Mater.*, vol. 22, no. 5, pp. 483–491, 2015, doi: 10.1007/s12613-015-1097-8.

[151] E. Pessard, F. Morel, C. Verdu, L. Flacelière, and G. Baudry, "Microstructural heterogeneities and fatigue anisotropy of forged steels," *Mater. Sci. Eng. A*, vol.

529, no. 1, pp. 289–299, 2011, doi: 10.1016/j.msea.2011.09.031.

[152] D. You, S. K. Michelic, G. Wieser, and C. Bernhard, “Modeling of manganese sulfide formation during the solidification of steel,” *J. Mater. Sci.*, vol. 52, no. 3, pp. 1797–1812, 2017, doi: 10.1007/s10853-016-0470-y.

[153] Z. Liu, Y. Kobayashi, J. Yang, K. Nagai, and M. Kuwabara, “Morphology and precipitation mechanism of copper sulfide in strip casting of low carbon steels,” *AISTech - Iron Steel Technol. Conf. Proc.*, vol. 1, no. May, pp. 891–902, 2006, doi: 10.13140/RG.2.1.3147.4963.

[154] A. Takahashi and M. Iino, “Microstructural refinement by Cu addition and its effect on strengthening and toughening of sour service line pipe steels,” *ISIJ Int.*, vol. 36, no. 2, pp. 241–245, 1996, doi: 10.2355/isijinternational.36.241.

[155] Z. Liu, Y. Kobayashi, and K. Nagai, “Effect of Nano-Scale Copper Sulfide Particles on the Yield Strength and Work Hardening Ability in Strip Casting Low Carbon Steel,” *Mater. Trans.*, vol. 45, no. 2, pp. 479–487, 2004, doi: 10.2320/matertrans.45.479.

[156] R. S. Lillard, M. A. Kashfipour, and W. Niu, “Pit Propagation at the Boundary between Manganese Sulfide Inclusions and Austenitic Stainless Steel 303 and the Role of Copper,” *J. Electrochem. Soc.*, vol. 163, no. 8, pp. C440–C451, 2016, doi: 10.1149/2.0461608jes.

[157] Z. Z. Liu, M. Kuwabara, B. H. Li, Y. Kobayashi, and K. Nagai, “Precipitation of Copper Sulfide and its effect on the Microstructure and Properties of Steel,” *Steel Res. Int.*, vol. 82, no. 5, pp. 557–565, 2011, doi: 10.1002/srin.201100037.

[158] J. Burja, M. Koležnik, Š. Župerl, and G. Klančnik, “Nitrogen and nitride non-metallic inclusions in steel,” *Mater. Tehnol.*, vol. 53, no. 6, pp. 919–928, 2019, doi: 10.17222/mit.2019.247.

[159] P. V. Bizyukov and S. R. Giese, “Effects of Zr, Ti, and Al Additions on Nonmetallic Inclusions and Impact Toughness of Cast Low-Alloy Steel,” *J. Mater. Eng. Perform.*, vol. 26, no. 4, pp. 1878–1889, 2017, doi: 10.1007/s11665-017-2583-0.

[160] L. P. Zhang, C. L. Davis, and M. Strangwood, “Dependency of fracture

toughness on the inhomogeneity of coarse TiN particle distribution in a low alloy steel," *Metall. Mater. Trans. A Phys. Metall. Mater. Sci.*, vol. 32, no. 5, pp. 1147–1155, 2001, doi: 10.1007/s11661-001-0125-7.

[161] L. P. Zhang, C. L. Davis, and M. Strangwood, "Effect of TiN particles and microstructure on fracture toughness in simulated heat-affected zones of a structural steel," *Metall. Mater. Trans. A Phys. Metall. Mater. Sci.*, vol. 30, no. 8, pp. 2089–2096, 1999, doi: 10.1007/s11661-999-0019-7.

[162] A. L. V. Da Costa E Silva, "Non-metallic inclusions in steels - Origin and control," *J. Mater. Res. Technol.*, vol. 7, no. 3, pp. 283–299, 2018, doi: 10.1016/j.jmrt.2018.04.003.

[163] S. Ji, L. Zhang, Y. Wang, W. Chen, X. Wang, and J. Zhang, "Effect of Electromagnetic Stirring on Inclusions in Continuous Casting Blooms of a Gear Steel," *Metall. Mater. Trans. B Process Metall. Mater. Process. Sci.*, vol. 52, no. 4, pp. 2341–2354, 2021, doi: 10.1007/s11663-021-02176-9.

[164] "ASTM E45-18a, Standard Test Methods for Determining the Inclusion Content of Steel, ASTM International, West Conshohocken, PA, 2018," .

[165] B. Bandi, B. Santillana, W. Tiekink, N. Koura, M. Williams, and P. Srirangam, "2D automated SEM and 3D X-ray computed tomography study on inclusion analysis of steels," *Ironmak. Steelmak.*, 2020, doi: 10.1080/03019233.2019.1652437.

[166] ASTM Committee E04, "ASTM E2142: Standard Test Methods for Rating and Classifying Inclusions in Steel Using the Scanning Electron Microscope," *Astm*, 2011, doi: 10.1520/E2142-08.Copyright.

[167] B. G. Bartosiaki, J. A. M. Pereira, W. V. Bielefeldt, and A. C. F. Vilela, "Assessment of inclusion analysis via manual and automated SEM and total oxygen content of steel," *J. Mater. Res. Technol.*, vol. 4, no. 3, pp. 235–240, 2015, doi: 10.1016/j.jmrt.2015.01.008.

[168] T. Saitoh, T. Kikuchi, and K. Furuya, "Application of laser microprobe mass spectrometry (LAMMS) to a state analysis of nonmetallic inclusions and precipitates in a Ti-added ultra low carbon steel," *ISIJ Int.*, vol. 36, no. SUPPL.,

pp. 21–24, 1996, doi: 10.2355/isijinternational.36.suppl_s121.

[169] J. G. Newman *et al.*, “Auger Electron Spectroscopy Analysis of Pit Initiation at MnS Nano-inclusions in Carbon Steel,” *Microsc. Microanal.*, vol. 23, no. S1, pp. 2258–2259, 2017, doi: 10.1017/s1431927617011953.

[170] Y. Kim *et al.*, “Detection of micro inclusions in steel sheets using high-frequency ultrasound speckle analysis,” *Sci. Rep.*, vol. 11, no. 1, pp. 1–12, 2021, doi: 10.1038/s41598-021-99907-4.

[171] H. Gruber, C. Luchian, E. Hryha, and L. Nyborg, “Effect of Powder Recycling on Defect Formation in Electron Beam Melted Alloy 718,” *Metall. Mater. Trans. A Phys. Metall. Mater. Sci.*, vol. 51, no. 5, pp. 2430–2443, 2020, doi: 10.1007/s11661-020-05674-8.

[172] J. Crahay, J. Edmundson, and A. Giannetti, “Technical Steel Research,” 2005.

[173] Y. Ren and L. Zhang, “Thermodynamic model for prediction of slag-steel-inclusion reactions of 304 stainless steels,” *ISIJ Int.*, vol. 57, no. 1, pp. 68–75, 2017, doi: 10.2355/isijinternational.ISIJINT-2016-509.

[174] K. Li, E. Halasz, and J.-M. Bohlen, “Ultra-fast quantitative analysis of non-metallic inclusions in steel,” *Finish. Process.*, pp. 179–182, 2011.

[175] L. Zhang and B. G. Thomas, “Inclusions in continuous casting of steel,” *XXIV Natl. Steelmak. Symp.*, pp. 138–183, 2003.

[176] ASTM, “E45-18a Standard Test Methods for Determining the Inclusion Content of Steel,” *ASTM Int. Conshohocken, PA, www.astm.org*, 2018, doi: 10.1520/E0045-18A.

[177] P. Kaushik, H. Pielet, and H. Yin, “Inclusion characterisation - Tool for measurement of steel cleanliness and process control: Part 1,” *Ironmak. Steelmak.*, vol. 36, no. 8, pp. 561–571, 2009, doi: 10.1179/030192309X12492910938131.

[178] R. Roberti and M. Faccoli, “On the step cooling treatment for the assessment of temper embrittlement susceptibility of heavy forgings in superclean steels,” *Metals (Basel).*, vol. 6, no. 10, 2016, doi: 10.3390/met6100239.

[179] M. Nuspl, W. Wegscheider, J. Angeli, W. Posch, and M. Mayr, “Qualitative and quantitative determination of micro-inclusions by automated SEM/EDX analysis,” *Anal. Bioanal. Chem.*, vol. 379, no. 4, pp. 640–645, 2004, doi: 10.1007/s00216-004-2528-y.

[180] W. Winkler, J. Angeli, and M. Mayr, “Automated SEM-EDX Cleanness Analysis and its Application in Metallurgy,” *BHM Berg- und Hüttenmännische Monatshefte*, vol. 152, no. 1, pp. 4–9, 2007.

[181] S. K. Michelic, G. Wieser, and C. Bernhard, “On the representativeness of automated SEM/EDS analyses for inclusion characterisation with special Regard to the measured sample area,” *ISIJ Int.*, vol. 51, no. 5, pp. 769–775, 2011, doi: 10.2355/isijinternational.51.769.

[182] L. E. K. Holappa and A. S. Helle, “Inclusion Control in High-Performance Steels,” *J. Mater. Process. Tech.*, vol. 53, no. 1–2, pp. 177–186, 1995, doi: 10.1016/0924-0136(95)01974-J.

[183] P. A. Thornton, “The influence of nonmetallic inclusions on the mechanical properties of steel: A review,” *J. Mater. Sci.*, vol. 6, no. 4, pp. 347–356, 1971, doi: 10.1007/PL00020378.

[184] J. Maciejewski, “The Effects of Sulfide Inclusions on Mechanical Properties and Failures of Steel Components,” *J. Fail. Anal. Prev.*, 2015, doi: 10.1007/s11668-015-9940-9.

[185] D. Spriestersbach, P. Grad, and E. Kerscher, “Influence of different non-metallic inclusion types on the crack initiation in high-strength steels in the VHCF regime,” *Int. J. Fatigue*, vol. 64, pp. 114–120, 2014, doi: 10.1016/j.ijfatigue.2014.03.003.

[186] J. Villavicencio, N. Ulloa, L. Lozada, M. Moreno, and L. Castro, “The role of non-metallic Al2O3 inclusions, heat treatments and microstructure on the corrosion resistance of an API 5L X42 steel,” *J. Mater. Res. Technol.*, vol. 9, no. 3, pp. 5894–5911, 2020, doi: 10.1016/j.jmrt.2020.03.116.

[187] X. Ma and D. Li, “Characterization and analysis about the heterogeneity of inclusions in a 500kg steel ball,” *Int. J. Cast Met. Res.*, vol. 32, no. 3, pp. 135–

144, 2019, doi: 10.1080/13640461.2018.1558965.

[188] F. H. Norton, *The creep of steel at high temperatures*. 1929.

[189] F. X. Liu, A. C. F. Cocks, and E. Tarleton, "Dislocation dynamics modelling of the creep behaviour of particle-strengthened materials," *Proc. R. Soc. A Math. Phys. Eng. Sci.*, 2021, doi: 10.1098/rspa.2021.0083.

[190] Z. Zhuang, Z. Liu, and Y. Cui, *Dislocation Mechanism-Based Crystal Plasticity*. 2019.

[191] M. E. Kassner and T. A. Hayes, "Creep cavitation in metals," *Int. J. Plast.*, vol. 19, no. 10, pp. 1715–1748, 2003, doi: 10.1016/S0749-6419(02)00111-0.

[192] Y. Gu, G. D. West, R. C. Thomson, and J. Parker, "Investigation of creep damage and cavitation mechanisms in P92 steels," in *Advances in Materials Technology for Fossil Power Plants - Proceedings from the 7th International Conference*, 2014.

[193] Q. Zhao, T. Li, X. Deng, and D. Cheng, "Microstructural evolution of P92 steel during creep," *Adv. Mater. Technol. Foss. Power Plants - Proc. from 6th Int. Conf.*, no. June, pp. 693–704, 2011.

[194] A. Benaarbia, X. Xu, W. Sun, A. A. Becker, and M. A. E. Jepson, "Investigation of short-term creep deformation mechanisms in MarBN steel at elevated temperatures," *Mater. Sci. Eng. A*, vol. 734, no. May, pp. 491–505, 2018, doi: 10.1016/j.msea.2018.06.063.

[195] S. D. Yadav, B. Sonderegger, B. Sartory, C. Sommitsch, and C. Poletti, "Characterisation and quantification of cavities in 9Cr martensitic steel for power plants," *Mater. Sci. Technol. (United Kingdom)*, vol. 31, no. 5, pp. 554–564, 2015, doi: 10.1179/1743284714Y.0000000635.

[196] A. International, "ASTM A182/A182M - 20 - Standard specification for forged or rolled alloy-steel pipe flanges , forged fittings , and valves and parts for high-temperature service," *Society*, 2004.

[197] F. Abe, *Grade 91 heat-resistant martensitic steel*, vol. 91. Woodhead Publishing Limited, 2014.

[198] ASTM-E384, “Knoop and Vickers Hardness of Materials,” *ASTM Stand.*, pp. 1–43, 2012, doi: 10.1520/E0384-11E01.2.

[199] D. W. Hetzner, “Developing ASTM E 2283: Standard practice for extreme value analysis of nonmetallic inclusions in steel and other microstructural features,” *J. ASTM Int.*, 2006, doi: 10.1520/JAI100418.

[200] G. E. Lloyd, “Atomic number and crystallographic contrast images with the SEM: a review of backscattered electron techniques,” *Mineral. Mag.*, vol. 51, no. 359, pp. 3–19, 1987, doi: 10.1180/minmag.1987.051.359.02.

[201] R. Bourne and R. Bourne, “ImageJ,” in *Fundamentals of Digital Imaging in Medicine*, 2010.

[202] N. W. M. Ritchie, “Getting Started with NIST DTSA-II,” *Micros. Today*, vol. 19, no. 1, pp. 26–31, 2011, doi: 10.1017/s155192951000132x.

[203] G. S. Wojcik, “Determining the uncertainty of x-Ray absorption measurements,” *J. Res. Natl. Inst. Stand. Technol.*, vol. 109, no. 5, pp. 479–496, 2004, doi: 10.6028/jres.109.035.

[204] L. Korcakova, J. Hald, and M. A. J. Somers, “Quantification of Laves phase particle size in 9CrW steel,” *Mater. Charact.*, 2001, doi: 10.1016/S1044-5803(01)00159-0.

[205] Q. Li, “Precipitation of Fe2W laves phase and modeling of its direct influence on the strength of a 12Cr-2W steel,” *Metall. Mater. Trans. A Phys. Metall. Mater. Sci.*, 2006, doi: 10.1007/s11661-006-0155-2.

[206] F. Abe, “Analysis of creep rates of tempered martensitic 9%Cr steel based on microstructure evolution,” *Mater. Sci. Eng. A*, vol. 510–511, no. C, pp. 64–69, 2009, doi: 10.1016/j.msea.2008.04.118.

[207] J. I. Goldstein, D. E. Newbury, J. R. Michael, N. W. M. Ritchie, J. H. J. Scott, and D. C. Joy, *Scanning electron microscopy and x-ray microanalysis*. 2017.

[208] E. D. Boyes, “Analytical potential of EDS at low voltages,” *Mikrochim. Acta*, vol. 138–139, no. 138/3-4,139/1-4, pp. 225–234, 2002, doi: 10.1007/s006040200026.

[209] M. Lückl, T. Wojcik, E. Povoden-Karadeniz, S. Zamberger, and E. Kozeschnik, “Co-Precipitation Behavior of MnS and AlN in a Low-Carbon Steel,” *Steel Res. Int.*, vol. 89, no. 3, pp. 1–9, 2018, doi: 10.1002/srin.201700342.

[210] Steel Data, “Top pouring and bottom pouring for conventional ingot casting,” 2018. [Online]. Available: https://www.steeldata.info/inclusions/demo/help/ingot.html. [Accessed: 23-Aug-2022].

Appendix A

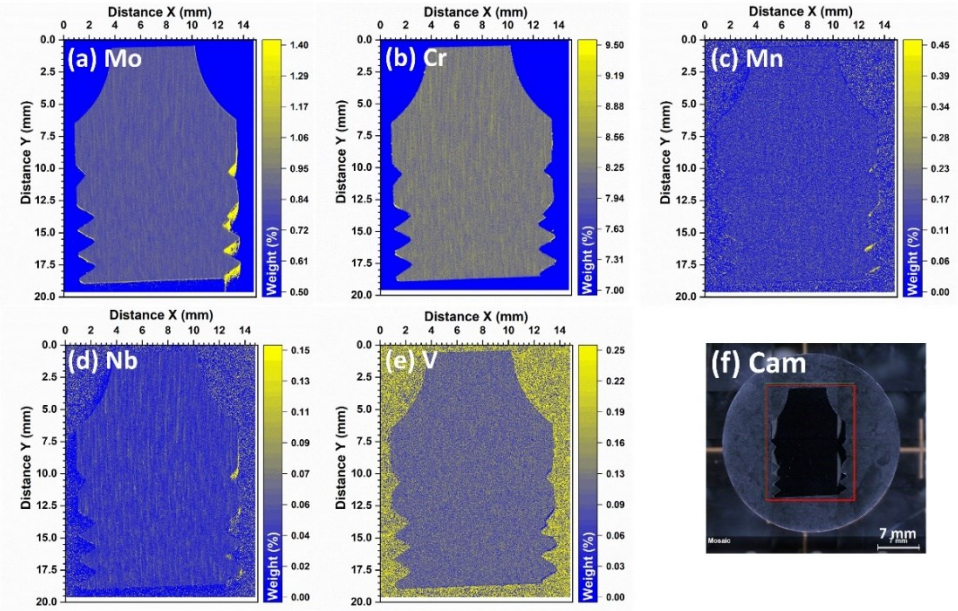

Figure 8.1: Centimetre-scale µ-XRF chemical distribution maps of steel ORNL-P from the head section, highlighting the chemical inhomogeneity in some of the major alloying elements (a) Mo (b) Cr (c) Mn (d) Nb (e) V (f) Navigation camera/mapped area photo (Red rectangle signifies mapped regions).

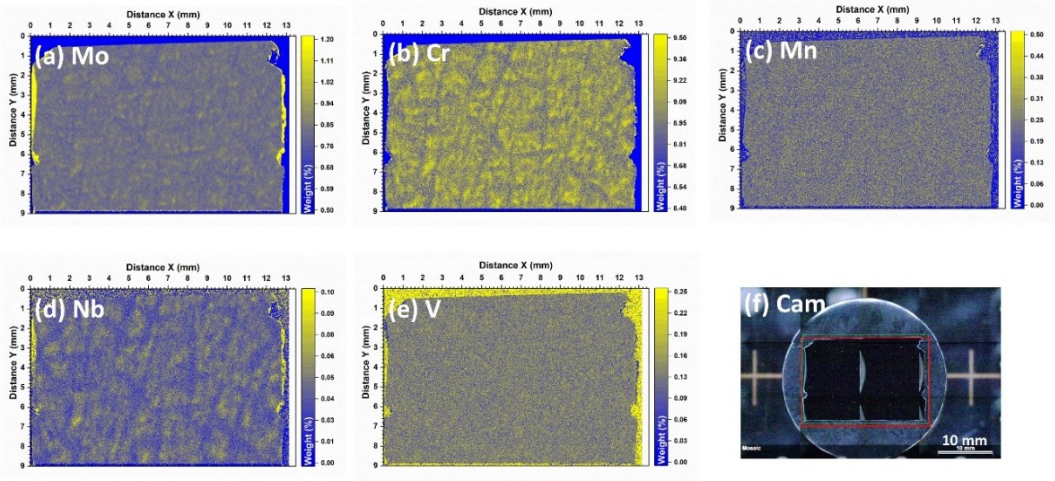

Figure 8.2: Centimetre-scale µ-XRF chemical distribution maps of steel ORNL-F from the head section, highlighting the chemical inhomogeneity in some of the major alloying elements (a) Mo (b) Cr (c) Mn (d) Nb (e) V (f) Navigation camera/mapped area photo (Red rectangle signifies mapped regions).

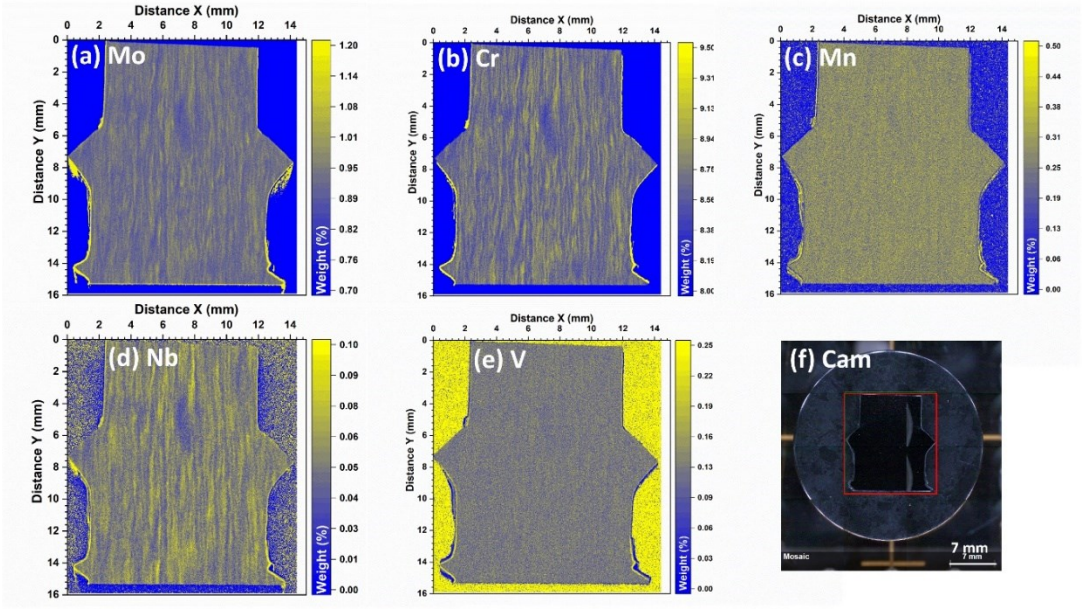

Figure 8.3: Centimetre-scale µ-XRF chemical distribution maps of steel Euro-Pi from the head section, highlighting the chemical inhomogeneity in some of the major alloying elements (a) Mo (b) Cr (c) Mn (d) Nb (e) V (f) Navigation camera/mapped area photo (Red rectangle signifies mapped regions).

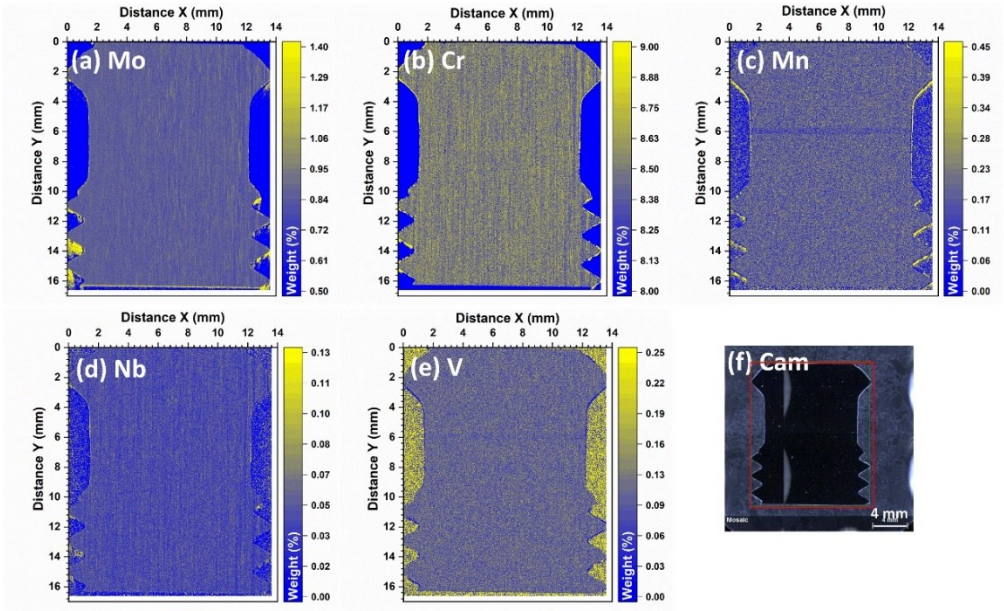

Figure 8.4: Centimetre-scale µ-XRF chemical distribution maps of steel Euro-P2 from the head section, highlighting the chemical inhomogeneity in some of the major alloying elements (a) Mo (b) Cr (c) Mn (d) Nb (e) V (f) Navigation camera/mapped area photo (Red rectangle signifies mapped regions).

Appendix B

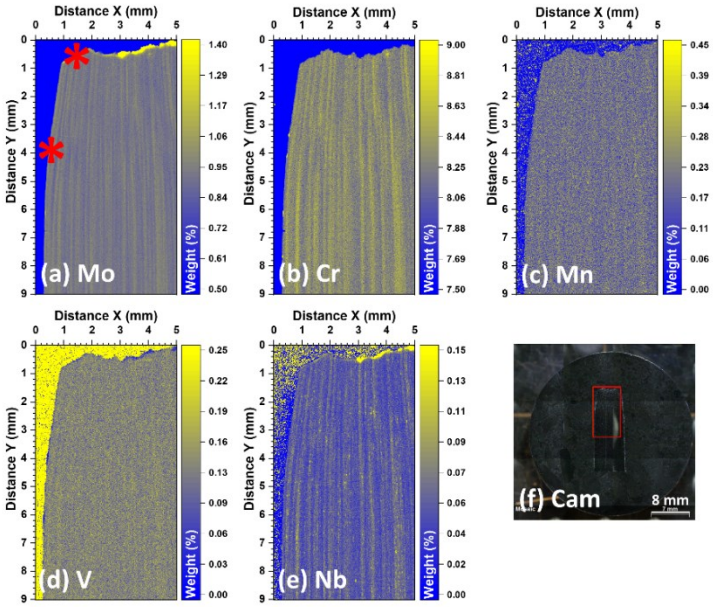

Figure 8.5: µ-XRF chemical distribution maps of steel ORNL-P from the gauge section, highlighting the chemical inhomogeneity in some of the major alloying elements (a) Mo (b) Cr (c) Mn (d) Nb (e) V (f) Navigation camera/mapped area photo (Red rectangle signifies mapped regions). (Asterisk marks the edges of the steel sample, these points were used as reference points for subsequent analysis in following chapters)

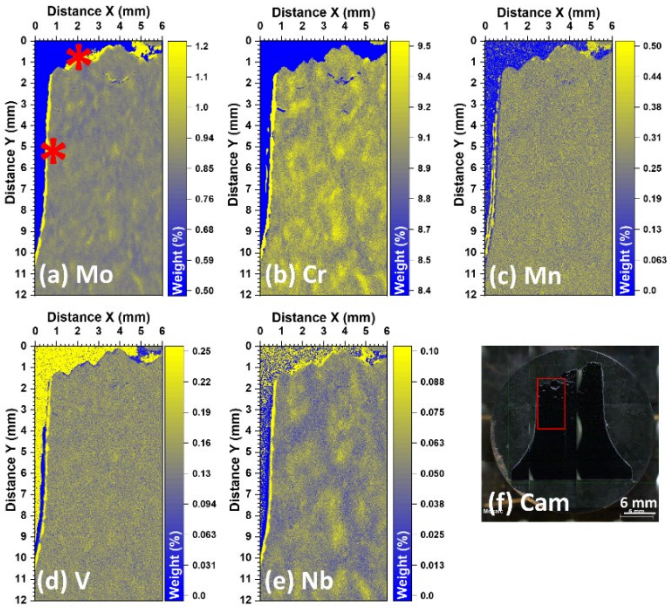

Figure 8.6: µ-XRF chemical distribution maps of steel ORNL-F from the gauge section, highlighting the chemical inhomogeneity in some of the major alloying elements (a) Mo (b) Cr (c) Mn (d) Nb (e) V (f) Navigation camera/mapped area photo (Red rectangle signifies mapped regions). (Asterisk marks the edges of the steel sample, these points were used as reference points for subsequent analysis in following chapters)

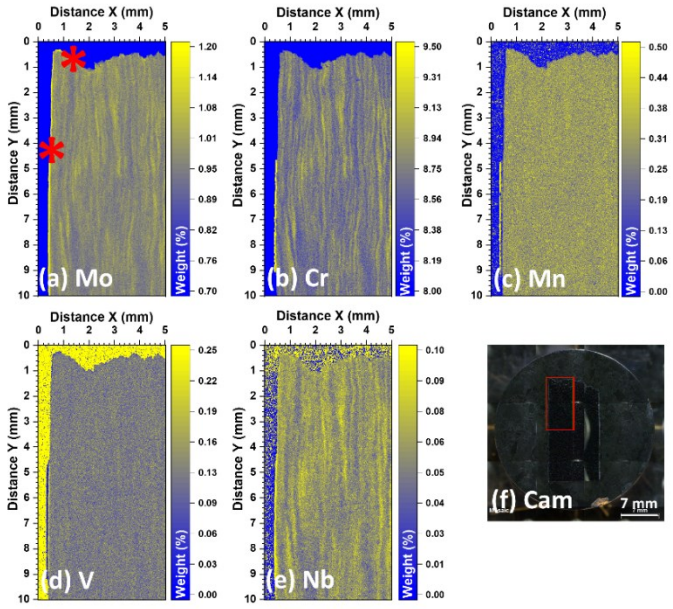

Figure 8.7: µ-XRF chemical distribution maps of steel Euro-Pi from the gauge section, highlighting the chemical inhomogeneity in some of the major alloying elements (a) Mo (b) Cr (c) Mn (d) Nb (e) V (f) Navigation camera/mapped area photo (Red rectangle signifies mapped regions). (Asterisk marks the edges of the steel sample, these points were used as reference points for subsequent analysis in following chapters)

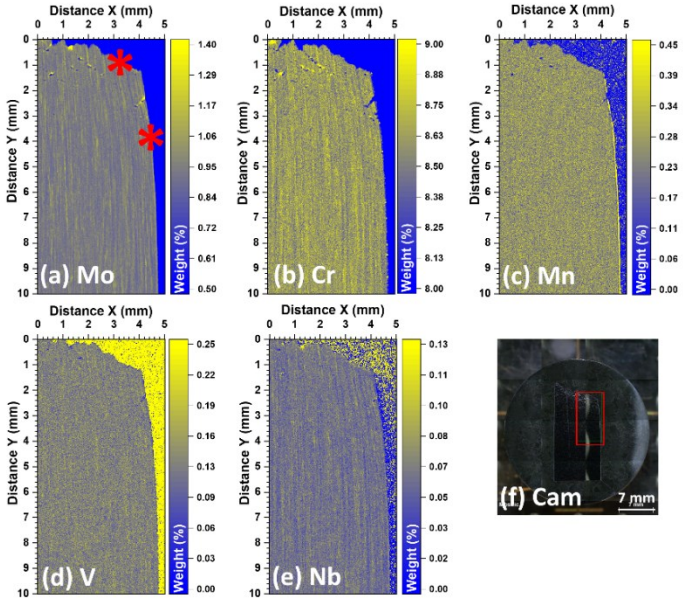

Figure 8.8: µ-XRF chemical distribution maps of steel Euro-P2 from the gauge section, highlighting the chemical inhomogeneity in some of the major alloying elements (a) Mo (b) Cr (c) Mn (d) Nb (e) V (f) Navigation camera/mapped area photo (Red rectangle signifies mapped regions). (Asterisk marks the edges of the steel sample, these points were used as reference points for subsequent analysis in following chapters)